Universidade do Minho
Instituto de Investigação em Biomateriais,
Biodegradáveis e Biomiméticos

Mariana Rodrigues de Carvalho

Tissue Engineered *In Vitro* Models on a Chip for Cancer Research

setembro de 2019

Tissue Engineered *In Vitro* Models on a Chip for Cancer Research
Mariana Rodrigues de Carvalho
UMinho | 2019

Universidade do Minho
Instituto de Investigação em Biomateriais,
Biodegradáveis e Biomiméticos

Mariana Rodrigues de Carvalho

Tissue Engineered *In Vitro* Models on a Chip for Cancer Research

Tese de Doutoramento em Engenharia de Tecidos, Medicina Regenerativa e Células Estaminais

Trabalho efetuado sob a orientação do
Professor Doutor Rui Luís Gonçalves dos Reis
e do
Doutor Joaquim Miguel Antunes Correia de Oliveira

setembro de 2019

ACKNOWLEDGMENTS

The preparation of this thesis would not be possible without the important contribution of several people, to which I am and always will be deeply thankful.

I would like to start by expressing my gratitude to my formal PhD supervisor, Prof. Rui Reis. He gave me the opportunity to join his research group as a researcher, and later as a PhD student, always supporting my work and progress. I would like to specially acknowledge his support and trust on me, for his huge assistance in the PhD scholarship application, and also for allowing me to work with such good co-supervisors. A special word of appreciation and gratitude goes to my co-supervisor, Dr. Joaquim Miguel Oliveira. Since the beginning I felt he accepted me and trusted me, as a person and as a researcher. Sometimes even acting as friend, always advising resilience, patience and hard work. A great person to share a beer after a conference or to discuss the best path of research, who understands the problems of life and of research. He trusted me with responsibilities and challenges, with goals that I didn't even know I could achieve. A big thank you to Dr. Roman Truckenmüller, Dr. Stephan Giselbrecht and Dr. Pamela Habibovic for giving me the opportunity to work at MERLN Institute, at Maastricht University. This world class institute provided me everything I needed to perform an excellent work. Especially friends such as David Barata, Liliana Teixeira and David Boaventura, who made my life richer, both professionally and personally. I am very grateful to my colleagues and friends in 3B's research group. We shared the good, the bad and the worst moments together, frustrations and achievements. They know who they are! A huge and special thank you to Raquel Maia, who I met during the "death valley" of my PhD, who basically thought me everything I know on science, thought me how to think and work rigorously. Thank you for always being bossy but always with a smile and a word of encouragement! To David Caballero, who joined me in a late phase of my PhD but gave me ideas and inputs that helped immensely. It was a great pleasure to work and learn from you. For all of these and much more, thank you David!

My truly and deeply-felt thanks to my parents, for being my safe harbor, my rock during the good and bad moments, for giving me much more than I could ever want or need, for making me the person I am today. I Love you so much! A big thank you to my twinnie sister, the best friend anyone could ever ask for, a part of me. Also, I can't forget to thank João, my new brother and faithful friend, always ready to help!

Finally, I acknowledge my PhD scholarship NORTE-08-5369-FSE-000044, funded by Programa Operacional Regional do Norte, Fundo Social Europeu, Norte2020 for the financial support.

STATEMENT OF INTEGRITY

I hereby declare having conducted this academic work with integrity. I confirm that I have not used plagiarism or any form of undue use of information or falsification of results along the process leading to its elaboration.

I further declare that I have fully acknowledged the Code of Ethical Conduct of the University of Minho.

ABSTRACT

Tissue Engineered *In Vitro* Models On A Chip For Cancer Research

By 2030, the global burden is expected to grow to 21.7 million new cancer cases and 13 million cancer deaths simply due to the growth and aging of the population. Among all types of cancer, colorectal cancer is a major cause of morbidity and mortality worldwide, and accounts for over 9 % of all cancer incidence. It is the third most common cancer worldwide and affects men and women equally.

In order to win the battle against cancer, further advances are in great need to unveil identification of cancer-causing agents in *in vitro* and *in vivo* animal models, as well as for the development of personalized therapies, drug screening, and to provide insightful knowledge on the mechanisms of tumor growth and metastasis. Microfluidic devices, together with tissue engineering strategies and nanotechnology have emerged as a powerful platform to tackle the previously mentioned hurdles. These themes are the focus of Section 1, in **Chapters I, II** and **III.**

In this thesis we focus on the application of CMCht/PAMAM dendrimer nanoparticles.as the synthesis, uptake efficiency/internalization and cytotoxic effect of fluorescent-labeled CMCht/PAMAM dendrimer nanoparticles was investigated using different cancer cell lines in both traditional culture flasks and under physiological flow inside a microfluidic platform (**Chapter V**). Other than nanoparticles, the use of different biomaterials to modulate 3D microenvironment of tumors is of the utmost importance. Therefore, the use of HRP-crosslinked SF hydrogels with spatial tunable properties was proposed in a colorectal cancer extravasation 3D model on a commercial chip Vena4™ (**Chapter VI**). To increase the complexity of the cancer models, a microfluidic chip was designed and fabricated for the incorporation of tumor and vascular parts, allowing for gradients of gemcitabine released from CMCht/PAMAM nanoparticles to be tested **(Chapter VII)**. Chemical modification in the CMCht/PAMAM dendrimer nanoparticles in order to target colorectal cancer was also achieved in **Chapter VIII**. In **Chapter IX,** a new proof of concept consisting of a microfluidic silk platform, flexible and implantable, was developed in house.

The results and platforms developed in this thesis are discussed in **Chapter X** and represent a strong advance in the field of lab-on-chip research and will be a useful tool for drug discovery and study of migration/metastasis phenomena, allowing for a versatile choice of tissues, biomaterials and biological assays.

Keywords: Biomaterials, Cancer models, Colorectal cancer, Microfluidics, Nanoparticles.

RESUMO

Modelos *In Vitro* Em Chips Baseados Na Engenharia De Tecidos Para Investigação Na Área Do Cancro

Até 2030, o número global de novos casos de cancro deverá crescer para 21,7 milhões, com cerca de 13 milhões de mortes, simplesmente devido ao crescimento e envelhecimento da população. Entre todos os tipos de cancro, o cancro colorretal é uma das principais causas de morbidade e mortalidade em todo o mundo, representando mais de 9 % entre todos os tipos de cancro. Com o objectivo de ganhar a guerra contra o cancro, novos avanços são rapidamente precisos, a fim de identificar, em modelos animais *in vitro* e *in vivo* os agentes causadores de cancro, bem como para o desenvolvimento de terapias personalizadas, teste de novos fármacos e aumentar o conhecimento actual sobre os mecanismos de crescimento tumoral e metástases. Dispositivos de microfluídica juntamente com estratégias de engenharia de tecidos e nanotecnologia surgiram como uma poderosa plataforma para lidar com os obstáculos mencionados anteriormente. Esses temas são o foco da Secção 1, nos **Capítulos I**, **II e III.** Nesta tese damos enfâse à aplicação de nanopartículas CMCht/PAMAM. A síntese, eficiência, internalização e efeito citotóxico das mesmas foram investigados usando diferentes linhas de células tumorais em frascos de cultura tradicionais e dentro de uma plataforma microfluídica (**Capítulo V**). Além das nanopartículas, o uso de diferentes biomateriais para modular o microambiente 3D de tumores é de extrema importância. Portanto, o uso de hidrogéis SF reticulados com HRP com propriedades mecânicas ajustáveis foi proposto num modelo 3D de extravasamento de cancro colorretal num chip comercial VenaT4™ **(Capítulo VI)**. Para aumentar a complexidade dos modelos de cancro em chips, uma plataforma microfluídica foi projetada e fabricada para a incorporação de ambas as partes tumorais e vasculares, permitindo testar gradientes de gemcitabina libertados das nanopartículas CMCht/PAMAM **(Capítulo VII)**. Modificações químicas nas nanopartículas para atingir especificamente células cancerígenas também foram alcançadas no **Capítulo VIII**. No **Capítulo IX**, uma nova prova de conceito consistindo numa plataforma microfluídica de seda, totalmente flexível e implantável, foi desenvolvida. Os resultados e plataformas desenvolvidos nesta tese representam um forte avanço no campo da investigação do cancro, e serão uma ferramenta útil para a descoberta de drogas e estudo de metastases, permitindo uma escolha versátil de tecidos, hidrogéis e ensaios biológicos.

Palavras-chave: Biomateriais, Cancro colorrectal, Microfluídica, Modelos de cancro, Nanopartículas.

TABLE OF CONTENTS

LIST OF ABBREVIATIONS

α – Alpha

AB – Alamar blue

Abs – Absorbance

ADSCs – Adipose-derived stem cells

AFM – Atomic force microscopy

AgNPs – Silver nanoparticles

ANOVA – Analysis of variance

APPACDM – The Portuguese Association of Parents and Friends of Mentally Disabled Citizens

ASCs – Adipose tissue derived stromal cells

ASGPRs – Asialoglycoprotein receptors

ATR – FTIR – Attenuated Total Reflectance Fourier Transform Infrared Spectroscopy

Au – Gold

AuNPs – Gold nanoparticles

AuNRs – Gold nanorods

B

β – Beta

β-sheet – Beta-sheet

BMSCs – Bone marrow derived mesenchymal stromal cells

BSA – Bovine serum albumin

C

CA – Chitosan-alginate scaffolds

Ca^{2+} – Calcium ions

Calcein-AM – Calcein-Acetoxymethy

CAM – Chick chorioallantoic membrane

CDDP – cis-diamine platinum

CDF – curcumin derivative

CHT – Chitosan

Cl^- – Chloride ion

cm – centimeter

cm^{-1} – Reciprocal wavelength centimeters

CMCht – CarboxymethylChitosan

CMCht/PAMAM – Carboxymethylchitosan/poly(amidoamine) dendrimers

CAN – Compartmentalized neuronal array

CNS – Central nervous system

CNT – Carbon nanotubes

CO_2 – Carbon dioxide

Cp – Heat capacity

CRC – Colorectal cancer

CTCs – Circulating tumor cells

D

°C – Degree Celsius

d – Days

Da – Dalton

DA – Degree of acetylation

DAPI – 4',6-diamidino-2-phenylindole

DGAV – Direcção Geral de Alimentação e Veterinária

DLS – Dynamic light scattering

DMEM – Dulbecco's modified Eagle's medium

DMSO – Dimethylsulfoxide

DNA – Deoxyribonucleic acid

DOX – Doxorubicin

DS – degree of substitution

DSC – Differential scanning calorimetry

2D – 2-Dimensions

3D – 3-Dimensions

E

E – Young modulus

e.g. – For example, from latin *exempli gratia*

E' – Elastic modulus

ECs – Endothelial cells

ECM – Extracellular matrix

EDA – Ethylenediamine

EDC – 1-Ethyl-(3-dimethylaminopropyl) carbodiimide hydrochloride

EDTA – Ethylenediaminetetraacetic acid

EHS – Engelbreth-Holm-Swarm

ELISA – Enzyme-linked immunosorbent Assay

EPR – Enhanced permeation and retention effect

Eq – Equation

EO – Ethylene oxide gas

ESB – European society for biomaterials

eSF – Enzymatically-crosslinked silk fibroin

et al. – And others

Ex/Em – Exitation/Emission

F

FBS – Fetal bovine serum

FDA – Food and drug administration

Fig. – Figure

FITC – Fluorescein isothiocyanate

FRA – Folate receptor-α

FTIR – Fourier transform infrared spectroscopy

G

g – grams

G1 – Generation 1

G2 – Generation 2

G3 – Generation 2

G' – Storage modulus

G'' – Loss modulus

GAGs – Glycosaminoglycans

GEM – Gemcitabine

GFs – Growth factors

GG – Gellan gum

H

H – Hours

HCC – Hepatocellular cellular carcinoma

HeLa – Cervical cancer cells

H&E – Hematoxylin–eosin

H_2O_2 – Hydrogen peroxide

HA – Hyaluronic acid

HA-GG – High acyl gellan gum

HBMSCs – Human bone marrow derived mesenchymal stromal cells

HCl – Hydrorochloric acid

HCO_3^{2-} – Bicarbonate ion

HCOMECS – Human colonic microvascular endothelial cells

HCT-119 – Colorectal cancer cell line

HFIP - Hexafluoroisopropanol

H^1 NMR – Proton nuclear magnetic resonance

HRP – Horseradish peroxidase

Hz – Hertz

I

i.e. – "In other words", from latin *id est*

IL – Interleukin

iPSCs – Induced pluripotent stem cells

K

K^+ – Potassium ion

KBr – Potassium bromide

kDa – KiloDalton

kg – Kilogram

kN – kiloNewton

kPa – KiloPascal

L

L – Liters

L929 – Murine fibroblast cell line

LA-GG – Low acyl gellan gum

LiBr – Lithium bromide

LNCaP – Lymph node carcinoma of the prostate

LT – Long-term

LVR – Linear viscoelastic region

M

m – meter

M – Molar

mA – Milliampere

MA-GG – Methacrylated gellan gum

MBP – Myelin basic protein

MCP-1 – Monocyte chemoattractant protein 1

MeCbl – Metil cobalamin

MEM – Minimum Essential Medium

MES - 2-(N-morpholino)ethanesulfonic acid

mg – milligram

Mg^{2+} – Magnesium ion

MenSCs – Human menstrual MSCs

Micro-CT – Micro computed tomography

Min – minute

miRNA – MicroRNAs

mL – Milliliter

mm – Millimeter

mM – Millimolar

Mf – Final mass

M_{Mw} – Medium molecular weight

Mw – Wet mass

MMP – Metalloproteinase

MNPs – Magnetic nanoparticles

Mol – Mole

MPa – megaPascal

MRI – Magnetic resonance image

MSCs – Mesenchymal derived stromal cells

MSCs – Mesenchymal stem cells

mw – Wet weight

MWCO – Molecular weight cut off

μm – micrometer

μ-PIV – Microparticle image velocimetry

N

n – Number of samples

N/A – Not applicable, Not available

Na^+ – Sodium ion

NaCl – Sodium chloride

NaOH – Sodium hydroxide

NCMC - N-carboxymethyl chitosan

NGF – Nerve growth factor

NIR – Near infrared

Nm – Nanometer

NOCMC – N,O-carboxymethyl chitosan

NPs – Nanoparticles

O

O_2 – Oxigen

OCMC – O-carboxymethyl chitosan

OX – Oxaliplatin

P

p – Statistical level of significance

Pa – Pascal

PAA - Polyacrylamide

PAMAM – Poly(amidoamine)

PAMAM-AT – poly(amidoamine)-amine terminated

PAMAM-CT – Poly(amidoamine)-carboxylic terminated

PBS – Phosphate buffer saline

PCL – Polycaprolactone

PDMS – Polydimethylsiloxane

PDX – Patient-derived xenograft

PEG – Poly (ethylene glycol)

PELA – Polyethylene glycol-co-polylactic acid

PGFs – Phosphate glass microfibers

pH – Potential hydrogenionic

PHBV – Polyhydroxybutyrate-co-hydroxyvalerate

PI – Propidium iodide

PL – Plantar muscles

PLA – Polylactic acid

PLCL – Poly(L-lactide-co-ε-caprolactone)

PLGA – Polylactic-co-glycolic

PLLA – Poly(L-lactic acid)

PVA – Polyvinyl alcohol

% – Percentage

R

Ref. – Reference

RGD – Arginine-glycine-aspartic acid (Arg-Gly-Asp)

RM – Regenerative medicine

RNA – Ribonucleic acid

RFU – Relative fluorescence units

ROS – Reactive oxygen species

Rpm – Rotations per minute

RT – Room temperature

RT-PCR – Real time polymerase chain reaction

S

SD – Standard deviation

SDS – Sodium dodecyl sulfate

SEM – Scanning electron microscopy

SF – Silk fibroin

SiO_2-NPs – Silica nanoparticles

SPIONs – Superparamagnetic iron oxide nanoparticles

ST – Short-term

T

TAF – Tumor associated fibroblasts

Tan δ – Loss factor

TCPs – Tissue culture polystyrene

TE – Tissue engineering

TERM – Tissue engineering and regenerative medicine

TG – Glass transition

TNF – Tumor necrosis factor

TRAIL – TNF-related apoptosis-inducing ligand

U

U – Units

UV – Ultraviolet

V

V – Volume

(v/v) – Percentage of volume/volume

VEGF – Vascular endothelial growth factor

X

XRD – X-ray diffraction

μg/mL – Microgram per milliliter

μL – Microliter

W

(w/v) – Percentage of weight/volume

WL – Weight loss

WU – Water uptake

%wt. – Percentage of weight

ϴ Water – Water contact angle

λ – Wavelength

Z

ZN – Zinc

ZnNPs – Zinc nanoparticles

LIST OF EQUATIONS

LIST OF FIGURES

LIST OF SUPPLEMENTARY FIGURES

LIST OF TABLES

SHORT *CURRICULUM VITAE*

Mariana Rodrigues de Carvalho was born in 1988 in Guimarães, Portugal. Nowadays, she works as a researcher in 3B's Research Group, I3Bs – Research Institute on Biomaterials, Biodegradables and Biomimetics, University of Minho, under the supervision of Prof. Rui L. Reis and Dr. Joaquim M. Oliveira.

Her background includes a five-year graduation (integrated masters) in Pharmaceutical Sciences at the Faculty of Pharmacy of the University of Porto finished in 2012. During the graduation she enrolled in research activities resulting in authorship of a paper entitled "Teas, dietary supplements and fruit juices: A comparative study regarding antioxidant activity and bioactive compounds". Also, in her last year, she had the opportunity to do a three-month internship at the World Health Organization Headquarters in Geneva, Switzerland. That gave her great insights into the Public Health field and the opportunity to work closely with global leaders in public health.

In the same year, she joined 3B's Research Group, after being awarded a grant under the scope of Fundação para a Ciência e Tecnologia (FCT) project OSTEOCART, under the supervision of Prof. Rui L. Reis and Dr. Miguel Oliveira. Since January of 2014, she continued her work at 3B's Research Group under the support of the FCT project PEst - 2013-2014, and European Commission (EC) founded project NOVOMAR, with supervision of Prof. Rui L. Reis and Dr. Joaquim M. Oliveira. During this period, she focused on studying several applications of CMCht/PAMAM dendrimer nanoparticles as well as microfluidic technologies applied in cancer research. Mariana Rodrigues de Carvalho has been involved in the preparation of FCT project proposals as well as European project proposals, related with her work. Additionally, she collaborated with her colleagues in different works, and different universities, including Medical Faculty of University of Zagreb and MERLN Institute at the University of Maastricht.

As a result of her research work, she is author or co-author of 8 papers in international journals (all published, including one published in Science Advances), 3 book chapters and 1 issued patent, 10 oral presentations and 9 poster presentations. She attended several important international meetings in the field of tissue engineering and regenerative medicine. Her work was constituted a press release in several occasions, by Associação Portuguesa de Investigação em Cancro (ASPIC), as well as the University of Minho official website. One of her original papers was also featured as the cover of the journal Global Challenges.

LIST OF PUBLICATIONS

The work performed during the PhD period resulted in the publications listed below.

Papers in international scientific journals with referees (as first author)

1. **M. R. Carvalho,** D. Lima, R. L. Reis, V. M. Correlo, J. M. Oliveira. "Evaluating biomaterials and microfluidics based 3D tumor models". Trends in Biotechnology, 2015, 33:667-678. doi: 10.1016/j.tibtech.2015.09.009.

2. **M. R. Carvalho,** D. Lima, R. L. Reis, J. M. Oliveira, V. M. Correlo. "Anti-cancer drug validation: the contribution of tissue engineered models", Stem Cells Reports and Reviews, 2017, 3:347-363. doi: 10.1007/s12015-017-9720-x.

3. **M. R. Carvalho,** R. L. Reis, J. M. Oliveira. "Mimicking the 3D biology of osteochondral tissue with microfluidic-based solutions: breakthroughs towards boosting drug testing and discovery". Drug Discovery Today, 2017, 3: 711-718. doi: 10.1016/j.drudis.2018.01.008.

4. **M. R. Carvalho,** F. R. Maia, J. Silva-Correia, B. M. Costa, R. L. Reis, J. M. Oliveira. "A semi-automated microfluidic platform for real-time tracking of cancer cells and investigation of nanoparticles cellular uptake". Nanomedicine, 2016, 2:581-596. doi: 10.2217/nnm-2016-0344.

5. **M. R. Carvalho,** F. R. Maia, S. Vieira, R. L. Reis, J. M. Oliveira. "Tuning Enzymatically-crosslinked Silk fibroin Hydrogel Properties for the Development of a Colorectal cancer Extravasation 3D Model on a Chip". Global Challenges, 2018, 2: 1870164. doi: 10.1002/gch2.201700100.

6. **M. R. Carvalho,** D. Barata, L. M.Teixeira, S. Giselbrecht, R. L. Reis, J. M. Oliveira, R. Truckenmüller, P. Habibovic. "Colorectal tumor-on-a-chip system: a 3D tool for precision onco-nanomedicine". Science Advances, 2019, 5: eaaw1317. doi: 10.1126/sciadv.aaw1317.

7. **M. R. Carvalho**, C. R. Carvalho, F.R. Maia, D. Caballero, S. C. Kundu, R. L. Reis, J. M. Oliveira. "Peptide-modified dendrimer nanoparticles for targeted therapy of colorectal cancer". Advanced Therapeutics, 2019, 1900132. doi: 10.1002/adtp.201900132.

Cover pictures in international scientific journals with referees

1. **M. R. Carvalho,** F. R. Maia, S. Vieira, R. L. Reis, J. M. Oliveira. Tuning Enzymatically-crosslinked Silk fibroin Hydrogel Properties for the Development of a Colorectal cancer Extravasation 3D Model on a Chip. Global Challenges, Vol. 2, No. 5/6, Published June 26, 2018.

Papers in international scientific journals with referees (as co-author)

1. S. Vieira, S. Vial, F. R. Maia, **M. R. Carvalho**, P. L. Granja, J. M. Oliveira. "Gellan Gum-coated Gold Nanorods: An intracellular nanosystem for bone tissue engineering". RSC Advances, 2015, 5: 77996-78005. doi: 10.1039/C5RA13556G.

Book Chapters

1. M. R. Carvalho, F. R. Maia, J. M. Oliveira, R. L. Reis. Advanced microfluidics for 3D biology in Osteochondral Tissue Engineering in Osteochondral Tissue Engineering - Nanotechnology, Scaffolding-Related Developments and Translation, Advances in Experimental Medicine and Biology, JM Oliveira, S Pina, RL Reis and JS Roman (Eds), Springer International Publishing AG, 2018, ISBN: 978-3-319-76710-9
2. M. R. Carvalho, R. Truckenmuller, R. L. Reis J. M. Oliveira, Biomaterial- and Microfluidic-Based 3D Models, Springer, Ed: J. Miguel Oliveira and Rui L. Reis (2019).
3. F. R. Maia, M. R. Carvalho, J. M. Oliveira and R. L. Reis. Tissue Engineering Strategies for Osteochondral Repair in Osteochondral Tissue Engineering - Challenges, Current Strategies, and Technological Advances, JM Oliveira, S Pina, RL Reis and JS Roman (Eds), S. Springer, 2018, ISBN: 978-3-319-76734-5.

Conference oral presentations

1. M. R. Carvalho, J. Mano, R. L. Reis, J. M. Oliveira. Investigation of Dendrimer-based nanoparticles cellular uptake and cell tracking in a semi-automated microfluidic platform. Society for Biomaterials 2015 – North Carolina, USA, 15th-18th April, 2015.
2. M. R. Carvalho, F. R. Maia, R. L. Reis, J. M. Oliveira. Investigation of Dendrimer-based nanoparticles cellular uptake and cell tracking in a semi-automated microfluidic platform. European Conference on Biomaterials (ESB2015), Krakow, Poland, 30th August to 3rd September, 2015.

3. S. Vial, S. Vieira, F. R. Maia, **M. R. Carvalho**, R. L. Reis, P. L. Granja, J. M. Oliviera. Gellan-Gum Coated Gold Nanorods as Intracellular Drug Release System for Osteogenic differentiation. European Conference on Biomaterials (ESB2015), Krakow, Poland, 30th August to 3rd September, 2015.

4. **M. R. Carvalho**, F.R. Maia, J. Silva-Correia, B. M. Costa, R.L. Reis, J. M. Oliveira. A microfluidic platform for the investigation of nanoparticles cellular uptake and cancer cells tracking in real-time. TermStem 2016, Guimarães, Portugal, 24th-26th October, 2016.

5. **M. R. Carvalho**, F.R. Maia, J. Silva-Correia, B. M. Costa, R.L. Reis, J. M. Oliveira. A semi-automated microfluidic platform for real-time tracking of cancer cells and investigation of nanoparticles cellular uptake. Society for Biomaterials 2017, Minneapolis, USA, 4th-8th April, 2017.

6. **M. R. Carvalho**, F. R. Maia, J. Silva-Correia, B. M. Costa, R. L. Reis, J. M. Oliveira. A microfluidic platform for the investigation of cancer cells' nanoparticle uptake and real time tracking. Chem2Nature Second School, Porto, Portugal, 5th to 9th of June, 2017.

7. **M. R. Carvalho**, D. Barata, L. M. Teixeira, S. Giselbrecht, R. L. Reis, J. M. Oliveira, R. Truckenmüller, P. Habivović. Engineering a microvascular 3D microenvironment of colorectal tumor-on-a-chip. The Netherlands Society for Biomaterials and Tissue Engineering (NBTE) 26th Annual Meeting, Luteren, Netherlands, 3rd-6th April, 2017.

8. **M. R. Carvalho**, D. Barata, L. M. Teixeira, S. Giselbrecht, R. L. Reis, J. M. Oliveira, R. Truckenmüller, P. Habivović. Engineering a microvascular 3D microenvironment of colorectal tumor-on-a-chip. MicroNano Conference, Amsterdam, Netherlands, 11th-12th December, 2018.

9. **M. R. Carvalho**, D. Barata, L. M. Teixeira, S. Giselbrecht, R. L. Reis, J. M. Oliveira, R. Truckenmüller, P. Habivović. Microfluidic gradient generator for drug testing on a colorectal tumor-on-a-chip disease model. Society for Biomaterials 2019, Seattle, USA, 4th-8th April, 2017.

10. **M. R. Carvalho**, C. Carvalho, F.R. Maia, D. Caballero, S. C. Kundu, R. L. Reis, J. M. Oliveira Targeting colorectal cancer using highly specific peptide-modified CMCht/PAMAM dendrimer nanoparticles. TERMIS-EU, Rhodes, Greece, 27th-31st May, 2019.

Conference posters

1. **M. R. Carvalho,** J. Mano, R. L. Reis, J. M. Oliveira. Dendrimer based Nanoparticles for intracellular delivery and cell tracking. TERMSTEM 2014 PT-Korea Symposium, Porto, Portugal, 23th and 24th October, 2014.
2. **M. R. Carvalho,** J. Mano, R. L. Reis, J. M. Oliveira. Novel Dendrimer nanoparticles for iPS generation in bone and cartilage regeneration. 3rd ICVS/3B's - Associate Laboratory Meeting, Braga, Portugal, 28th June, 2014.
3. S.Vial, S. Vieira, **M. R. Carvalho**, R. L. Reis, P. L. Granja, J. M. Oliveira. Gellan-Gum Coated Gold Nanorods as Intracellular Drug Release System for Regenerative Medicine. Society for Biomaterials, North Carolina, USA, 15th-18th April, 2015.
4. **M. R. Carvalho**, F. R. Maia, R. L. Reis, J. M. Oliveira. Investigation of Dendrimer-based nanoparticles cellular uptake and cell tracking in a semi-automated microfluidic platform. 10th World Biomaterial Congress, Montreal, Canada, May 17th to 22nd, 2016.
5. **M. R. Carvalho**, F. R. Maia, J. Silva-Correia, B. M. Costa, R. L. Reis, J. M. Oliveira. A microfluidic platform for the investigation of cancer cells' nanoparticle uptake and real time tracking. TERMIS-EU Meeting, Davos, Switzerland, 26th to 30th June, 2017. 20172013, DOI:10.1002/term.1822
6. **M. R. Carvalho**, D. Barata, L. M. Teixeira, S. Giselbrecht, R. L. Reis, J. M. Oliveira, R. Truckenmüller, P. Habivovic. Engineering a microvascular 3D microenvironment of colorectal tumor-on-a-chip. The Netherlands Society for Biomaterials and Tissue Engineering (NBTE) 26th Annual Meeting, Luteren, Netherlands, 28th-29th November, 2017.
7. **M. R. Carvalho**, F. R. Maia, S. Vieira, R. L. Reis, J. M. Oliveira. Tuning Enzymatically-crosslinked Silk fibroin Hydrogel Properties for the Development of a Colorectal cancer Extravasation 3D Model on a Chip. Chem2nature Summer School, Porto, Portugal, June 4th-8th, 2018.
8. **M. R. Carvalho**, D. Barata, L. M. Teixeira, S. Giselbrecht, R. L. Reis, J. M. Oliveira, R. Truckenmüller, P. Habivovic. Engineering a microvascular 3D microenvironment of a colorectal tumor-on-chip. ESB 2018, Maastricht, Netherlands, September 9th to 13th, 2018.

9. **M. R. Carvalho**, D. Barata, L. M. Teixeira, S. Giselbrecht, R. L. Reis, J. M. Oliveira, R. Truckenmüller, P. Habivovic. FORECAST Workshop, Porto, Portugal, June 8th-12th 2019.

Patents

1. **M. R. Carvalho**, D. Caballero, C. R. Carvalho, J. B. Costa, V. Ribeiro, Oliveira J. M., Kundu S. C., Reis R. L. Enzymatically Crosslinked Silk Fibroin hydrogel microfluidic platform, methods of production and uses thereof. (Filed, 2019).

Awarded grants

1. Horizonte Norte2020 PhD scholarship (Norte-08-5369-FSE-000044).
2. EMBO Short-Term Fellowship 7232.

Press Release

1. "Combinação de nanopartículas e dispositivos de microfluidos promete impulsionar a investigação sobre o cancro e terapias personalizadas", ASPIC, 15th March 2017 (http://www.aspic.pt/pt-pt/noticias/combina%C3%A7%C3%A3o-de-nanopart%C3%ADculas-e-dispositivos-de-microfluidos-promete-impulsionar#.W5E9pehKg2x).

2. "Grupo 3B's da UMinho desenvolve teste para medicamentos contra o cancro colorretal. O trabalho foi publicado na Science Advances e é "um avanço importante na nanomedicina de precisão", University of Minho Official website, July 25th 2019. (https://www.facebook.com/search/top/?q=universidade%20do%20minho%20-%20oficial&epa=SEARCH_BOX).

3. "Grupo 3Bs desenvolve teste para medicamentos do cancro colorectal", Reflexo Digital Official Website, July 22nd 2019. (https://reflexodigital.com/grupo-3bs-desenvolve-teste-para-medicamentos-do-cancro-colorectal/)

INTRODUCTION TO THE THESIS FORMAT

The present thesis is divided into four main sections (1 to 4) containing ten chapters (**I to X**). This structure was adopted to allow a proper organization of the data presented in the various chapters.

A general introduction (Section 1) can be found divided in three different chapters: **Chapters I, II and III.** An overall Materials and Methods section is represented in Section 2, **Chapter IV**. Section 3, in which **Chapters V** to **IX** can be found, focuses on the experimental studies and results obtained in the context of this thesis and their discussion. To finalize, Section 4 (**Chapter X**) completes this thesis with concluding remarks and future perspectives on the topic.

The main body of the thesis is based on a series of publications published in international journals or already submitted for publication. Each individual chapter is presented in a manuscript form, *i.e.* abstract, introduction, experimental section, results and discussion, conclusion, and acknowledgements. A list of relevant references is also provided as a subsection within each chapter. The contents of each part and chapter are described below in more detail.

Section 1 – General introduction

Chapter I – Evaluating Biomaterial and Microfluidic-Based 3D Tumor Models: This chapter presents an extensive overview on the development and combination of microfluidic and biomaterials for cancer research, as well as the several aspects that make this technology suitable for promising advances in cancer field, namely on angiogenesis and metastasis processes.

Chapter II – Biomaterials and Microfluidics for Drug Discovery and Development: This chapter reviews the current reports dealing with the combination of biomaterials and microfluidics for drug discovery in organ-on-chip, with special emphasis on tumor-on-a-chip.

Chapter III – Dendrimer Nanoparticles in CRC Applications: This chapter focuses on dendrimer nanoparticles, types, routes of synthesis, and main applications in cancer research (with emphasis in colorectal cancer research).

Section 2 – Detailed description of experimental materials and methodologies

Chapter IV – Materials and Methods: A list of the materials used and methods applied to obtain the results described further on is provided, being the basis to the whole work described in this thesis.

Section 3 – Experimental work regarding the biomaterials approach to cancer in vitro models on a chip

Chapter V – A Semi-automated Microfluidic Platform for Real-time Tracking of Cancer Cells and Investigation of Nanoparticles Cellular Uptake: In this chapter, several cancer cell lines were cultured in the presence of dendrimer nanoparticles, and its effects compared in dynamic (microfluidic platform) and static (traditional 2D culture flasks) conditions. Proof of the relevance of physiological aspect was achieved.

Chapter VI – Tuning Enzymatically-crosslinked Silk fibroin Hydrogel Properties for the Development of a Colorectal cancer Extravasation 3D Model on a Chip: This chapter focuses on the use of enzymatically crosslinked silk fibroin hydrogels with tunable mechanical properties to assess colorectal cancer cells' migration in response to the presence of hVCAM-1. Moreover, this chapter focuses on the fundamental differences between the traditional Boyden Chamber migration assay and a 3D microfluidic migration assay.

Chapter VII – Colorectal Tumor-on-a-chip System: A 3D tool for Precision Onco-nanomedicine: In this chapter, we move forward with the goal of creating an in-house tailored made microfluidic device for the development of an *in vivo* like model of colorectal cancer. This model comprises HCT-116 colorectal cancer cell embedded in Matrigel, connected to pair of laterally perfused channels with lumen-creating colonic microvascular endothelial cells. The effect of a gradient of gemcitabine released from dendrimer nanoparticles was evaluated, as well as gene expression.

Chapter VIII – Peptide-modified Dendrimer Nanoparticles for Targeted Therapy of Colorectal Cancer: In this chapter, it is described the use of CMCht/PAMAM dendrimer nanoparticles functionalized with YIGSR laminin receptor binding peptide for actively targeting and specific delivery of therapeutic agents into colorectal cancer cells, as well as a microcontact printing based proof-of-concept and comparisons between 2D and 3D settings.

Chapter IX – Enzymatically Crosslinked Silk Fibroin Hydrogel Microfluidic Platform, Methods of Production and Uses Thereof: This chapter describes the new methodology to produce enzymatically-crosslinked silk fibroin hydrogel microfluidic platform, which takes advantage of the tyrosine groups present in the structure of silk fibroin that are known to form a covalently-crosslinked hydrogel in amorphous and transparent state. The hydrogel based microfluidic platform was extensively characterized in order to demonstrate its application in several TE areas, but in particular in cancer research applications.

Section 4 – Concluding remarks

Chapter X – General Conclusions and Future Perspectives: The final section of the thesis presents the general conclusions and implications, current limitations and potential of the work described for application in microfluidic cancer models. The main conclusions of each chapter as well as future perspectives of the advanced strategies developed in this thesis are provided.

“Once you stop learning, you start dying”

—**Albert Einstein (1879-1955)**

SECTION 1

GENERAL INTRODUCTION

CHAPTER I

EVALUATING BIOMATERIALS AND MICROFLUIDICS BASED 3D TUMOR MODELS

Chapter I

Evaluating Biomaterials and Microfluidics based 3D Tumor Models[1]

I-1. ABSTRACT

Cancer is a major cause of morbidity and mortality worldwide, with a disease burden estimated to increase in the coming decades. Disease heterogeneity, limited information on cancer biology and disease mechanisms are aspects that 2D cell cultures fail to address. We review the current "state-of-the-art" in 3D Tissue Engineering (TE) models developed for and used in cancer research. Scaffold-based TE models and microfluidics are assessed for their potential to fill the gap between 2D models and clinical application. Recent advances in combining the principles of 3D TE models and microfluidics are discussed, with a special focus on biomaterials and the most promising chip-based 3D models.

Keywords: Cancer, Biomaterials, Microfluidics, 3D.

[1]This chapter is based on the following publication:

M.R. Carvalho, D. Lima, R. L. Reis, V. M. Correlo, J. M. Oliveira. "Evaluating biomaterials and microfluidics based 3D tumor models". Trends in Biotechnology, 2015, 33:667-678. doi: 10.1016/j.tibtech.2015.09.009.

I-2. THE IMPORTANCE OF 3D *IN VITRO* TISSUE MODELS FOR ADVANCED CANCER RESEARCH

Conventional approaches used in cancer research involve culturing of tumor cells in 2D surfaces and the use of animal models, which poorly correlate with human disease states. 2D cell cultures oversimplify the biological context of a tumor, which is influenced by intrinsic molecular features and external cues from its surrounding microenvironment [1]. Unlike cancer cells grown in 2D, those grown in 3D adopt a rounded shape, forming clusters that are suggestive of tumors *in vivo* [2, 3]. Cancer cells grown in 2D versus 3D also exhibit differential gene expression profiles for key genes involved in angiogenesis, cell migration, and invasion [4-8]. *Ex vivo* models or *in vivo* models such as animal or patient-derived xenograft (PDX) models are also popular tools for cancer research. Such models have advantages over cell cultures and do not suffer from the lack of 3D context, but they present their own set of limitations (Box 1).

I-2.1. BOX 1 - Advantages and disadvantages of *ex vivo* models, animal models, patient derived xenograft (PDX) models

Ex vivo models: *Ex vivo* tumor culture is performed using a thin slice of tumor tissue collected from human or animal sources and cultured on porous substrates or embedded in ECM like matrices [9]. These models generally preserve the native complex and differentiated 3D cell-matrix architecture, cell phenotype, complex architecture, logically providing a more accurate mimic of cell behavior. On the other hand, the main drawback of this type of model may be the absence of the absence of mechanical forces, and the lack of mechanical forces such as shear stress, perfusion and surrounding tissue may result in changes in the structure and cell behavior when comparing to original *in vivo* microenvironment. Another drawback is the need of harvesting tissue from human or animal subjects.

Animal models: Mouse models have proven essential in cancer research. These models yield better prediction of drug behavior and efficacy in human than 2D conventional culture. They are used to understand the genetic basis of tumor development and cancer progression. They can also be used to test the efficacies of different anti-cancer agents as they contain their intrinsic microenvironmental complexity. Animal models allow studies on defined mutations, including the analysis of the effects of these mutations in many genetic backgrounds. Growing demand from the public opinion to reduce the use of animals as experimental subjects [10-12], other limitations involve the inability to mimic human specific features regarding tumors, autoimmune conditions, stem cell differentiation and ultimately,

their responses to therapeutic drugs because physiology, metabolism, tumor cell interactions with the innate immune system, proliferation, metastasis and cells themselves in animals are different from humans. [13, 14].

PDX models: Models where surgically resected primary tumor samples are engrafted directly from patients onto immunodeficient mice. These allow preserving longer the molecular, genetic and histological heterogeneity of their parental tumors [15]. PDX models offer a powerful tool for cancer research and a route toward personalized medicine for cancer patients. These also enable the discovery of biomarkers predicting drug sensitivity and resistance and possibly monitoring the initiation and progression of metastasis as well as the fate of circulating tumor cells using in vivo flow cytometry of implanted humor tumors [16].

To address the limitations of conventional approaches, the 3D microenvironment of tumors must be taken into account to improve the physiological relevance of *in vitro* models [17, 18]. The integration of tissue engineering (TE) strategies and microfluidic technologies has recently sparked a breakthrough into the design of *in vitro* microfluidic culture models that better adapt to morphological changes in tissue structure and function over time, providing a level of precision control that could not be achieved before [19]. We review the current "state-of-the-art" on 3D TE models that have been developed and used in cancer research. The relevance of 3D cell models in cancer studies is critically assessed, and the main advantages and limitations discussed, with special emphasis on the biomaterials point of view. New approaches that integrate bioreactors and microfluidic technology are also discussed, along with the potential impact of 3D TE models in the cancer drug discovery process.

I-3. CLASSICAL 3D TE MODELS FOR CANCER RESEARCH

Classical 3D culture systems can be broadly subdivided as scaffold-free or scaffold-based methods [20]. Scaffold-free 3D cancer models are best exemplified by tumor spheroids (Box 2), but we will focus here on scaffold-based methods because they offer more opportunities for combination with other technologies. Scaffold materials can be of synthetic or natural origin [21]. Synthetic materials typically display better mechanical properties than natural ones **(Table I-1)**, but we focus our discussion on scaffolds made from naturally derived materials due to their greater physiological relevance. Biomaterials are being broadly used for their remarkable similarities to the extracellular matrix, typically good biological features such as, biocompatibility, biodegradability and bioavailability, as well as

inherent cellular interaction. Also, natural polymers can be engineered and their properties tuned to obtain desirable mechanical and physical characteristics [22].

I-3.1. Box 2 - *In vitro* 3D multicellular tumor spheroids

Spheroids form due to the ability of cells in suspension to self-assemble when cell-cell interactions are stronger than those between cells and substrate [23]. Their small size and the absence of vascularization create limitations to nutrients and oxygen diffusion, requiring cells of its core to adopt a glycolytic metabolic activity which causes an increasing pH gradient towards the outside [24]. This mimics what happens with actual tumors, which have regions of hypoxia and of acidity similarly structured as a function of the distance between the core and the tumor blood vessels [25-27]. Spheroids can be fabricated using several methods: i) hanging drop method, in which cells can aggregate freely at the bottom of an inverted cell suspension drop; ii) spinner flasks method, which provides constant agitation, allowing spontaneous cell aggregation; iii) static liquid overlay technique, which enables spheroid formation by preventing cell adhesion to the growth substrate; iv) centrifugation; and v) growing cells on non-adherent micropatterned surfaces in microfabricated devices to favor their aggregation [28]. Given their tumor-like features, *in vitro* multicellular spheroids have been particularly useful for studying the efficacy of novel chemotherapeutic agents or drug delivery systems. Significant differences in drug responses have been observed for numerous cancer types in spheroid culture, but increased chemical resistance appears to depend upon the type of cancer cells and the specific treatment under study [29-31]. The emerging resistance to chemotherapies expands the potential application for spheroid cancer models. Breast cancer tumor recurrence, a major cause of death, has recently been attributed to a small population of cells with stem-like characteristics, able to self-renew and promote tumor progression [32, 33]. A 3D spheroid tumor model with stem-like properties was used to discover a new inhibitor of spheroid formation [34]. This stem-like enriched spheroid formation technology could also be applied to drug discovery in other cancer types [35]. Despite the advantages of using spheroids in cancer research, they are still not routinely incorporated into drug discovery, most likely due to technical hurdles. For example, automated analysis systems are not compatible with loose spheroids, which can clog pipettes and tubing. Tethered spheroids may overcome this hurdle [36].

Table I-1 - Naturally Derived Matrices for 3D Tumor Engineering.

Material	Characteristics	Cancer research	References

		applications	
Matrigel® (natural)	3D hydrogel microenvironment for tumor growth and angiogenesis studies; Cytocompatibility, cell adhesion sites, tunable physical properties.	Human colon adenocarcinoma, colorectal cancer, prostate cancer, breast cancer;	[37, 38]
Collagen I (natural)	Multiple crosslinking methods; Biocompatibility, biodegradability, angiogenesis potential.	Human breast carcinoma, Human hepatocellular liver carcinoma;	[31, 39-41]
Fibrinogen (natural)	Blood clotting, cellular and matrix interactions, neoplasia; Architecture mimics native ECM, 3D microenvironment for cancer growth.	Melanoma, ovarian cancer cells, liver carcinoma;	[42, 43]
Hyaluronan (natural)	Glycosaminoglycan found in extracellular tissue in many parts of the body; Major component of the native brain extracellular matrix, studying tumor migration processes.	Prostate cancer, Glioma tumor;	[44, 45]
Chitosan (natural)	Analysis of interaction of prostate cancer tumor cells with immune cells, formation of tumor spheroids.	Prostate cancer, glioma tumor;	[46-48]
Alginate (natural)	Properties for cell transplantation, drug delivery and tissue engineering; Suitable for hydrogel microspheres, promotes the conversion of cultured cancer cells to a more malignant in vivo-like phenotype; Non-adhesive to cells.	Oral squamous cell carcinoma, Human hepatocellular carcinoma;	[48-51]
Fibroblast-derived matrices (natural)	Distinctly different cell morphology, aggregation pattern, proliferation profile and invasive potential, although these matrices do not fully represent the composition and structure of the tumor microenvironment.	Human colorectal carcinoma, Human pancreatic carcinoma;	[52, 53]
Silk fibroin (natural)	Unique mechanical properties, good biocompatibility, well-controlled degradability and versatile processability.	Human breast adenocarcinoma;	[54]
Agarose (natural)	Amenable mechanical and biological properties; More stable than traditional natural hydrogels.	Osteosarcoma and breast adenocarcinoma;	[55]
Polyethylene glycol (PEG) (synthetic)	Biocompatibility, high water content, and multi-tunable properties; Specific biological functionalities can be covalently incorporated.	Human epithelial ovarian cancer, Human pancreatic ductal adenocarcinoma;	[56-58]

Poly(lactic-co-glycolic) acid (PLGA) (synthetic)	Highly porous scaffolds; Convenient to handle and amenable to large-scale use.	Oral squamous, cell carcinoma;	[59, 60]
PCL (synthetic)	Biologically inert synthetic polymer, high porosity, a large surface area-to-volume ratio for cellular attachment, tunable fiber diameter, low cost.	Ewing sarcoma;	[61]
Synthetic Peptides (synthetic)	Controlled amino acid composition for easy incorporation of specific biological relevant ligands; Adequate physiological properties.	Human ovarian carcinoma, Human breast carcinoma;	[62-64]

I-3.2. *In vitro* 3D scaffold-based TE tumor models

Scaffold-based models have the advantage of allowing the study of tumor interactions with the microenvironment, in particular, phenomena such as tumor migration and invasion. Another advantage is the possibility to functionalize the scaffold materials to obtain desired physicochemical and biological characteristics. For example it is possible to incorporate bioactive molecules that promote cell-adhesion or matrix metalloproteinase (MMP) substrates that render the materials susceptible to degradation by cell-secreted proteases, thus mimicking the naturally occurring interactions of cells with ECM and its consequent remodeling [57].

Great care and attention are required when choosing the biomaterial for culturing cancer cells, in order to better emulate the physiology of their original ECM, since this facet alone is able to influence tissue organization [19, 65].

Models using Matrigel® as reconstituted basement membrane [66, 67] can mimic the pathophysiological context of cancer and have enabled advances in 3D tissue engineering. Development of Matrigel® grew from pioneering work on the isolation and purification of proteins such laminin and type IV procollagen and discovery of the biological activity of the reconstituted basement membrane [68, 69]. Matrigel®, has been to mimic breast cancer progression [70] and help gain understanding of how tissue organization itself influences the development of a malignant phenotype [67]. Despite being the most commonly used biomaterial in cancer research, Matrigel® has some disadvantages: As it is a biological animal derived product, it lacks human motifs (DNA with biological function); possible growth factor contamination; possible variation of endotoxin levels and stiffness between lots and the presence of undefined substances makes comparison between studies more challenging [71, 72].

Collagen I is a frequently used substrate for cell culture and tissue engineering applications because it contains the tripeptide RGD (Arg-Gly-Asp), a short amino acid sequence that preferentially binds to receptors on cell surfaces. Scaffolds made from Collagen I can be synthetically modified to provide a wider range of physicochemical properties. For example, collagen stiffness can be adjusted through covalent crosslinking by non-enzymatic glycation. One of the first organotypic models consisted of isolated human fetal colonic epithelial cells seeded on a collagen type I matrix with embedded colonic fibroblasts [73]. Collagen I was also used to produce a biologically relevant 3D tumor model that supported unconfined cellular proliferation and exhibited necrosis beyond a depth of ≈150 μm and also had angiogenic potential [39]. The biocompatibility and 3D architecture of collagen I hydrogels are suitable for reproducing the microenvironmental conditions of a solid tumor.

Fang *et al.* [49] chose alginate to recapitulate autocrine or paracrine functions in cancer. A 3D model to study paracrine function was currently lacking, being of great relevance since paracrine function is a major mechanism of cell-cell communication within tissue microenvironment in normal development and disease. The system studies paracrine influence between prostate cancer cell and normal prostate stromal cells in which direct interaction between epithelial and stromal cells is not allowed. Alginate was the chosen biomaterial because of its hydrophilic nature allowing a high cell loading functional in culture. Alginate hydrogels possess the adequate characteristics for cell transplantation, drug delivery and tissue engineering as its production and cell encapsulation can be achieved under mild conditions.

Fibrin (purified from fibrinogen) hydrogels are also used as a biomaterial in cancer research, supporting growth of cancer cells into colonies that resembled embryonic stem cell colonies [42]. Fibrin is present in connective tissue stroma in human malignant tumors, and fibrin and fibrinogen can increase the survival and metastatic potential of circulating tumor cells [42]. *In vitro* scaffold-based cancer models have been used in drug discovery, to understand mechanisms of action, find novel targets, or to address drug efficacy, toxicity and resistance events. For instance, the efficacy of three anti-cancer drugs (*e.g.,* camptothecin, docetaxel and rapamycin) in the treatment of bone metastatic prostate cancer has been assessed using Hyaluronic Acid (HA) derived hydrogels to grow the LNCaP (lymph node carcinoma of the prostate) [74]. The difference in efficacy between the three drugs may reflect their different mechanisms of action and chemical properties, emphasizing the importance of a proper microenvironment in anti-cancer drug efficacy assessments. HA allowed cells residing in the

hydrogel matrix to form distinct clustered structures which grew and merged, reminiscent of real tumors [74].

Other biocompatible hydrogels, such as those made of Gellan Gum or Silk [75, 76] can potentially be used in the development of complex microtissues for cancer research. These two naturally derived hydrogels attract a special interest since they may provide important chemical cues to the cells due to their resemblance to the natural extracellular matrix and their ability to easily achieve a 3D model architecture. Their biodegradability and biocompatibility have been extensively validated *in vitro* and *in vivo* [77]. Moreover, they show tunable mechanical properties ideal for cell encapsulation. Cancer models can therefore be created by including cancer cells, stromal fibroblasts, macrophages or growth factors.

I-3.2.1. Novel applications for scaffolds

Scaffold based TE strategies were also applied to cancer immunotherapy to develop an *in vitro* 3D scaffold model for examining the interaction of tumor-associated fibroblasts (TAF) with breast tumor cells and breast specific, neu antigen (p98) reactive T cells [78]. Breast cancer cells seeded on 3D chitosan-alginate (CA) scaffolds exhibited productive growth and formed distinct tumor spheroids. Antigen specific p98 T cells, but not naïve T cells, bound better to tumor cells on scaffolds. The p98 T cells induced potent tumor cell killing but T helper cell cytokine function was impaired in the presence of TAF co-seeding on scaffolds. From a biomaterials perspective, CA scaffolds are important because they are biocompatible and non-immunogenic, they have the proxy structure of glycosaminoglycans (GAGs) (major component of the native (ECM), and they are FDA approved for numerous biomedical applications. These kinds of strategies can bridge the gap between *in vitro* and pre-clinical testing of novel immunotherapies by enabling researchers to probe individual cell types and factors in a more physiologically relevant tumor-like microenvironment.

I-4. CHIP BASED 3D TE MODELS IN CANCER RESEARCH

TE based models still face difficult challenges, such as the requirement of functional vasculature networks to regulate the transport of nutrients and oxygen and the need to control metabolic or mechanical functions of the encapsulated cells within biocompatible scaffolds [79]. Combining TE

principles with microfluidic technologies has the potential to fulfill such gaps, since microfluidics allows the fabrication of three-dimensional architectures with controlled spatial relationships between cells, the presence of flow-induced signaling and transduction, and the capacity to introduce the chemical gradients necessary to reproduce the architecture of the *in vivo* microenvironment [80-82].

The combination of TE principles and microfluidic technologies can take the form of so-called "biochips" for 3D cell culture that better mimic the physiological environment and interactions observed *in vivo* [83, 84].

In vitro multi-tissue 3D tumor models on a chip can make it possible to obtain quantitative measurements on circulating tumor cells, extravasation and micrometastasis (**Figure I-1**). For example, a microfluidic platform was built to emulate the dynamic physiology of the bone marrow microenvironment, allowing realistic interaction of bone marrow cells and osteoblasts, so as to investigate multiple myeloma [85].

In combination with biomaterials-based approaches, several chip-based models (**Figure I-2**) have provided invaluable knowledge and previously unmeasurable or unobservable data (**Figure I-3**) about cancer related processes such as angiogenesis and metastasis, and have proved instrumental in drug discovery.

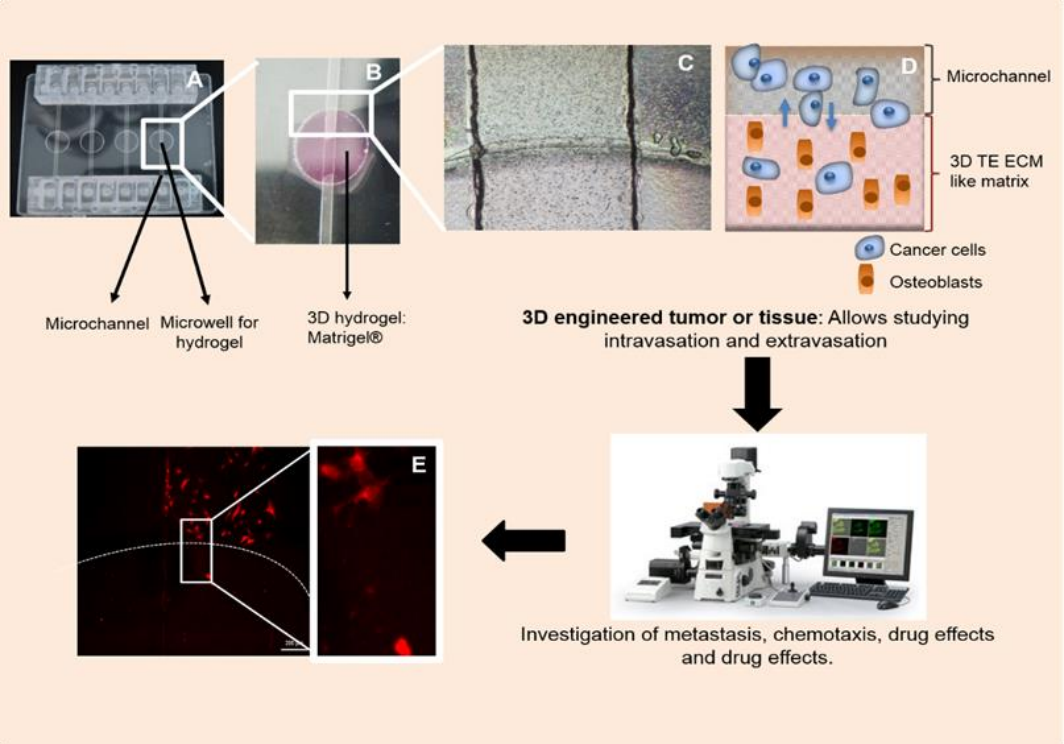

Figure I-1 - Chip-Based 3D Models in Cancer Research. Scheme of an example of a chip-based 3D model mimicking the native extracellular matrix (ECM) tumor microenvironment. The entry of tumor cells into the blood stream and the micrometastasis process in a variety of tissues, or in the presence of other relevant cell types, can be studied. The chip microwells could contain a 3D engineered hydrogel representing an ECM-like matrix, such as Matrigel®, in direct contact with microchannels mimicking blood vessels for intravasation and/or extravasation studies. The small blue arrows represent the migration of (cancer) cells from the microchannel and into the 3D tissue-engineered ECM-like matrix and vice-versa. (A) Cellix VenaT4chip; (B) The microwell filled with Matrigel® (3D); (C) Microscopy image of the channel–microwell interface; (D) Representation of cancer cells migrating from the microchannel to the 3D TE ECM-like matrix in the presence of osteoblasts; (E) fluorescence microscopy image of HeLA cells adhered to the channel migrating into the ECM-like matrix (Matrige®l) M. R. Carvalho, unpublished data, 2015).

I-4.1.1. Angiogenesis

Angiogenesis is a prerequisite for tumor growth, invasion, progression and metastasis, and thus crucial to include in cancer models. Organ-on chip models that integrate vasculature have the potential to transform *in vitro* approaches for the study of cancer [86, 87], offering the possibilities for spatially resolved delivery and extraction of solvents and solutes to control the biochemistry of tumor's microenvironment, growth of appropriate endothelium, delivery of circulating cells, as well as the possibility to control tension and shear stress during angiogenesis, tumor growth and drug delivery [88]. Physiological vascularized tumor conditions can be achieved by including mixed cell populations in the device: tumor cells, stroma cells, endothelial cells that line the vessels and also immune cells. Such an

approach would enable analysis of any circulating molecular and cellular components that may promote tumor angiogenesis [89]. The biomaterials that form the microfluidic scaffold would have to recapitulate matrix stiffness and withstand interstitial pressure, as well as convey mechanical cues that modulate cell signaling via mechanoreceptor signal transduction.

Microfluidic vascular models can be divided in two categories [90]: Microfabricated molds that confine biological hydrogels between parallel microfluidic channels [91], or *bona fide* vascular structures fully embedded within 3D ECM [92]. In an example of the microfabricated mold approach, a device was developed with a central microchannel embedded within a collagen hydrogel, which allowed tumor-relevant hydrodynamic stresses to be introduced and quantified using microparticle image velocimetry (μ-PIV) [93].

As an example of the second approach, a 3D microphysiological system is being developed. The model uses induced pluripotent stem cell technology (development of vessel networks derived from human iPSC-derived ECs in a cardiac-derived ECM to simulate the microcirculation), the cardiac muscle, and the solid tumor into a single integrated microphysiological system [94]. As a 3D matrix, a co-culture of endothelial colony-forming-derived endothelial cells and normal human lung fibroblasts are mixed with fibrin matrix.

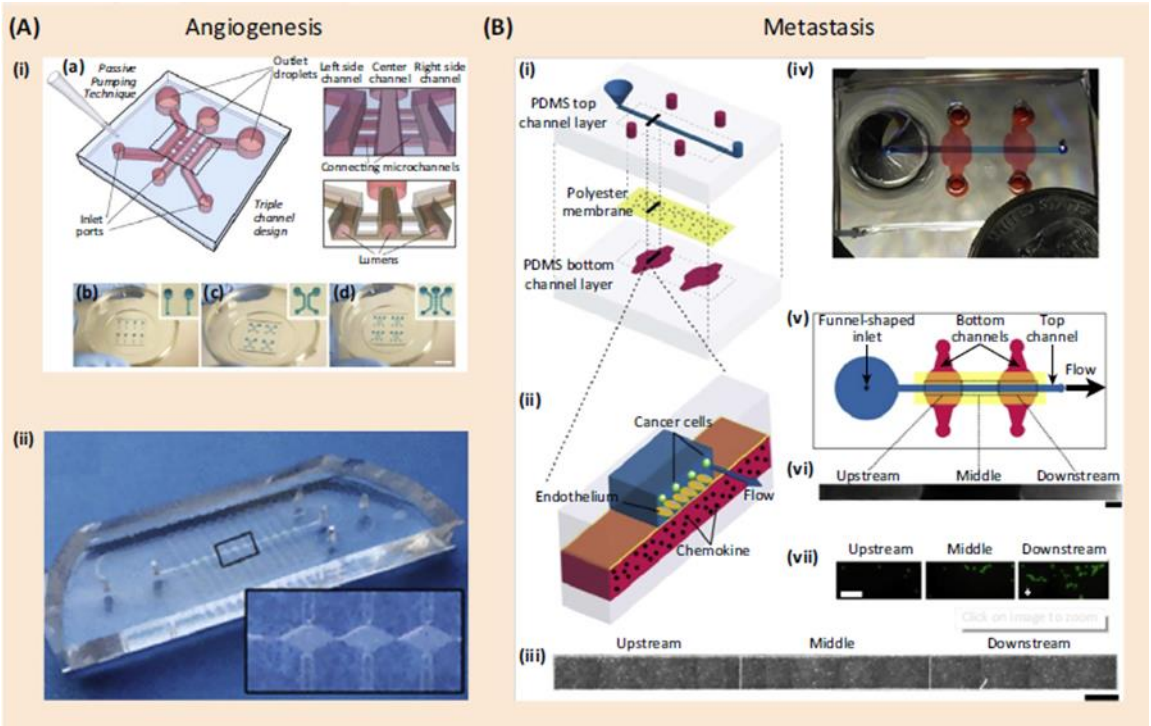

Figure I-2 - Microfluidic devices used in the study of angiogenesis (A) and metastasis (B). A1) Passive pumping-based microfluidic angiogenesis assay with 3D cylindrical lumens. (A) Illustration of a triple channel design with

connecting microchannels. (b–d) Microchannel systems can be (b) single, (c) double, or (d) triple channel designs, and are arrayable. Reprinted with permission from [95]. Copyright, 2012 Elsevier. a2) Perfusable three-dimensional microvessels are generated using an optically clear polydimethsiloxane microfluidic-based platform. Reprinted with permission from [94]. Copyright, 2013 BioMed Central Ltd. b) Microfluidic vasculature enables region-specific activation of endothelium under physiological flow conditions [96].

I-4.1.2. Metastasis

Metastasis is one of the most complex processes in cancer and likely one of the most difficult study and mimic using *in vitro* models [97, 98]. Therefore it is crucial to understand the molecular and cellular phenomena involved in the metastatic cascade [99-101]. Invasion of cancer cells through the basal membrane into a blood or lymphatic vessel (intravasation) followed by entrance in other tissue/organs (extravasation) are critical steps [102, 103]. Although significant progress has been made in visualizing tumor-cell motility *in vivo*, the underlying mechanism of cancer cell intravasation is largely unknown. Few studies have addressed the development of 3D models for metastasis studies **(Figure I-3)**. However, an *in vitro* 3D microfluidic model of the tumor-vascular interface was designed to integrate live imaging, precise control of microenvironmental factors and endothelial barrier measurement [102]. The chip consists of two independent channels in which tumor and endothelial cells are seeded, interconnected via a 3D ECM hydrogel made of collagen type I. This work sheds light on the influence of macrophage-secreted factors in intravasation processes. Thus, the formation of an endothelial monolayer on a 3D collagen type I hydrogel mimicking ECM enabled the precise quantification and control of critical microenvironmental factors.

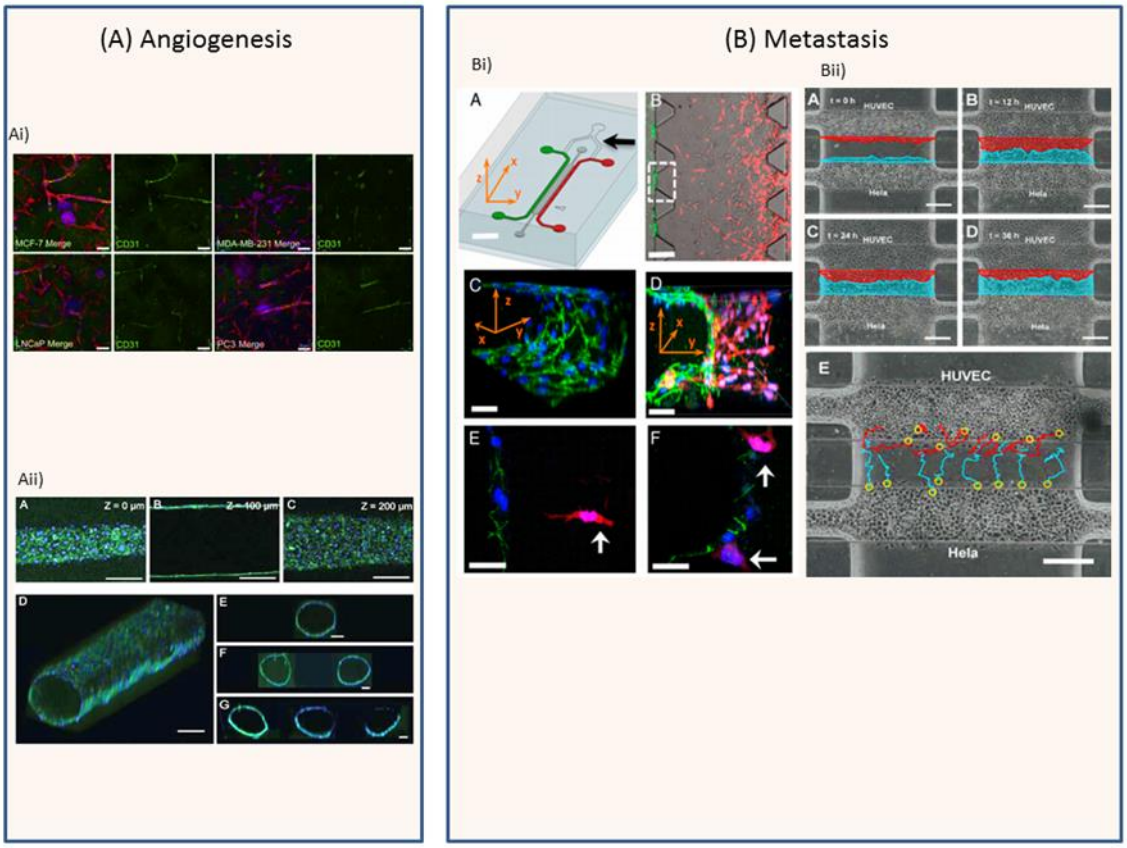

Figure I-3 - Outputs of angiogenesis (A) and metastasis (B) studies in TE designs. A1) Cultured breast or prostate epithelial carcinoma cells (MCF-7; LNCaP) with HUVECs and mesenchymal stromal cells (MSCs) within matrices fabricated from synthetic starPEG and maleimide-functionalized heparin to study 3D tumor angiogenesis microenvironments after 14 days: Extended focus confocal images displaying Phalloidin (red), Hoechst (blue) and CD31 (green) showing HUVEC and MSC to cancer cell interactions for each tumor cell type. Reprinted with permission from [104]. Copyright, 2015 Elsevier. A2) 3D endothelial-lined lumens (ELL) obtained by seeding Human umbilical vein endothelial cells (HUVECs) in a microfluidic chip. Reprinted with permission from [95]. Copyright, 2012 Elsevier. B1) Microfluidic tumor-vascular interface model: Endothelial channel (green), tumor channel (green) and 3D ECM (grey) between the two channels. White arrow shows Fibrosarcoma cells (HT1080) invading in 3D toward the endothelium. [102]. B2) Migration of HUVEC and Hela cells during co-culture on-chip. Reprinted with permission from [105]. Copyright, 2012 American Chemical Society.

I-4.1.3. Drug Discovery

Developing *in vitro* 3D chip-based tumor models will not only aid in investigating angiogenesis and metastasis, but can help provide a realistic preclinical assessment of anti-cancer drug efficacy and resistance. For example, a microfluidic chip-based, 3D co-culture drug sensitivity test platform was developed, in which a mono-lung cancer cell line, a mixture of lung cancer and stromal cell lines, and cells from fresh lung cancer tissues were and treated with anti-cancer drugs [106]. A gradient

concentration generator inside the chips allowed reconstructing tumor microenvironments *in vitro* with continuous nutrient and oxygen supplementation. Cell culture medium was introduced into the microchannels to generate a set of gradient concentrations for each drug or combination of drugs. Moreover, these drug sensitivity tests were carried out on the fresh tissues of cancer which allowed screening single or combination anti-cancer drug schemes efficiently and accurately for real patients.

In addition to the chips independently developed by researchers in academic laboratories, companies are emerging that produce microfluidic-based 3D cell culture devices that are approved for commercialization. For example, MIMETAS produces OrganoPlates™ which are microfluidics-based culture plates that enable culturing and screening of a large range of organ and tissue models. These platforms enable precise deposition of cells in a 3D culture matrix, and their patented liquid handling technology allows for better readout and quantification than conventional culture systems. The cells are contained in a gel that allows 3D tissue configurations and cell-cell interactions. A continuous perfusion of media through the plate mimics blood flow and exchange of nutrients, oxygen and metabolites.

Other companies in the market are also following this new trend. Cellix's VenaT4™ chip is suitable for ECM-matrix, collagen gels, hydrogels, Matrigel® or similar aqueous biomaterials and ideal for invasion assays in an *in vivo* like settings. Such companies will revolutionize the field by working closely with researchers and clinicians to develop a customized *in vivo* based accurate biomimicry.

I-5. CONCLUDING REMARKS AND FUTURE PERSPECTIVES

Bioengineered 3D microsystem technologies are relatively new and still require great effort to validate and characterize their properties, and suitability for practical biomedical applications. Despite the promise of microfluidic chip-based 3D cell culture systems for cancer research, there are some disadvantages compared to conventional techniques, and there are challenges that need to be addressed. Moving *in vitro* culture from macroscopic culture to PDMS based devices can come with unforeseen challenges. Changes in device material, surface coating, cell number per unit surface area or per unit media volume may all affect the outcome of otherwise standard protocols, and in this sense, surface materials and treatments deserve special attention. Although these systems present numerous advantages in terms of their ability to mimic what happens *in vivo* and to visualize cell growth, cell migration and cell-cell interactions, the small volumes used as well as the low numbers of cells within the microfluidic devices make conventional biochemical assays more challenging due to detection

limits, making it difficult to generate statistically significant amounts of data. Advancements in technologies that are sensitive enough to detect all-important genetic and transcriptomic changes are required for the discovery of novel biomarkers and critical events in cancer development. Regardless, their potential predicting clinical responses could have great effects on the way drug discovery and bioequivalence studies, pathogenesis of relevant diseases such as cancer can be investigated.

Further development of chip-based 3D cell culture in cancer research will be largely dependent on the improvement of biomaterials that emulate the ECM, and the capacity to scale-up these complex technologies. Integrating TE approaches and microfluidics into easy-to-use, scalable, reproducible and cost-effective systems will be the key to their success and future translation to the market. A 3D multi-tissue *in vitro* tumor model on a chip could contribute to accelerating the time-to-market for anti-cancer drugs, along with a well-defined regulatory and development strategy. 3D *in vitro* models could demonstrate whether different formulations of the same drug are bioequivalent. A straightforward bioequivalence trial comparing relevant pharmacokinetic parameters of both formulations would be instrumental in gaining FDA approval.

There is now a huge demand for new strategies and more suitable biomaterials to interface with microfluidic chips for cell biological studies. Clearly, there is still a long road ahead for this to become reality, but we believe this is the right direction to pursue in the search for novel and more efficacious treatments for cancer.

I-6. REFERENCES

1. Albini, A. and M.B. Sporn, *The tumour microenvironment as a target for chemoprevention.* Nat Rev Cancer, 2007. **7**(2): p. 139-47.
2. Fang, Q.B., et al., *Three Overlapping Balloon-expandable Stents Applied in Coeliac Artery Dissection: Case Report and Literature Review.* West Indian Med J, 2014. **63**(7): p. 791-2.
3. Gurski, L.A., et al., *3D matrices for anti-cancer drug testing and development.* Oncology Issues, 2010. **25**: p. 20-25.
4. Cheema, U., et al., *Spatially defined oxygen gradients and vascular endothelial growth factor expression in an engineered 3D cell model.* Cell Mol Life Sci, 2008. **65**(1): p. 177-86.
5. Kenny, P.A., et al., *The morphologies of breast cancer cell lines in three-dimensional assays correlate with their profiles of gene expression.* Mol Oncol, 2007. **1**(1): p. 84-96.
6. Kurisu, S., et al., *Rac-WAVE2 signaling is involved in the invasive and metastatic phenotypes of murine melanoma cells.* Oncogene, 2005. **24**(8): p. 1309-19.
7. Ridky, T.W., et al., *Invasive three-dimensional organotypic neoplasia from multiple normal human epithelia.* Nat Med, 2010. **16**(12): p. 1450-5.

8. Wozniak, M.A., et al., *Focal adhesion regulation of cell behavior.* Biochim Biophys Acta, 2004. **1692**(2-3): p. 103-19.
9. Goodman, T.T., C.P. Ng, and S.H. Pun, *3-D tissue culture systems for the evaluation and optimization of nanoparticle-based drug carriers.* Bioconjug Chem, 2008. **19**(10): p. 1951-9.
10. Lee, M.Y., et al., *Three-dimensional cellular microarray for high-throughput toxicology assays.* Proc Natl Acad Sci U S A, 2008. **105**(1): p. 59-63.
11. Meli, L., et al., *Influence of a three-dimensional, microarray environment on human cell culture in drug screening systems.* Biomaterials, 2012. **33**(35): p. 9087-96.
12. Mehling, A., et al., *Non-animal test methods for predicting skin sensitization potentials.* Arch Toxicol, 2012. **86**(8): p. 1273-95.
13. Yamada, K.M. and E. Cukierman, *Modeling tissue morphogenesis and cancer in 3D.* Cell, 2007. **130**(4): p. 601-10.
14. Rangarajan, A. and R.A. Weinberg, *Opinion: Comparative biology of mouse versus human cells: modelling human cancer in mice.* Nat Rev Cancer, 2003. **3**(12): p. 952-9.
15. Hao, C., et al., *Gene mutations in primary tumors and corresponding patient-derived xenografts derived from non-small cell lung cancer.* Cancer Letters, 2015. **357**(1): p. 179-185.
16. Hwu, D., et al., *Assessment of the role of circulating breast cancer cells in tumor formation and metastatic potential using in vivo flow cytometry.* J Biomed Opt, 2011. **16**(4): p. 040501.
17. Jason, E.E., et al., *Three-Dimensional Lung Tumor Microenvironment Modulates Therapeutic Compound Responsiveness In Vitro – Implication for Drug Development.* PLoS One, 2014. **9**(3).
18. Hsiao, A.Y., et al., *Microfluidic system for formation of PC-3 prostate cancer co-culture spheroids.* Biomaterials, 2009. **30**(16): p. 3020-7.
19. Elliott, N.T. and F. Yuan, *A review of three-dimensional in vitro tissue models for drug discovery and transport studies.* J Pharm Sci, 2011. **100**(1): p. 59-74.
20. Rimann, M. and U. Graf-Hausner, *Synthetic 3D multicellular systems for drug development.* Curr Opin Biotechnol, 2012. **23**(5): p. 803-9.
21. Peck, Y. and D.A. Wang, *Three-dimensionally engineered biomimetic tissue models for in vitro drug evaluation: delivery, efficacy and toxicity.* Expert Opin Drug Deliv, 2013. **10**(3): p. 369-83.
22. Mano, J.F., *Designing biomaterials for tissue engineering based on the deconstruction of the native cellular environment.* Materials Letters, 2015. **141**: p. 198-202.
23. Liang, Y., et al., *A cell-instructive hydrogel to regulate malignancy of 3D tumor spheroids with matrix rigidity.* Biomaterials, 2011. **32**(35): p. 9308-9315.
24. D'Souza, S., et al., *Gfi1 expressed in bone marrow stromal cells is a novel osteoblast suppressor in patients with multiple myeloma bone disease.* Blood, 2011. **118**(26): p. 6871-80.
25. Gatenby, R.A., et al., *Cellular adaptations to hypoxia and acidosis during somatic evolution of breast cancer.* Br J Cancer, 2007. **97**(5): p. 646-53.
26. Kazmi, N., et al., *Avascular tumour growth dynamics and the constraints of protein binding for drug transportation.* J Theor Biol, 2012. **313**: p. 142-52.
27. Tredan, O., et al., *Drug resistance and the solid tumor microenvironment.* J Natl Cancer Inst, 2007. **99**(19): p. 1441-54.
28. Fennema, E., et al., *Spheroid culture as a tool for creating 3D complex tissues.* Trends Biotechnol, 2013. **31**(2): p. 108-15.
29. Tung, Y.C., et al., *High-throughput 3D spheroid culture and drug testing using a 384 hanging drop array.* Analyst, 2011. **136**(3): p. 473-8.
30. Wen, Z., et al., *A spheroid-based 3-D culture model for pancreatic cancer drug testing, using the acid phosphatase assay.* Braz J Med Biol Res, 2013. **46**(7): p. 634-42.

31. Orlandi, P., et al., *Idarubicin and idarubicinol effects on breast cancer multicellular spheroids.* J Chemother, 2005. **17**(6): p. 663-7.
32. Clarke, M.F. and M. Fuller, *Stem cells and cancer: two faces of eve.* Cell, 2006. **124**(6): p. 1111-5.
33. Reya, T., et al., *Stem cells, cancer, and cancer stem cells.* Nature, 2001. **414**(6859): p. 105-11.
34. Wang, Y.C., et al., *Drug screening identifies niclosamide as an inhibitor of breast cancer stem-like cells.* PLoS One, 2013. **8**(9): p. e74538.
35. Jung, P., et al., *Isolation and in vitro expansion of human colonic stem cells.* Nat Med, 2011. **17**(10): p. 1225-7.
36. Shim, M.S., et al., *A bioreducible polymer for efficient delivery of Fas-silencing siRNA into stem cell spheroids and enhanced therapeutic angiogenesis.* Angew Chem Int Ed Engl, 2012. **51**(47): p. 11899-903.
37. Yeung, T.M., et al., *Cancer stem cells from colorectal cancer-derived cell lines.* Proc Natl Acad Sci U S A, 2010. **107**(8): p. 3722-7.
38. Benton, G., et al., *Multiple uses of basement membrane-like matrix (BME/Matrigel) in vitro and in vivo with cancer cells.* Int J Cancer, 2011. **128**(8): p. 1751-7.
39. Szot, C.S., et al., *3D in vitro bioengineered tumors based on collagen I hydrogels.* Biomaterials, 2011. **32**(31): p. 7905-12.
40. Chen, L., et al., *The enhancement of cancer stem cell properties of MCF-7 cells in 3D collagen scaffolds for modeling of cancer and anti-cancer drugs.* Biomaterials, 2012. **33**(5): p. 1437-44.
41. Yip, D. and C.H. Cho, *A multicellular 3D heterospheroid model of liver tumor and stromal cells in collagen gel for anti-cancer drug testing.* Biochem Biophys Res Commun, 2013. **433**(3): p. 327-32.
42. Liu, J., et al., *Soft fibrin gels promote selection and growth of tumorigenic cells.* Nat Mater, 2012. **11**(8): p. 734-41.
43. Mosesson, M.W., *Fibrinogen and fibrin structure and functions.* J Thromb Haemost, 2005. **3**(8): p. 1894-904.
44. Rao, S.S., et al., *Glioblastoma behaviors in three-dimensional collagen-hyaluronan composite hydrogels.* ACS Appl Mater Interfaces, 2013. **5**(19): p. 9276-84.
45. Xu, X., et al., *Recreating the tumor microenvironment in a bilayer, hyaluronic acid hydrogel construct for the growth of prostate cancer spheroids.* Biomaterials, 2012. **33**(35): p. 9049-60.
46. Berger, J., et al., *Structure and interactions in covalently and ionically crosslinked chitosan hydrogels for biomedical applications.* Eur J Pharm Biopharm, 2004. **57**(1): p. 19-34.
47. Florczyk, S.J., et al., *3D porous chitosan-alginate scaffolds: a new matrix for studying prostate cancer cell-lymphocyte interactions in vitro.* Adv Healthc Mater, 2012. **1**(5): p. 590-9.
48. Kievit, F.M., et al., *Chitosan-alginate 3D scaffolds as a mimic of the glioma tumor microenvironment.* Biomaterials, 2010. **31**(22): p. 5903-10.
49. Fang, X., et al., *Novel 3D co-culture model for epithelial-stromal cells interaction in prostate cancer.* PLoS One, 2013. **8**(9): p. e75187.
50. Fischbach, C., et al., *Cancer cell angiogenic capability is regulated by 3D culture and integrin engagement.* Proc Natl Acad Sci U S A, 2009. **106**(2): p. 399-404.
51. Xu, X.X., et al., *Encapsulated human hepatocellular carcinoma cells by alginate gel beads as an in vitro metastasis model.* Exp Cell Res, 2013. **319**(14): p. 2135-44.
52. Nyga, A., U. Cheema, and M. Loizidou, *3D tumour models: novel in vitro approaches to cancer studies.* J Cell Commun Signal, 2011. **5**(3): p. 239-48.
53. Serebriiskii, I., et al., *Fibroblast-derived 3D matrix differentially regulates the growth and drug-responsiveness of human cancer cells.* Matrix Biol, 2008. **27**(6): p. 573-85.

54. Talukdar, S. and S.C. Kundu, *A Non-Mulberry Silk Fibroin Protein Based 3D In Vitro Tumor Model for Evaluation of Anticancer Drug Activity.* Advanced Functional Materials, 2012. **22**(22): p. 4778-4788.
55. Xu, G., et al., *In vitro ovarian cancer model based on three-dimensional agarose hydrogel.* J Tissue Eng, 2014. **5**: p. 2041731413520438.
56. Gill, B.J., et al., *A synthetic matrix with independently tunable biochemistry and mechanical properties to study epithelial morphogenesis and EMT in a lung adenocarcinoma model.* Cancer Res, 2012. **72**(22): p. 6013-23.
57. Loessner, D., et al., *Bioengineered 3D platform to explore cell-ECM interactions and drug resistance of epithelial ovarian cancer cells.* Biomaterials, 2010. **31**(32): p. 8494-506.
58. Ki, C.S., H. Shih, and C.C. Lin, *Effect of 3D matrix compositions on the efficacy of EGFR inhibition in pancreatic ductal adenocarcinoma cells.* Biomacromolecules, 2013. **14**(9): p. 3017-26.
59. Fischbach, C., et al., *Engineering tumors with 3D scaffolds.* Nat Methods, 2007. **4**(10): p. 855-60.
60. Ho, W.J., et al., *Incorporation of multicellular spheroids into 3-D polymeric scaffolds provides an improved tumor model for screening anticancer drugs.* Cancer Sci, 2010. **101**(12): p. 2637-43.
61. Fong, E.L., et al., *Modeling Ewing sarcoma tumors in vitro with 3D scaffolds.* Proc Natl Acad Sci U S A, 2013. **110**(16): p. 6500-5.
62. Huang, H., et al., *Peptide hydrogelation and cell encapsulation for 3D culture of MCF-7 breast cancer cells.* PLoS One, 2013. **8**(3): p. e59482.
63. Xu, X., M.C. Farach-Carson, and X. Jia, *Three-dimensional in vitro tumor models for cancer research and drug evaluation.* Biotechnol Adv, 2014. **32**(7): p. 1256-68.
64. Yang, Z. and X. Zhao, *A 3D model of ovarian cancer cell lines on peptide nanofiber scaffold to explore the cell-scaffold interaction and chemotherapeutic resistance of anticancer drugs.* Int J Nanomedicine, 2011. **6**: p. 303-10.
65. Schmeichel, K.L. and M.J. Bissell, *Modeling tissue-specific signaling and organ function in three dimensions.* J Cell Sci, 2003. **116**(Pt 12): p. 2377-88.
66. Weaver, V.M., et al., *Reversion of the malignant phenotype of human breast cells in three-dimensional culture and in vivo by integrin blocking antibodies.* J Cell Biol, 1997. **137**(1): p. 231-45.
67. Li, Q., et al., *p21-Activated kinase 1 coordinates aberrant cell survival and pericellular proteolysis in a three-dimensional culture model for premalignant progression of human breast cancer.* Neoplasia, 2008. **10**(4): p. 314-29.
68. Terranova, V.P., et al., *Regulation of cell attachment and cell number by fibronectin and laminin.* J Cell Physiol, 1986. **127**(3): p. 473-9.
69. Kleinman, H.K., et al., *Isolation and characterization of type IV procollagen, laminin, and heparan sulfate proteoglycan from the EHS sarcoma.* Biochemistry, 1982. **21**(24): p. 6188-93.
70. Kenny, P.A. and M.J. Bissell, *Targeting TACE-dependent EGFR ligand shedding in breast cancer.* J Clin Invest, 2007. **117**(2): p. 337-45.
71. Wong, A.P., et al., *Partitioning microfluidic channels with hydrogel to construct tunable 3-D cellular microenvironments.* Biomaterials, 2008. **29**(12): p. 1853-61.
72. Lee, G.Y., et al., *Three-dimensional culture models of normal and malignant breast epithelial cells.* Nat Methods, 2007. **4**(4): p. 359-65.
73. Kalabis, J., et al., *Stimulation of human colonic epithelial cells by leukemia inhibitory factor is dependent on collagen-embedded fibroblasts in organotypic culture.* FASEB J, 2003. **17**(9): p. 1115-7.
74. Gurski, L.A., et al., *Hyaluronic acid-based hydrogels as 3D matrices for in vitro evaluation of chemotherapeutic drugs using poorly adherent prostate cancer cells.* Biomaterials, 2009. **30**(30): p. 6076-85.

75. Silva-Correia, J., et al., *Angiogenic potential of gellan-gum-based hydrogels for application in nucleus pulposus regeneration: in vivo study.* Tissue Eng Part A, 2012. **18**(11-12): p. 1203-12.
76. Yan, L.P., et al., *Tumor Growth Suppression Induced by Biomimetic Silk Fibroin Hydrogels.* Sci Rep, 2016. **6**: p. 31037.
77. Yan, L.P., et al., *In vitro evaluation of the biological performance of macro/micro-porous silk fibroin and silk-nano calcium phosphate scaffolds.* J Biomed Mater Res B Appl Biomater, 2015. **103**(4): p. 888-98.
78. Phan-Lai, V., et al., *Three-dimensional scaffolds to evaluate tumor associated fibroblast-mediated suppression of breast tumor specific T cells.* Biomacromolecules, 2013. **14**(5): p. 1330-7.
79. Chung, B.G., et al., *Microfluidic fabrication of microengineered hydrogels and their application in tissue engineering.* Lab Chip, 2012. **12**(1): p. 45-59.
80. Inamdar, N.K. and J.T. Borenstein, *Microfluidic cell culture models for tissue engineering.* Curr Opin Biotechnol, 2011. **22**(5): p. 681-9.
81. Chen, Y.A., et al., *Generation of oxygen gradients in microfluidic devices for cell culture using spatially confined chemical reactions.* Lab Chip, 2011. **11**(21): p. 3626-33.
82. Zhou, Y. and Q. Lin, *Microfluidic flow-free generation of chemical concentration gradients.* Sensors and Actuators B: Chemical, 2014. **190**(0): p. 334-341.
83. Choi, Y., et al., *Three dimensional MEMS microfluidic perfusion system for thick brain slice cultures.* Biomed Microdevices, 2007. **9**(1): p. 7-13.
84. Toh, Y.C., et al., *A novel 3D mammalian cell perfusion-culture system in microfluidic channels.* Lab Chip, 2007. **7**(3): p. 302-9.
85. Zhang, W., et al., *Patient-Specific 3D Microfluidic Tissue Model for Multiple Myeloma.* Tissue Eng Part C Methods, 2014.
86. Young, E.W., *Cells, tissues, and organs on chips: challenges and opportunities for the cancer tumor microenvironment.* Integr Biol (Camb), 2013. **5**(9): p. 1096-109.
87. Chrobak, K.M., D.R. Potter, and J. Tien, *Formation of perfused, functional microvascular tubes in vitro.* Microvasc Res, 2006. **71**(3): p. 185-96.
88. Jain, R.K., *Normalization of tumor vasculature: an emerging concept in antiangiogenic therapy.* Science, 2005. **307**(5706): p. 58-62.
89. Bergers, G., et al., *Benefits of targeting both pericytes and endothelial cells in the tumor vasculature with kinase inhibitors.* J Clin Invest, 2003. **111**(9): p. 1287-95.
90. Seo, B.R., P. DelNero, and C. Fischbach, *In vitro models of tumor vessels and matrix: Engineering approaches to investigate transport limitations and drug delivery in cancer.* Advanced Drug Delivery Reviews, 2014. **69–70**(0): p. 205-216.
91. Nguyen, D.H., et al., *Biomimetic model to reconstitute angiogenic sprouting morphogenesis in vitro.* Proc Natl Acad Sci U S A, 2013. **110**(17): p. 6712-7.
92. Miller, J.S., et al., *Rapid casting of patterned vascular networks for perfusable engineered three-dimensional tissues.* Nat Mater, 2012. **11**(9): p. 768-74.
93. Buchanan, C.F., et al., *Three-dimensional microfluidic collagen hydrogels for investigating flow-mediated tumor-endothelial signaling and vascular organization.* Tissue Eng Part C Methods, 2014. **20**(1): p. 64-75.
94. Moya, M., D. Tran, and S.C. George, *An integrated in vitro model of perfused tumor and cardiac tissue.* Stem Cell Res Ther, 2013. **4 Suppl 1**: p. S15.
95. Bischel, L.L., et al., *Tubeless microfluidic angiogenesis assay with three-dimensional endothelial-lined microvessels.* Biomaterials, 2013. **34**(5): p. 1471-7.
96. Song, J.W., et al., *Microfluidic endothelium for studying the intravascular adhesion of metastatic breast cancer cells.* PLoS One, 2009. **4**(6): p. e5756.

97. Harris, D.T., *Hormonal therapy and chemotherapy of renal-cell carcinoma.* Semin Oncol, 1983. **10**(4): p. 422-30.
98. Shablak, A., et al., *T cell-based immunotherapy of metastatic renal cell carcinoma: modest success and future perspective.* Clin Cancer Res, 2009. **15**(21): p. 6503-10.
99. Pouliot N, P.B., Burrows A, *Investigating Metastasis Using In Vitro Platforms. In: Madame Curie Bioscience Database*. 2000, Landes Bioscience: Austin (TX).
100. Valastyan, S. and R.A. Weinberg, *Tumor metastasis: molecular insights and evolving paradigms.* Cell, 2011. **147**(2): p. 275-92.
101. Chaffer, C.L. and R.A. Weinberg, *A perspective on cancer cell metastasis.* Science, 2011. **331**(6024): p. 1559-64.
102. Zervantonakis, I.K., et al., *Three-dimensional microfluidic model for tumor cell intravasation and endothelial barrier function.* Proc Natl Acad Sci U S A, 2012. **109**(34): p. 13515-20.
103. Bersini, S., et al., *A microfluidic 3D in vitro model for specificity of breast cancer metastasis to bone.* Biomaterials, 2014. **35**(8): p. 2454-61.
104. Bray, L.J., et al., *Multi-parametric hydrogels support 3D in vitro bioengineered microenvironment models of tumour angiogenesis.* Biomaterials, 2015. **53**(0): p. 609-620.
105. Zheng, C., et al., *Quantitative study of the dynamic tumor-endothelial cell interactions through an integrated microfluidic coculture system.* Anal Chem, 2012. **84**(4): p. 2088-93.
106. Xu, Z., et al., *Application of a microfluidic chip-based 3D co-culture to test drug sensitivity for individualized treatment of lung cancer.* Biomaterials, 2013. **34**(16): p. 4109-17.

Chapter II

Biomaterials and Microfluidics for Drug Discovery and Development

Chapter II

Biomaterials and Microfluidics for Drug Discovery and Development[1]

ABSTRACT

Microfluidic devices are one of the most promising tools to mimic *in vivo* like conditions, either in normal or disease scenarios, such as tumorigenesis or pathogenesis. The combination of microfluidics with biomaterials represents the ability to more closely mimic cells' natural microenvironment concerning its three-dimensional (3D) nature and continuous perfusion with nutrients and cells' crosstalk. Due to miniaturization and increased experimental throughput, microfluidics have generated significant interest in the drug discovery and development domain. Herein, the most recent advances in the field of microfluidics for drug discovery are overviewed, and the role of biomaterials in 3D *in vitro* models and the contribution of organ-on-a-chip technologies highlighted.

Keywords: Drug discovery; Microfluidics; Organ-on-chip.

[1]This chapter is based on the following publication:

M. R. Carvalho, R. Truckenmüller, R. L. Reis J. M. Oliveira, Biomaterial- and Microfluidic-Based 3D Models, Springer, Ed: J. Miguel Oliveira and Rui L. Reis (2019).

II-1. INTRODUCTION

Many diseases, particularly acute disorders, are now treatable or manageable very effectively. The discovery of new medications for health problems that affect a great part of the world's population, such as cancer, cardiovascular diseases, metabolic disorders, arthritis, depression, anxiety, gastrointestinal disorders, pain, infectious diseases, and many others, have led to an improvement in overall health [1]. As a result, the increased quality of life may lead to increased life expectancy [1].

The drug discovery process traditionally starts in the laboratory where cells are cultured on flat bottom cell culture flasks or Petri dishes and their response monitored upon the addition of a drug. If successful, the experimentation progresses through the established chain of drug development: animal and human clinical trials. Only then the product can be approved by the regulatory agencies, such as the Food and Drug Administration (FDA; US) or the European Medicines Agency (EMEA; EU), and commercialized [2]. However, it is well described in the literature that the vast majority of "hits" fail between animal testing and clinical trials (around 90 %). Among the primary causes of failure, non-clinical/clinical safety (>50 %) and efficacy (>10 %) stand out from all other factors (*e.g.*, strategic, commercial or operational) [3]. Finally, the drug that is successful in clinical assays takes between 12 to15 years to reach the market, and with a cost that can exceed $1 billion [4, 5].

Animal experimentation is still indispensable for evaluating the efficiency of drugs in terms of their adsorption, distribution, metalolism, excretion, and toxicity (ADMET). However, their present certain ethical and, in particular, clinical issues. This is because animal models, besides displaying a highly complex environment, they are not predictive of the effects of a drugs in humans. As an examples, studies regarding the efficiency of cancer drugs report that the average rate of successful translation from animal models to clinical cancer trials is less than 8 % [5, 6].

In order to improve the drug development pipeline, novel cell-based high-throughput screening (HTS) techniques have been developed. This have enabled the screening of more than a million compounds in a couple of months [2]. However, still only about 1 out of 5.000 promising drugs successfully makes it to the market. Even though HTS improves the screening speed and is now considered a standard platform for drug discovery, it leaves several unresolved issues, being the monetary costs and efficiency on top. Currently, pharmaceutical industries employ HTS primarily for chemical optimization at the early stage of the drug development [7]. Recent estimates predict that HTS products only contribute to 19–33 % (or less) to successful marketed drugs [8]. This may be the result

of the still limited performance of most of these conventional screening platforms due to their reliance on flat and static culture maintenance. To tackle these issues, 3D cell-based *in vitro* assays have been actively pursued, most of the times using hydrogels [9].

As a promising solution, microfluidic technologies emerged, in this case those also providing 3D microenvironments with microvascular-like perfusion and diffusion between mimicked micro-vessels and 3D cell culture, which is closer to what cells encounter in real tissues or organs.

Briefly, microfluidics is the manipulation of low volumes of fluids in channels with dimensions of tens of micrometers [10]. Microfluidic chips are small platforms typically made of elastomeric materials and comprising channel systems connected to liquid reservoirs by, for example, tubing systems in turn linked to syringes. [11].

In combination with appropriate biological assays and high-sensitivity detection techniques, microfluidic-based systems allow the identification and isolation of individual cells or molecules [12]. Indeed, (bio)sensors, detectors and optical components can be easily integrated on chip [13]. A great variety of microchip fabrication techniques and materials are available for producing highly sophisticated 2½D and 3D microstructures with integrated modules.

The high performance displayed by microfluidic-based systems holds very promising for biomedical research and, in particular, for cancer research. This is demonstrated by the rapid market growth of microfluidic-related products during the last years, with an emphasis on the translational research. In particular, currently in the USA, there are three companies using microfluidic chips for *in vivo* drug delivery, five microchip-based cancer cell/biomarker diagnostic companies, and about 10 companies working on microfabricated cell-based chips for drug screening and discovery applications [14]. The same market is growing also in Europe with very successful companies such as MIMETAS, Cellesce, Biond Solutions and Astraveus, among others (http://ufluidix.com/circle/microfluidic-companies/) (Assessed on 12/08/2019).

This chapter focuses on current and future applications of biomaterials in microfluidics, microfluidics systems in drug discovery and highlights the potential of "organ-on-a-chip" technology for drug discovery. Organ-on-a-chip are systems developed by combining microfluidic technologies and tissue engineering to mimic physiological conditions in the body [15].

II-2. BIOMATERIALS APPLIED IN MICROFLUIDIC SYSTEMS

Biomaterials are gradually being developed as *in vitro* microenvironments mimicking *in vivo* cell niches. They are also widely used in tissue engineering for the regeneration and modeling of a diverse variety of both normal and diseased tissues [16]. The development of 3D culture models with tunable biomaterials has facilitated the investigation of biological phenomena with a higher level of complexity and physiological relevance than the traditional 2D models [17].

The combination of microfluidic technologies and biomaterials enables the reproduction of important spatiotemporal features of complex native scenario. This facilitates the identification of new mechanisms of cell regulation and pathogenesis, profoundly impacting on drug discovery [18].

Among all the type of 3D biomaterials, hydrogels display advanced capabilities for their integration into microfluidic systems. Briefly, hydrogels can be derived from natural polymers or from synthetic origin. The formers include chitosan, alginate, hyaluronic acid (HA), gellan gum (GG), agarose, collagen, gelatin, or fibroin [19]. The latter include poly(ethylene glycol) (PEG), polyvinyl alcohol (PVA), poly(N,Ndimethylacrylamide), and methoxy poly(ethylene glycol)-poly(e-caprolactone), among others [20-24].

Cross-linked hydrogel networks can be engineered on a molecular basis to tune their physicochemical properties, such as their porosity or mechanical properties such as [25]. 3D hydrogel-based biomaterials, both natural and synthetic, are therefore able to match the physical, chemical, and mechanical properties of the native (ECM) network, justifying their widespread use as ECM mimics in microfluidic models [26, 27].

Various types of hydrogels have been used in microfluidic systems [28] being collagen [29, 30], PEG [18, 31], agarose [32], fibrin [30, 33], and Matrigel™ [34, 35] some of the most commonly employed.Toh *et al.* [30] used collagen to develop a microfluidic 3D hepatocyte chip ('3D HepaTox Chip') for *in vitro* drug toxicity testing. The 3D HepaTox Chip was based on multiplexed microfluidic channels where a 3D microenvironment was engineered in each of the eight channels to maintain the hepatocytes' metabolic functions [30]. Positively-charged methylated collagen and negatively-charged HEMA-MMA-MAA terpolymer were chosen to form a localized 3D matrix due to their ability to support hepatocyte functions.

Dinh *et al.* [31] combined PEG with microfluidics for precision single-cell handling. The resulting model comprised a compartmentalized neuronal array (CNA) microfluidic circuit that allowed high-throughput experimentation (**Figure II-1**) [31]. Similarly, Gao *et al.* [36] employed photolithography to geometrically encapsulate human hepatoma HepG2 and human lung epithelial A549 cells in a 3D PEG hydrogel inside a microfluidic device. The cells in the device were exposed to anticancer drugs and apoptosis was studied (**Figure II-2**). Two anticancer drugs (actinomycin D and methotrexate) exhibited distinct effects on the levels of intracellular glutathione and reactive oxygen species, indicating the selectivity of these drugs on the disturbance of redox balance within cells [36].

To address the global challenge of vascularization, Zhang *et al.* [37] employed additive manufacturing to build a blood vessel-like microfluidic structure, which was then embedded inside the bulk material. To achieve this, alginate and chitosan hydrogels were used for direct printing of the channels with a wall thickness below 200 μm. The printed microfluidic network was able to sustain media perfusion, both without and with being embedded in bulk hydrogels to support cell viability, representing an improvement towards vascularization models [37].

Regarding fibrin hydrogels, Carrion *et al.* [33] described a novel 3D microfluidic device as a model system to study the molecular regulation of perivascular stem cell niches. Endothelial cells (ECs) suspended within 3D fibrin hydrogels patterned in the device adjacent to stromal cells (either fibroblasts or human bone marrow-derived mesenchymal stromal cells, hBM-MSCs) executed a morphogenetic process similar to vasculogenesis, maturing into a robust capillary network with well-defined hollow lumens. Both MSCs and fibroblasts formed pericytic associations with the ECs but promoted capillary morphogenesis with distinct kinetics [33].

The fields of biomaterials engineering and microfluidics have advanced to impressive levels of sophistication. The pioneering efforts reported above to further integrate biomaterials technology into microfluidic chips tackle pertinent questions in several fields ranging from drug discovery to stem cell research.

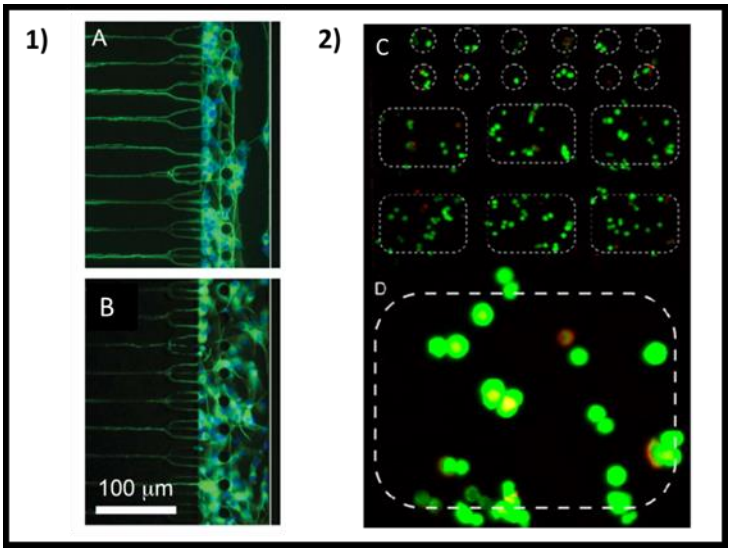

Figure II-1 - Biomaterials applied in microfluidic systems. 1) *In situ* neuron patterning. Differentiated human SH-SY5Y neurons cultured for 5 days within the CNA devices on a PL/PLL-g-PEG array of micro-sized channels (A) and on a continuous PL coating (B). Biomaterial patterning increases neurite guidance into the outgrowth microchannels. Reprinted with permission from [31]. Copyright © 2018 Royal Society of Chemistry. 2 - C) Optical image of hydrogel microstructure arrays containing two phenotypes of cells: HepG2 and A549 cells. HepG2 cells were encapsulated inside cylindrical hydrogel microstructures (78 µm Ø × 50 µm), while A549 cells were encapsulated inside rectangular hydrogel microstructures (330 µm × 217 µm × 50 µm). D) Corresponding fluorescence image for the cell viability expressed by live/dead assay (live cells green, dead cells red). Reprinted with permission from [36]. Copyright © 2010 Elsevier.

ECM-derived biomaterials approaches are currently being studied for their potential to preserve the tissue-specific biochemical composition as well as the ultrastructure of the native ECM [38]. The development of biomaterials that promote the formation of functional tissues in clinical applications is therefore of the utmost importance in tissue engineering and cancer research. So far, many studies have focused on the decellularization of tissues and organs, including small intestinal submucosa, heart valve, blood vessel, skin, nerve, tendon, ligament, bladder, amniotic membrane, heart, liver and lung [39-41]. For example, Choi *et al.* [40] decellularized an ECM scaffold derived from porcine cartilage and proved it was more efficient in maintaining chondrogenesis of rabbit mesenchymal stem cells (rMSCs) *in vitro* and in the nude mouse model *in vivo* than the PGA scaffold used as a control [40].

Uygun *et al.* [39] generated a transplantable liver graft using perfusion decellularization technique, and further introduced perfusion-seeding and culture techniques for the preparation of recellularized liver matrix for transplantation. The recellularized graft supported liver-specific function including albumin secretion, urea synthesis and cytochrome P450 expression at comparable levels to normal liver *in vitro* [39]. Inorganic compounds, such as hydroxyapatite, have also been integrated into

microfluidic models for mimicking bone tissues. For example, Jusoh *et al.* [42] developed a microfluidic platform that integrates fibrin ECM with the synthetic bone mineral hydroxyapatite nanoparticles to provide *in vivo*-like microenvironments for bone vessel sprouting. Results showed that fibrin with 0.2 % hydroxyapatite exhibited a higher number and length of sprouts [42].

II-3. MICROFLUIDICS IN DRUG DISCOVERY

Microfluidics represent an improvement to existing technologies in key areas of drug discovery. Microfluidics involves the use of materials and techniques for controlling the movement of minute quantities of fluids. Its ability to miniaturize assays and increase experimental throughput have generated significant interest of the drug discovery and development domain [43].

Microfluidics can be applied to drug discovery in a variety of ways. For instance, it can be used in (a) target identification, capture, and analysis, or (b) for developing dynamic cell culture platforms in which cell response to a drug is assessed in a more *in vivo*-like environment [44]. In the following, we briefly describe these two applications:

a) Target identification

In drug discovery, the signal transduction pathways and protein-protein interactions within cells must be understood. Microfluidic devices can be used to address this issue by manipulating, labeling, lysing, separating and quantifying protein contents in single cells by *e.g.*, single-molecule fluorescence counting [45] (**Figure II-2-1**). One of the many successful examples in the use of microfluidics in target identification is the measurement of the number of epitope-tagged human β_2-adrenergic receptors (β_2ARs), an important pharmacologic target in a number of airway and cardiovascular diseases [46]. Another interesting application of microfluidic devices in target identification is in ligand binding studies, where microfluidics can minimize the interaction times, improving sensitivity and increasing throughput. In this sense, a microfluidic platform was used to characterize DNA binding energy using four eukaryotic transcription factors to predict their *in vivo* function [47].

b) For hit identification

b1) *Compound generation:* Developments in combinatorial chemistry have greatly enhanced our ability to generate drug candidates [43]. Merging channel geometries, various reagents can be mixed and biochemical reactions can be induced in a well-controlled and precise manner. Reduction of

reaction chamber's size, and consequently, in the amount of reagents and time needed for reaction empower this strategy. Mitchell *et al.* [48] developed a miniaturized-synthesis/total analysis system that incorporated a chemical microprocessor with time-of-flight mass spectrometry (TOF-MS), which has been used in the generation of compound libraries [48]. This system enabled real-time processing of many reactions due to the integration of continuous-flow synthesis and provision for on-line analysis within a microfabricated structure. In another example, Zhou *et al.* [49] developed a microfluidic pico-array device for the synthesis and purification of oligonucleotides. This device consisted of fluidic channels and 3,698 individual pico-reaction chambers for parallel synthesis of oligonucleotides [49]. Microfluidic systems can be also used to understand and assess natural drug candidates. Natural products are undoubtedly one of the major sources of new chemical entities, with an increase in world market growth rate [50]. Natural molecules are "evolutionarily optimized" as drug-like molecules and remain one of the best sources of drug leads [50]. To identify the physiological action of a natural compound out of a complex array of constituent molecules in the source material, microfluidic devices can also be used. Gramowski *et al.* [51] applied multielectrode microchips for the screening of herbal medicines. The screening of complex mixtures of neuroactive substances was assessed in the chip, where changes in the spontaneous activity of cultured networks of primary cortical neurons were quantified to evaluate the action of the drugs [51].

b2) *Compounds screening:* HTS is considered one of the most important methods for identifying "hit" compounds [52]. Over the last decades, pharmaceutical companies established HTS as a major tool to screen the properties of new chemical entities. A significant number of microfluidic technologies can now be used to enable HTS studies, including multiplexed systems, microwell arrays, plug-based methods and gradient-generating devices [53]. Khademhosseini *et al.* [54] studied the response of multiple cell types (*e.g.* hepatocytes, fibroblasts, and embryonic stem cells) to different compounds by seeding cells within microwells that were integrated within an array of reversibly sealed microfluidic channels **(Figure II-2)**. The ability to position many cell types on a single chip could be useful for studying the effects of a series of compounds on different cell types. Concentration gradients also have a great role in drug screening and cell-based studies. A gradient-generating microfluidic device can generate a certain range of doses and thereby control different cell behaviors at the same time. By using gradients, cells can be stimulated with controlled temporal and spatial resolution to study the effects of drug concentration on chemotaxis. Occhetta *et al.* [55] introduced a branched channel to generate a gradient and culture 3D micro-masses of adult hBM-MSCs under continuous and controlled

laminar flow perfusion [55]. Moreover, the platform allowed for conditioning the cellular micro-aggregates with different combinations of growth factors, morphogens or drug molecules, in a high-throughput fashion.

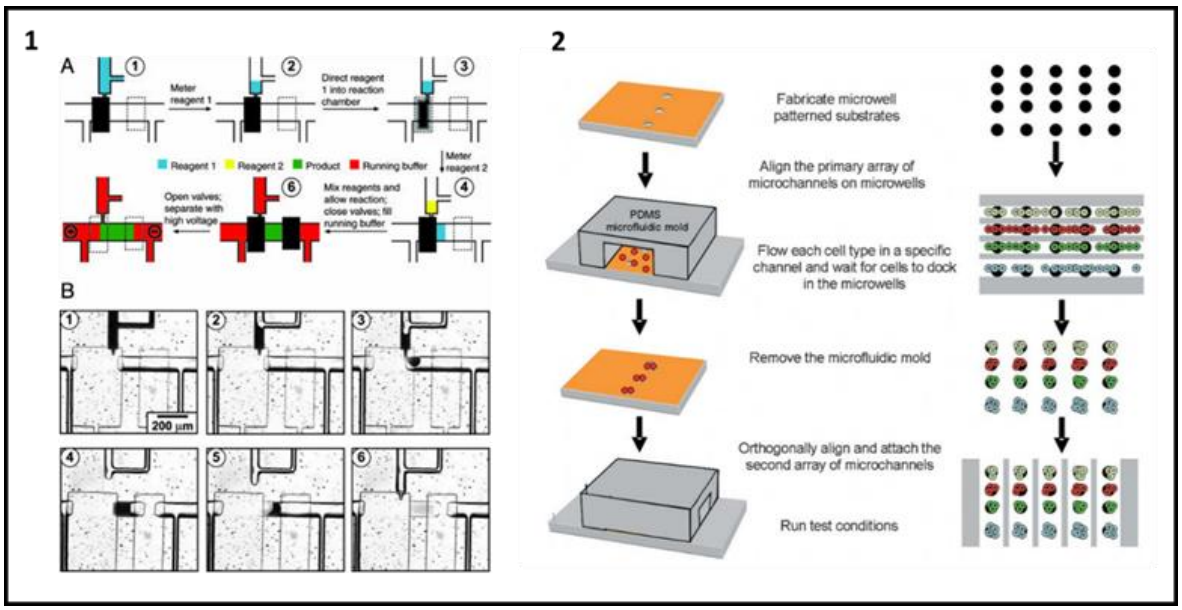

Figure II-2 - Microfluidics in drug discovery. 1) On-chip reaction. (A) Schematic of the on-chip reaction process. (B) Time frames of a video that correspond to the steps described in A. A concentrated solution of crystal violet (a pH indicator) in 0.1 N sodium hydroxide solution is loaded into the microchamber with the three-state valve half-open; loading an equal amount of 1 N HCl into the chamber turns the solution from blue to yellow. Reprinted with permission from [45]. Copyright © 2004 The National Academy of Sciences; 2) Schematic diagram of reversible sealing of microfluidic arrays onto microwell-patterned substrates to fabricate multiphenotype cell arrays. Initially, a PDMS microfluidic mold in the form of an array of microchannels was aligned on an array of microwells. Each cell type was flown through an independent channel. The cells docked onto the corresponding micro-wells, which resulted in a patterned array of cells. To deliver multiple solutions, the PDMS microfluidic mold was removed and replaced with another mold, which was placed orthogonally to create multiphenotype cell arrays inside each microchannel. Reprinted with permission from [54]. Copyright © 2018 Copyright Clearance Center, Inc.

II-4. ORGAN-ON-A-CHIP AND DRUG DISCOVERY

The combination of microfluidics with human cells, together with developments in areas such as stem cell research, regenerative medicine, biomaterials, and tissue engineering, have resulted into the development of new generation of 3D *in vitro* models that better mimic *in vitro* human tissues and organs. These new models are coined "organs-on-chip" devices and reproduce the functional unit of a human organ and tissue. Therefore, organs-on-a-chip provide not only the biological relevance but also the needed high-throughput characteristics needed in drug discovery applications. In the following, we

provide an overview of the developed technologies of organ-on-chip devices and their role on drug testing and discovery.

II-4.1. Lung–on-a-chip

The seminal paper by Huh *et al.* [56] described the development of a biomimetic lung-on-a-chip model capable to reconstitute organ-level lung functions to create a model pathologic pulmonary edema (**Figure II-3-1**). In this model, the authors cultured two types of human lung cells (epithelial and endothelial primary lung cells) in stacked parallel microchannels separated by a (porous) PDMS membrane. Alike the human lung, the upper alveolar channel was filled with air, whereas the lower microvascular channel was filled with liquid. Stretch was cyclically applied to the membrane by additional vacuum actuator channels to mimic the physiological breathing movements of the lung. After adding interleukin-2 (IL-2) to the microvascular channel, the fluid started to leak into the air compartment, mimicking pulmonary edema. The authors tested this pulmonary disease model against the pharmacological agent GSK2193874. This compound blocks ion channels activated by mechanical strain, and inhibited leakage of fluid to the air compartment, suggesting it would be a viable option for patients with pulmonary edema. The next step will be to hook this lung up to other chip-based organs with the goal of being able to rapidly screen many drugs across many organs [56].

Jain *et al.* [57] developed another lung-on-a-chip with primary lung alveolar and endothelial cells. This new chip design enabled whole human blood to be perfused through the vascular channel without producing thrombus formation, while allowing high-resolution, real-time analysis of interactions between human blood cells and endothelial cells in an *in vivo*-like context. Using this technology and, in combination with novel analytical tools for quantitation of dynamic platelet-endothelial interactions and clot formation, the authors demonstrated a key role of the epithelium in inflammation-driven vascular thrombosis during lipopolysaccharide endotoxin (LPS)-induced acute lung injury. The study showed that the model can be used to evaluate *in vitro* cytoprotective effects of Protease-activated Receptor-1 (PAR-1), a potential therapeutic with anti-thrombotic and anti-inflammatory activities [57].

II-4.2. Liver-on-a-chip

The liver is one of the most relevant organs involved in maintaining physiological homeostasis. *In vitro* models that could recapitulate functional liver tissue could have an enormous impact in the pharmaceutical field, allowing for toxicity assessment of new drugs [39]. To develop such models, hepatocytes with membrane polarity and functional bile canaliculi are essential [58]. Lee *et al.* [59] created a biologically-inspired artificial liver sinusoid with a microfluidic endothelial-like barrier having mass transport properties similar to the liver acinus (**Figure II-3-2**). This unit consisted of a cord of hepatocytes (50 μm x 30 μm x 500 μm) fed by diffusion of nutrients across the microfluidic endothelial-like barrier from a convective transport vessel. Combining photolithography-based microfluidic technologies and primary cell culture, the team was able to assess liver toxicity of diclofenac, since it has long been implicated in drug-related liver damage [59].

Following Lee's work, Nakao *et al.* [58] presented a microfluidic device comprising an hepatic cord-like structure model with primary rat hepatocytes, which was proven functional. Computer simulation results showed that the flow velocity in the medium (1 mm⁄s), matched the respective blood flow velocity *in vivo*. Moreover, when 5-(and-6)-carboxy-2′,7′-dichloro-fluorescein diacetate (CDFDA) was injected into the device, it was readily absorbed by the cells and metabolized into CDF by esterase. The metabolites were actively excreted into bile canaliculi by the MRP2 protein [58].

II-4.3. Kidney-on-a-chip

Standard photolithography technology was used by Jang *et al.* [60] to develop a simple multi-layer microfluidic device by integrating a PDMS microfluidic channel and a porous polyester membrane substrate (0.4 μm pore size; 10 μm thickness) to culture primary rat inner medullary collecting duct (IMCD) cells [60]. In order to evaluate molecular transport in renal tubule cells, water and sodium uptake was measured after hormonal stimulations of the IMCD cells using vasopressin and aldosterone. The cells were subjected to a fluidic shear stress of 1 dyn/cm^2 for the time period of 5 h on the porous membrane, which was found to be sufficient for the IMCD cells to enhance cell polarization and rearrange cytoskeleton and cell junctions [60].

II-4.4. Heart-on-a-chip

Agarwal *et al.* [61] developed anisotropic cardiac microtissues recapitulating the laminar architecture of the heart ventricle, which were engineered on cantilevers. The sub-millimeter-sized thin film cantilevers of soft elastomers were fabricated by a laser-based process **(Figure II-3-3)** [61]. They used the microdevice seeded with cardiac myocytes from mice to test the positive inotropic effect of isoproterenol on cardiac contractility at dosages ranging from 1 nM to 100 μM. Tissues were exposed to different drug concentrations with the advantage of complete washout between dosages, leading to a fast collection of data from just one chip [61].

II-4.5. Bone marrow-on-a-chip

Torisawa *et al*. [62] developed a tissue-engineered bone marrow model that is able to retain hematopoietic stem and progenitor cells in *in vivo*-like conditions for one week. In this example, the bone marrow is first generated in mice, and then explanted as a whole and maintained *in vitro* within a microfluidic device fabricated using standard photolithography **(Figure II-3-4)**. The obtained results show that this model mimics the complex tissue-level responses to Υ-radiation toxicity normally observed *in vivo*, as well as to a therapeutic counter-measure agent (G-CSF) that is known to accelerate recovery from radiation-induced toxicity in cancer patients [62]. Moreover, this research sheds light on the fact that it is crucial to keep the whole hematopoietic niche to obtain an *in vivo*-like response, rather than culturing particular cell types [62].

II-4.6. Intestine-on-a-chip

When discussing drug development, the small intestine is crucial, given that orally administered drugs are mainly absorbed in the small intestine [63]. There they diffuse across a mucous layer covering an epithelial cell layer lining the intestinal wall. Therefore, it is logical that drugs and chemicals are tested on intestinal cells and tissues to assess the pharmacodynamics and pharmacokinetics of drugs, such as absorption, distribution, metabolism, elimination and toxicity (ADMET).

Having this in mind, several groups started developing *in vitro* models for absorption and metabolism studies. Realistic models should include certain key components such as cellular (*i.e.*

enterocytes, goblet and vascular endothelial cells), structural (*i.e.* villi and,mucus) and dynamic (*i.e.* peristalsis) features. Kimura *et al.* [64] engineered an intestinal model with a membrane and vascular flow simulating the epithelial barrier and the epithelial-endothelial interface. The microfluidic model comprised optical fiber inserts for on-line and real-time pharmacokinetic measurements to detect the amount of fluorescence of rhodamine-123 in culture, working as a tracer substrate to study diffusion [64].

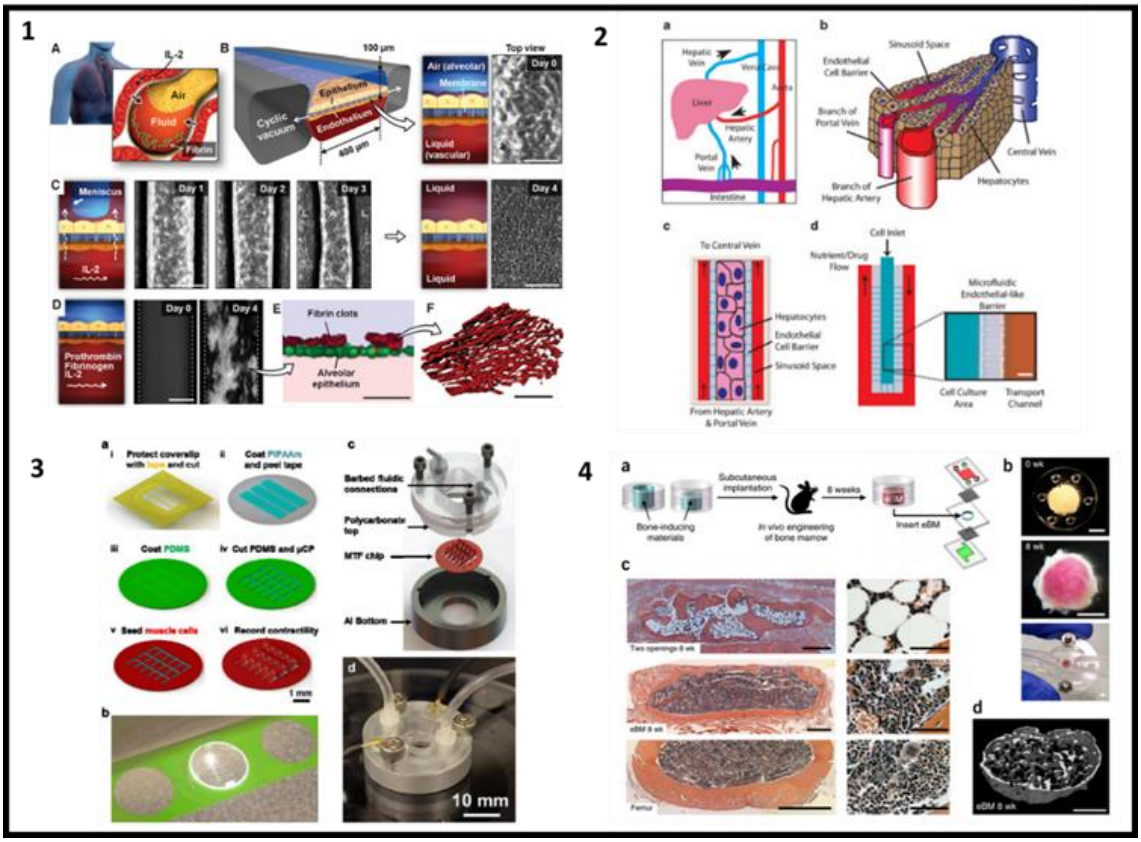

Figure II-3 - Organs-on-chip models: 1) A microengineered lung-on-a-chip model of human pulmonary edema. (A) IL-2 therapy is associated with vascular leakage. (B) IL-2–induced pulmonary edema is modeled in the lung-on-a-chip. The top or "air" portion is the alveolar channel; the bottom or "liquid" portion is the vascular channel. Scale bar represents 200 μm. (C) Endothelial exposure to IL-2 (1000 U/mL) causes liquid from the lower, microvascular channel to leak into the upper, alveolar chamber. Scale bars represent 200 μm. (D) During IL-2 treatment, prothrombin (100 μg/mL) and fluorescently labeled fibrinogen (2 mg/mL) introduced into the microvascular channel form fluorescent fibrin clots (white) over the course of 4 days. Scale bar represents 200 μm. (E) A fluorescence confocal microscopic image shows that the fibrin deposits (red) in (D) are found on the upper surface of the alveolar epithelium (green). Scale bar represents 50 μm. (F) The clots in (D) and (E) are highly fibrous networks. Scale bar represents 5 μm. Reprinted with permission from [56]. Copyright © 2012, American Association for the Advancement of Science. 2) Microfluidic liver-on-a-chip model. (a) The liver receives blood flow from the hepatic artery and the portal vein, which carries xenobiotics such as ingested drugs from the small intestine to be metabolized. (b) Schematic of the hepatocyte microenvironment in liver tissue. (c) The sinusoid space is bordered by a sheet of highly fenestrated

endothelial cells. (d) The single microfluidic sinusoid had three fluid terminals: a flow inlet, a flow outlet, and a cell inlet. Scale bar represents 20 μm. Reprinted with permission from [59]. Copyright © 2007 Wiley Periodicals, Inc. 3) Higher-throughput heart-on–a-chip model. (a) Schematic of the fabrication process. (b) Image of the engraving laser processing of Muscular Thin Films (MTFs) in the 18 mm diameter chip. (c) Exploded view of the conception and assembly of the fluidic device which fits the chip. (d) Image of an actual device in action. Reprinted with permission from [61]. Copyright © 2018 Royal Society of Chemistry. 4) *In vivo* bone marrow-on-a-chip model. (a) Workflow to generate a bone marrow-on-a-chip system (b) PDMS device containing bone-inducing materials in its central cylindrical chamber before implantation (top). (c) Low- (left) and high-magnification views (right) of histological hematoxylin-and-eosin–stained sections of the bone marrow formed in the PDMS device with two openings (top) or one lower opening (center) at 8 weeks. Reprinted with permission from [62]. Copyright © 2014, Springer Nature.

II-4.7. Tumor-on-a-chip

Cancer remains one of the main causes of death, despite the enormous efforts to cure the disease [65, 66]. Solid evidences have shown this key role of the tumor microenvironment (TME) in the onset and progression of the disease. A better understanding of the tumor microenvironment is therefore needed to improve our knowledge about the mechanistic determinants of the disease. However, the TME is extremely complex from a structural, cellular, and dynamic perspective, and therefore, very difficult to investigate *in vitro* and *in vivo*. The emerging tumor-on-a-chip technology can be of extreme usefulness in these processes. as well as screening platforms to evaluate the efficiency of anti-cancer drugs [67, 68].

In an approach to better understand breast cancer metastasis to bone, Jeon *et al.* [69] developed a microfluidic model of a human vascularized organ-specific microenvironment, which was used to explore and tune the extravasation process of metastatic tumor cells [69]. The experiment comprised an organ-specific model that enabled the study of human metastatic breast cancer cell extravasation within a perfusable human microvascularized bone-mimicking microenvironment. The microfluidic model was characterized by anastomoses with the lateral media channels. MDA-MB-231 breast cancer cells were introduced and extravasation events monitored. The platform was used to understand the anti-metastatic role of adenosine in the human breast cancer metastasis to bone [69].

In its turn, Bischel *et al.* [70] integrated a microfluidic co-culture platform with a multi-photon imaging-based technique to determine phenotypic cell behavior and flavin adenine dinucleotide (FAD) fluorescence intensity and fluorescence lifetime simultaneously in the same cell. This platform combined two independent assays normally performed with two different cell populations into a single device, allowing researchers to simultaneously assess both phenotypic cell behavior and enzyme activity

[70]. The metastasis towards bone was mimicked by differentiating MC3T3-E1 cells (osteoblast precursor cell line) towards osteoblast lineage and seeded on the sidewall of a microchannel. Next, a collagen I hydrogel coating was applied as extracellular matrix, either Lymph Node Carcinome of the Prostate cells (LNCaP) or (Bone metastatic LNCaP-derivative C4-2B**)** C4-2B cells were seeded into the channel. By engineering this cancer-bone microenvironment, it was demonstrated that the cross-talk between a bone metastatic prostate cancer cell line, C4-2B, and bone stromal cells, MC3T3-E1, increased the invasive behavior of the C4-2Bs, possibly by an increase in reactive oxygen species (ROS)-producing N1-acetyl polyamine oxidase (APAO) activity [70].

Sung *et al.* [71] presented a microscale cell culture analog (mCCA), which is basically a microfluidic device based on pharmacokinetics-pharmacodynamics (PK-PD) mathematical models. In this model, multiple cell culture chambers were connected with fluidic channels to mimic multi-organ interactions and test drug toxicity in a pharmacokinetic-based manner [71]. Three cell lines representing the liver, a tumor and bone marrow were cultured in the three-chamber microCCA to test the toxicity of an anticancer drug, 5-fluorouracil (5-FU). The result was analyzed with the PK-PD model of the device, and compared with the result of the static conditions (cell culture flasks). Each cell type exhibited differential responses to 5-FU, and the responses in the microfluidic environment were different from those in the static environment. The authors showed a relatively new approach based on the combination of mathematical modeling and an *in vitro* experimentation, with improved predictability for testing drug toxicity.

More recently, Wong *et al.* [72] exploited a 2.4 × 2.4 cm PDMS-based microfluidic chip to generate droplets and perform drug screening against suspended and adherent cancer cell lines, as well as cells dissociated from primary tumors of human patients. Bortezomib and Vorinostat were chosen as target drugs for leukemia in conjunction with Jurkat cells, whereas Cisplatin and Epirubicin were chosen as target drugs for breast cancer in conjunction with MDA-MB-231 cells. Cell viability was measured by ethidium homodimer-1 staining, enabling the capture of single cell drug response, without compromising population analysis. This method provided a versatile and rapid drug screening method using cells in different states [72].

II-5. CONCLUSION AND FUTURE TRENDS

New micro-engineering-based strategies have significantly improved the drug development process. Microfluidics makes possible to assess their therapeutic activity by enabling high-throughput functional readouts; to conduct high-throughput screens for drug discovery in realistic engineered 3D culture microenvironments; to develop organ-on-a-chip platforms to screen those drugs, which would probably fail during the expensive animal testing and human clinical trials later in the drug discovery process pipeline. Critical challenges remain in making these technological advances practically feasible for real-world pharmaceutical discovery. Thus, the optimal solution for drug discovery may rely on sufficiently complex and realistic technology, while being simple enough to allow for assay readouts, reliability and operational simplicity. In addition, mathematical and computational modeling will guide the design of the next generation of organ-on-chip devices, and bio-sensing will enable the real-time and *in situ* monitoring of the cellular metabolic responses.

Regarding biomaterials, *in vitro* platforms are just a scientific attempt at mimicking the natural system. It is therefore important to make the right choice of the function to be mimicked, as this choice will eventually determine whether a system is considered valuable or not. Because of this, there is now a huge demand for new and tunable biomaterials to interface with microfluidic chips for cell biological studies.

However, the reality is that despite rapid development of expertise in designing, fabricating and operating microfluidic systems for nearly twenty years now, no commercially available drugs have been discovered as a unique result of microfluidic technologies, to the best of our knowledge.

Griffith, a world-class scientist in organ-on-a-chip research said that more questions would be answered if Pharma collaborated more with engineers, as Pharma knows what problems it needs to solve, but engineers know how to build chips. Therefore, success in this endeavor must start with alliances between the fields of pharmaceutical industry, engineering, medicine, biology and computational biology. Maybe that is our future answer.

II-6. REFERENCES

1. Mullard, A., *2010 FDA drug approvals.* Nat Rev Drug Discov, 2011. **10**(2): p. 82-5.
2. Hughes, J.P., et al., *Principles of early drug discovery.* British Journal of Pharmacology, 2011. **162**(6): p. 1239-1249.
3. Hay, M., et al., *Clinical development success rates for investigational drugs.* Nature Biotechnology, 2014. **32**: p. 40.
4. Paul, S.M., et al., *How to improve R&D productivity: the pharmaceutical industry's grand challenge.* Nat Rev Drug Discov, 2010. **9**(3): p. 203-14.
5. Mak, I.W., N. Evaniew, and M. Ghert, *Lost in translation: animal models and clinical trials in cancer treatment.* Am J Transl Res, 2014. **6**(2): p. 114-8.
6. Szymański, P., M. Markowicz, and E. Mikiciuk-Olasik, *Adaptation of High-Throughput Screening in Drug Discovery—Toxicological Screening Tests.* International Journal of Molecular Sciences, 2012. **13**(1): p. 427-452.
7. Zheng, X.T., et al., *On-chip investigation of cell-drug interactions.* Adv Drug Deliv Rev, 2013. **65**(11-12): p. 1556-74.
8. Khanna, I., *Drug discovery in pharmaceutical industry: productivity challenges and trends.* Drug Discovery Today, 2012. **17**(19): p. 1088-1102.
9. Chandrasekaran, A., M. Abduljawad, and C. Moraes, *Have microfluidics delivered for drug discovery?* Expert Opinion on Drug Discovery, 2016. **11**(8): p. 745-748.
10. Whitesides, G.M., *The origins and the future of microfluidics.* Nature, 2006. **442**: p. 368.
11. Bettinger, C.J. and J.T. Borenstein, *Biomaterials-based microfluidics for engineered tissue constructs.* Soft Matter, 2010. **6**(20): p. 4999-5015.
12. Dittrich, P.S. and A. Manz, *Lab-on-a-chip: microfluidics in drug discovery.* Nature Reviews Drug Discovery, 2006. **5**: p. 210.
13. Tsao, C.-W., *Polymer Microfluidics: Simple, Low-Cost Fabrication Process Bridging Academic Lab Research to Commercialized Production.* Micromachines, 2016. **7**(12).
14. FluidicMEMS. *List of microfluidics companies*. 2018; Available from: http://fluidicmems.com/list-of-microfluidics-lab-on-a-chip-and-biomems-companies/.
15. Tian, C., et al., *Recent advances in microfluidic technologies for organ-on-a-chip.* TrAC Trends in Analytical Chemistry, 2019.
16. Shantanu, P., et al., *Polymeric Biomaterials for In Vitro Cancer Tissue Engineering and Drug Testing Applications.* Tissue Engineering Part B: Reviews, 2016. **22**(6): p. 470-484.
17. Carvalho, M.R., et al., *Significance of Tissue-engineered 3D in-vitro models for cancer research and drug screening.* Trends Biotechnol, 2015.
18. Kobel, S. and M.P. Lutolf, *Biomaterials meet microfluidics: building the next generation of artificial niches.* Current Opinion in Biotechnology, 2011. **22**(5): p. 690-697.
19. Radhakrishnan, J., et al., *Injectable and 3D Bioprinted Polysaccharide Hydrogels: From Cartilage to Osteochondral Tissue Engineering.* Biomacromolecules, 2017. **18**(1): p. 1-26.
20. Lai, J.H., et al., *Stem cells catalyze cartilage formation by neonatal articular chondrocytes in 3D biomimetic hydrogels.* 2013. **3**: p. 3553.
21. Cui, X., et al., *Direct human cartilage repair using three-dimensional bioprinting technology.* Tissue Eng Part A, 2012. **18**(11-12): p. 1304-12.
22. Bichara, D.A., et al., *Osteochondral defect repair using a polyvinyl alcohol-polyacrylic acid (PVA-PAAc) hydrogel.* Biomed Mater, 2014. **9**(4): p. 045012.

23. de Girolamo, L., et al., *Repair of osteochondral defects in the minipig model by OPF hydrogel loaded with adipose-derived mesenchymal stem cells.* Regen Med, 2015. **10**(2): p. 135-51.
24. Inagaki, Y., et al., *Effects of culture on PAMPS/PDMAAm double-network gel on chondrogenic differentiation of mouse C3H10T1/2 cells: in vitro experimental study.* BMC Musculoskelet Disord, 2014. **15**: p. 320.
25. Zeng, L., et al., *Effect of microcavitary alginate hydrogel with different pore sizes on chondrocyte culture for cartilage tissue engineering.* Materials Science and Engineering: C, 2014. **34**: p. 168-175.
26. Lutolf, M.P. and J.A. Hubbell, *Synthetic biomaterials as instructive extracellular microenvironments for morphogenesis in tissue engineering.* Nat Biotechnol, 2005. **23**(1): p. 47-55.
27. Barata, D., C. van Blitterswijk, and P. Habibovic, *High-throughput screening approaches and combinatorial development of biomaterials using microfluidics.* Acta Biomaterialia, 2016. **34**: p. 1-20.
28. Wan, J., *Microfluidic-Based Synthesis of Hydrogel Particles for Cell Microencapsulation and Cell-Based Drug Delivery.* Polymers, 2012. **4**(2).
29. Baker, B.M., et al., *Microfluidics embedded within extracellular matrix to define vascular architectures and pattern diffusive gradients.* Lab Chip, 2013. **13**(16): p. 3246-52.
30. Toh, Y.C., et al., *A microfluidic 3D hepatocyte chip for drug toxicity testing.* Lab Chip, 2009. **9**(14): p. 2026-35.
31. Dinh, N.D., et al., *Microfluidic construction of minimalistic neuronal co-cultures.* Lab Chip, 2013. **13**(7): p. 1402-12.
32. Si, G., et al., *A parallel diffusion-based microfluidic device for bacterial chemotaxis analysis.* Lab on a Chip, 2012. **12**(7): p. 1389-1394.
33. Bita, C., et al., *Recreating the perivascular niche ex vivo using a microfluidic approach.* Biotechnology and Bioengineering, 2010. **107**(6): p. 1020-1028.
34. Anguiano, M., et al., *Characterization of three-dimensional cancer cell migration in mixed collagen-Matrigel scaffolds using microfluidics and image analysis.* PLoS One, 2017. **12**(2): p. e0171417.
35. Chaw, K.C., et al., *Matrigel coated polydimethylsiloxane based microfluidic devices for studying metastatic and non-metastatic cancer cell invasion and migration.* Biomed Microdevices, 2007. **9**(4): p. 597-602.
36. Gao, D., et al., *A microfluidic approach for anticancer drug analysis based on hydrogel encapsulated tumor cells.* Anal Chim Acta, 2010. **665**(1): p. 7-14.
37. Zhang, Y., Y. Yu, and I.T. Ozbolat, *Direct Bioprinting of Vessel-Like Tubular Microfluidic Channels.* Journal of Nanotechnology in Engineering and Medicine, 2013. **4**(2): p. 0210011-0210017.
38. Hussey, G.S., J.L. Dziki, and S.F. Badylak, *Extracellular matrix-based materials for regenerative medicine.* Nature Reviews Materials, 2018.
39. Uygun, B.E., et al., *Organ reengineering through development of a transplantable recellularized liver graft using decellularized liver matrix.* Nat Med, 2010. **16**(7): p. 814-20.
40. Choi, K.-H., et al., *The chondrogenic differentiation of mesenchymal stem cells on an extracellular matrix scaffold derived from porcine chondrocytes.* Biomaterials, 2010. **31**(20): p. 5355-5365.
41. Lu, H., et al., *Autologous extracellular matrix scaffolds for tissue engineering.* Biomaterials, 2011. **32**(10): p. 2489-99.
42. Jusoh, N., et al., *Microfluidic vascularized bone tissue model with hydroxyapatite-incorporated extracellular matrix.* Lab Chip, 2015. **15**(20): p. 3984-8.
43. Kang, L., et al., *Microfluidics for Drug Discovery and Development: From Target Selection to Product Lifecycle Management.* Drug discovery today, 2008. **13**(1-2): p. 1-13.

44. Barata, D., et al., *Development of a shear stress-free microfluidic gradient generator capable of quantitatively analyzing single-cell morphology.* Biomed Microdevices, 2017. **19**(4): p. 81.
45. Wu, H., A. Wheeler, and R.N. Zare, *Chemical cytometry on a picoliter-scale integrated microfluidic chip.* Proc Natl Acad Sci U S A, 2004. **101**(35): p. 12809-13.
46. Huang, B., et al., *Counting low-copy number proteins in a single cell.* Science, 2007. **315**(5808): p. 81-4.
47. Maerkl, S.J. and S.R. Quake, *A systems approach to measuring the binding energy landscapes of transcription factors.* Science, 2007. **315**(5809): p. 233-7.
48. Mitchell, M.C., V. Spikmans, and A.J.d. Mello, *Microchip-based synthesis and analysis: Control of multicomponent reaction products and intermediates.* Analyst, 2001. **126**(1): p. 24-27.
49. Zhou, X., et al., *Microfluidic PicoArray synthesis of oligodeoxynucleotides and simultaneous assembling of multiple DNA sequences.* Nucleic Acids Res, 2004. **32**(18): p. 5409-17.
50. Shen, B., *A New Golden Age of Natural Products Drug Discovery.* Cell, 2015. **163**(6): p. 1297-1300.
51. Gramowski, A., et al., *Functional screening of traditional antidepressants with primary cortical neuronal networks grown on multielectrode neurochips.* Eur J Neurosci, 2006. **24**(2): p. 455-65.
52. Chandrasekaran, A., M. Abduljawad, and C. Moraes, *Have microfluidics delivered for drug discovery?* Expert Opin Drug Discov, 2016. **11**(8): p. 745-8.
53. Du, G., Q. Fang, and J.M.J. den Toonder, *Microfluidics for cell-based high throughput screening platforms—A review.* Analytica Chimica Acta, 2016. **903**: p. 36-50.
54. Khademhosseini, A., et al., *Cell docking inside microwells within reversibly sealed microfluidic channels for fabricating multiphenotype cell arrays.* Lab Chip, 2005. **5**(12): p. 1380-6.
55. Occhetta, P., et al., *High-Throughput Microfluidic Platform for 3D Cultures of Mesenchymal Stem Cells, Towards Engineering Developmental Processes.* Scientific Reports, 2015. **5**: p. 10288.
56. Huh, D., et al., *A human disease model of drug toxicity-induced pulmonary edema in a lung-on-a-chip microdevice.* Sci Transl Med, 2012. **4**(159): p. 159ra147.
57. A, J., et al., *Primary Human Lung Alveolus-on-a-chip Model of Intravascular Thrombosis for Assessment of Therapeutics.* Clinical Pharmacology & Therapeutics, 2018. **103**(2): p. 332-340.
58. Nakao, Y., et al., *Bile canaliculi formation by aligning rat primary hepatocytes in a microfluidic device.* Biomicrofluidics, 2011. **5**(2): p. 22212.
59. Lee, P.J., P.J. Hung, and L.P. Lee, *An artificial liver sinusoid with a microfluidic endothelial-like barrier for primary hepatocyte culture.* Biotechnol Bioeng, 2007. **97**(5): p. 1340-6.
60. Jang, K.J. and K.Y. Suh, *A multi-layer microfluidic device for efficient culture and analysis of renal tubular cells.* Lab Chip, 2010. **10**(1): p. 36-42.
61. Agarwal, A., et al., *Microfluidic heart on a chip for higher throughput pharmacological studies.* Lab on a chip, 2013. **13**(18): p. 3599-3608.
62. Torisawa, Y.-s., et al., *Bone marrow–on–a–chip replicates hematopoietic niche physiology in vitro.* Nature Methods, 2014. **11**: p. 663.
63. Fasinu, P., et al., *Diverse approaches for the enhancement of oral drug bioavailability.* Biopharm Drug Dispos, 2011. **32**(4): p. 185-209.
64. Kimura, H., et al., *An integrated microfluidic system for long-term perfusion culture and on-line monitoring of intestinal tissue models.* Lab Chip, 2008. **8**(5): p. 741-6.
65. Stroock, A.D. and C. Fischbach, *Microfluidic culture models of tumor angiogenesis.* Tissue Eng Part A, 2010. **16**(7): p. 2143-6.
66. Buchanan, C. and M.N. Rylander, *Microfluidic culture models to study the hydrodynamics of tumor progression and therapeutic response.* Biotechnol Bioeng, 2013. **110**(8): p. 2063-72.

67. Carvalho, M.R., et al., *Anti-Cancer Drug Validation: the Contribution of Tissue Engineered Models.* Stem Cell Rev, 2017.
68. Carvalho, M.R., et al., *Evaluating Biomaterial- and Microfluidic-Based 3D Tumor Models.* Trends in Biotechnology. **33**(11): p. 667-678.
69. Jeon, J.S., et al., *Human 3D vascularized organotypic microfluidic assays to study breast cancer cell extravasation.* Proceedings of the National Academy of Sciences, 2015. **112**(1): p. 214-219.
70. Bischel, L.L., et al., *A microfluidic coculture and multiphoton FAD analysis assay provides insight into the influence of the bone microenvironment on prostate cancer cells.* Integrative Biology, 2014. **6**(6): p. 627-635.
71. Sung, J.H., C. Kam, and M.L. Shuler, *A microfluidic device for a pharmacokinetic-pharmacodynamic (PK-PD) model on a chip.* Lab Chip, 2010. **10**(4): p. 446-55.
72. Wong, A.H.-H., et al., *Drug screening of cancer cell lines and human primary tumors using droplet microfluidics.* Scientific Reports, 2017. **7**(1): p. 9109.

Chapter III

Dendrimer Nanoparticles in CRC applications

Chapter III

Dendrimer Nanoparticles in CRC applications

ABSTRACT

Cancer nanotechnology is a prolific field of research, where nanotools are employed to diagnose and treat cancer with unprecedented precision. Targeted drug delivery is fundamental for more efficient cancer treatments. For this, nanoparticles have been extensively used during the last years in order to improve the specificity, selectivity and controlled release of drug delivery. It holds potential in minimizing systemic toxicity through the development of functionalized particles for targeted treatment. Among all the type of nanoparticles, dendrimers display several advantages, which make them ideal candidates for improved and targeted drug delivery in cancer research. Dendrimers can transport large amount of drug into specific areas. In addition, they can be employed for monitoring the progress of the treatment process, with an unprecedented theranostic capability. They can help to limit the side effects of anticancer drugs and limit their action toward specific regions. This chapter provides a brief overview on the types of dendrimer nanoparticles, their synthesis routes, as well as the preferred employed strategies for producing drug-loaded/functionalized NP's for cancer therapy in the last years. Special emphasis is given in colorectal cancer, which has shown a dramatic increase in its incidence during the last years, especially in industrialized countries.

Keywords: Colorectal cancer; Dendrimer nanoparticles; Targeting.

III-1. INTRODUCTION

Nanotechnology is an emerging field of research that is expected to play a definitive role in biomedicine in the near future, particularly for the targeted delivery of drugs at pathological sites inside the human body [1]. Nanoparticles (NPs) can be defined as particulate matter ranging between 1 and 100 nm in diameter, with a high surface area-to-volume ratio, and specialized surface characteristics [2-4]. The use of NPs as drug carriers in oncology started in 1986, when it was reported that NPs showed a tendency to accumulate in tumoral tissues [5]. This passive accumulation, also known as passive or primary targeting, is known as "Enhanced Permeability and Retention" (EPR) effect, and is one of the milestones of cancer treatment using NPs. Therefore, the use of NPs for cancer therapeutics holds very promising due to their high specificity and accumulation in tumor sites, as well as their long blood circulation time **(Figure III-1)**.

However, one of the major problems related to cancer treatment is its intrinsic anti-cancer drug resistance, which can appear prior to chemotherapy as well as acquired resistance due to drug treatment [6]. The selectivity improvement yielded by NPs resulted in a great enhancement in the efficacy of the transported drug, while the occurrence of side effects in the patient was reduced. Hence, targeted nanomedicine offers innovative therapeutic strategies to overcome the various limitations of conventional chemotherapy, such as drug resistance, enabling enhanced selectivity, and early and more precise cancer diagnosis [7]. Moreover, it is possible to incorporate targeting moieties selective for cancer cell biomarkers, which improves even more the selectivity and specificity of the treatment [8]. The main types of targeting moieties that are used for decorating and targeting NPs are: i) Antibodies [9]; ii) Peptide-based targeting [10]; iii) Small molecule-based targeting [11]; and iv) Aptamer-based targeting [12].

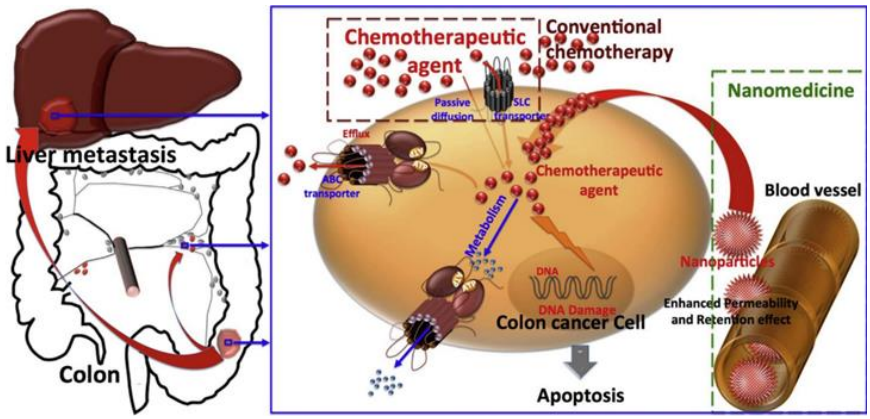

Figure III-1 - Rationale for nanomedicine approach in cancer-therapy. Reprinted with permission from [1].

The discovery of non-biodegradable nanoparticles including micelles, nanogels, liposomes, nanoemulsions, polymeric NPs, gold NPs and magnetic NPs, as agents in nano-drug delivery and imaging at pathological sites has enhanced delivery at lower doses and increased aqueous solubility and bioavailability of the drug with reduced side effects [13]. Nevertheless, the clinical application of these NPs to CRC therapy remains limited, as can be seen in **Table III-1**.

Table III-1 - Current nanotechnology applications in colorectal cancer clinical trials and status.

Study Title	Identifier	Intervention	Status
Targeted polymeric nanoparticles loaded with cetuximab and decorated with somatostatin analogue to colon cancer	NCT03774680	Cetuximab NPs/ Oral approved anticancer drug.	Recruiting
Targeted silica nanoparticles for real time image-guided intraoperative mapping of nodal metastasis	NCT02106598	Fluorescent cRGDY-PEG-Cy5.5-C dots	Recruiting
TKM 080,301 (Lipid nanoparticles containing siRNA against the PLK1 gene product) in patients with colorectal, pancreas, gastric, breast, ovarian and esophageal cancer with hepatic/ TKM 080,301 for primary or secondary liver cancer	NCT01437007	Drug: TKM-080,301	Completed
Pharmacokinetic, safety and efficacy study of nanoparticle paclitaxel in patients with peritoneal cancer/ A Phase I study of intraperitoneal nanoparticle paclitaxel in patients with peritoneal malignancies	NCT00666991	Nanoparticulate paclitaxel	Completed
Neoadjuvant chemoradiotherapy with CRLX-101 and capecitabine for rectal cancer	NCT02010567	CRLX101/ Capecitabine/ Radiotherapy	Active/ Not recruiting
Liposomal irinotecan, fluorouracil, leucovorin calcium and rucaparib in treating patients with metastatic pancreatic, colorectal,	NCT03337087	5-FU/ Leucovorin calcium/ liposomal irinotecan, rucaparib	Recruiting

gastroesophageal or biliary cancer			

Moreover, as can be seen from **Table III-1**, none of the ongoing clinical trials using nanotechnology in colorectal cancer comprises the use of dendrimer nanoparticles. After literature research, it was found that there is only one clinical trial using dendrimers, with application in inoperable liver cancers. This dendrimer consists of poly-L-lysine dendrimer as nanovector mixed with complex of 188-Rhenium-ligand (nitro-imidazole-methyl-1,2,3-triazol-methyl-di-[2-pycolyl] amine) [14]. Although a very popular type of nanoparticles, inclusively used in clinical trials for other pathologies such as breast cancer and HIV prevention (VivaGel®), scientific advances are needed for dendrimer applications in the clinical setting.

III-2. DENDRIMER NANOPARTICLES

III-2.1. Properties

Among the innumerous types of NPs available, dendrimers offer multiple advantages. They are highly branched polymers, and therefore specific moieties and drugs can be easily conjugated and encapsulated. Herein, we focused on polyamidoamine (PAMAM) dendrimer NPs. PAMAM dendrimers are the most common class of dendrimers, suitable for many tissue engineering and regenerative medicine (TERM), materials science, and biotechnology applications [15]. They contain an inner alkyl-diamine core and a peripheral shell made of tertiary amine branches [16]. They have a well-designed branching architecture with abundant terminal groups [17]. Therefore, the high level of control over dendritic architectures makes dendrimers ideal carriers in biomedical applications [18]. In addition, the toxicity of dendrimers mainly comes from the high cationic charge density in the periphery, where charges interact with biological cell membrane, resulting in membrane disruption, hurdle that can be easily overcome by surface modification. Dendrimers have the advantages of being biocompatible upon modification and easily eliminated from the body [19] through the kidneys along the same metabolic pathways taken by folate, peptides and antibodies [20-22].

Since dendrimers possess high density of surface functional molecules, they are easily conjugated with several targeting agents for selective delivery of chemotherapeutics to the tumor tissue. Furthermore, they contain internal cavities for macromolecule encapsulation, being able to transport highly hydrophobic drugs **(Figure III-2)** [23].

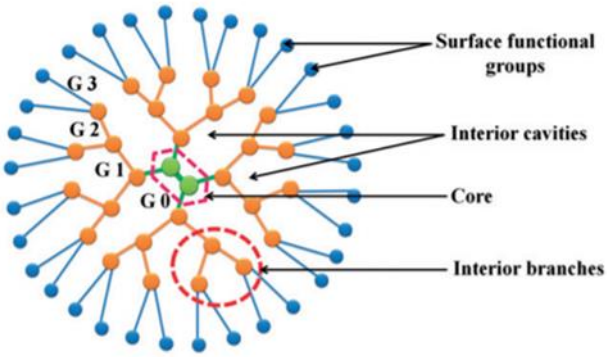

Figure III-2 - Dendrimer branched architecture, representing the increasing generations (G). Reprinted with permission from [24].

III-2.2. Synthesis and types of Dendrimers

Dendrimers have been traditionally synthesized by two major routes: the divergent method, introduced by Tomalia [17], and the convergent one, developed by Hawker and Frechet [25]. In the first method (divergent), the final molecule grows radially from a core by the sequential addition of layers of monomers, each layer constituting a new generation (G). The number of surface groups multiplies according to the functionalities in each monomer ramification [26]. It is important that every step of the reaction is fully completed before the addition of a new generation to avoid defects in the branches. One of the main advantages of this approach is that in the final step of the reaction, the surface of the dendrimer can be easily modified with desired functional groups. Moreover, it is a fast synthesis which allows the preparation of large dendrimers. The main drawbacks of this approach is the extensive purification it is required, since the final product and the intermediate reactants have similar molecular weights, charge, and polarity [27]. Also, the higher the generation, the greater the chances are of having branching defects, since the presence of bulky branches creates difficulties in the coupling of new ones. Despite these obstacles, the advantages of this strategy have made it the main route for dendrimer production.

In a reverse way from the divergent synthesis, dendrimers can also be synthesized starting from the surface towards de inner core. The growth of the molecule starts from the ends of the chain, beginning by integrating the various branching points with other monomers that will constitute the dendrimers. Finally, these branches are attached to a central core when they reach the desired

generation size [28]. In contrast to the divergent growth, this method permits easier purification due to bigger differences between the final products and the initial reagents. Other advantages include higher monodispersity for low generations and fewer branch defects. The main downsides are low yield and difficulties in obtaining higher generations due to steric interferences when the branches are connected to the core [29].

Regarding the available types of dendrimers, Poly(propylene imine) (PPI) dendrimers were the first ones to be reported by in the 70's. Together with PAMAM, they represent the most widely studied type. PPI dendrimers can be based on a 1,4-diaminobutane (DAB) core, but also be synthesized from an ethylenediamine nucleus and other core molecules by a double Michael addition reaction. PPI monomers are used as branching units. Hence their interior contains various tertiary tris-propylene amines, and they form full generations with primary amines as surface ends [30].

Another common type of dendrimers are the Poly-l-lysine (PLL) dendrimers, mostly used as gene carriers due to their excellent condensation with oligonucleotides. Among their favorable characteristics are good biocompatibility, water solubility, biodegradability, and flexibility, similar to other dendrimers. With peptide bonds in their structures, both their core and branching units are commonly based on the amino acid lysine PLL dendrimers differ from the general concept of PAMAM and PPI dendrimers since they are mostly asymmetrical [31]. However, they are still precise molecules, with a controlled number of lysines branching out from the core, and terminal amine residues. The lysine in the terminal group of PLL contains two primary amines that are frequently modified for better biological performance [32].

There are many more types of dendrimer nanoparticles, although less used. They can be classified according to their shape, structure, branching, solubility, chirality and attachment, which can be seen in **Figure III-3.**

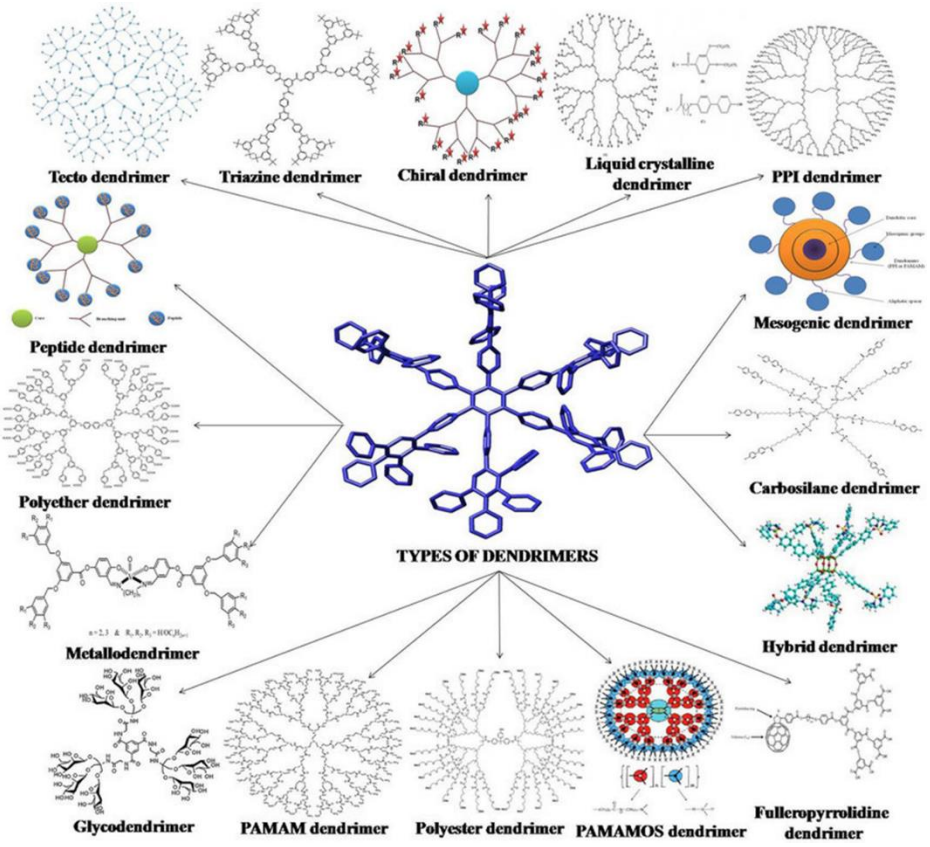

Figure III-3 - Different types of dendrimers. Reprinted with permission from [33].

When compared to other dendritic NPs, PAMAM surpasses them due to the ease of its preparation, desirable chemical and physical properties, surface functional groups, and comparatively lower toxicity to other dendrimers [22].

A variety of dendrimers have been developed and used since the 1980s, but the ones derived from polyamidoamine (PAMAM) are undeniably the most employed. They are generally, biocompatible, and non-immunogenic systems, which favors their use in drug delivery. The core of PAMAM is most commonly ethylenediamine, although more hydrophobic molecules such as diaminododecane, diaminoexane, and diaminobutane may also be used [34].

Functionalization is an integral part of dendrimer multiple uses. Functionalization is the process of incorporating multiple active sites in dendrimers in order to generate macromolecules with multifunctional architecture. Functionalized dendrimers have at least six well defined nanoscale features known as “Critical Nanoscale Design Parameters” (CNDPs). These parameters consist of size, shape, surface chemistry, flexibility, rigidity, architecture and elemental composition [35]. These CNPDs may be systematically employed to produce a wide range of new emerging properties that may be desirable

and critical for different clinical applications. The functionalization serves a variety of purposes, namely to reduce cytotoxicity and enhance transepithelial transport [36], for interaction with coupling molecules such as natural-based polymers [36], fluorescent probes [36], and an inner hydrophobic core where other molecules can be trapped [37, 38]. Among the myriad possibilities, dendrimers can find applications as delivery carriers of drugs and DNA (transfection) [39], imaging agents [37, 40, 41], and scaffolds for TERM [42].

III-3. DENDRIMER APPLICATIONS IN CANCER RESEARCH

A strong body of evidence now suggests that NPs in the form of dendrimers may be of added value in the future of oncology-related theranostics [43, 44]. Other than the flexibility for functionalization using diverse ligands and its low-nanometer size, the introduction of stimuli responsive functionality on dendrimers allows the release of payloads in response to specific triggers. These triggers could be endogenous in nature (acid, enzyme, and redox potentials) or it could be applied externally (light and temperature) [45-47]. One of these examples is the recent work developed by Nigam *et al.* [48] on cervical cancer, where iron oxide NPs were modified with Generation 2 (G2) PAMAM dendrimers and loaded with doxorubicin (DOX), therefore combining magnetic chemotherapy and hyperthermia on HeLa cancer cells [48]. When exposed to alternating current magnetic field, results show enhanced cell death as result of fatal synergistic contribution of DOX and high temperatures. Interestingly, the combinatorial treatment reduced cancer cell viability from 100 % to 3.6 % [48].

In a unique strategy to fight lung cancer, Amreddy *et al.* [49] designed a targeted drug delivery system to co-encapsulate functionally different agents, such as a combination of siRNA and chemotherapy. For targeting purposes, folic acid was conjugated to PAMAM dendrimer NPs [49]. The team developed a new NP system for co-delivery of siRNA against HuR mRNA (HuR siRNA) and *cis*-diamine platinum (CDDP) to folate receptor-α (FRA) overexpressing H1299 lung cancer cells. Results showed negligible toxicity towards non-cancerous MRC9 lung fibroblast cells, as well as the ability of dendrimer nanoparticles for targeted co-delivery of siRNA and chemotherapy agents together in lung cancer cells [49].

For breast cancer, one good example of dendrimer application is the work of Chittasupho *et al.* [50]. Having in mind that breast tumors preferentially metastasize to the lung, bone and distant lymph nodes (that secret high levels of CXCL12), the team hypothesized that targeted inhibition of CXCR4 in

breast cancer cells should suppress CXCR4-positive tumor cells toward secondary metastatic sites. The efficacy of CXCR4 targeted dendrimers carrying doxociclin (LFC131-DOX-D4) on cellular binding, cytotoxicity, and migration of BT-549-Luc and T47D breast cancer cells was investigated. Results showed enhanced *in vitro* cellular toxicity as compared with non-targeted dendrimers. The modified dendrimers exhibited remarkable reduced migration of BT-549-Luc breast cancer cells towards the used chemoattractant. This report demonstrated the potential utility of LFC131-dendrimer conjugates for breast cancer therapy and metastasis.

In the case of liver cancer, due to lack of cell surface biomarkers and highly metastatic nature, early detection and targeted therapy of hepatocellular cellular carcinoma (HCC) is an unmet clinical need [51]. Galactosamine (Gal) is among the few selective ligands used for targeting HCCs due to its high binding affinity to asialoglycoprotein receptors (ASGPRs) overexpressed in HCC. In a recent work, Yousef *et al.* [51] engineered a nanoscale G4 PAMAM dendrimer NP anchored to Gal and loaded with the potent anticancer curcumin derivative (CDF) as a platform for targeted drug delivery to HCC. Surprisingly, in an *in vivo* xenograft model, cytotoxicity assays in HCC cell lines showed that CDF was more potent as a chemotherapeutic anticancer than the currently in use Doxorubicin, Sorafenib and Cisplatin chemotherapeutic agents [51].

Glioblastoma is the most common type of malignant brain tumor and one of the deadliest cancers [52]. It has been described that dendrimers have affinity to cross blood–brain barrier after systemic administration [53]. Liu *et al.* [54] utilized a combined chemo- and gene-therapy approach for effective glioma treatment and developed DOX-loaded dendrigraft poly-l-lysine (DGL) dendrimer surface modified with TNF (tumor necrosis factor) related apoptosis-inducing ligand (TRAIL) for the tumor targeting specifically of T7 peptide, a TfR-specific peptide. This approach was based on the knowledge that DOX increased the anticancer effect of TRAIL by regulating the expression of death receptors, as well as stimulation of apoptotic pathways [54, 55].

Other than targeting and locally releasing drugs, advances in nanotechnology have enabled the development of different dendrimers that can be used as diagnostic aids in several imaging applications. In particular, diagnostic applications including magnetic resonance imaging (MRI) [56]. For example, Langereis *et al.* [57] reported the synthesis of 5–6-nm gadolinium-diethylene triamine penta-acetic acid (Gd-DTPA)-terminated poly(propylene imine) (PPI) dendrimers as MRI agent. Talanov *et al.* [58] reported a PAMAM dendrimer-based nanoprobe with dual MR and fluorescence (FI) modalities. Gd (III) was covalently attached to a dendrimer to create a fresh macromolecular contrast MRI agent. The

authors used 2-(4-isothiocyanatobenzyl)-6-methyl diethylenetriaminepentaacetic acid (1B4M-DTPA) and Cy5.5 as a bifunctional chelating agent. The PAMAM dendrimers covalently attached to the Gd (III)-DTPA chelates and units of the near-infrared (NIR) fluorescent dye, Cy5.5, to form a dual-modality MRI-FI agent [58].

The development of new dendrimers as drug-carriers continues to be essential in cancer therapy. They can be easily functionalized with a diverse variety of ligands to reach the tumor through the different body barriers in the body with minimal loss of activity. This results in the selectively targeting and killing of tumor cells without affecting the normal cells and most importantly, with an actively controlled release mechanism.

III-4. Dendimer Nanoparticles in Colorectal Cancer

Colorectal cancer (CRC) is the third leading cause of cancer death in the U.S. and additionally the third widely diagnosed cancer in the world [59].

The chemotherapeutic approach alone has not been found to be very efficient in CRC as the drug molecules may not reach the target site with an effective concentration and suffer a non-specific distribution, with only a small fraction of the drug reaching the tumor [60, 61].

These unique "polymeric compounds" can form intelligent species after modification, transporting drugs into specific areas and at the same time can be used for monitoring the state of organs attacked by cancer cells, as well as the progress of the curing process [13]. Recent advances in nanotechnology have rendered it an attractive approach for designing novel clinical solutions for CRC [13].

When tumor cells are shed from primary tumors or metastatic sites of early-stage cancer patients and enter the bloodstream, they are called circulating tumor cells (CTCs). Detection and capture of CTCs is of upmost importance because they provide information about the tumor origin. However, they are very challenging to capture due to their low concentrations in peripheral blood. In order to make advances in this area, Xie *et al.* [62] reported an effective approach to specifically bind and capture colon cancer HT29 cells by using multiple Sialyl Lewis X antibodies (aSlex)-conjugated with PAMAM dendrimers. Since Sialyl Lewis X is a type II carbohydrate antigen for mediating the CRC metastatic process, it was expected to capture the antigen positive CTCs in artificial blood samples [62] **(Figure III-5A)**. Results indicated that the conjugate showed the enhanced capture of HT29 cells in a

concentration-dependent manner and the maximum capture efficiency of 77.88 % was obtained within 1 hour exposure [62]. This work provided a novel conceptual guidance for the effective prevention of cancer metastasis.

Capecitabine is one of the most used anticancer drugs in CRC, and is converted into 5-FU by various metabolic enzymes involved in DNA damage and tumor growth inhibition [63]. However, capecitabine has multiple adverse side effects affecting the blood, hair cells, bone marrow, and liver. In this context, Nabavizadeh *et al.* [61] induced colon adenocarcinoma in mouse models with azoxymethane, a carcinogen agent, and then investigated the potentiality of non-modified G4 PAMAM dendrimers to improve capecitabine therapeutic index and decrease its adverse side effects on liver and bone marrow [61]. Although no targeting was performed, the team compared the effects of free and conjugated capecitabine form on tumor size and blood cell lines abnormalities. Results showed reduced side effects in the liver and blood along with decreased tumor size when compared with the free form [61].

In a recent work, Aliboland *et al.* [12] encapsulated gold (Au) NPs inside PAMAM dendrimer NPs. The aim of this study was to investigate the theranostic capability of curcumin-loaded dendrimer-gold hybrid structures **(Figure III-5B)**. Moreover, the curcumin-loaded PEGylated Au dendrimer was further conjugated to MUC-1 aptamer (Apt-PEG-AuPAMAM-CUR) in order to target the mucin-1 overexpressing cancer colorectal adenocarcinoma cells *in vitro* and *in vivo*. The obtained results confirmed higher cellular uptake, internalization and cytotoxicity of Apt-PEG-AuPAMAM-CUR in comparison with PEG-AuPAMAM-CUR in C26 and HT29 colorectal cancer cell lines. Moreover, the system worked as an effective anti-tumor therapy and accurate computed tomography imaging of C26 tumor-bearing mice due to gold accumulation [12].

Similarly, Alibolandi *et al*. [64] developed camptothecin-loaded pegylated PAMAM dendrimer **(Figure III-5C)**. For targeting purposes, the team functionalized the system with AS1411 anti-nucleolin aptamers for site-specific targeting against CRC cells, which overexpresses nucleolin receptors [64]. Remarkably, aptamer AS1411 has now entered clinical trials (phase II/III trials) for acute leukaemia therapy [65]. Comparative *in vitro* cytotoxicity experiments demonstrated that the targeted camptothecin loaded-pegylated dendrimers had higher anti-proliferation activity towards nucleolin-positive HT29 and C26 colorectal cancer cells than nucleolin-negative CHO cell line. The same system was tested *in vivo* on C26 tumor-bearing mice with promising results.

Another anti-cancer drug currently used in the clinics is irinotecan [66]. However, its utility is limited by its narrow therapeutic index. Theoretically, a possibility to improve therapeutic index consists on increasing drug exposure in the diseased tissue, without accumulation in the healthy tissues. Dendrimer nanotechnology offers this possibility, as shown by England *et al.* [66]. They modified generation 5 L-lysine dendrimer with a polyoxazoline as a drug delivery vehicle for improving the therapeutic index of SN-38, the active metabolite of irinotecan **(Figure III-5D)**. This extensive study comprised different linker technologies to obtain diverse pharmacokinetic profiles of drug release. Three conjugates with plasma release half-lives of 2.5 h, 21 h, and 72 h were tested for efficacy and toxicity using a mouse SW620 xenograft model. The linker with a plasma release half-life of 21 h achieved sustained SN-38 exposure in blood, above the target concentration. Overall, these extensive studies allowed to identify a linker, a dose and dosing regimen for SN-38 conjugated to polyoxazoline-modified dendrimer that maximized efficacy and minimized adverse side effects [66].

Narmani *et al.* [67] studied the anti-cancer efficacy of oxaliplatin (OX) using a nanocarrier system with enhanced targeting efficacy towards folic acid receptors (FAR) expressing CRC cells *in vitro* [67]. This system consisted of PAMAM dendrimers G4 imprinted with polyethyleneglycol (PEG) and folic acid. Polyethelen glycation of polymeric NPs is frequently applied to increase stability, and thus the half-life, as well as the non-immunogenic and non-antigenic properties [24, 68]. The PEG-PAMAM nano-complex containing OX was shown to have a superior cellular uptake in SW480 cell line. The cell viability tests clearly demonstrated the cancer cell growth inhibition effects of PEG-PAMAM-FA-OX. These fundamental scientific advances **(see Table III-2)**, coupled with practical methods to covalently conjugate a wide range of bioactive molecules to the surface of a dendrimer or encapsulate them as guest molecules within void spaces, provide a highly versatile and potentially extremely powerful technological platform to fight colorectal cancer.

Table III-2 - Summary of different strategies using dendrimer NP for CRC therapy.

Type of Dendrimer	Target	Anti-cancer drug	Reference
PAMAM G4	N/A	Capecitabine	[61]
Gold NPs inside PAMAM	MUC-1 aptamer	Curcumin	[12]
Pegylated PAMAM	AS1411 anti-nucleolin aptamers	Camptothecin	[64]
L-lysine dendrimer G5 modified with	N/A	SN-38 (active metabolite of Irinotecan)	[66]

polyoxazoline			
PAMAM G4	Folic acid	Oxaliplatin	[67]

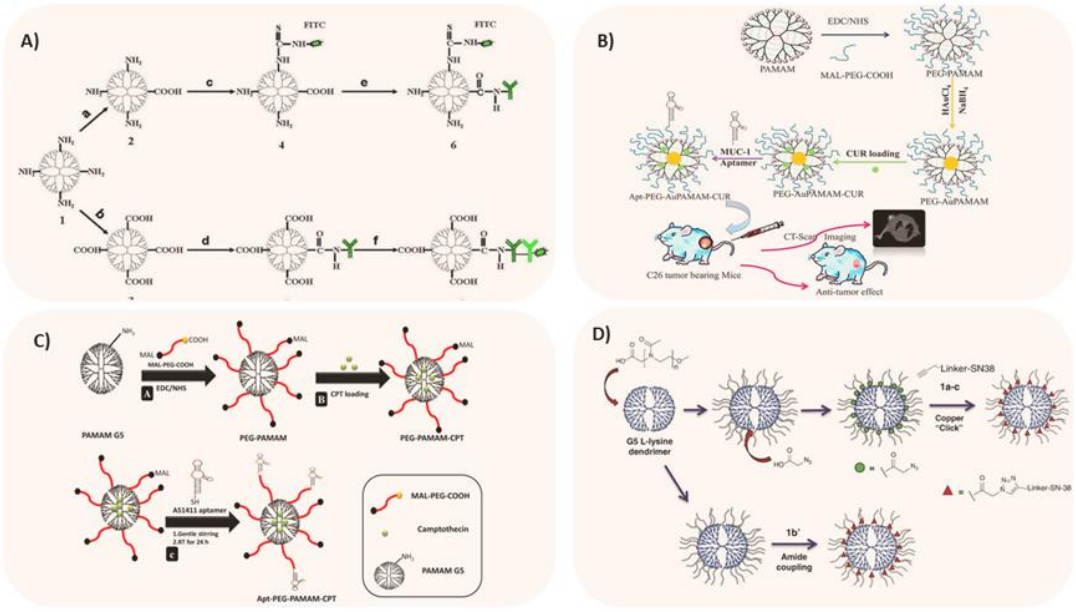

Figure III-4 - Different strategies for employing dendrimer NPs in CRC research. A) Two synthetic procedures of aSlex-conjugated dendrimers with FITC labeling by sequential conjugation of the completely carboxylated PAMAM dendrimers with FITC and aSlex (a–c–e) or by sequential conjugation of the partially carboxylated PAMAM dendrimers with aSlex and IgG/IgM-FITC (b–d–f). 1, PAMAM with amine groups; 2, PAMAM with the partially carboxylated groups; 3, PAMAM with the completely carboxylated groups; 4, PAMAM linked with FITC; 5, PAMAM conjugated with primary antibody; 6, FITC-labeled PAMAM conjugated with antibody; 7, Primary antibody-coated PAMAM conjugated with FITC-labeled secondary antibody. Reprinted with permission from [62]. Copyright © 2015 Nature. B) Dendrimer-gold hybrid structure synthesized by complexing $AuCl_4^-$ ions with PEGylated amine-terminated generation 5 PAMAM dendrimer. The resultant hybrid system was loaded with curcumin. The curcumin-loaded PEGylated Au dendrimer was further conjugated to MUC-1 aptamer in order to target the colorectal adenocarcinoma *in vitro* and *in vivo*. Reprinted with permission from [12]. Copyright © 2018 Elsevier. C) Schematic representation of (A) synthesis of pegylated PAMAMdendrimer (PEG-PAMAM); (B) camptothecin (CPT) loading in the cavities of PEG-PAMAM; (C) conjugation of thiolated AS1411 aptamers to the maleimide groups of MAL-PEG-PAMAM-CPT and preparation of Apt-PEG-PAMAM-CPT. Reprinted with permission from [64]. Copyright © 2017 Elsevier. D) Synthetic route to polyoxazoline-modified dendrimers with linker-SN38 conjugation. Reprinted with permission form [66]. Copyright © 2017 Elsevier.

III-5. CONCLUSIONS

The inefficacy of conventional chemotherapeutic methods has led to the development of new strategies, which can be used to improve the efficiency of anti-cancer drug delivery into tumors while minimizing distribution and toxicity in healthy tissues as well as novel imaging tools. These novel strategies based on the use of NPs loaded with drugs offer unprecedented opportunities both at the

preclinical and clinical levels. However, some challenges still remain, such as improving the localization, biodistribution, biocompatibility, and efficacy of these nano-drug systems *in vivo*, to meet the requirements of precision cancer diagnosis and therapy. In the current scenario, among the new nanotechnology platforms, dendrimer-based chemotherapeutics have emerged as one of the most promising nanotools over the available conventional chemotherapies for the treatment of a variety of tumors. However, their application in colorectal cancer is still in its infancy.

An ideal therapeutic must have the ability to target cancer cells, image the extent of the tumor and sense its signatures, deliver a therapeutic, and monitor cells for their response. Although we are not there yet, this is the goal for our nanotherapeutics.

III-6. REFERENCES

1. Kotelevets, L., et al., *Nanotechnologies for the treatment of colon cancer: From old drugs to new hope.* International Journal of Pharmaceutics, 2016. **514**(1): p. 24-40.
2. Gatoo, M.A., et al., *Physicochemical properties of nanomaterials: implication in associated toxic manifestations.* Biomed Res Int, 2014. **2014**: p. 498420.
3. Tekchandani, P., B.D. Kurmi, and S.R. Paliwal, *Nanomedicine to Deal With Cancer Cell Biology in Multi-Drug Resistance.* Mini Rev Med Chem, 2017. **17**(18): p. 1793-1810.
4. Bar-Zeev, M., Y.D. Livney, and Y.G. Assaraf, *Targeted nanomedicine for cancer therapeutics: Towards precision medicine overcoming drug resistance.* Drug Resist Updat, 2017. **31**: p. 15-30.
5. Maeda, H., H. Nakamura, and J. Fang, *The EPR effect for macromolecular drug delivery to solid tumors: Improvement of tumor uptake, lowering of systemic toxicity, and distinct tumor imaging in vivo.* Adv Drug Deliv Rev, 2013. **65**(1): p. 71-9.
6. Da Silva, C.G., et al., *The potential of multi-compound nanoparticles to bypass drug resistance in cancer.* Cancer chemotherapy and pharmacology, 2017. **80**(5): p. 881-894.
7. Zhitomirsky, B. and Y.G. Assaraf, *Lysosomes as mediators of drug resistance in cancer.* Drug Resist Updat, 2016. **24**: p. 23-33.
8. Villegas, M.R., et al., *Multifunctional Protocells for Enhanced Penetration in 3D Extracellular Tumoral Matrices.* Chemistry of Materials, 2018. **30**(1): p. 112-120.
9. Van Cutsem, E., et al., *Cetuximab and chemotherapy as initial treatment for metastatic colorectal cancer.* N Engl J Med, 2009. **360**(14): p. 1408-17.
10. Kopansky, E., Y. Shamay, and A. David, *Peptide-directed HPMA copolymer-doxorubicin conjugates as targeted therapeutics for colorectal cancer.* J Drug Target, 2011. **19**(10): p. 933-43.
11. Landmark, K.J., et al., *Synthesis, characterization, and in vitro testing of superparamagnetic iron oxide nanoparticles targeted using folic Acid-conjugated dendrimers.* ACS Nano, 2008. **2**(4): p. 773-83.

12. Alibolandi, M., et al., *Curcumin-entrapped MUC-1 aptamer targeted dendrimer-gold hybrid nanostructure as a theranostic system for colon adenocarcinoma.* International Journal of Pharmaceutics, 2018. **549**(1): p. 67-75.
13. Pavitra, E., et al., *Engineered nanoparticles for imaging and drug delivery in colorectal cancer.* Seminars in Cancer Biology, 2019.
14. Belhadj-Tahar, H., et al., *In situ anti-cancer agent derived from [188re]rhenium nitro-imidazole ligand loaded poly-l-lysine dendrimer administrated by direct CT guided stereotactic intrahepatic injection.* Journal of Clinical Oncology, 2018. **36**(15_suppl): p. e15569-e15569.
15. Araújo, R.V.d., et al., *New Advances in General Biomedical Applications of PAMAM Dendrimers.* Molecules (Basel, Switzerland), 2018. **23**(11): p. 2849.
16. Lee, S., et al., *Polyamidoamine (PAMAM) Dendrimers Modified with Cathepsin-B Cleavable Oligopeptides for Enhanced Gene Delivery.* Polymers, 2017. **9**(6): p. 224.
17. Tomalia, D.A. and J.M.J. Fréchet, *Discovery of dendrimers and dendritic polymers: A brief historical perspective*.* Journal of Polymer Science Part A: Polymer Chemistry, 2002. **40**(16): p. 2719-2728.
18. Oliveira, J.M., et al., *Dendrimers and derivatives as a potential therapeutic tool in regenerative medicine strategies—A review.* Progress in Polymer Science, 2010. **35**(9): p. 1163-1194.
19. Srinageshwar, B., et al., *PAMAM Dendrimers Cross the Blood-Brain Barrier When Administered through the Carotid Artery in C57BL/6J Mice.* International journal of molecular sciences, 2017. **18**(3): p. 628.
20. Hill, E., et al., *Synthetic PAMAM-RGD conjugates target and bind to odontoblast-like MDPC 23 cells and the predentin in tooth organ cultures.* Bioconjug Chem, 2007. **18**(6): p. 1756-62.
21. Salimi, M., et al., *Biodistribution, pharmacokinetics, and toxicity of dendrimer-coated iron oxide nanoparticles in BALB/c mice.* Int J Nanomedicine, 2018. **13**: p. 1483-1493.
22. Thomas, T.P., et al., *In vitro targeting of synthesized antibody-conjugated dendrimer nanoparticles.* Biomacromolecules, 2004. **5**(6): p. 2269-74.
23. Sharma, A.K., et al., *Dendrimer nanoarchitectures for cancer diagnosis and anticancer drug delivery.* Drug Discov Today, 2017. **22**(2): p. 314-326.
24. Castro, R.I., O. Forero-Doria, and L. Guzman, *Perspectives of Dendrimer-based Nanoparticles in Cancer Therapy.* An Acad Bras Cienc, 2018. **90**(2 suppl 1): p. 2331-2346.
25. Hawker, C.J. and J.M.J. Frechet, *Preparation of polymers with controlled molecular architecture. A new convergent approach to dendritic macromolecules.* Journal of the American Chemical Society, 1990. **112**(21): p. 7638-7647.
26. Abbasi, E., et al., *Dendrimers: synthesis, applications, and properties.* Nanoscale research letters, 2014. **9**(1): p. 247-247.
27. Tomalia, D.A., *Birth of a new macromolecular architecture: dendrimers as quantized building blocks for nanoscale synthetic polymer chemistry.* Progress in Polymer Science, 2005. **30**(3): p. 294-324.
28. Palmerston Mendes, L., J. Pan, and V.P. Torchilin, *Dendrimers as Nanocarriers for Nucleic Acid and Drug Delivery in Cancer Therapy.* Molecules (Basel, Switzerland), 2017. **22**(9): p. 1401.
29. Pedziwiatr-Werbicka, E., et al., *Dendrimers and hyperbranched structures for biomedical applications.* European Polymer Journal, 2019. **119**: p. 61-73.
30. Shukla, S.K., P.P. Govender, and A. Tiwari, *Chapter Six - Polymeric Micellar Structures for Biosensor Technology*, in *Advances in Biomembranes and Lipid Self-Assembly*, A. Iglič, C.V. Kulkarni, and M. Rappolt, Editors. 2016, Academic Press. p. 143-161.
31. Kaur, D., et al., *A review on comparative study of PPI and PAMAM dendrimers.* Journal of Nanoparticle Research, 2016. **18**(6): p. 146.

32. Madaan, K., et al., *Dendrimers in drug delivery and targeting: Drug-dendrimer interactions and toxicity issues.* Journal of pharmacy & bioallied sciences, 2014. **6**(3): p. 139-150.
33. Kesharwani, P., K. Jain, and N.K. Jain, *Dendrimer as nanocarrier for drug delivery.* Progress in Polymer Science, 2014. **39**(2): p. 268-307.
34. Chang, H., et al., *Surface-engineered dendrimers with a diaminododecane core achieve efficient gene transfection and low cytotoxicity.* Bioconjug Chem, 2014. **25**(2): p. 342-50.
35. Chauhan, A.S. and M. Kaul, *Engineering of "critical nanoscale design parameters" (CNDPs) in PAMAM dendrimer nanoparticles for drug delivery applications.* Journal of Nanoparticle Research, 2018. **20**(9): p. 226.
36. Oliveira, J.M., et al., *Surface Engineered Carboxymethylchitosan/Poly(amidoamine) Dendrimer Nanoparticles for Intracellular Targeting.* Advanced Functional Materials, 2008. **18**(12): p. 1840-1853.
37. Carvalho, M.R., et al., *Colorectal tumor-on-a-chip system: A 3D tool for precision onco-nanomedicine.* Sci Adv, 2019. **5**(5): p. eaaw1317.
38. Oliveira, J.M., et al., *The osteogenic differentiation of rat bone marrow stromal cells cultured with dexamethasone-loaded carboxymethylchitosan/poly(amidoamine) dendrimer nanoparticles.* Biomaterials, 2009. **30**(5): p. 804-13.
39. Qu, Y., et al., *Self-Assembled DNA Dendrimer Nanoparticle for Efficient Delivery of Immunostimulatory CpG Motifs.* ACS Applied Materials & Interfaces, 2017. **9**(24): p. 20324-20329.
40. Zhao, L., X. Shi, and J. Zhao, *Dendrimer-based contrast agents for PET imaging.* Drug Delivery, 2017. **24**(2): p. 81-93.
41. Huang, Y., et al., *Dendrimer-Based Responsive MRI Contrast Agents (G1–G4) for Biosensor Imaging of Redundant Deviation in Shifts (BIRDS).* Bioconjugate Chemistry, 2015. **26**(12): p. 2315-2323.
42. Caminade, A.-M., et al., *The key role of the scaffold on the efficiency of dendrimer nanodrugs.* Nature Communications, 2015. **6**: p. 7722.
43. Baker, J.R., Jr., *Dendrimer-based nanoparticles for cancer therapy.* Hematology Am Soc Hematol Educ Program, 2009: p. 708-19.
44. Saluja, V., et al., *Smart dendrimers: Synergizing the targeting of anticancer bioactives.* Journal of Drug Delivery Science and Technology, 2019. **52**: p. 15-26.
45. Mura, S., J. Nicolas, and P. Couvreur, *Stimuli-responsive nanocarriers for drug delivery.* Nature Materials, 2013. **12**: p. 991.
46. Gai, S., et al., *Recent advances in functional nanomaterials for light–triggered cancer therapy.* Nano Today, 2018. **19**: p. 146-187.
47. Choi, S.K., et al., *Light-controlled release of caged doxorubicin from folate receptor-targeting PAMAM dendrimer nanoconjugate.* Chem Commun (Camb), 2010. **46**(15): p. 2632-4.
48. Nigam, S. and D. Bahadur, *Dendrimer-conjugated iron oxide nanoparticles as stimuli-responsive drug carriers for thermally-activated chemotherapy of cancer.* Colloids and Surfaces B: Biointerfaces, 2017. **155**: p. 182-192.
49. Amreddy, N., et al., *Chemo-biologic combinatorial drug delivery using folate receptor-targeted dendrimer nanoparticles for lung cancer treatment.* Nanomedicine: Nanotechnology, Biology and Medicine, 2018. **14**(2): p. 373-384.
50. Chittasupho, C., S. Anuchapreeda, and N. Sarisuta, *CXCR4 targeted dendrimer for anti-cancer drug delivery and breast cancer cell migration inhibition.* European Journal of Pharmaceutics and Biopharmaceutics, 2017. **119**: p. 310-321.

51. Yousef, S., et al., *Development of asialoglycoprotein receptor directed nanoparticles for selective delivery of curcumin derivative to hepatocellular carcinoma.* Heliyon, 2018. **4**(12): p. e01071-e01071.
52. Lee, T.J., et al., *RNA Nanoparticle-Based Targeted Therapy for Glioblastoma through Inhibition of Oncogenic miR-21.* Mol Ther, 2017. **25**(7): p. 1544-1555.
53. Mishra, V. and P. Kesharwani, *Dendrimer technologies for brain tumor.* Drug Discovery Today, 2016. **21**(5): p. 766-778.
54. Liu, S., et al., *Gene and doxorubicin co-delivery system for targeting therapy of glioma.* Biomaterials, 2012. **33**(19): p. 4907-16.
55. Wu, X.X., et al., *Doxorubicin enhances TRAIL-induced apoptosis in prostate cancer.* Int J Oncol, 2002. **20**(5): p. 949-54.
56. Sharma, A.K., et al., *Dendrimer nanoarchitectures for cancer diagnosis and anticancer drug delivery.* Drug Discovery Today, 2017. **22**(2): p. 314-326.
57. Zhou, Z. and Z.-R. Lu, *Gadolinium-based contrast agents for magnetic resonance cancer imaging.* Wiley interdisciplinary reviews. Nanomedicine and nanobiotechnology, 2013. **5**(1): p. 1-18.
58. Talanov, V.S., et al., *Dendrimer-based nanoprobe for dual modality magnetic resonance and fluorescence imaging.* Nano Lett, 2006. **6**(7): p. 1459-63.
59. Siegel, R.L., K.D. Miller, and A. Jemal, *Cancer statistics, 2018.* 2018. **68**(1): p. 7-30.
60. Yan, W., et al., *Overcoming Drug Resistance in Colon Cancer by Aptamer-Mediated Targeted Co-Delivery of Drug and siRNA Using Grapefruit-Derived Nanovectors.* Cellular Physiology and Biochemistry, 2018. **50**(1): p. 79-91.
61. Nabavizadeh, F., et al., *Evaluation of Nanocarrier Targeted Drug Delivery of Capecitabine-PAMAM Dendrimer Complex in a Mice Colorectal Cancer Model.* Acta Med Iran, 2016. **54**(8): p. 485-493.
62. Xie, J., et al., *Multivalent Conjugation of Antibody to Dendrimers for the Enhanced Capture and Regulation on Colon Cancer Cells.* Scientific Reports, 2015. **5**: p. 9445.
63. Gulbake, A., et al., *Insight to drug delivery aspects for colorectal cancer.* World journal of gastroenterology, 2016. **22**(2): p. 582-599.
64. Alibolandi, M., et al., *Smart AS1411-aptamer conjugated pegylated PAMAM dendrimer for the superior delivery of camptothecin to colon adenocarcinoma in vitro and in vivo.* Int J Pharm, 2017. **519**(1-2): p. 352-364.
65. Fan, X., et al., *Bioactivity of 2'-deoxyinosine-incorporated aptamer AS1411.* Sci Rep, 2016. **6**: p. 25799.
66. England, R.M., et al., *Tumour regression and improved gastrointestinal tolerability from controlled release of SN-38 from novel polyoxazoline-modified dendrimers.* J Control Release, 2017. **247**: p. 73-85.
67. Narmani, A., et al., *Targeting delivery of oxaliplatin with smart PEG-modified PAMAM G4 to colorectal cell line: In vitro studies.* Process Biochemistry, 2018. **69**: p. 178-187.
68. Fox, M.E., et al., *Synthesis and in vivo antitumor efficacy of PEGylated poly(l-lysine) dendrimer-camptothecin conjugates.* Molecular pharmaceutics, 2009. **6**(5): p. 1562-1572.

SECTION 2

MATERIALS AND METHODS

Chapter IV

Materials and methods

Chapter IV

Materials and Methods

Overview

This chapter intends to provide a detailed overview on the experimental procedures behind the results presented in Section 3. Moreover, some considerations will be made regarding the selection of the materials and hydrogels processing methodologies, the microfluidic devices, as well as the physicochemical and biological characterization techniques used to sustain the proposed methodologies. With this, it is expected to present a clearer perspective of the developed work in this thesis and how it can be correlated. Despite all the following chapters already having a "materials and methods" sub-section, herein these are presented in a general perspective, while providing more detailed information in all the specific steps followed for each work.

IV-1. MATERIALS

European Society for Biomaterials' (ESB), current definition for "biomaterial" is a material intended to interface with biological systems to evaluate, treat, augment or replace any tissue, organ or function of the body [1]. Natural biomaterials were considered vital in the conception of this thesis. The TE systems developed in this thesis were based on different types of biomaterials: Carboxymethylchitosan to modify the dendrimer nanoparticles, silk and Matrigel as extra-cellular matrix mimics in the developed 3D tumor models and silk fibroin as the biomaterial to produce a microfluidic platform.

IV-1.1. Carboxymethylchitosan (CMCht)

Chitin and chitosan are attractive macromolecules, but their use is restricted due to their poor water-solubility **(Figure IV–1)** [2]. Chemical modifications in chitosan molecular structure are feasible due to the reactive functional groups (*e.g.* amine -NH2 and hydroxyl -OH), allowing to tailor its degradation profile and widen its applications [3]. Thus, to develop biomaterials with improved physicochemical properties, attempts have been made to modify its structure by introducing acetyl, carboxymethyl, sulfuryl, or phosphoryl groups, among others [4]. In one hand, chitin is a linear, high molecular weight, crystalline polysaccharide, theoretically comprised entirely by N-acetylated D-glucosamine units. On the other hand, chitosan, known as poly-(β-1/4)-2-amino-2-deoxy-D-glucopyranose is a hydrophilic polycationic copolymer made of D-glucosamine and N-acetyl-D-glucosamine, which are linked with β (1–4) bonds.

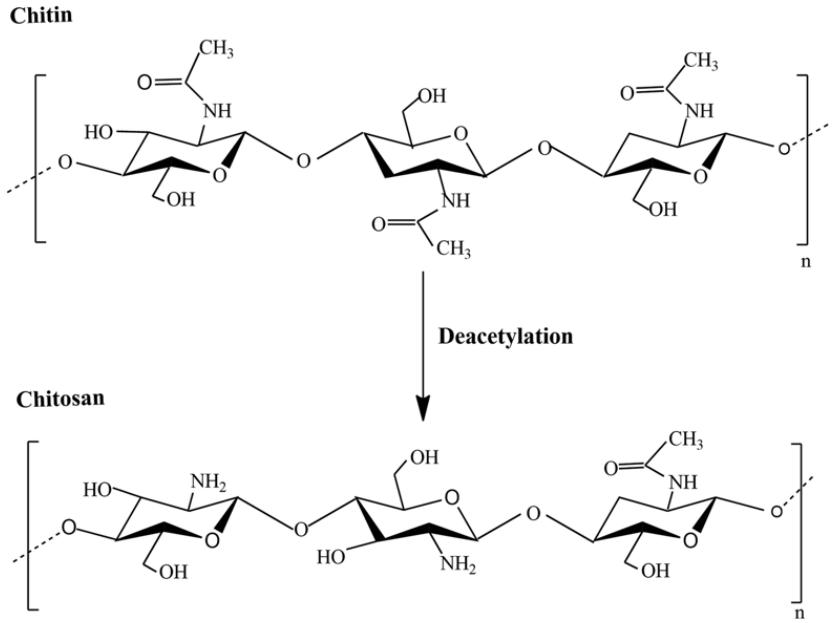

Figure IV-1 - Chemical structure of chitin and chitosan. Reprinted with permission from [5].

Deacetylation of chitin results in chitosan, a polymer, widely studied for its pharmaceutical and non-pharmaceutical applications. The hurdle in comprehending these applications is its limited solubility. Carboxymethylation of chitosan helps to surmount this hurdle with its improved solubility in water. Carboxymethylchitosan (CMCht) is soluble in a wide range of pH and its properties, namely low toxicity and antimicrobial activity, may wider its application, including medical and pharmaceutical areas - mainly for the controlled release of drugs [6].

The chitosan derivatives obtained by its carboxymethylation are old in the art with three types: N-carboxymethyl chitosan (NCMC) [7], O-carboxymethyl chitosan (OCMC) [8], and N,O-carboxymethyl chitosan (NOCMC) [9], being the choice of the appropriate reaction conditions and reagents determinant for the preparation of N-, O-, N,O- or N,N-dicarboxymethylchitosan **(Figure IV-2)**.

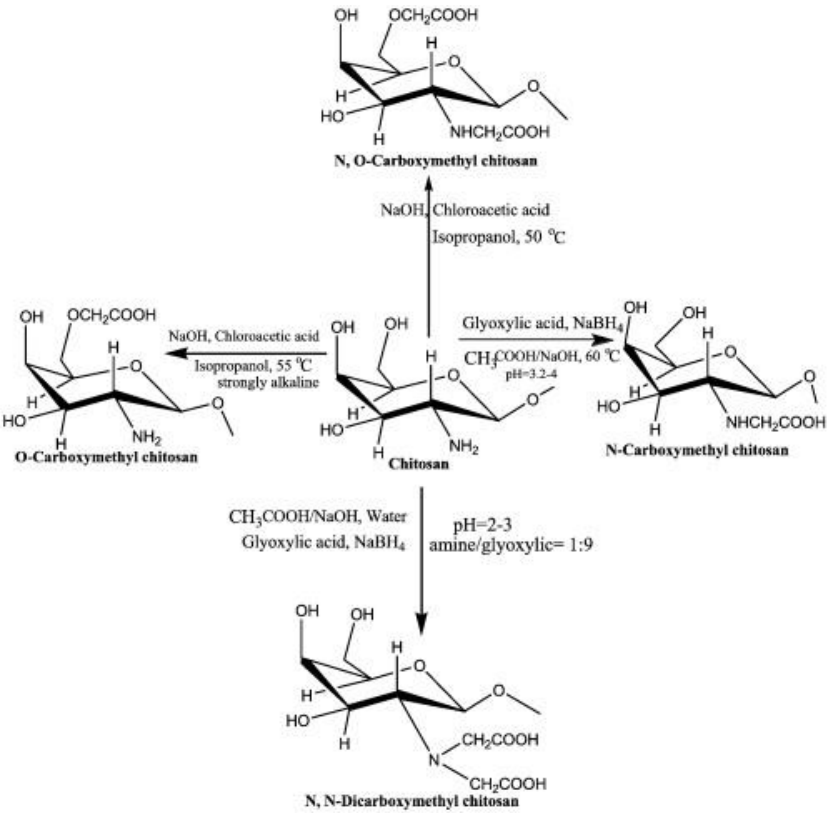

Figure IV-2 - Preparative methods of different types of Carboxymethylchitosan. Reprinted with permission from [10].

Thus, the properties and applications of carboxymethylchitosan are strongly dependent on its structural characteristics, mainly the degree of substitution (DS). For the purpose of this thesis, reagent grade chitosan particles with a DS of ~91 %, monochloroacetic acid, 1 % acetic acid solution, 40 % sodium hydroxide solution, and acetone were used in the preparation of CMCht. The methodology used has been previously reported by Chen *et al.* [11]. Briefly, chitosan (5 g), 40 % sodium hydroxide solution and isopropanol (100 mL) were added into a flask (500 mL) to alkalize at RT for 1 hour. Then, monochloroacetic acid (18 g) was added into the reaction vessel dropwise for 30 minutes and reacted for 2 hours at 60 °C. The reaction was stopped by adding 70 % ethanol (200 mL). The solid was filtered and rinsed in 70-90 % ethanol to de-salt and de-water, and vacuum dried at room temperature. Finally, the H-form of CMCht was obtained by suspending the Na salt CMCht in 80 % ethanol aqueous solution (100 mL) and 37 % hydrochloric acid (10 mL) for 30 minutes, under agitation. The solid was filtered and rinsed in 70-90 % ethanol to neutral, frozen at -80 °C and freeze-dried (Telstar-Cryodos -80, Spain). CMCht with a DD of 80 % and DS of 47 % was chosen for being used in the production of composite scaffolds and to surface modify the dendrimers, due to the previously highlighted advantages.

IV-1.2. Silk fibroin

Silk fibers are obtained from various animals such as spiders, silkworms, scorpions, mites and flies [12]. Silk is widely considered a good source for the development of biomedical devices. Being one of the oldest natural polymers discovered by men, silk has evolved during its history of over 380 million years [13]. It possesses good biocompatibility, suitable mechanical properties and is produced in bulk in the textile sector [14]. The unique combination of elasticity and strength along with mammalian cell compatibility makes silk fibroin an attractive material for tissue engineering. These fibers are composed of a fibrous protein core, composed of fibroin, with a surrounding glue protein, sericin. More specifically, two parallel fibroin fibers are held together with a layer of sericin on their surfaces. According to the silk fibers origin, its amino acid composition varies, as can be seen in **Table IV-1.**

Table IV-1 - Comparative data on amino acid composition of *B. mori*, *N. edulis* and *N. clavipes* silks. Reprinted with permission from [15].

Amino acid	*B. mori*	*N. edulis*	*N. clavipes*
Ala	30.0	24.0	22.71
Gly	42.9	38.2	9.96
Tyr	4.8	5.2	2.99
Ser	12.2	1.7	2.24
Asp	1.9	1.5	1.06
Arg	0.5	2.3	1.76
His	0.2	Trace	0.21
Glu	1.4	12.8	11.02
Lys	0.4	0.3	0.10
Val	2.5	0.7	0.89
Leu	0.6	2.4	4.26
Ile	0.6	0.4	0.07
Phe	0.7	0.3	0.26
Pro	0.5	9.4	2.04
Thr	0.9	0.4	0.34
Met	0.1	0.3	0.04

Cys	0.0	ND	0.06

Silkworm's silk is an established fiber extensively used. On the other hand, the cannibalistic nature of spiders restricts its commercial production of silk [16]. Additionally, the yield of fiber from a single silk cocoon is 600–1500 m, compared to only ~137 m from a spider [16]. Spider silks are also heterogeneous in nature. Therefore, silk-based biomaterials are commonly prepared from silkworm silk. In this thesis, the silk used was produced by *Bombyx mori*, a member of the *Bombycidae* family. *B. mori* silk is also known as mulberry silk. Another silk producing family is *Saturniidae* and the silk is known as non-mulberry silk.

Depending on the silkworm sources, different processing methodologies are used for silk purification. In the case of the *Bombyx mori* silk fibroin, this process is routinely established, involving a simple alkali- or enzyme-mediated degumming procedure to extract sericin from the cocoons and obtain SF at 70 % off the original cocoon mass [17, 18].

Upon degumming the raw silk to remove the sericin, the obtained fibroin fibers appear shiny and feel soft to the touch [19, 20]. Moreover, the fibroin fibers are endowed with a combination of attractive strength, toughness, biocompatibility/biodegradability and thermal stability, representing one of the most impressive natural protein fibers [21].

Sericin (20-310 kDa) is a gum-like protein produced with silk, currently suggested by the scientific community as an inducer of *in vivo* inflammatory response in its native state [22], vindicating the necessity to extract this protein from the cocoons before processing silk fibroin (SF) for biomedical applications.

However, recent studies now claim that silk sericin can accelerate cell proliferation and attachment; however, sircerin can be extracted by various methods, which results in different physical and biological properties. Also, through different treatments, SF can be prepared to hold a wide range of forms, such as solution, powder, fibers, films, hydrogels, and sponges; this allows the use of SF for constructing many different scale structures, ranging across the nano-, micro-, and macro-dimensions [23]. Related to its chemical structure, SF is formed by heavy (H) and light (L) chains linked by a disulfide bond, with hydrophobic domains of the H-chains interspaced by hydrophilic regions at the L-chains. The hydrophobic domains contain highly ordered Glycine-X (X being Alanine, Serine, Tyrosine, Valine) repeats that form stacked anti-

parallel β-sheets (silk II) of crystalline structure. The hydrophilic regions constitute the amorphous phase of the protein. Processed in a variety of forms, silk-based materials include porous scaffolds [24] and sponges [25], films [26], tubes [27], electrospun [28] or micro-fibers [29], hydrogels [30] and textiles [31].

There are several developed protocols and techniques to transform SF raw material into regenerated SF solutions, usually involving harsh, chaotic solvents such as strong acids or ionic concentrated salt solutions, such as the organic solvent hexafluoroisopropanol (HFIP), concentrated lithium bromide solution, ionic liquids, lithium thiocyanate, or a calcium chloride/ethanol/water ternary solvent [32-34]. The constructs produced from these solutions acquire β-sheet conformation. Temperature and pH variations, ultrasonication or vortex also induce β-sheet conformation. The presence of β-sheet crystalline structure in SF has shown to significantly improve the mechanical properties, water insolubility and degradability of the SF-based structures. However, SF hydrogels and membranes prepared in an amorphous state, also showed good specificities for soft tissues clinical application materials to be prepared in a friendly processing, which favors the incorporation of bioactive proteins, drugs and cells [35].

. Thus, SF has been exploited with different biomedical purposes, as a result of its processing versatility and extensive knowledge on how to control its properties, including mechanical strength, elasticity, biocompatibility, and controlled biodegradability. Therefore, in this thesis, *Bombyx mori* silk cocoons were used purified in order to isolate SF used for preparing SF-based hydrogels, either as an alternative to Matrigel as ECM material in **Chapter VI**, or for the production of a microfluidic platform in **Chapter IX**. For the production of silk in this thesis, all the cocoons were supplied by the Portuguese Association of Parents and Friends of Mentally Disabled Citizens (APPACDM, Castelo Branco, Portugal).

IV-1.3. Matrigel®

Matrigel® is a soluble and sterile extract of basement membrane proteins derived from the Engelbreth-Holm-Swarm (EHS) tumor, crosslinking into a 3D gel at 37 °C, able to support cell morphogenesis, differentiation, and tumor growth **(Figure IV-2)** [36].

Matrigel® was first subject to scientific publication in 1977, developed by Roslyn Orkin who studied a mouse tumor with an abundant extracellular matrix, originally identified as a poorly

differentiated chondrosarcoma [37]. Structural and amino acid analyses proposed that the tumor matrix was distinct from cartilage, and instead resembled basement membrane. It was finally named EHS tumor to acknowledge J. Engelbreth-Holm of Denmark, who discovered it, and Richard Swarm, who maintained and characterized it [38].

Methods for culturing mammalian cells *ex vivo* are increasingly needed to study cell and tissue physiology and to grow replacement tissue for regenerative medicine. Two-dimensional culture has been the paradigm for typical *in vitro* cell culture, however, it has been demonstrated that cells behave more natively when cultured in three-dimensional environments [39].

The *in vivo* and *in vitro* extracellular matrix (ECM) is known to play a key role in numerous outcomes that direct cell fate and behavior [40, 41]. Characteristic ECM proteins comprise laminin, collagens, glycoproteins, and proteoglycans [42]. The main function of the ECM is to support the growth and maintenance of a variety of cells. *In vitro* growth matrices can be a variety of materials, such as chemically treated culture dish plastic, or layers of deposited protein. Often these matrices are very simple, consisting of a mixture of purified proteins such as collagen and laminin. Matrices such as these, which contain only major ECM proteins, are not applicable to all cell types [43].

The basement membrane extracellular matrix contacts epithelial, endothelial, fat and smooth muscle cells. Because this extracellular matrix is so thin, it has been hard to study its composition, structure, and function. The extract of a tumor was found to contain all of the components present in basement membrane and to be very biologically active. This extract, sold as Matrigel®, Cultrex®, or EHS matrix®, acts as a substrate or physical support for cultured cells helping to create more *in vivo*-like extracellular matrices promotes cell differentiation, and is used to measure the invasive activity of tumor cells. *In vivo*, it is used for migration assays [44], sprouting assays [45], capillary-like tube formation [46], differentiation of stem cells [47], measuring angiogenic inhibitors and stimulators [48], to improve graft survival [49], repair damaged tissues, and increase tumor growth [39, 50] and tumor cell interactions study [51].

However, Matrigel® is not a well-defined matrix, and therefore can produce a source of variability in experimental results. The presence of several growth factors was detected (basic fibroblast growth factor, epidermal growth factor, insulin-like growth factor 1, transforming growth

factor β, platelet-derived growth factor, and nerve growth factor) in standard Matrigel® through the use of immunoassays.

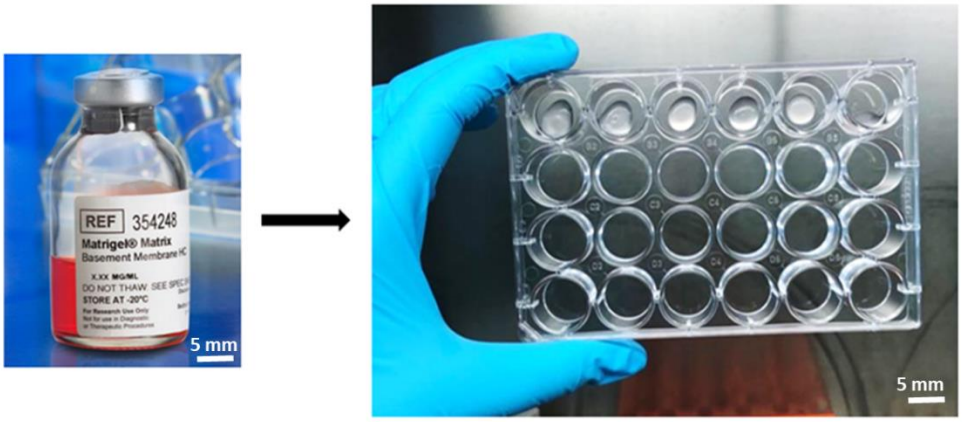

Figure IV-3 – Matrigel® in its original packing and after cell encapsulation.

IV-1.4. Polydimethylsiloxane (PDMS)

Polydimethylsiloxane (PDMS) $[(CH_3)_2SiO]_n$ is by far the most widely used polymer in siloxane ("silicone") elastomers [52]. Substituent groups other than methyl, such as phenyl or trifluoropropyl can be incorporated, often as copolymers with PDMS. Apart from the effects of cross-links, the macromolecular chains must be free to move reversibly past one another. PDMS is a mineral-organic polymer (containing carbon and silicon) of the siloxane family (word derived from silicon, oxygen and alkane). It has been used as a food additive (E900) in shampoos, and as an anti-foaming agent in beverages [53].

In the last years, rapid progress in micro and nanotechnologies such as lab-on-a-chip (microfluidic networks, sensors, actuators, and connectors), soft lithography (replica moulding, microcontact printing and affinity contact printing), and stretchable transparent electronics has strongly benefitted from high-performance polymers like PDMS that are suited for high-fidelity microsystem construction and rapid prototyping [54]. For the fabrication of microfluidic devices, PDMS (liquid) mixed with a cross-linking agent is poured into a microstructured mold and heated to obtain an elastomeric replica of the mold. The PDMS is also easy to mold, because, even when mixed with the cross-linking agent, it remains liquid at RT for many hours. The PDMS can mold structures at high resolutions inclusive of a few nanometers [55].

Furthermore, PDMS oxidation using plasma changes the PDMS surface chemistry and produces silanol terminations (SiOH) on its surface [56]. This process also makes the surface resistant to the adsorption of hydrophobic and negatively-charged molecules. In addition, PDMS plasma oxidation is used to functionalize the PDMS surface with trichlorosilane or to covalently bond PDMS (at the atomic scale) on an oxidized glass surface by the creation of a Si-O-Si bonds [55].

PDMS presents several characteristics that allowed it to be the most widely used polymer in microfluidics:

a) It is transparent at optical frequencies (240 nM – 1100 nM), allowing for content observation in microchannels, either visually or through a microscope; also, it has a low auto-fluorescence [57];

b) It is gas permeable and considered "cell friendly" (with few restrictions) [58];

c) The PDMS bonds tightly to glass (**Figure IV-4**) or another PDMS layer with a simple plasma treatment, allowing the production of multilayers of PDMS;

d) During cross-linking, it can be coated with a controlled thickness on a substrate using a simple spin coating. This allows the fabrication of multilayer devices and the integration of micro valves;

e) It is deformable, which allows the integration of microfluidic valves using the deformation of PDMS micro-channels, the easy connection of leak-proof fluidic connections and its use to detect very low forces like biomechanics interactions from cells [59];

f) It is inexpensive compared to previously used materials (*e.g.* silicon).

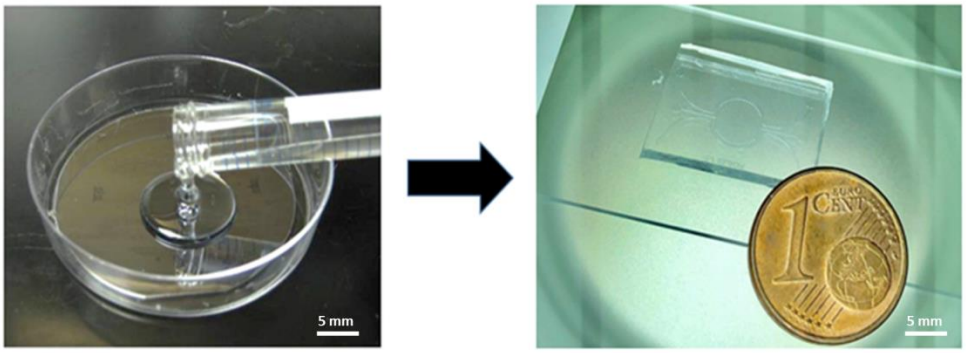

Figure IV-4 – PDMS before and after crosslinking and plasma treatment (adhered to glass).

IV-1.5. YIGSR Peptide

Laminin-111 is a large trimeric basement membrane glycoprotein with many active sites. In particular, four peptides active in tumor malignancy studies have been identified in laminin-111 using a systematic peptide screening method. Two of the peptides (IKVAV and AG73) are found on the α1 chain, one (YIGSR) **(Figure IV–5)** of the β1 chain and one (C16) on the γ1 chain [60].

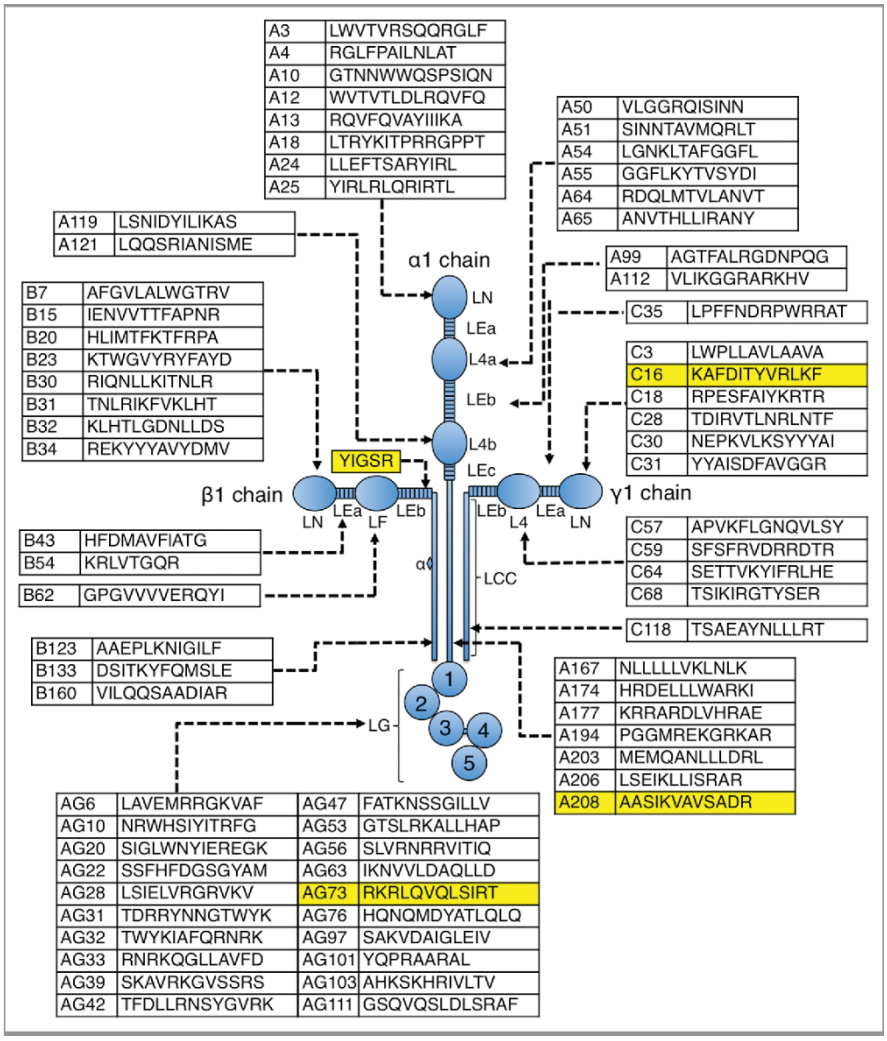

Figure IV-5 - Schematic model of Laminin-111 showing the location of peptides that exhibit cell attachment activity. Laminin-111 is composed of three subunits, α, β and ϒ chains. Forty-five active peptides are localized in α1 chain, 14 active peptides in β1 chain and 12 active peptides in ϒ1 chain. The four highlighted peptides described here are active in tumor malignancy. Reprinted with permission from [60].

The first described and most studied Laminin-111-derived active peptide, YIGSR (Tyr–Ile–Gly–Ser–Arg),**(Figure IV-5)** from the β1 chain binds to the 32/67 kDa cell surface receptor and has many activities related to its inhibition of malignancy [60].

The peptide YIGSR comprised of residues 929–933 on the β1 chain has been found to inhibit tumor growth and metastasis [61]. Literature shows that both polymerized and polyethylene glycol-conjugated YIGSR peptides significantly improved the inhibitory effect of tumor metastasis [62]. YIGSR peptide was also shown to stimulate the apoptosis of fibrosarcoma cells,

but not of colon adenocarcinoma cells, suggesting cell-type specificity, which is not totally understood [63].

Regarding its receptor, while 37/67 LR was the first laminin receptor to be identified, its characterization is still incomplete and has been complicated by the fact that it is also involved in a variety of other unrelated roles. Indeed, beside its ability to interact directly with laminin through most likely the YIGSR sequence on the laminin β1 chain short arm, 37/67 LR can play additional roles in the cell [64].

Various groups have used the YIGSR peptide to localize tumors cells and to target tumor cells with drug delivery based on the peptide binding to the 32/67 kDa receptor [60]. This is because YIGSR laminin receptor binding peptide has demonstrated to be a promising class of targeting ligand for specific drug delivery in cancer treatment. Cancer cells from various sources have been reported to express high levels of the 67 kDa laminin receptor (67 LR) [64], including bile duct carcinoma, colorectal carcinoma, cervical cancer, and breast carcinoma [65], which have shown to correlate with tumor invasiveness [66]. Earlier work have demonstrated that the laminin binding capacity of plasma membranes isolated from human invasive breast carcinomas is 50-fold greater than that of membranes from benign lesions or normal tissue [67].

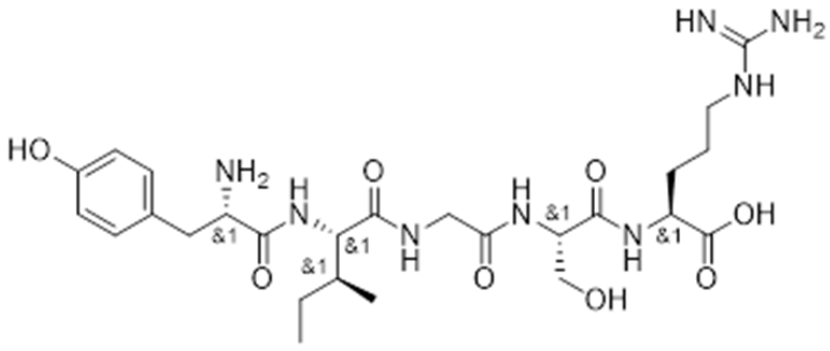

YIGSR (Tyr–Ile–Gly–Ser–Arg)

Figure IV-6 Structure of Laminin-related peptide TYR-ILE-GLY-SER-ARG.

Active targeting is usually based on coupling of tumor-specific ligands on the NPs, resulting in specific attraction between the NPs and the cancerous cells. Cancer cells from various sources have been reported to express high levels of the 67 kDa laminin receptor, the entity responsible for the interactions between cells and laminin of the extracellular matrix.

In this thesis, specifically in **Chapter VIII** it is described the development of carboxymethylchitosan/poly(amidoamine) (CMCht/PAMAM) dendrimer nanoparticles functionalized with YIGSR laminin receptor binding peptide for the actively targeting and specific delivery of therapeutic agents into colorectal cancer cells.

IV-2. REAGENTS

Unless addressed otherwise, all the reagents used in this thesis were purchased from Sigma-Aldrich (St. Louis, MO, USA).

IV-3. METHODOLOGIES FOR PROCESSING OF BIOMATERIALS

Regarding the fabrication of the scaffold itself, there is no idyllic methodology or common biomaterial processing that meets all the scaffolding requirements for tissue regeneration. Different tissues, as well as different biomaterials, require specific physical, mechanical and degradation properties [68].

Knowing that the classic TE paradigm relies on a combination of biomaterial scaffolds, cells, and bioactive molecules to orchestrate tissue formation and integration within the host environment [69], biomaterials processing plays a vital role in the regenerative process. TE strategies are premeditated to influence the physical, chemical and biological environment surrounding the damaged tissue. The processing method is the key factor that mostly contributes to control all the parameters that will influence its behavior *in vitro* and *in vivo* [70]. The different biomaterials used in this thesis were processed in a variety of ways, namely in the form of freeze-dried nanoparticles, membranes or hydrogels.

IV-4. DENDRIMER NANOPARTICLE PRODUCTION

Many scientific efforts are directed at improving the characteristics of biomacromolecules for applications as host-guest chemistry, nanocarriers, and catalysts, among others. As discussed in

Chapter III, dendrimers are among such type of macromolecules since it offers a lot of possibilities in the molecular design, namely in the field of cancer research.

Dendrimers are well-defined, multivalent molecules, having branched structures of nanometer size, and also referred to as "star-like polymers" [71, 72]. The two most commonly used dendrimers are polyamidoamine (PAMAM) dendrimers and polypropylene imine dendrimers [73]. The terminal functional group of dendrimers can easily be utilized for engineering the interaction between molecules of interest with dendrimers. Such chemical versatility also allows producing multifunctional nanobiomaterials.

The biotechnological applications of dendritic polymers in nanotechnology and regenerative medicine are immense, as thoroughly described by Oliveira *et al*. [74]: from osteochondral application [75], central nervous system [76], gene delivery [77] and theranostic applications [78], dendrimers have caught the attention of scientific community in the last decades.

Dendrimers may be created by two main methods: In the divergent method, employed in early times, the synthesis begins from the core of the dendrimers to which the arms are attached by adding building blocks in an extensive and step-wise manner. This process enables dendrimers with incrementally cumulative generation numbers. Nonetheless, only one type of reaction can be executed at each step, yielding an even exhibition of only one functional group on the exterior surface. Major advantages are associated with this type of synthesis, namely the speed of the process, cheap reagents, exponential growth and possibility to prepare large dendrimers [79]. In the convergent method, initiated by Fréchet *et al.* [80], synthesis begins from the exterior, starting with the molecular structure that eventually becomes the outermost arm of the final dendrimer structure. In this tactic, the ultimate generation number is predetermined, compelling the synthesis of branches of the different desired sizes in advance for each generation [80].

In this thesis, we modify amine-terminated PAMAM dendrimers with water-soluble CMCht as an attempt to functionalize the dendrimers and neutralize the amine groups, which have been found to be accountable for the toxicity of the dendrimers [81]. Research priorities for intracellular delivery and imaging are addressed simultaneously.

IV-4.1. Carboxymethylchitosan/poly(amidoamine) dendrimer (CMCht/PAMAM) nanoparticles

For the synthesis of the CMCht/PAMAM dendrimer macromolecules, carboxymethylchitosan with a DD of 80 % and DS of 47 % was used. Starburst® poly(amidoamine)-carboxylic terminated dendrimers, PAMAM-CT (G1.5, 20 % (w/v) methanolic solution) with an ethylenediamine core were purchased from Aldrich. CMCht/PAMAM nanoparticles were prepared in a stepwise manner (divergent method) as follows: (i) increasing the generation of the PAMAM-CT (G1.5), (ii) obtaining a PAMAM-methyl ester terminated dendrimer, (iii) reaction of PAMAM and CMCht, *i.e.* the reaction goes through a condensation reaction between the methyl ester and amine groups, and (iv) modifying the methyl ester groups that do not react with carboxylic ones in the CMCht/PAMAM dendrimer, followed by precipitation. The increase of the dendrimers' generation was carried by means of transferring an appropriate volume of PAMAM-CT (G1.5) in methanol (MeOH) to a 2 mL volumetric flask. The solvent was evaporated off under nitrogen gas, and the traces dried under vacuum in order to completely remove the methanol. The starting compound was re-dissolved in ultra-pure water to give a final concentration of 10 mg/mL and the pH was adjusted to 6.5 with dilute hydrochloric acid solution (HCl) solution. Then, 1-ethyl-3(3-dimethylaminopropyl) carbodiimide hydrochloride (EDC) was added to the solution at a molar ratio sufficient to modify the carboxylate residue of the dendrimers and kept under agitation for 30 minutes at RT. Ethylenediamine (EDA) was added to the solution at a molar ratio equal to that of EDC and let react for at least 4 hours. After this period, the exceeding EDC was removed by dialysis (benzoylated cellulose tubing for separating compounds with a molecular weight of ≤ 1.200 from compounds with a molecular weight > 2,000). The compound was used without purification in the next step. After preparing the poly(amidoamine)-amine terminated (PAMAM-AT), an exhaustive alkylation of primary amines (Michael addition) was carried [82]. An appropriate volume of PAMAM-AT (~8.4 mmol) was transferred to a 50 mL flask and 30 mL of MeOH and 1.14 mL of methyl methacrylate (MA, ~12.6 mmol) were added. The solution was kept under agitation in a water bath for 24 hours at 50 °C, to obtain the compound (PAMAM-methyl ester). The carboxymethylchitosan (100 mg) dissolved in ultrapure water (10 mL) was mixed with the latter obtained PAMAM-methyl ester dendrimer (50 mg), which was previously dissolved in a 20/80 water/methanol (v/v) solution. The final solution was diluted by adding 30 mL of methanol and kept under agitation for 72 hours. After this period, CMCht/PAMAM dendrimer with carboxylic-terminated groups were obtained. CMCht/PAMAM dendrimer

nanoparticles were then precipitated after addition of an appropriate volume of a saturated sodium carbonate, Na_2CO_3 solution and acetone.

The synthesis of CMCht/PAMAM was crucial in this thesis. In **Chapter V**, the CMCht/PAMAM effect on a variety of cancer cell lines' viability and internalization levels under static and dynamic culturing were analyzed. A number of different cancer cell types such as glioblastoma, cervical cancer and colorectal cancer cells were screened.

IV-4.2. Incorporation of Gemcitabine (GEM) into the carboxymethylchitosan/poly(amidoamine) dendrimer nanoparticles

CMCht/PAMAM dendrimer nanoparticles were mixed with a GEM solution with a final concentration of $1x10^{-4}$ M under agitation (w/w). The mixture was then added to the precipitation media consisting of a saturated sodium carbonate, (Na_2CO_3) and acetone solution, under vigorous agitation. Precipitates were collected by filtration and dispersed in ultrapure water for dialysis during the period of 48 hours. Both CMCht/PAMAM and GEM-loaded CMCht/PAMAM dendrimer nanoparticles were obtained by freezing the solution at -80 °C and freeze-drying (Telstar-Cryodos -80, Spain) up to 7 days to complete remove the solvent. It is noteworthy that the CMCht/PAMAM dendrimer nanoparticles and GEM-loaded CMCht/PAMAM dendrimer nanoparticles are water-soluble at physiological pH.

IV-4.3. Investigation of GEM release from CMCht/PAMAM dendrimer nanoparticles

Encapsulation efficiency, drug loading efficiency and release profile studies were performed for the use of anti-cancer drug GEM. For assessing encapsulation efficiency, CMCht/PAMAM (50 mg) was dissolved in 50 mL deionized water. GEM, (7 mg) in 2 mL deionized water was added drop-wise to the dendrimer solution and stirred for 30 minutes. Precipitation of the dendrimers and consequent encapsulation of the drug was induced as described before. Samples were taken before and after precipitation, centrifuged, analyzed by UV-Vis spectrophotometer at 275 nm, in a Hellma Quartz Plate, and compared to a calibration curve.

For evaluating drug-loading efficiency, pre-weighted amount of GEM-loaded CMCht/PAMAM (50 mg) was added to distilled water and sonicated to extract GEM. The extracted GEM

concentration was analyzed by UV-Vis spectrophotometer at 270 nm and compared to a calibration curve. The absorbance was used to calculate the percentage of GEM encapsulated. The following equations (Eq.) were used:

Equation IV-1 – Encapsulation efficiency.

$$\textbf{Eq. 1)}\ \textit{Encapsulation Efficiency}\ (\%) = \frac{\textit{Amount of gemcitabine encapsulated}}{\textit{Total gemcitabine added}}\ X\ 100$$

Equation IV-2 – Drug loading efficiency.

$$\textbf{Eq. 2)}\ \textit{Drug loading Efficiency}\ (\%) = \frac{\textit{Amount of gemcitabine encapsulated}}{\textit{Total weight of nanoparticles}}\ X\ 100$$

GEM release from nanoparticles was measured by UV spectrophotometry (Shimadzu) at 275 nm, in a Hellma Quartz Plate, after dissolution of 50 m of GEM-loaded CMCht/PAMAM dendrimer nanoparticles in 5 mL of phosphate buffer saline solution (PBS) with sodium azide 0.01 % (w/v). The *in vitro* release was performed at 37 °C under stirring at 60 rpm.

These studies were performed on **Chapter VII**, when GEM was encapsulated in the dendrimer nanoparticles and applied and released in a dynamic microfluidic platform, which aimed at mimicking the 3D colorectal tumor microenvironment.

IV-4.4. Labeling of carboxymethylchitosan/poly(amidoamine) dendrimer nanoparticles with fluorescein isothiocyanate

Labeling the dendrimer NPs with a fluorescent molecule is of crucial importance, either as a tracking tool to assess their uptake, and to track the delivery of encapsulated drugs in real time. For this, fluorescein isothiocyanate (FITC) was chosen.

In order to label the CMCht/PAMAM dendrimer with FITC, a 10 mg/mL FITC solution was prepared in anhydrous dimethyl sulfoxide (DMSO), in dark conditions. Conjugates of FITC-CMCht/PAMAM were prepared by covalently bonding the amine group of CMCht and the isothyocianate group of FITC (thiourea bond). Firstly, a 10 mg/mL CMCht/PAMAM dendrimer nanoparticles solution was prepared in a carbonate/bicarbonate coupling buffer of pH 9.2. Then,

50 µL of the FITC/DMSO solution was added per each mL of CMCht/PAMAM dendrimer nanoparticle buffered solution under agitation, and kept in dark at 4 °C for 8 hours. The FITC-labeled CMCht/PAMAM dendrimer nanoparticles solution was dialyzed against ultrapure water in order to remove unlinked FITC for 24 hours and filtered (pore size < 220 nm) in sterile and dark conditions. The final product was obtained as an orange powder after freeze-drying for 7 days.

This process was applied in all the Chapters that involve dendrimer NP: **Chapter V**, **Chapter Chapter VII** and **Chapter VIII**.

IV-4.5. Synthesis of YIGSR – CMCht/PAMAM dendrimer nanoparticles

The attachment of YIGSR peptide (Genscript Corp, Piscataway, NJ, USA) to the NPs was performed via carbodiimide chemistry to form an amide bond between the carboxyl groups on the NPs and the amine groups at the peptide N-terminal end group **(Figure VI-7)**. Briefly, CMCht/PAMAM 1 % (w/v) was prepared in MES buffer (2-(N-morpholino)ethanesulfonic acid), and mixed with the appropriate amount of NHS-Sulfo, EDC and a 10 mg/mL peptide solution (dissolved in MES buffer). The solution was stirred for 24 hours and the NPs were then recovered by dialysis against ultrapure water for 48 hours, followed by freeze-drying process for 7 days.

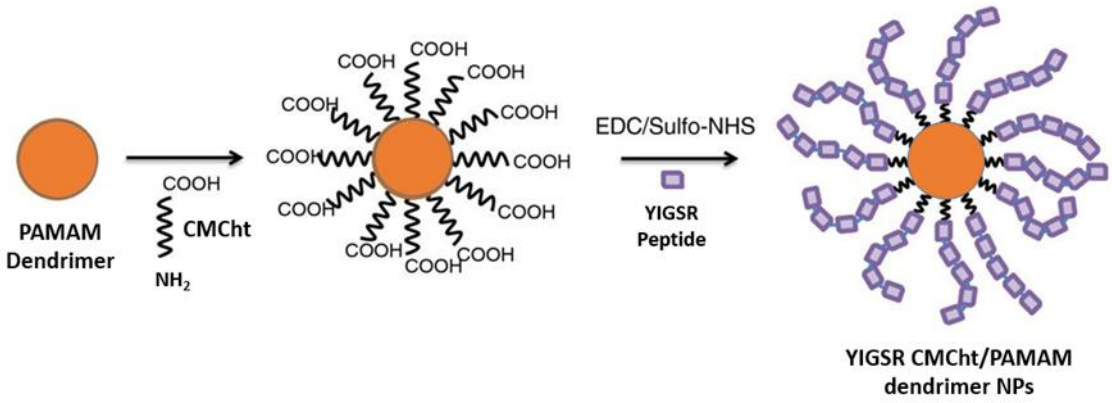

Figure IV-7 - Schematic representation of dendrimer nanoparticles successive modifications with carboxymethilChitosan and YIGSR peptide from laminin via carbodiimide chemistry.

This reaction was performed on **Chapter VIII,** when aiming at targeting dendrimer nanoparticles towards HCT-116 colorectal cancer cells, using YIGSR laminin peptide.

IV-5. HYDROGELS PREPARATION

Current research has validated that tumor microenvironments play pivotal roles in tumor development and metastasis over various physical, chemical, and biological factors, including ECM composition, matrix remodeling, oxygen tension, pH, cytokines, and matrix stiffness [83]. An emerging trend in cancer research involves the creation of engineered 3D tumor models using bioinspired hydrogels that accurately recapitulate the native tumor microenvironment. With recent advances in materials engineering, many researchers are developing engineered tumor models, which are promising platforms for the study of cancer biology and for screening of therapeutic agents for better clinical outcomes [84].

Hydrogels are three-dimensional polymeric networks filled with water [85]. Its application for several TE applications involve cell encapsulation strategies or drug delivery systems [86]. Typical composition of hydrogels varies from synthetic (*e.g.* polyethylene glycol (PEG), polyacrylamide (PAA), polydimethylsiloxane (PDMS)) to natural polymers (*e.g.* collagen, gelatin, alginate, hyaluronic acid (HA), and chitosan). The gelation of hydrogels is enabled by either physical or chemical cross-link methods. Physical gelation is possible through weak interactions between polymer networks, whereas chemical cross link forms strong bonds between polymer chain [87].

The enzymatic crosslinking reactions can be advantageous for several reasons, including the fact that this reaction process occurs at physiological conditions, without need any external stimuli and taking only a few minutes to induce gelation. From the different enzymatic crosslinking methods applied for TE purposes, it was reported that water-soluble polymers containing phenol groups, aminophenol, tyramine or tyrosine can be crosslinked by the horseradish peroxidase (HRP)/hydrogen peroxide (H_2O_2) complex system [88]. In this sense, the SF protein can take advantage of its ~5 % tyrosine groups to form enzymatically crosslinked SF hydrogels via a peroxidase-mediated system [89, 90]. This is another goal of this thesis, *i.e.* to take advantage of the easy processing of enzymatically crosslinked SF in order to create hydrogel-based systems for TE and cancer research applications.

SF hydrogels previously proposed were prepared from a conformational transition of the SF protein from random coil to β-sheet, using extreme physical treatments [91-93] or chemical reagents [94], which in many cases involved long gelation times and harsh preparation conditions that limited their use as ECM models. At the same time, these hydrogels showed

homogeneous and highly tunable physicochemical properties, allowing for the modulation of matrix stiffness [95].

Another purpose of this thesis was to take advantage from the peroxidase-mediated crosslinked SF hydrogels and apply it to build a silk hydrogel microfluidic platform.

IV-5.1. Production of SF hydrogels

Along this thesis, SF was purified from the *Bombyx mori* cocoons in order to extract the glue-like protein sericin and wax. For that, 5 g of cocoons were previously cut and cleaned into several pieces and boiled for 1 hour in 2 L of sodium carbonate solution (0.02 M). Then, the purified SF was washed for 1 hour in 1 L of boiling distilled water, followed by washing in distilled water several times. Afterwards, SF was dried in a clean place. In order to obtain aqueous SF solution, 5 g of purified SF were dissolved in 25 mL of lithium bromide solution (9.3 M) at 70 °C for 1 hour, yielding a solution around 20 % (w/v) [96]. The solution was dialyzed in distilled water for 2 days, using a benzoylated dialysis tubing (Molecular weight cut-off (MWCO): 2 kDa), changing the distilled water at least 3 times per day. After this, it followed a concentration in a 20 wt.% poly(ethylene glycol) solution (20,000 g/mol) for at least 6 hours [97]. The dialysis tubing was carefully washed in distilled water and the solution collected to a 50 mL centrifuge tube (Thermo Fisher Scientific, Waltham, MA, USA) **(Figure IV-8)**. The final concentration of the SF solution was determined by weight measurement. For that, around 500 µL of SF solution were weighted (wet weight) and dried overnight at 70 °C in an over. Then, the dry weight of the sample was determined and the concentration obtained by dividing the dry weight by the wet weight.

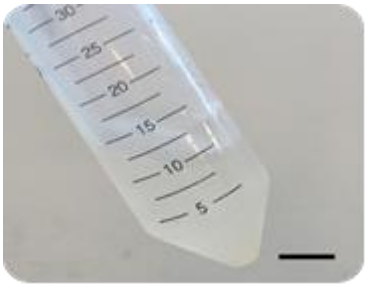

Figure IV-8 - Concentrated aqueous SF solution in a 50 mL Falcon. Scale bar: 1.5 cm.

The SF solution was stored at 4 °C until further use. HRP solution (0.84 mg/mL) and (H_2O_2) solution (0.36 wt.%) were both prepared in PBS solution. The SF solutions (pH ~7.0) were

diluted into 16 wt.% by PBS and used for the hydrogels preparation. Micropipettes M100 and M1000 (Gilson, Middleton, WI, USA) and corresponding tips were used for preparing the reaction mixtures.

Figure IV-9 - Micropipettes Gilson M100 and M1000, specifically designed for hydrogel use. Scale bar: 1 cm.

In **Chapter VI**, each mL of SF solution was mixed with 100 μL of HRP and 65 μL of H_2O_2 solutions and left at 37 °C for the crosslinking. For the 3D dynamic migration assays performed in **Chapter VI**, 2 % and 3 % eSF hydrogel discs were prepared by adding 30 μL of the mixture solutions in a 6 mm diameter silicon mold and placed at 37 °C for crosslinking during 20 minutes. This mold size was used for the crosslinked hydrogel to fit in the Vena4™ micro-wells. For the SF hydrogels supplemented with hVCAM-1 (10 %) (Prepotech, Portugal), the solution was mixed with hVCAM-1 (20 μg/mL) and then placed in silicon molds for crosslinking for 20 minutes. Afterward, hydrogels were taken out of the molds, placed in Vena4™ micro-well and sealed **(Figure IV-10).**

Figure IV-10 – Vena4™ empty and with silk hydrogels placed on the microwells. Scale bar: 6 mm.

IV-5.2. Production of Matrigel® coating and hydrogel

In the same **Chapter VI**, Matrigel was suggested and applied as ECM control material in the form of coating (as suggested by manufacturers) and hydrogel at stock concentration (as a direct comparison with silk), to study its influence in cancer cell migration. Matrigel coating in outward cell migration (modified Boyden chamber) were reconstituted from Matrigel (BD Biosciences) and diluted (250 μg/mL in 0.01 M Tris) (pH 8.0), NaCl (0.7 %) (Laborspirit, Portugal), according to manufacturer's instructions. Diluted Matrigel was carefully added to the top of the membrane and incubated at 37 °C for 2 hours. Then, the remaining liquid (coating buffer) was carefully removed from the permeable support membrane without disturbing the layer of Matrigel. For the 3D hydrogels, Matrigel were added to the 6 mm diameter silicon molds (30 μL) and placed at 37 °C for 30 minutes. For the hydrogels supplemented with hVCAM-1 (10 %), Matrigel was mixed with hVCAM-1 and then placed in silicon molds for crosslinking for 30 minutes.

IV-6. MICROFABRICATION

Microfabrication describes 'cleanroom' fabrication processes for engineering solid flat substrates [98]. It includes photolithography, direct-write laser (e-beam, X-ray) lithography, wet etching, reactive ion etching, film deposition (plasma, chemical vapour, sputtering) and bonding (eutectic, anodic, thermal, adhesion) [99]. It is mostly used for micro-electronic circuit fabrication, but also for 'lab-on-a-chip'.

IV-6.1. Photolithography

In this thesis, photolithography principles were used to fabricate the microfluidic platforms in **Chapter VII** and **IX**. Photolithography, also called optical lithography or UV lithography, is a process used in microfabrication to pattern parts of a thin film or the bulk of a substrate (also called a wafer)[100]. It uses light to transfer a geometric pattern from a photomask (also called an optical mask) to a photosensitive chemical photoresist on the substrate. A series of chemical treatments then either etches the exposure pattern into the material or enables deposition of a new material in the desired pattern upon the material underneath the photoresist **(Figure IV-11)**. This method can create exceedingly small patterns, down to the nanometers size. It provides precise control of the shape and size of the objects it creates and can create patterns over an entire surface cost-effectively [101].

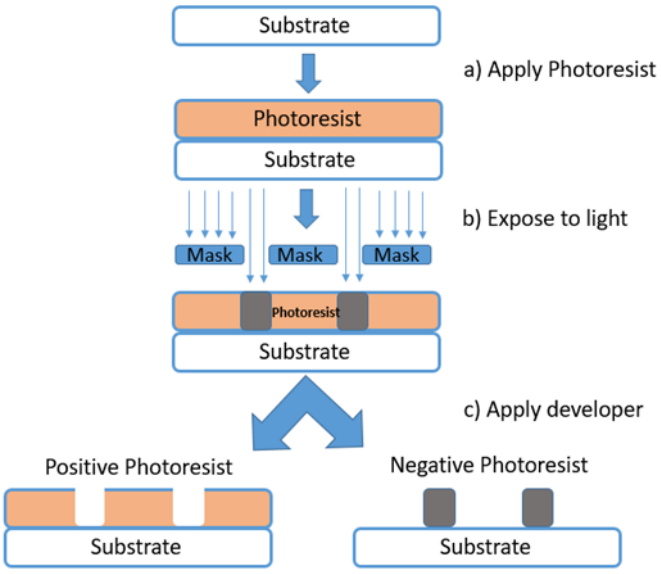

Figure IV-11 - Simplified illustration of photolithography microfabrication.

In **Chapter VII** the microfluidic device fabricated was designed using computer assisted design software on a photolithography mask (Clewin 5). The designed microfluidic chip was composed by three main compartments which consisted of: a large central chamber for an ECM like hydrogel (5 mm diameter) and a pair of perfusable channels flanking the center chamber (connected to the central chamber by a range of pillars to create superficial tension and avoid hydrogels leakage into the lateral channels) **(Figure IV-12)**. The microfluidic device in PDMS (Down Corning) elastomer was fabricated by replica molding from a SU-8 (Microchem)/silicon

master, based on a 10:1 ratio to curing agent. The master mold was produced by photolithography. After pouring PDMS on mold, the mixture was degassed in a vacuum chamber for air bubble removal, and cured at 80 °C for 1 hour in the oven. The devices were then cut out by a razor blade, the fluidic connection ports punched, and bonding to a glass slide done after oxygen plasma of both surfaces and conformal contact (Plasma cleaner/sterilizer Harrick®, high RF level, 4 mbar, 120 seconds). The oxygen plasma treatment is a free-solvent method for surface modification of polymer surfaces [102]. The plasma treatment has its only action at the very top of structures, used to assemble the device to a glass slides. The PDMS microfluidic network was irreversibly bonded to the glass substrate after both surfaces were treated with air plasma.

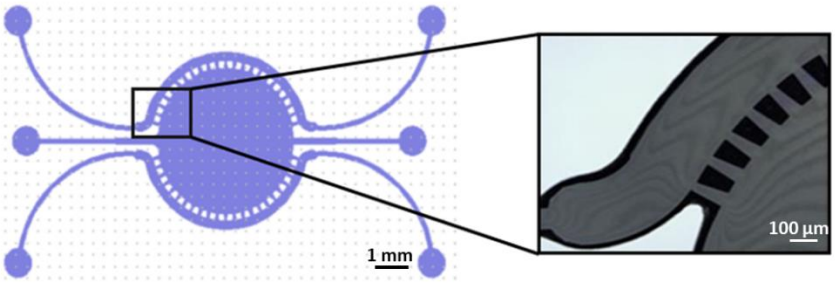

Figure IV-12 - Clewin 5 software design of microfluidic chip with close up on microchannel/microwell interface.

IV-6.2. Soft-Lithography

Soft lithography is a field that covers a number of different techniques. Soft lithography can be broken into three different major categories (each of which can be further divided up): printing, replica molding and embossing. Soft lithography provides access to 3D and curved structures, tolerates a wide variety of materials, generates well-defined and controllable surface chemistries, and is generally compatible with biological applications. It is also low in cost, experimentally convenient and has emerged as a technology useful for a number of applications that include cell biology, microfluidics, lab-on-a-chip, micro-electromechanical systems and flexible electronics/photonics [103]. In this thesis we have applied two of the sub-categories of soft-lithography: Replica molding and microcontact printing (µCP).

IV-6.2.1. Replica Molding

Replica molding is a process for shaping flexible polymer materials using a micro-sized rigid frame or model called a 'mold'. A mold is a cast from the object to be replicated. This mold is then filled with a pre-polymer, which is cross-linked and the resulting polymer is peeled off the mold [104]. Using a mold, rather than the object itself, allows multiple copies to be made without damaging the original.

This technique was applied in **Chapter IX,** where a silk hydrogel microfluidic device was developed. The method for producing it also comprises photolithography as an initial step. As proof of concept, a simple serpentine channel was designed using Autocad software. The silk fibroin hydrogel-based microfluidic device was produced as follows: (i) the use of UV-photolithography for the fabrication of microfluidic channels; (ii) replica moulding of the fabricated structures using (PDMS; (iii) TCS-silanization and second replica moulding of the microfluidic structures using a polymeric material (PDMS); (iv) replication of the microfluidic structures using silk fibroin hydrogel **(Figure IV-13)**.

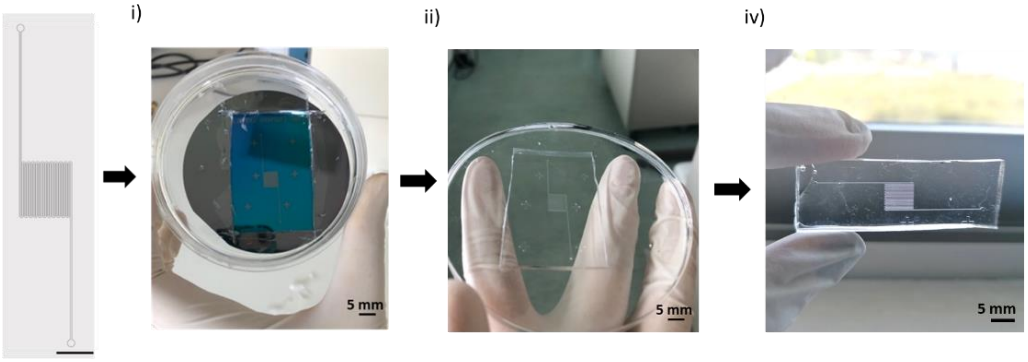

Figure IV-13 – Example of serpentine like microchannels and stages of producing silk hydrogel microfluidic platform.

IV-6.2.2. Microcontact printing

Microcontact printing (μCP) is a soft lithography method whereby a PDMS stamp with a desired motif is used to deposit molecules of interest onto a surface [105].

PDMS (1:10 w/w, Sylgard 184; Dow Corning) stamps were replicated from an SU-8 mold (MicroChem) fabricated by UV-photolithography (MIDAS MDA-400MA). The PDMS stamp was rendered hydrophilic by plasma treatment to maximize 67LR protein patterning. Glass coverslips

were plasma treated for 1 minute and incubated for 1 hour under anoxic conditions in anhydrous methanol solution of 5 % (v/v) in (3-aminopropyl)triethoxysilane (APTES). Next, the samples were washed with methanol and ultrapure water. Then, APTES-functionalized coverslips were incubated for 30 minutes in a solution of 1 % (v/v) glutaraldehyde in ultrapure water. The micropatterned PDMS stamp was incubated with 10 μg/mL 67LR protein (Abcam, Portugal) solution for 2 hours and the excess was removed by nitrogen drying. Immediately, the PDMS stamp containing the laminin receptor protein was placed in contact with the functionalized glass coverslip for 5 minutes. After releasing the stamp, FITC-labeled YIGSR-CMCht/PAMAM dendrimer NPs were incubated overnight. This experiment was performed in order to prove the YIGSR laminin protein attached to the FITC labeled NPs selectively binds to the patters containing 67LR protein.

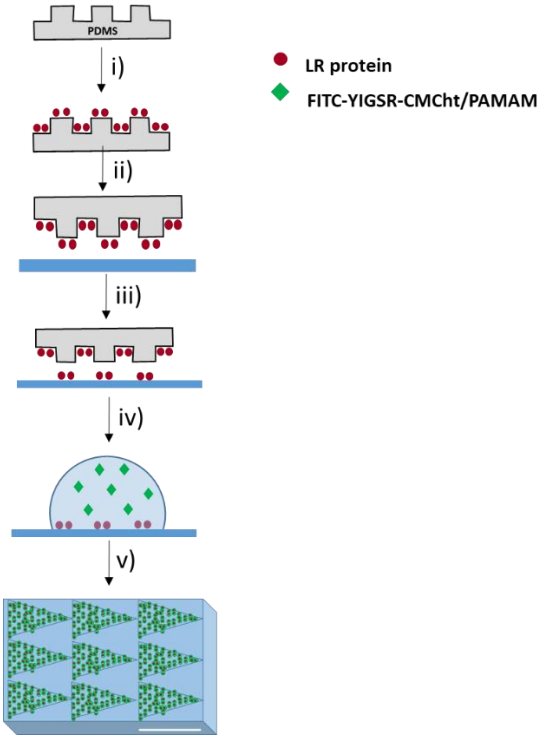

Figure IV-14 - μCP strategy applied in this thesis as proof-of-concept.

IV-6.2.3. Generation of stable gradients inside microfluidic chip

Chemical gradients play a key role in many biological processes and regulate a number of cellular functions *in vivo*. Indeed, there are several examples of gradient-dependent phenomena in nature, being a critical one the chemotaxis, *i.e.* the cell migration triggered by chemical

gradients [106]. Moreover, chemical gradients have shown to have an impact various cell behaviors, such as migration, proliferation, differentiation during development, wound healing, inflammation, and tumorigenesis processes [107, 108].

Gradients generation can also have an impact in drug screening. The present state of screening methods for drug discovery is still riddled with several ineptitudes [109]. Although some widely used high-throughput screening platforms may enhance the drug screening process, their cost and oversimplification of cell–drug interactions present a translational difficulty. Microfluidic technology, and its advantage to use gradients may resolve many issues found in conventional HTS technology. Moreover, they provide benefits such as reduced sample quantity and integration of 3D cell culture physically more representative of the physiological/pathological microenvironment [110].

In **Chapter VII** a gradient of nanoparticles was generated in the fabricated microfluidic platform. For this, CMCht/PAMAM dendrimer nanoparticles were modified with a green fluorescent molecule FITC as described before. Matrigel was injected into the central chamber with a syringe and allowed to crosslink for 30 minutes at 37 °C. After this, a source-sink mechanism was created, with one solution of 0.5 mg/mL FITC-labeled nanoparticles in PBS perfused through one side channel and PBS was perfused through the other inlet, using a Nexus 3000 syringe pump (Chemix). Syringes of 3 mL syringes were used to introduce PBS with or without the NP at a rate of 8 μL/hour. The experiment was performed in a Nikon Eclipse Ti-E fluorescence microscope (Nikon Instruments, Japan) for time lapse imaging of the gradient formation. Profile and stability of the dynamic gradient was analyzed using NIS-Elements AR (Nikon) software. The chips were analyzed at different time points between 0 and 12 hours with continuous perfusion. Built-in "plot profile" module was used for assessing the gradient intensity and stability over time. **Figure IV–14** represents the process of placing the microfluidic platform on the fluorescence microscope and analyze in real time the formation of a gradient of fluorescent labeled dendrimer NPs.

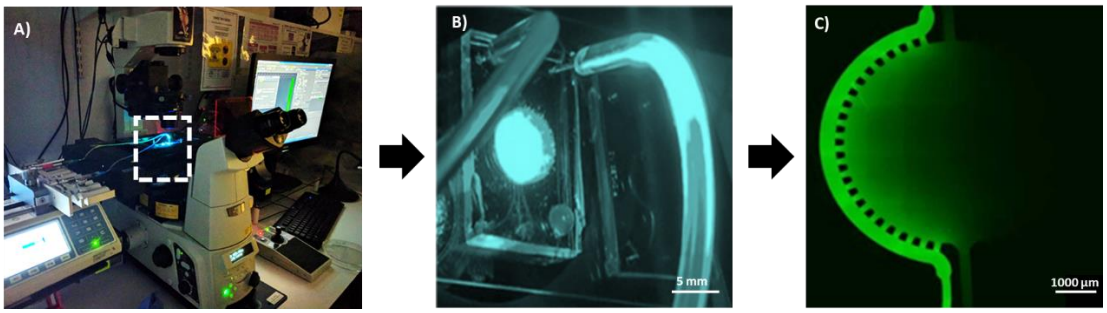

Figure IV-15 - A) Apparatus for generating gradients in real time. B) Microfluidic device under perfusion to create a gradient. C) Fluorescence image of the FITC-CMCht/PAMAM nanoparticles' gradient.

IV-7. PHYSICOCHEMICAL CHARACTERIZATION TECHNIQUES

IV-7.1. Morphological/morphometric evaluation

IV-7.1.1. Scanning electron microscopy (SEM)

Scanning Electron Microscopy (SEM), is an imaging technique that produces images of a sample by scanning the surface with focused beam of electrons. When in contact with the atoms at the sample's surface, the electrons produce several signals containing the collected information. Thus, the qualitative information regarding the surface morphology of samples and elemental information can be obtained [111].

In **Chapter VIII,** the microstructure of the surface of L929 and HCT-116 cells were analyzed on top of polystyrene coverslips in order to detect if the fluorescent signal of nanoparticles obtained in confocal microscope was due to the presence of nanoparticles at the surface or internalized at the cell's cytoplasm, using scanning electron microscope, SEM (Leica Cambridge S-360, UK). Prior to, specimens were coated with carbon (Fisons Instruments, Polaron SC 508, UK) and gold (Fisons Instruments, Polaron SC 502, UK), respectively. The current was set at 18 mA with a coating time of 120 seconds.

In **Chapter IX** SEM was also applied to study the fidelity of the silk hydrogel microfluidic platform. Samples were produced by enzymatic crosslinking as described before, and then dried in a sequence of ethanol solution from 10 % to 100 % (v/v). After dehydration, samples were

dried using critical point dryer (Autosamdri-815 Series A, Tousimis, USA). Using such approach, the samples were heated up to 37 °C and pressurized until 90 bar for 45 minutes.

Figure IV-16 - SEM with EDS analyzer. The SEM (JSM-6010 LV, JEOL, Japan) instrument is equipped with the low vacuum mode as a standard feature. The low vacuum mode allows non-conductive specimens to be observed and analyzed without conductive coating. This SEM is equipped with an energy dispersive spectroscope (EDS). Scale bar: 10 cm.

IV-7.1.2. Fourier Transform Infrared Spectroscopy (FTIR)

Fourier Transform Infrared Spectroscopy (FTIR) is a cost-effective technique. It is a form of vibrational spectroscopy that is useful in the study of a variety of chemical processes. It identifies polymers and analyzes polymer chemical modifications. Fourier transformation algorithm allied to IR spectroscopy gives a spectrum of IR absorption per frequency/wavelength. Similar chemical groups absorb in the IR at similar frequencies, enabling to identify the chemical structure of a compounds, and to identify chemical modifications [112]. IR spectrum is specific for each compound. FTIR was performed to verify the presence of covalently liked carboxymethylchitosan in dendrimer NP in **Chapter V**, as well as the chemical modification with YIGSR peptide in **Chapter XIII**. A transmittance spectrum was obtained on an IR Prestige-21 FTIR spectrometer (Shimadzu) by performing 32 scans in each spectrum over a range of 400-4400 cm^{-1} and with a resolution of 4 cm^{-1}. In **Chapter IX**, the silk hydrogel protein conformation was evaluated by an Attenuated Total Reflectance (ATR) model (IRPrestige-21, Shimadzu, Japan) in a FTIR equipment

(Perkin-Elmer 1600 series equipment, CA, USA) equipped with a Germanium crystal, as can be seen in **Figure IV-16**. All spectra were obtained between 400-4400 cm^{-1}, at a 4 cm^{-1} resolution for an average of 50 scans.

Figure IV-17 - The Fourier transform infrared (FTIR) spectrometer is used as a standard chemical characterization technique. The samples can be analyzed as films, KBr discs, powder or liquids. The available methodologies comprise transmittance, specular reflectance, diffuse reflectance and attenuated total reflectance (ATR). Scale bar: 10 cm.

IV-7.1.3. Transmission Electron Microscopy (TEM)

Transmission Electron Microscopy (TEM) is a damaging imaging system that provides high-resolution images. The principle of the technique consists of electron beams that pass through the samples and interact with the atoms at different depths. The transmitted electrons originate signals which are detected by the TEM equipment and converted into a two-dimensional image. Importantly, TEM's resolution is about 0.2 nm, which is more than a thousand-fold greater than the resolution of the light microscope [113]. **In Chapter V**, a JEOL JEM 1400 TEM (Tokyo, Japan) equipment was used to investigate and measure the CMCht/PAMAM dendrimer NP.

In **Chapter VIII**, TEM was used to compare and analyze CMCht/PAMAM dendrimer nanoparticles with and without the peptide YIGSR attachment, since an increase in size would be expected. For the analysis, samples were mounted on a 200-mesh copper or nickel grids, stained with 2 % Phosphotungstic acid and examined. Images were digitally recorded using a CCD digital camera (Orious 1100W Tokyo, Japan).

IV-7.1.4. Atomic Force Microscopy (AFM)

Atomic Force Microscopy (AFM) technique allows the observation and measurement of the surface structure of samples with an unprecedented resolution and accuracy. Through this analysis, it is possible to obtain images showing the arrangement of individual atoms in a surface sample, or to see the structure of individual molecules [114]. Comparing to the optical or electron microscopes, AFM does not form an image by focusing light or electrons onto a surface. It "senses" the samples surface with a sharp probe or cantilever and builds a map covering the height or topography of the samples surface. The type of images generated by this microscope can reach a magnification greater than 1000 x. On the other hand, from an imaging microscope, only a 2D projection of a samples surface can be reached without any height information included. Furthermore, besides being an imaging tool AFM has several spectroscopic modes that measure other samples properties as nanoscale [114]. **In Chapter V** the morphology of the NPs was investigated using AFM available in the research facilities **(Figure VI–17)**. First, the freeze-dried CMCht/PAMAM dendrimer NPs were dispersed in ultrapure water to obtain a solution with final concentration of 1 mg/mL and then one drop was placed over a 9.9 mm mica disc (Agar Scientific, Essex, England) and blown dried with nitrogen gas for subsequent characterization. Then, the samples were analyzed using the Tapping Mode™ with a MultiMode AFM connected to a NanoScope III controller, both from Veeco (NY USA), with noncontact silicon nanoprobes (ca. 300 kHz) from Nanosensors, Switzerland. All images were plane-fitted using the third-degree-flatten procedure included in the Nano-Scope software version 4.43r8. The morphometric analysis was performed using the same software.

In **Chapter VIII**, AFM analysis was performed using the same exact procedure described for **Chapter V**, this time in order to compare CMCht/PAMAM dendrimer NPs to YIGSR modified CMCht/PAMAM dendrimer NPs.

Figure IV-18 - The AFM is able to acquire images of flat surfaces that can encode the surface topography, mechanical response, among other properties. The equipment presents a series of accessories that allows the acquisition of data in liquids and air. In the case of liquids, it is also possible to control the temperature of the experiments. Scale bar: 10 cm.

IV-7.1.5. Differential scanning calorimeter (DSC)

Differential scanning calorimeter (DSC) is an important instrument in thermal analysis, being useful to understand amorphous and crystalline behavior, eutectic transitions, curing and degree of cure, and many other material's properties used to design, manufacture, and test products. This technique allows to study the material's heat capacity (Cp) as function of the temperature. A sample of known mass is heated or cooled and the changes in its Cp are tracked as changes in the heat flow, which allows the detection of transitions such as melting, glass transitions, among others parameters [115]. The DSC experiments performed in this thesis were carried out using DSC Q100 V9.8 Build 296 apparatus, which can be seen in **Figure IV-18**. **In Chapter V,** we decided to study the thermal stability and changes in crystallinity over a range of temperatures of the developed CMCht/PAMAM dendrimer nanoparticles. For that, the samples were placed in aluminum pans and heated at a rate of 10 °C/min from 20 to 220 °C, cooled to 20 °C and heated at 5 °C/minute until 200 °C. Standard calibrations were performed using indium leads.

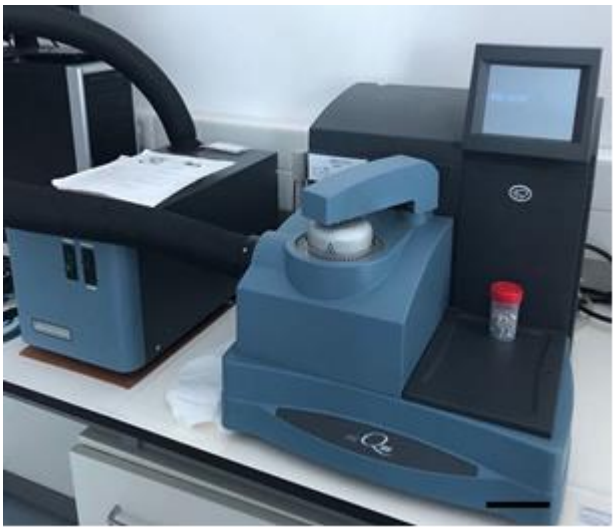

Figure IV-19 - Differential scanning calorimetry is a thermal analysis technique that detects the temperatures and heat flows caused by changes in heat capacity or by endothermic and exothermic processes of materials as a function of time and temperature. Scale bar: 10 cm.

IV-7.1.6. Nuclear Magnetic Resonance Spectroscopy (NMR)

Nuclear magnetic resonance (NMR) is a phenomenon which occurs when the nuclei of certain atoms are immersed in a static magnetic field and exposed to a second oscillating magnetic field. Some nuclei experience this phenomenon, and others do not, dependent upon whether they possess a property called spin. H^1NMR is the application of nuclear magnetic resonance in NMR spectroscopy with respect to hydrogen nuclei within the molecules of a substance. This is a non-destructive technique that allows determining the structure of organic compounds. Simple NMR spectra are recorded in solution, and solvent protons must not be allowed to interfere. In this thesis, H^1NMR analysis was performed twice, first to investigate the structure and the successful modification of PAMAM dendrimers with CMCht in **Chapter V**, and then to assess the covalent link of YIGSR peptide to CMCht/PAMAM in **Chapter VIII.** For this purpose, nanoparticles were dissolved in deuterated water (D_2O). The NMR spectra were obtained with a Mercury -400BB operating at a frequency of 399.9 MHz at 50 °C. The one-dimensional 1H spectra were acquired using a 45° pulse, a spectral width of 6.3 kHz and an acquisition time of 2.001 seconds.

IV-7.1.7. Zeta potential and particle size analysis

Adequate characterization of NPs is of paramount importance to develop well-defined nanoformulations of therapeutic relevance. Determination of particle size and surface charge of NPs are indispensable for proper characterization of NPs. DLS (dynamic light scattering) and ZP (zeta potential) measurements have gained popularity as simple, easy and reproducible tools to ascertain particle size and surface charge [116].

Almost all particulate or macroscopic materials in contact with a liquid acquire an electronic charge on their surfaces [117]. ZP is an important and useful indicator of this charge which can be used to predict and control the stability of colloidal suspensions or emulsions, for example. The greater the zeta potential the less likely the suspension is to be aggregated. On the other hand, particle size can be determined by measuring the random changes in the intensity of light scattered from a suspension or solution. This technique is commonly known as DLS, but is also called photon correlation spectroscopy (PCS) and quasi-elastic light scattering (QELS). ZP and particle size of the CMCht/PAMAM dendrimer nanoparticles and YIGSR-CMCht/PAMAM dendrimer nanoparticles were measured in a particle size analyzer (Zetasizer Nano ZS, Malvern Instruments, UK) **(Figure IV–19)** in **Chapters V** and **VIII**. By analyzing the size of particles and surface charge, important considerations can be made on the success of engineering these particles.

Figure IV-20 - Zetasizer Nano ZS, Malvern Instruments. Scale bar: 10cm.

ZP was calculated by determining the electrophoretic mobility and then applying the Henry equation. The electrophoretic mobility is obtained by performing an electrophoresis experiment on the sample and measuring the velocity of the particles using Laser Doppler Velocimetry (LDV).

The Henry equation is:

Equation IV-3 – Henry equation.

$$\mu_e = \frac{2 \cdot \epsilon \cdot z \cdot f(k \cdot \alpha)}{3 \cdot \eta}$$

z: Zeta potential;

UE: Electrophoretic mobility;

ε: Dielectric constant;

η: Viscosity;

f(Ka): Henry's function; the value used was 1.5 and is referred to as the Smoluchowski approximation.

Electrophoretic determinations of ZP were investigated using the universal 'dip' cell, using H_2O and phosphate buffered saline (PBS) solutions pH 7.4.

IV-7.1.8. Micro-BCA

Micro BCA™ Protein Assay Kit is a detergent-compatible bicinchoninic acid formulation for the colorimetric detection and quantitation of total protein. A purple-colored reaction product is formed by the chelation of two molecules of BCA with one cuprous ion (Cu^{+1}). This water-soluble complex exhibits a strong absorbance at 562 nm that is linear with increasing protein concentrations. Moreover, the macromolecular structure of protein, the number of peptide bonds and the presence of four amino acids (cysteine, cystine, tryptophan and tyrosine) are reported to be responsible for color formation [118]. In **Chapter VIII**, Micro BCA Kit (Thermo Fisher) was used to measure the protein concentration of grafted YIGSR peptide onto CMCht/PAMAM dendrimer nanoparticles. Since the peptide sequence YIGSR incorporates the amino acid tyrosine, this technique was chosen for protein concentration quantification. Samples of CMCht/PAMAM and modified YIGSR-CMCht/PAMAM dendrimer NPs were dissolved in ultrapure water at a final concentration of 1 % and compared to standards for protein quantification in triplicates using the microplate reader (Synergy HT, BioTek Instruments, USA) at 562 nm.

IV-7.1.9. Mechanical properties - Rheological analysis

Rheology is the study of flow and deformation of materials under applied forces which is routinely measured using a rheometer. The measurement of rheological properties is applicable to all materials from fluids such as dilute solutions of polymers and surfactants through to concentrated protein formulations, to semi-solids such as pastes and creams, to molten or solid polymers as well as asphalt [119]. This technique gives the elasticity, viscosity and plastic behavior of materials under changes of strain, frequency, time, or temperature. Moreover, the existence of any chemical reactions in the flows that induce gelation or polymerization can also be detected with high sensitivity through this technology.

In **Chapter VIII**, a rheological experiment were performed to characterize the SF and Matrigel hydrogels using a Kinexus pro+ rheometer (Malvern Instruments, UK), equipped with the

acquisition software rSpace **(Figure IV-20)**. SF hydrogel discs were first prepared in PDMS silicone molds (8 mm diameter and 2 mm height), and after each time point were analyzed by oscillatory experiments. For that, the measuring system was equipped with stainless steel (316 grade) parallel plates: an upper measurement geometry plate (8 mm diameter) and a lower pedestal (20 mm diameter) with roughened finish. The influence of polymer type and concentration of the used hydrogels was studied in terms of their rheological behavior in order to analyze the mechanical properties of the hydrogels. Stress sweeps (0.1 Hz) were first performed to determine the linear viscoelastic region (LVR) for all the tested conditions. Frequency sweeps (0.01–10 Hz) were then performed within the LVR. The values of the shear storage modulus (G′) and loss modulus (G″) were obtained at a frequency of 0.1 Hz. Storage modulus G′ is known as the "solid-like" or elastic component of the gel, and G″ (Loss modulus) as the "liquid like" or viscous component. The system is considered a gel if the value of G′ is greater than G″, which was expected since the samples being analyzed were hydrogels.

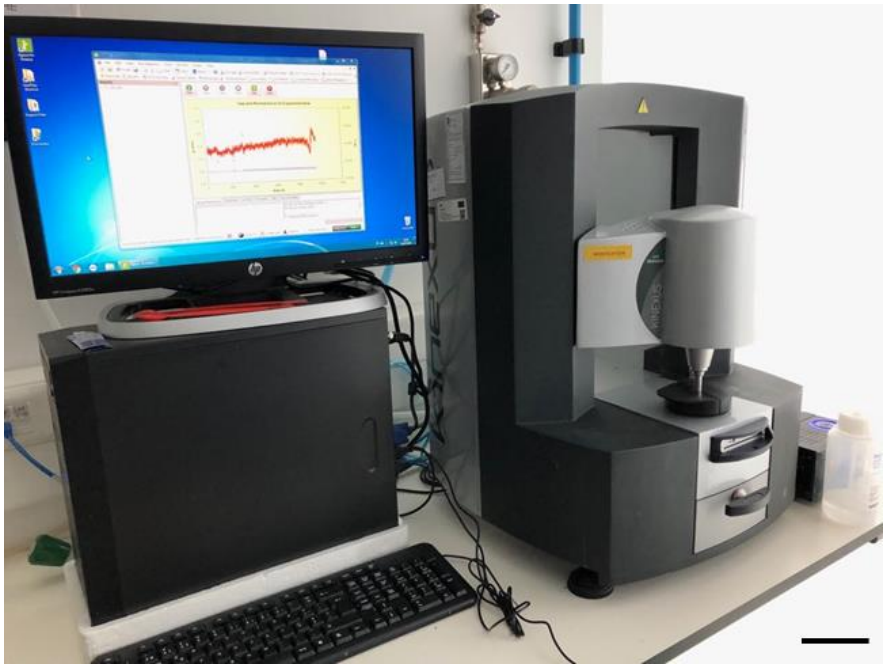

Figure IV-21 – Rheometer apparatus, Malvern Instruments. Scale bar: 10 cm.

IV-8. *IN VITRO* BIOLOGICAL TESTING

IV-8.1. Cell sources

Most of the cellular work performed in this thesis was carried out using cell lines. Cells lines are immortalized cells that present the ability to proliferate indefinitely either due to a random mutation or due to a programmed modification. Cell lines are useful models for doing research, because they provide reliability in experimental results due to the possibility to obtain large amounts of cells for prolonged use [120].

Furthermore, since this thesis was developed in the context of cancer research, immortalized cancer cells were abundantly used.

IV-8.1.1. HCT-116 cells

HCT-116 cancer cell line was purchased from ATCC (USA), (Ref. ATCC® CCL-247). Cells were cultured in low glucose Dulbecco's modified Eagle's medium (DMEM), supplemented with 44 mM of sodium bicarbonate, 10 % (v/v) of fetal bovine serum (FBS; Biochrom, Berlin,

Germany), and 1 % (v/v) of antibiotic/antimycotic solution (prepared with 10,000 units/mL penicillin G sodium, 10.000 μg/mL streptomycin sulfate, and 25 μg/mL amphotericin B as Fungizone (R) in 0.85 % saline; Gibco®, Life Technologies, Carlsbad, CA, USA). Cells were routinely trypsinized (0.25 % trypsin–EDTA solution; Life Technologies, Carlsbad, CA, USA) for 2-3 minutes at 37 °C, centrifuged at 300 g for 5 minutes (Eppendorf 5810R centrifuge equipped with an A-4-62 rotor), and re-suspended at a density of $1x10^6$ cells in T150 cell culture flasks (BD Biosciences, Enzifarma, Porto, Portugal).

IV-8.1.2. HeLa cells

HeLa cell line (from cervical cancer cells) was generously donated by Prof. Joseph Costello (California University, Neurosurgery Department, San Francisco, USA) and further provided by Prof. Rui M. Reis (Life and Health Science Research Institute, University of Minho, ICVS/3B's – PT Government Associate Laboratory, Portugal). Cells were cultured in low glucose Dulbecco's modified Eagle's medium (DMEM), supplemented with 44 mM of sodium bicarbonate, 10 % (v/v) of fetal bovine serum (FBS; Biochrom, Berlin, Germany), and 1% (v/v) of antibiotic/antimycotic solution (prepared with 10,000 units/mL penicillin G sodium, 10.000 μg/mL streptomycin sulfate, and 25 μg/mL amphotericin B as Fungizone (R) in 0.85 % saline; Gibco®, Life Technologies, Carlsbad, CA, USA). The L929 cells were incubated in an atmosphere containing 5 % CO_2 at 37 °C, and the medium changed every 2-3 days. Cells were routinely trypsinized (0.25 % trypsin–EDTA solution; Life Technologies, Carlsbad, CA, USA) for 2-3 minutes at 37 °C, centrifuged at 300 g for 5 minutes (Eppendorf 5810R centrifuge equipped with an A-4-62 rotor), and re-suspended at a density of $1X10^6$ cells in T150 cell culture flasks (BD Biosciences, Enzifarma, Porto, Portugal).

IV-8.1.3. GBM cells

Human neuronal glioblastoma U87MG cell line was generously donated by Prof. Joseph Costello (California University, Neurosurgery Department, San Francisco, USA) and further provided by Prof. Rui M. Reis (Life and Health Science Research Institute, University of Minho, ICVS/3B's – PT Government Associate Laboratory, Portugal). The use of U87MG cell line was

approved by the Ethics Committee of University of Minho. Cells were cultured in low glucose Dulbecco's modified Eagle's medium (DMEM), supplemented with 44 mM of sodium bicarbonate, 10 % (v/v) of fetal bovine serum (FBS; Life Technologies, Carlsbad, CA, USA), and 1 % (v/v) of antibiotic/antimycotic solution. The U87MG cells were incubated in an atmosphere containing 5 % CO_2 at 37 °C, and the medium changed every 2-3 days. Cells were routinely trypsinized (TryplE™ Express) for 5 minutes at 37 °C, centrifuged at 300 g for 5 minutes, and re-suspended at a density of $1X10^6$ cells in T75 cell culture flasks.

IV-8.1.4. L929 cells

L929 cell line from mouse C3H/An connective tissue (purchased from ECACC, UK) was cultured in low glucose Dulbecco's modified Eagle's medium (DMEM), supplemented with 44 mM of sodium bicarbonate, 10 % (v/v) of fetal bovine serum (FBS; Biochrom, Berlin, Germany), and 1 % (v/v) of antibiotic/antimycotic solution (prepared with 10.000 units/mL penicillin G sodium, 10.000 μg/mL streptomycin sulfate, and 25 μg/mL amphotericin B as Fungizone (R) in 0.85% saline; Gibco®, Life Technologies, Carlsbad, CA, USA). The L929 cells were incubated in an atmosphere containing 5 % CO_2 at 37 °C, and the medium changed every 2-3 days. Cells were routinely trypsinized (0.25% trypsin–EDTA solution; Life Technologies, Carlsbad, CA, USA) for 2-3 minutes at 37°C, centrifuged at 300 g for 5 minutes (Eppendorf 5810R centrifuge equipped with an A-4-62 rotor), and re-suspended at a density of $1X10^6$ cells in T150 cell culture flasks (BD Biosciences, Enzifarma, Porto, Portugal).

IV-8.1.5. HCOMECS cells

Human Colonic Microvascular Endothelial Cells were isolated by ScienCell research laboratories from human colonic tissue and purchased from Innoprot (Ref. P10769, The Netherlands) cryopreserved (liquid nitrogen) at a cell density of $5x10^5$ cells/vial (1 mL) as primary cultures and delivered by the company frozen. The cell content in each vial was dispensed into a T75 cell culture flask at a density of $5x10^3$ cells/cm^2 and cultured in endothelial medium (Ref. P60104, purchased from Innoprot, The Netherlands). Culture medium was changed every 3 days, until reaching approximately 70 % confluence. Cells were routinely trypsinized (0.25 %

trypsin–EDTA solution) for 2-3 minutes at 37 °C, centrifuged (200 g, 5 minutes) and re-suspended at a density of $1x10^6$ cells in T150 cell culture flasks.

IV-8.2. Cryopreservation

The cryopreservation of the cells used in this thesis was performed using a Statebourne Biosystem 24 cryogenic tank (Statebourne Cryogenics Ltd., UK). Briefly, cell suspensions of $1x10^6$ cells/mL were prepared in a cryopreservation solution, consisting of 10 % (v/v) DMSO (N182, VWR, Radnor, PA, USA) in FBS, and transferred into 1.5 mL cryovials (479-6841, VWR, Radnor, PA, USA). Then, cell suspensions were gently cooled down, first at -20 °C for at least 2 hours and then moved to -80 °C freezer for a minimum period of 12 hours. The cryovials were subsequently stored at -176 °C in the gas nitrogen phase of the cryogenic tank.

IV-8.3. Cell seeding techniques

IV-8.3.1. Seeding on Vena8™ chips

In **Chapter V** a variety of cancer cells lines including HeLa cells, HCT-116 cells and GBM cells were seeded in Vena8™ microfluidic chip in order to compare the effect of CMCht/PAMAM nanoparticles in terms of cytotoxicity in static (2D culture flasks) and dynamic (2D under flow). For this, a semi-automated microfluidic platform, Vena8™ biochip with a glass coverslip (Tebu-Bio, Portugal), was used to mimic physiological flow conditions though the perfusion of cell culture medium in the microchannels. Each chip microchannel was coated with fibronectin (Sigma, Germany) and then placed in a humidified sterile Petri dish, incubated at 37 °C for 1.5 hours. After the incubation period, the confluent cells were detached from the T150 cell culture flasks using trypsin (0.25 % trypsin–EDTA solution (v/v)), centrifuged at 300 g for 5 minutes, counted in a cell counter KOVA® Glasstic® slide 10 chamber with grids (Garden Grove, CA, USA) and diluted in a new cell suspension. For the seeding, 15.000 cells (HeLa, U87MG or HCT-116) were gently added into each microchannel and kept in a sterile Petri dish in the incubator for 2 hours to allow cell adhesion. To prevent drying, after the initial 30 minutes of incubation, complete medium DMEM was added to the channels.

IV-8.3.2. Seeding on Vena4™ chips

In **Chapter VI** this thesis starts to focus only on colorectal cancer models. Therefore, HCT-116 cells were seeded on Vena4™ chips' microchannel in order to evaluate the influence of SF and Matrigel's mechanical properties, as well as the influence of hVCAM-1 molecule in cell migration. All the procedures were performed under aseptic condition. Confluent cells were detached from the T150 cell culture flasks using trypsin (0.25 % (v/v) trypsin–EDTA solution), centrifuged at 300 g for 5 minutes, and diluted in a new cell suspension in PBS for labeling with CellTracker™ CM-DiI fluorescent dye. This dye has been designed to freely pass through cell membranes into cells, where it is transformed into cell membrane-impermeant reaction products. CellTracker™ CM-DiI dye is retained in living cells through several generations. It is stable, nontoxic at working concentrations, well retained in cells, and brightly fluorescent at physiological pH. HCT-116 cells were pre-labeled with red cell tracker CM-DiI Dye ($1x10^{-6}$ M in PBS) (Invitrogen, Portugal) and incubated at 37 °C for 30 minutes. After this, labeled cells were centrifuged again at 300 g for 5 minutes, counted in a cell counter KOVA® Glasstic® slide 10 chamber with grids (Garden Grove, CA, USA) and seeded on Vena4™ microchannels using a standard yellow pipette (30.000 cells/channel). In order to prevent drying, after the initial 30 minutes of incubation, complete medium DMEM was added to the channels.

IV-8.3.3. Seeding on fabricated microfluidic chip

Our goal in **Chapter VIII** was to develop a complex 3D microfluidic chip-based *in vitro* model that could emulate the human colorectal tumor microenvironment. In this sense, the designed and fabricated microfluidic device has three compartments: a circular central chamber for the ECM like hydrogel, (where HCT-116 cancer cells are encapsulated in Matrigel to mimic the tumor), laterally sided by a pair of perfused channels. The two lateral channels are not interconnected between them, and are used to mimic the vascular part of the tumor by seeding colonic endothelial cells.

IV-8.3.3.1 *Encapsulation of HCT-116 in Matrigel*

In **Chapter VIII** HCT-116 cancer confluent cells were detached from the T150 cell culture flasks using trypsin (0.25 % (v/v) trypsin–EDTA solution), centrifuged at 300 g for 5 minutes, diluted in a new cell suspension and counted in a cell counter KOVA® Glasstic® slide 10 chamber with grids (Garden Grove, CA, USA). After this, HCT-116 cells were re-suspended in Matrigel supplemented with VEFG (100 ng/mL) (R&D Systems) in a density of $10x10^6$ cells/mL, and injected in the central chamber of the microfluidic device using a syringe. It was let to incubate for 15 minutes at 37 °C for crosslinking.

IV-8.3.3.2 *Seeding of HCOMECS in lateral microchannels*

The lateral channels were pre-coated using a 10 % (v/v) Matrigel solution in DMEM complete medium and incubated for 30 minutes at 37 °C. HCoMECs confluent cells were detached from the T150 cell culture flasks using trypsin (0.25 % (v/v) trypsin–EDTA solution), centrifuged at 300 g for 5 minutes, diluted in a new cell suspension and counted in a cell counter KOVA® Glasstic® slide 10 chamber with grids (Garden Grove, CA, USA). Using the same the same density as for the cancer cells ($10x10^6$ cells/mL), cells were seeded on the lateral channels using a yellow pipette and left to adhere for 6 hours. Then, cells were exposed to a perfusion flow regime at a flow rate of 8 μL/hour for the duration of the experiments. At days 1 and 5 days, the cell culture was evaluated using bright field/fluorescence microscopy.

IV-8.4. Cell migration assays

Migration is often used as broad term in biology to describe any directed cell movement within the body. The ability to migrate allows cells to change their position within organs or tissues [121]. In pathology, invasion of carcinomas for example is defined as the penetration of tissue barriers, such as passing the basement membrane and infiltration into the underlying interstitial tissues by malignant tumor cells [122]. Intestinal cancers for example are classified as invasive when the tumor mass has crossed the basal membrane and entered the submucosal muscle layer. Therefore, migration can occur on 2D surfaces without any obstructive fiber network. However, invasion is defined as cell movement through a 3D matrix, which is generally

complemented by a restructuring of the surrounding 3D environment [44]. Determining the migratory and invasive capacity of tumor cells and clarifying the underlying mechanisms is of upmost relevancy for novel strategies in cancer diagnosis, prognosis, drug development and treatment. As such, there are several migration/invasion assays described in the literature [123], some of which were performed in this thesis, as follows.

IV-8.4.1. Outward Cell Migration (Modified Boyden Chamber Assay)

The transwell assay was originally introduced by Boyden (often called Boyden chamber assay) to analyze the chemotactic responses of leukocytes [123]. The principle of this assay is based on two medium containing chambers separated by a porous membrane through which cells transmigrate. Generally, cells are seeded in the upper part and can migrate in vertical direction through the pores of the membrane and into the lower compartment. This lower compartment usually contains an attractant or simply higher serum [124]. Alternatively, and similar to what was used in **Chapter VI**, dark colored porous membranes are available, which block light transmission (FluoroBlok, Becton Dickinson) from unmigrated cells. Therefore, the detection and quantification of the migrated labeled cells is simplified and there is no need to remove the remaining cells from the top-side of the membrane. In **Chapter VI** this assay was modified and adapted to our needs **(Image IV–21)**, in order to compare the migration results to a microfluidic dynamic platform. For this, the upper and lower compartments were separated not only by a porous black membrane, but also by a layer of the proposed studied hydrogels. First, the SF hydrogels and Matrigel coating were produced as described before. Then, HCT-116 cells were pre-labeled with Cell Tracker Red ($5x10^{-3}$ M) (Invitrogen, Portugal) for 20 minutes, and then seeded on top of the coating/hydrogels (30 000 cells/well). In the upper chamber, either DMEM medium with 10 % (v/v) FBS or Serum free medium were added (300 μL). In the lower chamber, either DMEM medium with 10 % (v/v) FBS (control), DMEM supplemented with 10 % (v/v) h-VCAM1 or with 30 % (v/v) FBS were added (500 μL). At different time points, fluorescence intensity from the bottom was measured using a microplate spectrofluorimeter (BioTek, Portugal) in area-scan bottom-reading mode, at excitation/emission wavelengths of 553/570 nm. Results are presented as the increase in fluorescence in relation to the time point 0 hours. For qualitative analysis, in the last time point (48 hours), cells were fixed with formalin (10 % v/v) (Sigma,

Germany) and stained for F-actin filaments of the cytoskeleton and nuclei with Texas Red-X phalloidin (Molecular Probes, Invitrogen, USA) and with 4,6-diamidino-2-phenylindole, dilactate (DAPI blue, Molecular Probes, USA), respectively, following supplier's protocol. Fluorescence images of migrating cells were collected using an inverted fluorescence microscope (Leica, Germany).

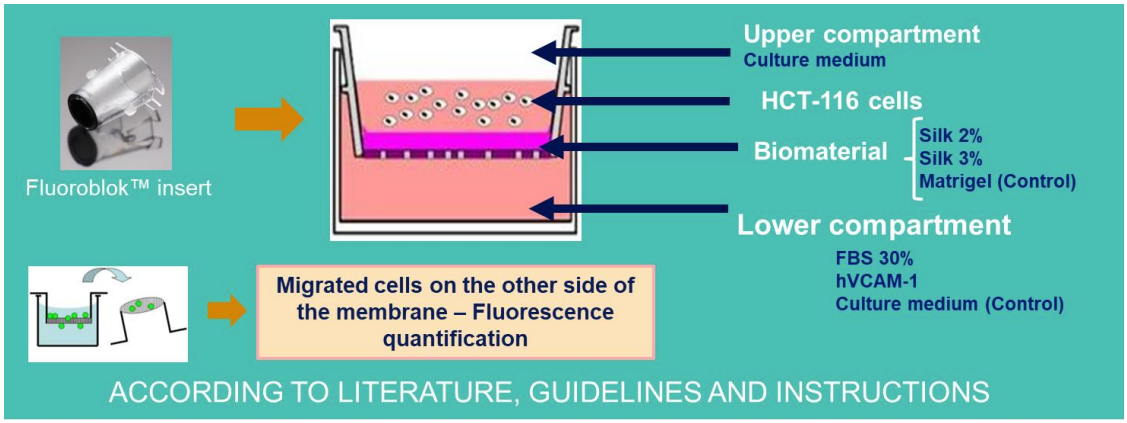

Figure IV-22 – Schematics of Modified Boyden Chamber assay with the experimental conditions used in Chapter VI.

IV-8.4.2. Cell Migration Assay in 3D VenaT4 Biochips

In **Chapter VI**, cancer cell migration was tested and compared in the Modified Boyden Chamber invasion assay and in the 3D platform Vena4™ (Cellix, Ireland).

Each chip's microchannel was coated with fibronectin (Sigma, Germany) (100 µg/mL), placed in a humidified sterile Petri dish and incubated at 37 °C for 1.5 hours. After the incubation period, HCT-116 confluent cells were detached from the T150 cell culture flasks using trypsin (0.25 % (v/v) trypsin–EDTA solution), centrifuged at 300 g for 5 minutes, diluted in a new cell suspension and counted in a cell counter KOVA® Glasstic® slide 10 chamber with grids (Garden Grove, CA, USA). Cells were pre-labeled with red cell tracker CM-DiI Dye ($1x10^{-6}$ M) (Invitrogen, Portugal) and incubated at 37 °C for 30 minutes. After, labeled cells were seeded on Vena4™ microchannels using a standard yellow pipette (30,000 cells/channel). In order to prevent drying, after the initial 30 minutes of incubation, complete medium DMEM was added to the channels. The hydrogels (3 % and 2 % SF and Matrigel), previously crosslinked in the silicon molds, were placed in the microwell and sealed. At determined time points (0 and 48 hours), the

chip was observed under confocal laser scanning microscopy (Leica, Germany) to monitor pre-labeled cells' migration toward the hydrogel with and without hVCAM-1.

IV-8.4.3. Endothelial cell Invasion

Cancer has the ability to spread to adjacent or distant organs, which makes it life threatening. Tumor cells can penetrate blood or lymphatic vessels, circulate through the intravascular stream, and then proliferate at another site: metastasis. For the metastatic spread of cancer tissue, angiogenesis is important [125]. Angiogenesis is a complex morphogenetic process where endothelial cells from pre-existing vessels invade the matrix as sprouts to form new vessels [125]. For capillary sprouting and blood vessel formation, both proliferation and migration are essential, but how these two events are coordinated is not fully clear [126]. Angiogenesis occurs in several well-characterized stages: At first, stimulatory signals bind to surface receptors on vascular endothelial cells. Activated endothelial cells then release proteases that degrade the underlying basement membrane and allow endothelial cells to migrate out of the existing blood vessel. The endothelial cells begin to proliferate and form sprouts that extend toward the source of the angiogenic stimulus. Subsequent lumenation of these primary sprouts leads to formation of capillary loops, which is followed by synthesis of a new basement membrane and blood vessel maturation to complete tube-like structures through which blood can flow. Pro-angiogenic signals, such as VEGF, are known to promote processes such as proliferation, endothelial motility, and filopodia extension [127].

Angiogenesis inhibitors can be designed to block the formation of new blood vessels, and the growth of tumors would thereby be halted but not eliminated; hence, anti-angiogenesis monotherapies are not effective in humans as was hoped for. Thus, combinatorial treatments with conventional chemotherapy drugs are required. These inhibitors sometimes may not eliminate tumors and in order to achieve optimal treatment, a combination of anti-angiogenesis and conventional chemotherapy may be required [125]

In **Chapter VII,** the 3D formation of endothelial sprouts in a microfluidic device and the changes in cellular organization during early stages of invasion were examined. Seeding of colonic microvascular endothelial cells on fabricated microfluidic chip was performed as described in section "Seeding of HCOMECS in lateral microchannels". During cell culture, bright

field images were taken with inverted microscope to analyze and quantify in which extent endothelial cells remain on the lateral microchannels or respond to VEGF present in the Matrigel in the central chamber **(Figure IV-22)**. Three images of each time point (day 0, day 2, day 3 and day 5) were analyzed. The length was measured using Image J (Fiji), from the outer limit of the microchannels/hydrogel interface, until the furthest point of the elongated cell(s).

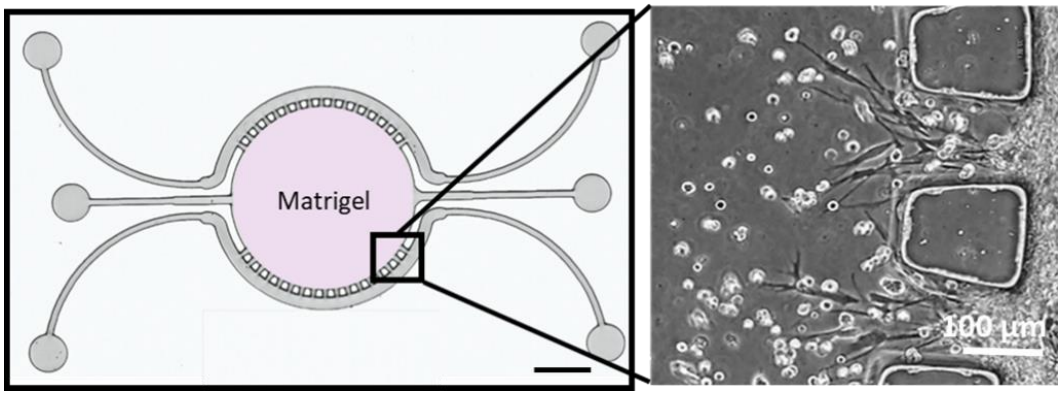

Figure IV-23 - Scheme representation of endothelial cell invasion from lateral channels towards the central chamber following VEGF gradient. Scale bar: 1 mm.

IV-8.5. Metabolic activity and cell viability examination

IV-8.5.1. Alamar blue assay

Alamar blue assay is used to evaluate the metabolic activity of cells. It is a cell viability reagent that works by using the reducing power of living cells to quantitatively measure their metabolic activity. When cells are metabolically active they maintain a reducing environment within the cytosol [128]. Resazurin is the active molecule of AlamarBlue® reagent, blue in color, non-toxic and cell permeable. Upon within the cells, resazurin is reduced to resorufin, turning from blue to red and highly fluorescent. Viable cells continuously convert resazurin to resorufin, increasing the overall fluorescence and color of the media surrounding the cells, that can be measured [129].

In **Chapter VIII**, Alamar blue was performed to assess the effect of CMCht/PAMAM, YIGSR-CMCht/PAMAM and GEM-loaded YIGSR-CMCht/PAMAM dendrimer NPs in terms of metabolic activity in each cell type separately (HCT-115 and L929). Cells were grown in Dulbecco's

Modified Eagle Medium (DMEM, Gibco, Invitrogen) supplemented with 10 % (v/v) fetal bovine serum and 1 % (v/v) penicillin/streptomycin at 37 °C and 5 % CO_2. Subcultures of cells were performed when confluence reached values of ~90 %. Then, cells were plated at an initial density of $1x10^4$ cells per well in a 24-well plate. The working solution consists of 20 % (v/v) AlamarBlue® (BioRad, Hercules, CA, USA) solution and 80 % culture medium, which was prepared and protected from light (Alamar Blue working solution). At the end of each time-point, cells were washed with PBS solution and immersed in 500 µL of Alamar Blue working solution. The culture plates were kept in the dark, at 37 °C in the CO_2 incubator for 4 hours. The reacted AlamarBlue was read in a microplate reader (Synergy HT, BioTek, Instruments, USA) using 100 µL supernatant per well, at an excitation wavelength of 530/25 nm and at an emission wavelength of 590/35 nm. Three independent experiments were performed. The metabolic activity values were calculated by normalization with the mean fluorescence value obtained for the controls (Tissue culture polystyrene; TCPs) with and without cells.

IV-8.5.2. ATP bioluminescence assay

In **Chapter VI**, a CellTiter-Glo® Luminescent Cell Viability Assay (Promega, WI, USA) was used to evaluate the viability of the HCT-116 that had migrated towards the center of the SF hydrogels in the response to the chemoattractant hVCAM-1 (and without). This is a homogeneous and reproducible method for the determination of cell viability based on the quantification of the existing Adenosine Triphospate (ATP), which directly quantifies the metabolic activity of cells. This assay was designed for direct use in multi-well culture plates, making it ideal for an automated screening of cells cytotoxicity, and highly reproducible. This assay involves adding a single reagent (CellTiter-Glo® Reagent) directly to the cultured cells/hydrogels, prepared in the corresponding serum-free culture medium. The contact with this reagent induces cell lysis and generation of a luminescent signal proportional to the amount of the present ATP. The amount of ATP is directly proportional to the number of cells in culture [130].

In **Chapter VI**, the cell-laden hydrogels were retrieved from Vena4™ chips after each timepoint and placed in 24-well plates; washed with PBS solution and incubated in 1 mL of ATP working solution, consisting of CellTiter-Glo® Reagent and serum-free cell culture medium DMEM (without phenol red), in a 1:1 ratio. The specimens were incubated for 30 minutes at RT, in an

orbital shaker (KS 260 control, Wilmington, NC, USA). The reacted ATP solution was read in the microplate reader using 100 µL supernatant per well, and the emitted luminescence was detected using a sensitivity of 120. Different concentrations of ATP disodium salt solution, ranging between 0 and 2 µmol/L, were used to prepare a standard curve for the calculation of ATP concentration, relating quantity of ATP and luminescence intensity. Three specimens were tested at each time-point. Three independent experiments were performed.

IV-8.5.3. DNA Quantification

DNA content was analyzed by the total double stranded DNA (dsDNA) by using the Pico-Green® dsDNA quantification assay. This colorimetric assay employs fluorescence to evaluate cell proliferation through the measurement of the dsDNA of samples. When the PicoGreen® fluorescent marker is added to the solution, it specifically binds to the dsDNA emitting fluorescence, read at 480 nm (excitation) and 520 nm (emission). DNA content is further determined through a DNA standard curve, prepared using standard dsDNA solutions with concentrations ranging from 0 to 2 µg/mL.

In **Chapter V**, after the determined timepoints, HeLa, GBM and HCT-116 cancer cells were washed with sterile PBS and were lysed with 1 mL of ultrapure water in each well. The cellular suspensions were transferred into microtubes and incubated in a water bath at 37 °C for 1 hour, then stored at -80 °C for further analysis (at least 6 hours before the DNA quantification assay).

In **Chapter VIII** DNA quantification was performed to assess the effect of CMCht/PAMAM, YIGSR-CMCht/PAMAM and GEM loaded-YIGSR-CMCht/PAMAM dendrimer NPs on cancer cells and fibroblasts separately. After the determined timepoints, cells seeded were washed with sterile PBS and lysed with 1 mL of ultrapure water in each well. The cellular suspensions were transferred into microtubes, incubated in a water bath at 37 °C for 1 hour, and stored at -80 °C for further analysis.

For the DNA quantification, the samples were defrosted at RT, and then underwent ultrasonication treatment for 1 hour at 37 °C to release the DNA. The doublestranded DNA (dsDNA) was quantified by using the Quant-iT™ Pico-Green® dsDNA kit 2000 assays (Thermo Fisher Scientific, Waltham, MA, USA) according to the manufacturer's instructions. Briefly, 28.7 µL of sample or standard were added to a 96-well white opaque plate, mixed with 100 µL of 1X

Tris-EDTA buffer (10 mmol/L Tris-HCl, 1 mmol/L EDTA, pH 7.5) and 71.3 μL of 1X Quant-iT™ PicoGreen® reagent, in a total volume of 200 μL. The plate was incubated at RT for 10 minutes and read in the microplate reader (ex/em 485/528). Three specimens of each group were tested at each time-point. Three independent experiments were performed.

IV-8.5.4. MTS

The MTS assay is a colorimetric method commonly used for determining the number of viable cells in proliferation or cytotoxicity assays. In this protocol, MTS assay is designed to assess the short-term cytotoxicity of polymeric biomaterials, in this case NPs developed along this thesis. The MTS assay is based on bio-reduction of a tetrazolium compound, 3-(4,5-dimethylthiazol-2-yl)-5-(3-carboxymethoxyphenyl)-2-(4-sulfofenyl)-2H-tetrazolium (MTS), into a brown formazan product that is soluble in tissue culture medium. This conversion is presumably accomplished by NADPH or NADH produced by dehydrogenase enzymes in metabolically active cells. The quantity of formazan product, as measured by the amount of 490 nm absorbance, is directly proportional to the number of living cells in culture

In **Chapter V**, MTS viability test was performed to determine the cytotoxicity of CMCht/PAMAM dendrimer NPs in HeLa, U87MG and HCT-116 cancer cells in static and dynamic conditions. Cells were continuously grown in DMEM (Gibco, MD, USA; Invitrogen, CA, USA) supplemented with 10 % (v/v) fetal bovine serum and 1% (v/v) penicillin and streptomycin under standard conditions (37 °C in a humidified atmosphere containing 5 % CO_2). Subcultures of cells were performed when confluence reached values of approximately 90 %. Then, cells were plated at an initial density of $2x10^4$ cells/well in 24-well plates and exposed to three concentrations of CMCht/PAMAM dendrimer NPs (0.1, 0.5 and 1 mg/mL) for short-term exposures comprised between 1 and 3 days. By the end of the timepoints, cells cultures (n=3) were placed in culture medium containing MTS in a 5:1 ratio and incubated in a humidified atmosphere at 37 °C and 5 % CO_2. After three hours of incubation, 100 μL of solution from each well were transferred to a 96-well TCPS plate and the optical density was determined at 490 nm. Cultures that were not exposed to the CMCht/PAMAM dendrimer NPs were used as controls. In the case of the Vena8™ chip, to test cell viability using the MTS method, cells from each channel were detached using Tryple Express (Alfagene, Portugal). Cells were aspirated and collected in a

1.5 mL tube. After centrifugation (5 minutes, 1500G), cells were incubated with culture medium containing MTS in a 5:1 ratio and analyzed as aforementioned for 2D standard cell cultures.

IV-8.5.5. Flow cytometry analysis

Flow cytometry is a sophisticated instrument that can measure multiple physical characteristics of a single cell such as size and granularity simultaneously, as the cell flows in suspension through a measuring device. Its working depends on the light scattering features of the cells under investigation, which may be derived from dyes or monoclonal antibodies targeting either extracellular molecules located on the surface or intracellular molecules inside the cells. This approach makes flow cytometry a powerful tool for detailed analysis of complex populations in a short period of time [131].

In **Chapter V,** flow cytometry was used as a quantitative method for determining cell viability levels of labeled CMCht/PAMAM dendrimer nanoparticles inside of GBM, HeLa and HCT-116 cells under static and dynamic conditions. In static conditions, cancer cells were cultured in the presence of 0.5/mg mL FITC-labeled CMCht/PAMAM dendrimer NPs in a 6-well plate ($2x10^5$ cells/well). Cells cultured in complete culture medium were used as controls. Cells were released from a substratum and a cell strainer was used to avoid cell clusters. Afterward, 0.5 mL of DMEM complete medium was added to each well and samples transferred to cytometry tubes. In dynamic conditions, cancer cells were cultured in the presence of 0.5 mg/mL FITC-labeled CMCht/PAMAM dendrimer NPs in the microfluidic chips. Cells cultured in complete culture medium were used as controls. Flow cytometry analysis was carried out to perform quantitative analysis on the internalization efficiency as well as cell viability, as follows: each channel was washed with PBS. Then, PBS was aspirated, and cells from each channel were detached using 10 µL of TrypleExpress and collected in an FACS tube. After centrifugation at 1500×r.p.m. for 5 minutes, cells were re-suspended. in 800 µL of a 2 % (v/v) fetal bovine serum in PBS solution. Afterward, 5 µL of 7-Aminoactinomycin D (7-AAD; Taper group, Portugal) was added to each sample for determining the number of dead cells. After this step, cells were loaded in FACSCalibur flow cytometer (BD Biosciences Immunocytometry Systems, CA, USA). Calibrate beads three-color kit (BD CaliBRITE™ beads, CA, USA) was used to adjust the equipment

instrument settings before samples are run on the flow cytometer. Finally, data were treated using the Flowing Software 2.

In **Chapter VIII**, flow cytometry was used to quantify the number of dead cells in a co-culture of HCT-116 and L929 cells cultured in DMEM supplemented with to 0.5 mg/mL of GEM loaded YIGSR-CMCht/PAMAM. Cells were grown in Dulbecco's Modified Eagle Medium (DMEM, Gibco, Invitrogen) supplemented with 10 % (v/v) fetal bovine serum and 1 % (v/v) penicillin/streptomycin at 37 °C and 5 % CO_2. Subcultures of cells were performed when confluence reached values of ~90 %. Then, co-culture was achieved by plating an initial density of $1x10^4$ of each cell type per well in a 24-well plate. Cells were cultured in medium supplemented with 0.5 mg/mL of GEM-loaded YIGSR-CMCht/PAMAM. After 24 and 72 hours, cells were trypsinized (TrypleX) and a cell strainer was used to avoid cell clusters. Next, 0.5 mL of DMEM complete medium was added to each well and samples transferred to cytometry tubes. To distinguish cells in co-culture, 10 µL of FITC-CD44 antibody (Abcam, Portugal, Ref. ab27285) was incubated with co-cultured cells for 30 minutes at RT. After washing with 2 mL of 2 % FBS (v/v) in PBS, the tubes were centrifuged at 300 rpm for 5 minutes and re-suspended in 500 µL of % FBS (v/v) in PBS. Cell suspensions were analyzed in FACSCalibur flow cytometer after adding 1 µL of Propidium iodide (PI). For the flow cytometry cell viability assays in 3D, cells encapsulated in Matrigel were retrieved using 500 µL of Corning™ Cell Recovery Solution for 30 minutes at 4 °C and the subsequent protocol was performed as previously described. For all assays, calibrate beads three-color kit (BD CaliBRITE™ beads, USA) was used to adjust the equipment instrument settings before samples are run on the flow cytometer. Finally, data was analyzed using the FLOWING SOFTWARE 2.

IV-8.5.6. Live/Dead staining assay

Calcein-acetoxymethyl (Calcein-AM)/Propidium iodide (PI) staining was used. It is a method for the visualization of cell viability and death. In this method, cells are incubated with Calcein-AM, which is a non-fluorescent and cell-permeant derivative of calcein, transported through the cellular membrane. When the intracellular esterases of living cells remove the acetomethoxy group, this probe becomes green fluorescent. However, it stays non-fluorescent when the acetoxymethyl ester is intact because of the non-active esterases of dead cells. The specific

visualization of dead cells can be performed by incubation with fluorescent PI, which shows enhanced fluorescence when binding with high affinity to DNA. Contrary to calcein-AM, PI does not permeant the cellular membrane, it binds to the cytoplasmic DNA when the cellular membrane of dead cells is disrupted [132]. Instead of PI, ethidium homodimer (EthD-1) can also be used.

In **Chapter VI**, Live/dead staining was used to determine whereas cells that migrated from the microchannels of Vena4™ into the SF and Matrigel hydrogels were viable. This would be a good indicator that the hydrogels allow cell migration but also if they allow flow of nutrients enough to keep the cells alive. For this, the cell-laden SF and Matrigel constructs were removed from the Vena4™ chip and washed with PBS solution. Next, cells were stained with calcein-AM (1 μg/mL) and PI (2 μg/mL), followed by incubation for 15 minutes in the dark, at 37 °C in the CO_2 incubator. Samples are immediately observed under fluorescence microscopy (Calcein-AM ex/em 495/515 nm; PI ex/em 495/635 nm) in the transmitted and reflected light microscope. Images were acquired using the Zen microscope processing software, connected to the digital camera AxioCam MR3. A Z-stack function was used to combine images at different depths into one final image.

In **Chapter VII** the viability of cells cultured in the microfluidic chip's central chamber was assessed in the presence or absence of GEM loaded dendrimer nanoparticles using the Live/dead assay. For this, at endpoints, the chip side-channels were washed with PBS (Sigma), and then a solution of Calcein AM (1 μM) and EthD-1 (6 μM) was perfused thought the lateral channels and let to incubated for 40 minutes, to reach the cells in the center of the chamber. After this, the lateral channels were washed with PBS. Microfluidic chips were then imaged with fluorescence microscope using automated acquisition for Z-stack and multicolor-channel. Acquired multi-frame multicolour images were combined either using Nikon AR or FIJI software (open-source software ImageJ focused on biological image analysis) for operations of processing such as rotation, crop, color balance and related assemblies, considering initial scales and aspect ratios. High-resolution Z-stack images were processed for 3D reconstruction through deconvolution and 3D projections made by NIS-Elements AR (Nikon) software.

In **Chapter VIII**, cell viability of HCT-116 and L929 in co-culture in the presence of GEM loaded YIGSR-CMCht/PAMAM was also assessed by Live/Dead staining. HCT-116 and L929

confluent cells were detached from the T150 cell culture flasks using trypsin (0.25 % (v/v) trypsin–EDTA solution), centrifuged at 300 g for 5 minutes, diluted in a new cell suspension and counted in a cell counter KOVA® Glasstic® slide 10 chamber with grids (Garden Grove, CA, USA). L929 were pre-labeled with blue cell tracker CellTracker Blue CMAC (Alfagene, Portugal) ($1x10^{-6}$ M) and incubated at 37 °C for 30 minutes, whereas HCT-116 cells were left unstained. At the end of the last time-point (72 hours), three samples were washed with PBS and incubated in 1 μg/mL calcein-AM and 2 μg/mL PI prepared in DMEM low glucose supplemented with sodium bicarbonate and 1 % (v/v) antibiotic/antimycotic solution for 10 minutes in the dark at 37 °C in the 5 % CO_2. After washing in PBS, samples were immediately analyzed in a confocal microscopy (Calcein-AM in green: ex/em 495/515 nm; PI in red: ex/em 495/635 nm; Cell Tracker Blue CMAC in blue: ex/em 353/466 nm) (Leica, SP8, Germany).

In **Chapter IX**, Live/dead assay was performed again. This time to prove HCT-116 cancer cells encapsulated in the silk hydrogel microfluidic platform were viable, receiving enough oxygen and nutrients, until transformation of silk proteins conformation from amorphous to β-sheet. For this, at the end of each time point (24 hours and 3 days), three samples were washed with PBS and incubated in 1 μg/mL calcein-AM and 2 μg/mL EthD-1 prepared in DMEM low glucose supplemented with sodium bicarbonate and 1 % (v/v) antibiotic/antimycotic solution for 10 minutes in the dark at 37 °C in the 5 % CO_2.

IV-8.6. Assessment of FITC-labeled CMCht/PAMAM dendrimer nanoparticles internalization

IV-8.6.1. Fluorescence microscopy and fluorescence-activated cell sorting (FACS) analyses

In this thesis, the internalization of the FITC-labeled CMCht/PAMAM dendrimer nanoparticles and FITC-YIGSR-CMCht/PAMAM dendrimer nanoparticles were investigated using different cell types (**Chapters V and VIII**), both by fluorescence microscopy and flow cytometry analyses.

Regarding fluorescence microscopy, it is a major tool with which to monitor cell physiology, and in this case, the internalization of fluorescent labeled NPs. In **Chapter V,** to assess the internalization but also possible cell morphological changes, fluorescence microscopy was used. A cell suspension was prepared and seeded on tissue culture polystyrene coverslips (Sarstedt

Inc., USA) in 24-well plates ($2x10^4$ cells/well) and cultured with 0.5 mg/mL FITC labeled CMCht/PAMAM dendrimer NPs, in standard culture conditions for 1 and 3 days. Then cells were fixed with 4 % (v/v) formalin (Sigma, Germany) and stained for F-actin filaments of the cytoskeleton and nuclei with Texas Red-X phalloidin (Molecular Probes, Invitrogen, USA) and with 4,6-diamidino-2-phenylindole, dilactate (DAPI blue, Molecular Probes), respectively, following supplier's protocol. For dynamic cultures, cells were cultured as described previously in the microfluidic platform and were fixed with 10 µL per channel of 4 % (v/v) formalin (Sigma, Germany) for 10 minutes. Then, 10 µL per channel of DAPI and Texas Red-X Phalloidin were perfused into the microchannels to stain the nuclei and the cytoskeleton F-actin filaments, respectively, and washed with PBS after 30 minutes. Finally, cells were observed under the fluorescence microscope (AxioImager Z1, Zeiss Inc., Oberkochen, Germany), in triplicates.

In **Chapter V,** flow cytometry was performed to quantify and compare the internalization levels of FITC-labeled CMCht/PAMAM dendrimer NPs in static and dynamic cultures in three cancer cell lines (GBM, HeLa and HCT-116). In static conditions, cancer cells were cultured in the presence of 0.5 mg/mL FITC-labeled CMCht/PAMAM dendrimer NPs in a 6-well plate ($2x10^5$ cells/well). Cells cultured in complete culture medium were used as controls. Cells were released from the substratum with Tryple Express and a cell strainer was used to avoid cell clusters. Afterwards, 0.5 mL of DMEM complete medium was added to each well and samples transferred to cytometry tubes, centrifuged and re-suspended in 800 µL of a 2 % (v/v) fetal bovine serum in PBS solution. In dynamic conditions, cancer cells were cultured in the presence of 0.5 mg/mL FITC-labeled CMCht/ PAMAM dendrimer NPs in the microfluidic chips. Cells cultured in complete culture medium were used as controls. Each channel was washed with PBS. Then, PBS was aspirated and cells from each channel were detached using 10 µL of Tryple Express and collected in an FACS tube. After centrifugation at 1,500 g for 5 minutes, cells were re-suspended in 800 µL of a 2 % (v/v) fetal bovine serum in PBS solution.

In **Chapter VIII**, when studying the possible targeted internalization analysis of the modified YIGSR dendrimer nanoparticles, L929 and HCT-116 cells were co-cultured in medium supplemented with 0.5 mg/mL of FITC-labeled YIGSR-CMCht/PAMAM dendrimer NPs in 24-well plates ($1x10^4$ cells each type/well). Cells cultured in complete culture medium were used as controls. After 24 and 72 hours, cells were trypsinized and a cell strainer was used to avoid cell clusters. Next, 0.5 mL of DMEM complete medium was added to each well and samples

transferred to cytometry tubes and centrifuged. To distinguish cells in co-culture, 10 µL of PE-CD44 antibody (Abcam, Portugal, Ref. ab46793) was incubated with cell suspension for 30 minutes at room temperature in 2 % (v/v) FBS in PBS. CD44 binds only to HCT-116 cancer cells, and not the L929 cells. After washing with 2 mL of 2 % (v/v) FBS in PBS, the tubes were centrifuged at 300 g for 5 minutes and re-suspended in 1 % (v/v) formalin in PBS. Cell suspensions were analyzed in FACSCalibur flow cytometer. Finally, data was analyzed using the FLOWING SOFTWARE 2.

IV-8.7. Gene expression profiles

IV-8.7.1. RNA isolation and first-strand cDNA synthesis

The expression of mRNA for specific apoptosis and proliferation-related genes of interest was measured by real-time PCR analysis. Extraction of high-quality RNA is a crucial step in gene expression profiling, and previous studies have shown that using kits for RNA extraction allows to obtain a higher purity and efficiency in the process [133].

In **Chapter VII**, different extraction kits were used for total RNA isolation. The great challenge in this genetic analysis was thee retrieval of cells from Matrigel and from the central chamber of the microfluidic chip. For this, after each culture time, Matrigel from the central chamber was retrieved by punching out with a 5 mm sterile biopsy punch (WPI, The Netherlands) and placed in 24 well plates. The PDMS was separated from the hydrogel. Samples were washed with PBS solution and Matrigel was depolymerized by incubation with 1 mL of Cell Recovery Solution™ (BD Biosciences, The Netherlands) for 30 minutes at 4 °C. After complete release from the Matrigel, cells were transferred to an Eppendorf tube and centrifuged to a pellet by centrifugation at 300 G for 5 minutes. Cells were washed with cold PBS and centrifuged again. Total RNA was extracted from cells recovered from the 3D cultures using Phasemaker™ Tubes (Invitrogen), following the manufacturer's instructions. The pellet was then immersed in 500 mL TRIZOL reagent and stored at 80 °C until further use. Next, the samples were transferred to Phasemaker™ Tubes and incubated for 5 minutes to permit complete dissociation of the nucleoproteins complex. 0.2 mL of chloroform per 1 mL of TRIzol™ Reagent used for lysis was added and shaken vigorously by hand for 15 seconds. After a 15 minutes incubation at RT, samples were centrifuged for 5

minutes at 12000 g at 4 °C. The mixture separates into a lower red phenol-chloroform, and interphase, and a colorless upper aqueous phase. The Phasemaker™ Gel forms a barrier between the upper and lower phases. Then, 0.5 mL of isopropanol was added to the aqueous phase and incubated for 10 minutes, followed by a 10 minutes centrifugation at 4 °C. The pellet is re-suspended in 75 % ethanol. The supernatant is discarded with a pipette and the pellet left to dry.

RNA quantification and purity were assessed using a NanoDrop ND-1000 spectrophotometer (NanoDrop Technologies). Afterwards, samples were defrosted at RT and underwent ultrasonication treatment for 15 minutes at 20 °C to ensure complete lysis and collection of the cells from constructs. Samples with a 260/280 ratio between 1.6 and 2.0 were used for first-strand complementary DNA (cDNA) synthesis, performed with the iScript cDNA Synthesis kit (Quanta Biosciences, MD, USA). The obtained cDNA was used as template for the amplification of the target genes using the iQSYBR Green Supermix (Bio-Rad), according to manufacturer's instructions. Briefly, 100 ng of the total RNA of each sample were used to generate single-stranded cDNA by random priming with iScript Reverse Transcriptase (RT). A reaction mixture consisting of 4 µL qScript Reaction Mix, 1 µL iScript Reverse Transcriptase (RT), RNA template (100 ng) and nuclease-free water was prepared in a final volume of 20 µL. The single-strand cDNA synthesis occurred by incubating the complete reaction mixture for 5 minutes at 22 °C, followed by 30 minutes at 42 °C and terminated with an incubation of 5 minutes at 85 °C.

IV-8.7.2. Real-time polymerase chain reaction (Real-time PCR)

Real time polymerase chain reaction (PCR) was used in Chapter VIII, as technique for detecting and measuring PCR products of interest [134]. For starting the RNA is reverse-transcripted into a single-strand cDNA chain using a reverse transcriptase polymerase chain reaction (RT-PCR), as described in the section above. Afterwards, the oligonucleotide primers (specific for the target genes) are allowed to anneal to the template cDNA, and with a Taq polymerase starting reaction, a double-strand cDNA is produced. The three steps process of denaturation, primer annealing and extension are repeated in at least 40 cycles to yield PCR products, detected in real-time as the reaction progresses. The real-time detection of PCR products is made by including in the reaction a fluorescent molecule that reports an increase in

the amount of DNA. The measured fluorescence reflects the amount of amplified product in each reaction cycle. The amplification of the target cDNA for real-time PCR quantification was performed using the PerfeCta SYBR Green FastMix kit (Quanta Biosciences, Gaithersberg, MD, USA), according to the manufacturer's instructions. Briefly, 1 µL of single-strand cDNA products, 1 µmol/L of primer forward and reverse, 10 µL PerfeCta SYBR Green FastMix and nuclease-free water, in a final volume of 20 µL, were prepared as reaction mixture. The primers sequence, specific for each gene of interest, are described in **Table IV-2**. Each real-time PCR run was carried out with an initial incubation at 95 °C for 2 minutes, followed by 45 cycles of denaturation (95 °C, 10 seconds), annealing (specific for each gene, 25 seconds) and extension (72 °C, 30 seconds) in a Mastercycle® ep realplex real-time PCR system (Eppendorf, Hamburg, Germany). The transcripts expression data were normalized to the endogenous housekeeping gene Ubiquitin-40S ribosomal protein S27a (RPS27A) and the relative quantification was calculated using as calibrators the results obtained for each target gene at day 1 in basal culture conditions, according to the Livak ($2^{-\Delta\Delta CT}$) method [135]. Briefly, the ΔCt values were obtained by the difference between the Ct values of the target genes and the GAPDH gene. These values were then normalized by subtracting the ΔCt value of the calibrator samples, in order to obtain the ΔΔCt values.

Table IV-2 - Primers list for the studied genes.

Gene	Forward Primer	Reverse Primer
RPS27A	GCTTGCCAGCAAAGATCAGT	GAGGTTGAACCCTCGGATAC
Caspase - 3	GAAATTGTGGAATTGATGCGTGA	CTACAACGATCCCCTCTGAAAAA
MMP-1	GGGGCTTTGATGTACCCTAGC	TGTCACACGCTTTTGGGGTTT
KI67	GCTGGCTCCTGTTCACGTA	CTGGGCTACACTGAGCACC

IV-8.8. Immunocytochemistry

Immunocytochemistry is a detection method used for the visualization of specific antigens in cells, detected by antigen-antibody binding [136]. The principle of this technique consists in the use of specific fluorescent-labeled secondary antibodies that bind to the primary antibodies, visualized under a fluorescence microscope. This procedure involves some preliminary steps after cell culturing, including cell fixation, cell membrane permeabilization, which enables the antibodies to enter into the cells when searching for intracellular antigens, and a blocking step that blocks unspecific bindings of antibodies. These steps are intercalated with washing steps to remove unbound antibodies. All the antibodies used in this thesis can be found in Table IV – 3.

In **Chapter VII**, this technique was applied after each timepoint. The chip was washed with PBS through the lateral channels, and then cells were fixed with 4 % (v/v) paraformaldehyde in PBS for 30 minutes at (RT), and washed again with PBS. Permeabilization of cells was done with 0.1 % (v/v) Triton X-100 (Sigma-Aldrich) for 15 minutes at RT, followed by washing and incubation with blocking solution CAS-Block (Thermo Fisher Scientific) for 30 minutes at 37 °C. Primary antibody for Ki-67 diluted in CAS Block (rabbit, ab833 R&D Systems, 1:100) was subsequently incubated overnight at 4 °C. Samples were washed with PBS and incubated with the secondary antibody Alexa Fluor ® 488 conjugated (1:500, anti-rabbit, R&D Systems) together with high-affinity filamentous 698 actin probe phalloidin conjugated with Alexa Fluor ® 594 (Invitrogen™, 1:80) in CASblock for 3 hours at RT. The samples were then washed with PBS, incubated with 4',6-700 diamidino-2-phenylindole (Invitrogen™, DAPI, 1:100 in PBS) for 10 minutes at RT, and finally washed twice with PBS. The samples were kept in PBS in the dark at 4 °C until image analysis. High magnification images were acquired with Nikon Eclipse Ti-E, using 703 automated acquisition for Z-stack and multicolor-channel.

In **Chapter VIII**, HCT-116 and L929 cells in co-culture were fixed with 4 % (v/v) formalin for 10 minutes and washed with PBS. Cells were permeabilized with 0.1 % (v/v) Triton X-100 in PBS for 5 minutes and blocked with 3 % (v/v) BSA in PBS for 30 minutes. Immunolabeling was performed using a Rabbit anti-human monoclonal antibody against 67 kDa LR (Abcam, 1:200) as primary antibody, prepared in PBS 1 % (wt%.) BSA and incubated overnight at 4 °C. The coverslips were incubated for 1 hour at RT with the respective secondary fluorochrome-conjugated antibodies, anti-rabbit/mouse IgG (Invitrogen, dilution 1:1000), with Phalloidin

(1:200) for 30 minutes (F-actin filaments) (WVR, Portugal) and with 4,6-Diamidino-2-phenyindole, dilactate (DAPI 1:1000) (WVR, Portugal) for nuclei staining for 15 minutes. Immunofluorescence was observed under transmitted and fluorescence microscopy (Zeiss, Germany) (LR in green: ex/em 488/517; Phalloidin in red: ex/em 594/618; DAPI in blue: ex/em 358/461).

Table IV-3 – Antibodies list used in immunocytochemistry.

Antibody	Type	Reference	Host	Dilution	Reactivity
Ki-67	Primary	ab833	Rabbit	1:100	Human, Mouse, Rat
67kDa Laminin receptor	Primary	ab133645	Rabbit	1:500	Human, Mouse, Rat
Antibody to rabbit IgG (Alexa Fluor 488)	Secondary	IC1051G	Donkey	1:500	Human
Antibody to rabbit IgG (Alex Fluor 488)	Secondary	A21206	Donkey	1:1000	Human

IV-9. STATISTICAL ANALYSIS

All quantitative data are presented as mean ± standard deviation (SD). Statistical analysis was performed using Graph Pad Prism 6.00 software (San Diego, USA). Statistical significances ($*p \leq 0.05$, $**p \leq 0.01$ and $***p \leq 0.001$) were determined using specific statistical tests described in the subsection of materials and methods in the different chapters.

In **Chapter V**, all the performed tests were conducted in triplicate and the obtained data points are presented as mean ± standard deviation (SD). The nonparametric Mann–Whitney test was used to compare two groups and the Tukey's test was used to compare results of dendrimers' cytotoxicity after normalization. Statistical significance was defined as $p<0.05$ for a 95% CI. All measurements were taken in triplicate.

In **Chapter VI,** the nonparametric Mann-Whitney test was used to compare two groups, whereas comparison between more than two groups was performed using the Kruskal-Wallis test followed by Dunn's comparison test. A value of $p<0.05$ was considered statistically significant. All measurements were taken in triplicate.

In **Chapter VII**, the nonparametric Mann-Whitney test was used to compare two groups. A value of $p<0.05$ was considered statistically significant. For multiple comparisons, the parametric test one-way analysis of variance (ANOVA) was used, with $P<0.05$ considered statistically significant. All measurements were taken in triplicate.

In **Chapter VIII,** the non-parametric Mann–Whitney test was used to compare two groups, whereas comparison between more than two groups was performed using the Kruskal–Wallis test followed by Dunn's comparison test. A value of $p<0.05$ was considered statistically significant**.** All measurements were taken in triplicate.

IV-10. REFERENCES

1. O'Brien, F.J., *Biomaterials & scaffolds for tissue engineering.* Materials Today, 2011. **14**(3): p. 88-95.
2. Tolesa, L.D., B.S. Gupta, and M.-J. Lee, *Chitin and chitosan production from shrimp shells using ammonium-based ionic liquids.* International Journal of Biological Macromolecules, 2019. **130**: p. 818-826.
3. Philibert, T., B.H. Lee, and N. Fabien, *Current Status and New Perspectives on Chitin and Chitosan as Functional Biopolymers.* Appl Biochem Biotechnol, 2017. **181**(4): p. 1314-1337.
4. Fiamingo, A. and S.P. Campana-Filho, *Structure, morphology and properties of genipin-crosslinked carboxymethylchitosan porous membranes.* Carbohydr Polym, 2016. **143**: p. 155-63.
5. Khattak, S., et al., *Applications of cellulose and chitin/chitosan derivatives and composites as antibacterial materials: current state and perspectives.* Applied Microbiology and Biotechnology, 2019. **103**(5): p. 1989-2006.
6. de Abreu, F.R. and S.P. Campana-Filho, *Characteristics and properties of carboxymethylchitosan.* Carbohydrate Polymers, 2009. **75**(2): p. 214-221.
7. Song, Q., et al., *Synthesis and property studies of N-carboxymethyl chitosan.* Journal of Applied Polymer Science, 2011. **119**(6): p. 3282-3285.
8. Zheng, M., et al., *Synthesis, characterization and biological safety of O-carboxymethyl chitosan used to treat Sarcoma 180 tumor.* Carbohydrate Polymers, 2011. **86**(1): p. 231-238.
9. Ren, C., D. Zhao, and L. Zhu, *Use of N,O-carboxymethyl chitosan to prevent postsurgical adhesions in a rabbit double uterine horn model: a randomized controlled design.* Sci China Life Sci, 2016. **59**(5): p. 504-9.

10. Upadhyaya, L., et al., *The implications of recent advances in carboxymethyl chitosan based targeted drug delivery and tissue engineering applications.* Journal of Controlled Release, 2014. **186**: p. 54-87.
11. Chen, X.-G. and H.-J. Park, *Chemical characteristics of O-carboxymethyl chitosans related to the preparation conditions.* Carbohydrate Polymers, 2003. **53**(4): p. 355-359.
12. Kundu, B., et al., *Silk fibroin biomaterials for tissue regenerations.* Advanced Drug Delivery Reviews, 2013. **65**(4): p. 457-470.
13. Yang, M., et al., *Preparation of porous scaffolds from silk fibroin extracted from the silk gland of Bombyx mori (B. mori).* Int J Mol Sci, 2012. **13**(6): p. 7762-75.
14. Dinjaski, N. and D.L. Kaplan, *Recombinant protein blends: silk beyond natural design.* Curr Opin Biotechnol, 2016. **39**: p. 1-7.
15. Fu, C., Z. Shao, and V. Fritz, *Animal silks: their structures, properties and artificial production.* Chemical Communications, 2009(43): p. 6515-6529.
16. Omenetto, F.G. and D.L. Kaplan, *New opportunities for an ancient material.* Science, 2010. **329**(5991): p. 528-31.
17. Ribeiro, V.P., et al., *Rapidly responsive silk fibroin hydrogels as an artificial matrix for the programmed tumor cells death.* PLOS ONE, 2018. **13**(4): p. e0194441.
18. Vollrath, F., D. Porter, and C. Dicko, *5 - The structure of silk*, in *Handbook of Textile Fibre Structure*, S.J. Eichhorn, et al., Editors. 2009, Woodhead Publishing. p. 146-198.
19. Koh, L.-D., et al., *Structures, mechanical properties and applications of silk fibroin materials.* Progress in Polymer Science, 2015. **46**: p. 86-110.
20. Altman, G.H., et al., *Silk-based biomaterials.* Biomaterials, 2003. **24**(3): p. 401-16.
21. Tao, H., et al., *Metamaterial silk composites at terahertz frequencies.* Adv Mater, 2010. **22**(32): p. 3527-31.
22. Castrillón Martínez, D.C., et al., *Characterization of sericin obtained from cocoons and silk yarns.* Procedia Engineering, 2017. **200**: p. 377-383.
23. Qi, Y., et al., *A Review of Structure Construction of Silk Fibroin Biomaterials from Single Structures to Multi-Level Structures.* Int J Mol Sci, 2017. **18**(3).
24. Zeng, C., et al., *Silk fibroin porous scaffolds for nucleus pulposus tissue engineering.* Mater Sci Eng C Mater Biol Appl, 2014. **37**: p. 232-40.
25. Panda, D., et al., *Synthesis and viscoelastic characterization of microstructurally aligned Silk fibroin sponges.* J Mech Behav Biomed Mater, 2017. **71**: p. 362-371.
26. Jackman, S.L., et al., *Silk Fibroin Films Facilitate Single-Step Targeted Expression of Optogenetic Proteins.* Cell Rep, 2018. **22**(12): p. 3351-3361.
27. Carvalho, C.R., et al., *Tunable Enzymatically Cross-Linked Silk Fibroin Tubular Conduits for Guided Tissue Regeneration.* Adv Healthc Mater, 2018. **7**(17): p. e1800186.
28. Fang, Y., L. Xu, and M. Wang, *High-Throughput Preparation of Silk Fibroin Nanofibers by Modified Bubble-Electrospinning.* Nanomaterials (Basel, Switzerland), 2018. **8**(7): p. 471.
29. Zhang, X., et al., *Silk fibroin microfibers and chitosan modified poly (glycerol sebacate) composite scaffolds for skin tissue engineering.* Polymer Testing, 2017. **62**: p. 88-95.
30. Ribeiro, V.P., et al., *Rapidly responsive silk fibroin hydrogels as an artificial matrix for the programmed tumor cells death.* PloS one, 2018. **13**(4): p. e0194441-e0194441.
31. Ribeiro, V.P., et al., *Silk-based anisotropical 3D biotextiles for bone regeneration.* Biomaterials, 2017. **123**: p. 92-106.
32. Abdel-Fattah, W.I., N. Atwa, and G.W. Ali, *Influence of the protocol of fibroin extraction on the antibiotic activities of the constructed composites.* Progress in biomaterials, 2015. **4**(2-4): p. 77-88.

33. Chen, X., et al., *Regenerated Bombyx silk solutions studied with rheometry and FTIR.* Polymer, 2001. **42**(25): p. 09969-09974.
34. Pawcenis, D., et al., *Size exclusion chromatography for analyses of fibroin in silk: optimization of sampling and separation conditions.* Applied Physics A, 2014. **114**(2): p. 301-308.
35. Karageorgiou, V., et al., *Porous silk fibroin 3-D scaffolds for delivery of bone morphogenetic protein-2 in vitro and in vivo.* Journal of Biomedical Materials Research Part A, 2006. **78A**(2): p. 324-334.
36. Hughes, C.S., L.M. Postovit, and G.A. Lajoie, *Matrigel: a complex protein mixture required for optimal growth of cell culture.* Proteomics, 2010. **10**(9): p. 1886-90.
37. Orkin, R.W., et al., *A murine tumor producing a matrix of basement membrane.* The Journal of experimental medicine, 1977. **145**(1): p. 204-220.
38. Kleinman, H.K. and G.R. Martin, *Matrigel: basement membrane matrix with biological activity.* Semin Cancer Biol, 2005. **15**(5): p. 378-86.
39. Hughes, C.S., L.M. Postovit, and G.A. Lajoie, *Matrigel: A complex protein mixture required for optimal growth of cell culture.* PROTEOMICS, 2010. **10**(9): p. 1886-1890.
40. Kleinman, H.K., R.J. Klebe, and G.R. Martin, *Role of collagenous matrices in the adhesion and growth of cells.* The Journal of cell biology, 1981. **88**(3): p. 473-485.
41. Erickson, A.C. and J.R. Couchman, *Still more complexity in mammalian basement membranes.* J Histochem Cytochem, 2000. **48**(10): p. 1291-306.
42. Tibbitt, M.W. and K.S. Anseth, *Hydrogels as extracellular matrix mimics for 3D cell culture.* Biotechnology and bioengineering, 2009. **103**(4): p. 655-663.
43. Frantz, C., K.M. Stewart, and V.M. Weaver, *The extracellular matrix at a glance.* Journal of cell science, 2010. **123**(Pt 24): p. 4195-4200.
44. Justus, C.R., et al., *In vitro cell migration and invasion assays.* Journal of visualized experiments : JoVE, 2014(88): p. 51046.
45. Yin, G.N., et al., *Matrigel-based sprouting endothelial cell culture system from mouse corpus cavernosum is potentially useful for the study of endothelial and erectile dysfunction related to high-glucose exposure.* J Sex Med, 2012. **9**(7): p. 1760-72.
46. DeCicco-Skinner, K.L., et al., *Endothelial cell tube formation assay for the in vitro study of angiogenesis.* Journal of visualized experiments : JoVE, 2014(91): p. e51312-e51312.
47. Uemura, M., et al., *Matrigel supports survival and neuronal differentiation of grafted embryonic stem cell-derived neural precursor cells.* J Neurosci Res, 2010. **88**(3): p. 542-51.
48. Tahergorabi, Z. and M. Khazaei, *A review on angiogenesis and its assays.* Iranian journal of basic medical sciences, 2012. **15**(6): p. 1110-1126.
49. Li, L., et al., *How to Improve the Survival of Transplanted Mesenchymal Stem Cell in Ischemic Heart?* Stem cells international, 2016. **2016**: p. 9682757-9682757.
50. Albini, A., *Extracellular Matrix Invasion in Metastases and Angiogenesis: Commentary on the Matrigel "Chemoinvasion Assay".* Cancer Research, 2016. **76**(16): p. 4595.
51. Anguiano, M., et al., *Characterization of three-dimensional cancer cell migration in mixed collagen-Matrigel scaffolds using microfluidics and image analysis.* PloS one, 2017. **12**(2): p. e0171417-e0171417.
52. Wolf, M.P., G.B. Salieb-Beugelaar, and P. Hunziker, *PDMS with designer functionalities—Properties, modifications strategies, and applications.* Progress in Polymer Science, 2018. **83**: p. 97-134.
53. Dinh, T.-H.-N., et al., *Mechanical Characterization of PDMS Films for the Optimization of Polymer Based Flexible Capacitive Pressure Microsensors.* Journal of Sensors, 2017. **2017**: p. 9.

54. Larson, B.J., et al., *Long-term reduction in poly(dimethylsiloxane) surface hydrophobicity via cold-plasma treatments.* Langmuir, 2013. **29**(42): p. 12990-6.
55. Xu, B.-Y., et al., *One step high quality poly(dimethylsiloxane)-hydrocarbon plastics bonding.* Biomicrofluidics, 2012. **6**(1): p. 16507-165078.
56. Kim, B., K.P. ET, and I. Papautsky, *Long-term stability of plasma oxidized PDMS surfaces.* Conf Proc IEEE Eng Med Biol Soc, 2004. **7**: p. 5013-6.
57. Piruska, A., et al., *The autofluorescence of plastic materials and chips measured under laser irradiation.* Lab Chip, 2005. **5**(12): p. 1348-54.
58. Peterson, S.L., et al., *Poly(dimethylsiloxane) thin films as biocompatible coatings for microfluidic devices: cell culture and flow studies with glial cells.* J Biomed Mater Res A, 2005. **72**(1): p. 10-8.
59. Zhou, J., A.V. Ellis, and N.H. Voelcker, *Recent developments in PDMS surface modification for microfluidic devices.* Electrophoresis, 2010. **31**(1): p. 2-16.
60. Kikkawa, Y., et al., *Laminin-111-derived peptides and cancer.* Cell adhesion & migration, 2013. **7**(1): p. 150-256.
61. Fridman, R., et al., *Enhanced tumor growth of both primary and established human and murine tumor cells in athymic mice after coinjection with Matrigel.* J Natl Cancer Inst, 1991. **83**(11): p. 769-74.
62. Kawasaki, K., et al., *Amino acids and peptides. XIV. Laminin related peptides and their inhibitory effect on experimental metastasis formation.* Biochem Biophys Res Commun, 1991. **174**(3): p. 1159-62.
63. Yoshida, N., et al., *The laminin-derived peptide YIGSR (Tyr-Ile-Gly-Ser-Arg) inhibits human pre-B leukaemic cell growth and dissemination to organs in SCID mice.* British journal of cancer, 1999. **80**(12): p. 1898-1904.
64. Khalfaoui, T., et al., *Laminin receptor 37/67LR regulates adhesion and proliferation of normal human intestinal epithelial cells.* PLoS One, 2013. **8**(8): p. e74337.
65. Kumazoe, M., et al., *67-kDa laminin receptor increases cGMP to induce cancer-selective apoptosis.* J Clin Invest, 2013. **123**(2): p. 787-99.
66. Vacca, A., et al., *Melanocyte tumor progression is associated with changes in angiogenesis and expression of the 67-kilodalton laminin receptor.* Cancer, 1993. **72**(2): p. 455-61.
67. Shi, Y.E., et al., *Expression of 67 kDa laminin receptor in human breast cancer cells: regulation by progestins.* Clin Exp Metastasis, 1993. **11**(3): p. 251-61.
68. Vince, D.G., J.A. Hunt, and D.F. Williams, *Quantitative assessment of the tissue response to implanted biomaterials.* Biomaterials, 1991. **12**(8): p. 731-6.
69. Nerem, R.M. and S.C. Schutte, *Chapter 2 - The Challenge of Imitating Nature*, in *Principles of Tissue Engineering (Fourth Edition)*, R. Lanza, R. Langer, and J. Vacanti, Editors. 2014, Academic Press: Boston. p. 9-24.
70. Meek, M.F., et al., *In vitro degradation and biocompatibility of poly(DL-lactide-epsilon-caprolactone) nerve guides.* J Biomed Mater Res A, 2004. **68**(1): p. 43-51.
71. Abbasi, E., et al., *Dendrimers: synthesis, applications, and properties.* Nanoscale research letters, 2014. **9**(1): p. 247-247.
72. Tomalia, D.A. and J.M.J. Fréchet, *Discovery of dendrimers and dendritic polymers: A brief historical perspective*.* Journal of Polymer Science Part A: Polymer Chemistry, 2002. **40**(16): p. 2719-2728.

73. Palmerston Mendes, L., J. Pan, and V.P. Torchilin, *Dendrimers as Nanocarriers for Nucleic Acid and Drug Delivery in Cancer Therapy.* Molecules (Basel, Switzerland), 2017. **22**(9): p. 1401.
74. Oliveira, J.M., et al., *Dendrimers and derivatives as a potential therapeutic tool in regenerative medicine strategies—A review.* Progress in Polymer Science, 2010. **35**(9): p. 1163-1194.
75. Oliveira, J.M., et al., *The osteogenic differentiation of rat bone marrow stromal cells cultured with dexamethasone-loaded carboxymethylchitosan/poly(amidoamine) dendrimer nanoparticles.* Biomaterials, 2009. **30**(5): p. 804-13.
76. Xu, L., H. Zhang, and Y. Wu, *Dendrimer advances for the central nervous system delivery of therapeutics.* ACS Chem Neurosci, 2014. **5**(1): p. 2-13.
77. Dufes, C., I.F. Uchegbu, and A.G. Schatzlein, *Dendrimers in gene delivery.* Adv Drug Deliv Rev, 2005. **57**(15): p. 2177-202.
78. Sk, U.H. and C. Kojima, *Dendrimers for theranostic applications.* Biomol Concepts, 2015. **6**(3): p. 205-17.
79. Li, D.-Y., et al., *On-surface synthesis of planar dendrimers via divergent cross-coupling reaction.* Nature Communications, 2019. **10**(1): p. 2414.
80. Hawker, C. and J.M.J. Fréchet, *A new convergent approach to monodisperse dendritic macromolecules.* Journal of the Chemical Society, Chemical Communications, 1990(15): p. 1010-1013.
81. Jevprasesphant, R., et al., *Engineering of Dendrimer Surfaces to Enhance Transepithelial Transport and Reduce Cytotoxicity.* Pharmaceutical Research, 2003. **20**(10): p. 1543-1550.
82. Han, W., et al., *Synthesis of novel poly(ester amine) dendrimers by Michael addition and acrylate esterification.* Designed Monomers and Polymers, 2013. **16**(1): p. 67-71.
83. Tam, R.Y., L.J. Smith, and M.S. Shoichet, *Engineering Cellular Microenvironments with Photo- and Enzymatically Responsive Hydrogels: Toward Biomimetic 3D Cell Culture Models.* 2017. **50**(4): p. 703-713.
84. Li, Y. and E. Kumacheva, *Hydrogel microenvironments for cancer spheroid growth and drug screening.* Science advances, 2018. **4**(4): p. eaas8998-eaas8998.
85. Geckil, H., et al., *Engineering hydrogels as extracellular matrix mimics.* Nanomedicine (London, England), 2010. **5**(3): p. 469-484.
86. Hoffman, A.S., *Hydrogels for biomedical applications.* Advanced drug delivery reviews, 2012. **64**: p. 18-23.
87. Singh, N.K. and D.S. Lee, *In situ gelling pH- and temperature-sensitive biodegradable block copolymer hydrogels for drug delivery.* Journal of Controlled Release, 2014. **193**: p. 214-227.
88. Teixeira, L.S.M., et al., *Enzyme-catalyzed crosslinkable hydrogels: emerging strategies for tissue engineering.* Biomaterials, 2012. **33**(5): p. 1281-1290.
89. Yan, L.P., et al., *Core - shell silk hydrogels with spatially tuned conformations as drug - delivery system.* Journal of tissue engineering and regenerative medicine, 2016.
90. Yan, L.P., et al., *Tumor Growth Suppression Induced by Biomimetic Silk Fibroin Hydrogels.* Scientific Reports, 2016. **6**: p. 31037.
91. Yucel, T., P. Cebe, and D.L. Kaplan, *Vortex-induced injectable silk fibroin hydrogels.* Biophysical journal, 2009. **97**(7): p. 2044-2050.
92. Fini, M., et al., *The healing of confined critical size cancellous defects in the presence of silk fibroin hydrogel.* Biomaterials, 2005. **26**(17): p. 3527-3536.

93. Wang, X., et al., *Sonication-induced gelation of silk fibroin for cell encapsulation.* Biomaterials, 2008. **29**(8): p. 1054-1064.
94. Yan, L.-P., et al., *Macro/microporous silk fibroin scaffolds with potential for articular cartilage and meniscus tissue engineering applications.* Acta biomaterialia, 2012. **8**(1): p. 289-301.
95. Liu, B., et al., *Silk structure and degradation.* Colloids and Surfaces B: Biointerfaces, 2015. **131**: p. 122-128.
96. Sofia, S., et al., *Functionalized silk-based biomaterials for bone formation.* Journal of Biomedical Materials Research, 2001. **54**(1): p. 139-148.
97. Jin, H.-J. and D.L. Kaplan, *Mechanism of silk processing in insects and spiders.* Nature, 2003. **424**(6952): p. 1057-1061.
98. Olanrewaju, A., et al., *Capillary microfluidics in microchannels: from microfluidic networks to capillaric circuits.* Lab Chip, 2018. **18**(16): p. 2323-2347.
99. Huh, D., et al., *Microfabrication of human organs-on-chips.* Nat Protoc, 2013. **8**(11): p. 2135-57.
100. King, M.C., *Chapter 2 - Principles of Optical Lithography*, in *VLSI Electronics Microstructure Science*, N.G. Einspruch, Editor. 1981, Elsevier. p. 41-81.
101. Brower, K., A.K. White, and P.M. Fordyce, *Multi-step Variable Height Photolithography for Valved Multilayer Microfluidic Devices.* J Vis Exp, 2017(119).
102. Liston, E.M., L. Martinu, and M.R. Wertheimer, *Plasma surface modification of polymers for improved adhesion: a critical review.* Journal of Adhesion Science and Technology, 1993. **7**(10): p. 1091-1127.
103. Qin, D., Y. Xia, and G.M. Whitesides, *Soft lithography for micro- and nanoscale patterning.* Nature Protocols, 2010. **5**: p. 491.
104. Maghsoudi, K., et al., *Micro-nanostructured polymer surfaces using injection molding: A review.* Materials Today Communications, 2017. **13**: p. 126-143.
105. Pugieux, C., et al., *Chapter Twenty-Four - Spindle Assembly on Immobilized Chromatin Micropatterns*, in *Methods in Enzymology*, R.D. Vale, Editor. 2014, Academic Press. p. 435-448.
106. Al-Abboodi, A., et al. *Microfluidic chip containing porous gradient for chemotaxis study*. 2011.
107. Saadi, W., et al., *A parallel-gradient microfluidic chamber for quantitative analysis of breast cancer cell chemotaxis.* Biomed Microdevices, 2006. **8**(2): p. 109-18.
108. Deneke, V.E. and S. Di Talia, *Chemical waves in cell and developmental biology.* The Journal of Cell Biology, 2018. **217**(4): p. 1193.
109. Damiati, S., et al., *Microfluidic Devices for Drug Delivery Systems and Drug Screening.* Genes, 2018. **9**(2): p. 103.
110. Weltin, A., et al., *Cell culture monitoring for drug screening and cancer research: a transparent, microfluidic, multi-sensor microsystem.* Lab Chip, 2014. **14**(1): p. 138-46.
111. Hayes, T.L. and R.F.W. Pease, *The Scanning Electron Microscope: Principles and Applications in Biology and Medicine*, in *Advances in Biological and Medical Physics*, J.H. Lawrence and J.W. Gofman, Editors. 1968, Elsevier. p. 85-137.
112. Ismail, A.A., F.R. van de Voort, and J. Sedman, *Chapter 4 Fourier transform infrared spectroscopy: Principles and applications*, in *Techniques and Instrumentation in Analytical Chemistry*, J.R.J. Paré and J.M.R. Bélanger, Editors. 1997, Elsevier. p. 93-139.
113. Winey, M., et al., *Conventional transmission electron microscopy.* Mol Biol Cell, 2014. **25**(3): p. 319-23.

114. Marrese, M., V. Guarino, and L. Ambrosio, *Atomic Force Microscopy: A Powerful Tool to Address Scaffold Design in Tissue Engineering.* Journal of functional biomaterials, 2017. **8**(1): p. 7.
115. *A Practical Introduction to Differential Scanning Calorimetry*, in *Principles and Applications of Thermal Analysis*.
116. Bhattacharjee, S., *DLS and zeta potential – What they are and what they are not?* Journal of Controlled Release, 2016. **235**: p. 337-351.
117. Hepokur, C., et al., *Silver nanoparticle/capecitabine for breast cancer cell treatment.* Toxicology in Vitro, 2019. **61**: p. 104600.
118. Nejadnik, M.R. and W. Jiskoot, *Measurement of the average mass of proteins adsorbed to a nanoparticle by using a suspended microchannel resonator.* J Pharm Sci, 2015. **104**(2): p. 698-704.
119. Barnes, H.A., J.F. Hutton, and K. Walters, *An introduction to rheology*. Vol. 3. 1989: Elsevier.
120. Kaur, G. and J.M. Dufour, *Cell lines: Valuable tools or useless artifacts.* Spermatogenesis, 2012. **2**(1): p. 1-5.
121. Entschladen, F., et al., *Tumour-cell migration, invasion, and metastasis: navigation by neurotransmitters.* Lancet Oncol, 2004. **5**(4): p. 254-8.
122. Gupta, G.P. and J. Massagué, *Cancer Metastasis: Building a Framework.* Cell, 2006. **127**(4): p. 679-695.
123. Boyden, S., *The chemotactic effect of mixtures of antibody and antigen on polymorphonuclear leucocytes.* J Exp Med, 1962. **115**: p. 453-66.
124. Chen, H.C., *Boyden chamber assay.* Methods Mol Biol, 2005. **294**: p. 15-22.
125. Nishida, N., et al., *Angiogenesis in cancer.* Vascular health and risk management, 2006. **2**(3): p. 213-219.
126. Yeon, J.H., et al., *In vitro formation and characterization of a perfusable three-dimensional tubular capillary network in microfluidic devices.* Lab Chip, 2012. **12**(16): p. 2815-22.
127. Weis, S., et al., *Endothelial barrier disruption by VEGF-mediated Src activity potentiates tumor cell extravasation and metastasis.* J Cell Biol, 2004. **167**(2): p. 223-9.
128. Rampersad, S.N., *Multiple applications of Alamar Blue as an indicator of metabolic function and cellular health in cell viability bioassays.* Sensors (Basel, Switzerland), 2012. **12**(9): p. 12347-12360.
129. O'brien, J., et al., *Investigation of the Alamar Blue (resazurin) fluorescent dye for the assessment of mammalian cell cytotoxicity.* The FEBS Journal, 2000. **267**(17): p. 5421-5426.
130. Crouch, S., et al., *The use of ATP bioluminescence as a measure of cell proliferation and cytotoxicity.* Journal of immunological methods, 1993. **160**(1): p. 81-88.
131. Adan, A., et al., *Flow cytometry: basic principles and applications.* Crit Rev Biotechnol, 2017. **37**(2): p. 163-176.
132. Kaneshiro, E.S., et al., *Reliability of calcein acetoxy methyl ester and ethidium homodimer or propidium iodide for viability assessment of microbes.* Journal of Microbiological Methods, 1993. **17**(1): p. 1-16.
133. Kim, J.-H., et al., *Comparison of three different kits for extraction of high-quality RNA from frozen blood.* Springerplus, 2014. **3**(1): p. 76.
134. Arya, M., et al., *Basic principles of real-time quantitative PCR.* Expert review of molecular diagnostics, 2005. **5**(2): p. 209-219.

135. Livak, K.J. and T.D. Schmittgen, *Analysis of relative gene expression data using real-time quantitative PCR and the 2− Δ Δ CT method.* methods, 2001. **25**(4): p. 402-408.

136. Maity, B., D. Sheff, and R.A. Fisher, *Immunostaining: detection of signaling protein location in tissues, cells and subcellular compartments.* Methods Cell Biol, 2013. **113**: p. 81-105.

SECTION 3

EXPERIMENTAL SECTION

Chapter V

A Semiautomated Microfluidic Platform for Real-time Investigation of Nanoparticles' Cellular Uptake and Cancer Cell's Tracking

Chapter V

A Semiautomated Microfluidic Platform for Real time Investigation of Nanoparticles' Cellular Uptake and Cancer Cell's Tracking[1]

ABSTRACT

Aim: Develop a platform composed of labeled dendrimer nanoparticles (NPs) and a microfluidic device for real-time monitoring of cancer cells fate. **Materials & methods:** Carboxymethylchitosan/poly(amidoamine) dendrimer NPs were labeled with fluorescein-5(6)-isothiocyanate and characterized using different physicochemical techniques. After, HeLa, HCT-116 and U87MG were cultured in the presence of NPs, and cell viability and internalization efficiency in static (standard culture) and dynamic (microfluidic culture) conditions were investigated. **Results:** Cancer cells cultured with NPs in dynamic conditions were viable and presented higher internalization levels as compared with static 2D cultures. **Conclusion:** This work demonstrated that the proposed microfluidic-based platform allows real-time monitoring, which upon more studies, namely, the assessment of an anticancer drug release effect could be used for cancer theranostics.

Keywords: Cell tracking; Circulating tumor cells; Microfluidics; Nanoparticles; Theranostics.

[1]This chapter is based on the following publication:

M.R. Carvalho, F. R. Maia, J. Silva-Correia, B. M. Costa, R. L. Reis, J. M. Oliveira. "A semi-automated microfluidic platform for real-time tracking of cancer cells and investigation of nanoparticles cellular uptake". Nanomedicine, 2016, 2:581-596. doi: 10.2217/nnm-2016-0344.

V-1. GRAPHICAL ABSTRACT

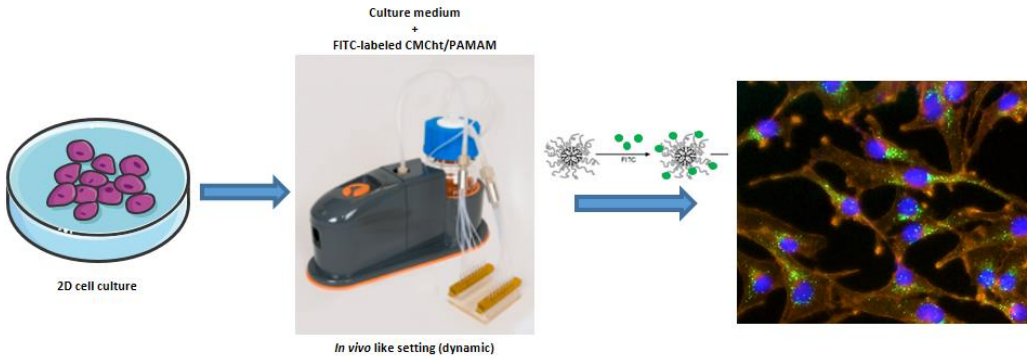

V-2. INTRODUCTION

Cancer is a major cause of mortality, being directly responsible for 1.665.540 new cancer cases and 585.720 cancer deaths in the United States in 2014 [1]. Its incidence is estimated to increase up to 13 million by 2030, worldwide [2]. The metastasis process, where circulating tumor cells (CTCs) migrate and colonize distant organs, is responsible for about 90 % of deaths [3]. Thus, CTCs have been highly studied and new information has arisen regarding its fate and subsequent host interaction, the importance of shear stress and real time visualization in understanding these processes [4]. New strategies for cancer diagnosis and treatment have become more sophisticated and high throughput processes have been applied due to forward-thinking nanotechnology techniques, such as the use of nanoparticles (NP). In fact, NP can be modified to target specific cells, as CTCs, and induce specific cancer cell death [5]. Additionally, these nanometer size structures are very attractive for health-related applications, as they can be rationally designed taking advantage of the cut-off pore size of the vasculature, *i.e.*, enhanced permeation and retention (EPR) effect, allowing to be used for imaging, diagnosis and therapy, holding great promise in the cancer field [6, 7]. The possibility of being designed on demand is one of the major advantages of such nanotools. In this reasoning, they can be used both in the preparation of cell-tracking tools (such as migration patterns and response to physical and

chemical factors) and the visualization of delivery and distribution of drugs in real time [8]. Recently, imaging tools such as microscopy images obtained in static 2D conditions have been used to determine abnormal cellular distribution patterns [9], which could indicate loss of adherence, a crucial step for cancer progression. However useful, 2D culture conditions do not satisfyingly emulate the *in vivo* scenario, and new information on cancer cell behavior could be exposed under a more relevant physiological environment [10].

Microfluidic technologies have been proposed as improved *in vitro* tools, once they can be projected to display complex structures within dynamic environments [11]. A microfluidic device, such as Vena8™ biochip, is able to realize functions that are not easily imaginable in conventional two-dimensional (2D) biological analysis, such as highly parallel, sophisticated high-throughput analysis and single-cell analysis, in terms of morphology, secretome and the influence of growth factors in a well-defined manner that could be beneficial in cancer research [12, 13]. Its microfluidic channels on a micrometer and sub-micrometer scale are made to mimic human capillaries and allow controlling the flow forces, the mixture of solutions, and the supply of nutrients and biochemical agents in gradients. Moreover, we hypothesized that this model with particular *in vivo* like features such as the presence of shear stress, flow and confinement, will shed light on what happens when nanoparticles are injected *in vivo* and disclose different interactions from those observed in traditional 2D *in vitro* assays. Other advantage of microfluidics is the inherent miniaturization with a reduction in cell density and amount of material needed for an experiment, which can increase efficiency when working with primary cells, while testing different concentrations of extracts or drugs can be performed simultaneously [14, 15]. In fact, the combination of microfluidics with tissue engineering to study cancer has been recently reported with very promising results in angiogenesis and metastasis [16, 17]. These two mechanisms are essential to understand the complex development of cancer [18, 19], by providing new data on crosstalk among several cell types.

The association of nanoparticles tracking systems with microfluidics holds great promise as an accurate platform for the *in vitro* validation of new therapies, and consequently expediting the translation of those therapies into the clinic. In fact, a major problem that has been hampering this translation is the lack of proper *in vitro* models capable of emulating the *in vivo* environment, including all the barriers naturally present, such as the blood flow and the interactions with the

endothelium and with cells, which are not usually taken in consideration, and the absence of fluorescent-labeled drug delivery systems that prevents the monitoring of therapy efficiency [6, 20, 21]. Additionally, little is known about nanoparticles effect when submitted to a physiologically-relevant environment similar to the one that cells are surrounded of, further highlighting limitations of the conventional 2D culture conditions. In the work of Fede and colleagues, it is possible to observe the effect of directional flow, as observed in blood vessels, in the cellular uptake of gold nanoparticles, and their non-cytotoxicity as compared with cells cultured under static conditions [22]. To address the aforementioned problems, we hypothesized that the use of labeled nanoparticles together with a microfluidic platform is suitable for cancer cell and drug delivery system tracking in real time, which better mimics the *in vivo* microenvironment than traditional static cultures. This platform works as a transitional model for the assessment of dynamic nanoparticle internalization and cancer cell tracking, which will be useful in subsequent studies with 3D models. The labeled nanoparticles were achieved by grafting the fluorescent label probe Fluorescein-5(6)-isothiocyanate (FITC) to poly(amidoamine)/carboxymethilchytosan (CMCht/PAMAM) dendrimer nanoparticles. It is noteworthy that dendrimer nanoparticles can be easily labeled with different fluorochromes, depending on the need for combining different co-stainings. In this work, surface modified dendrimers were used due to its remarkable physicochemical and biological properties, and have great potential to be used in fundamental cell biology [23-25]. Moreover, since the biological properties of poly(amidoamine) dendrimers can be tuned with respect to their terminal functionality, it is important to investigate the biocompatibility of any new classes of derivatives of PAMAM dendrimers proposed for biological applications.

The modified nanoparticles were characterized with several physicochemical techniques, such as dynamic light scattering (DLS), proton nuclear magnetic resonance (H^1 NMR), transmission electron microcopy (TEM), atomic force microcopy (AFM) and differential scanning calorimetry (DSC). Cytotoxicity was screened using three different human cancer cell lines: U87MG (glioblastoma); HeLa (cervical cancer) and HCT-116 (colon cancer) by means of performing a tetrazolium reduction (MTS) assay. Proliferation studies were carried out using a DNA quantification assay. Cancer cell lines were exposed to different concentrations of CMCht/PAMAM dendrimer nanoparticles over a period of 3 days in conventional 2D standard

conditions. After finding the highest non-cytotoxic concentration, the internalization efficiency was assessed, both qualitatively and quantitatively (using fluorescence microscopy and flow cytometry, respectively), in static 2D cultures and dynamic conditions using Vena8™ biochips.

V-3. MATERIALS AND METHODS

V-3.1. Synthesis of the CMCht/PAMAM dendrimer nanoparticles

CMCht with a degree of deacetylation of 80 % and degree of substitution of 47 % was synthesized by a chemical modification route of chitin (Sigma, Germany) as described by Chen *et al.*[26].

Starburst PAMAM carboxylic acid terminated dendrimers, hereafter designated as PAMAM-CT (generation 1.5, 20 %wt. methanolic solution) with an ethylenediamine core were purchased (Sigma-Aldrich). CMCht/PAMAM dendrimer nanoparticles were prepared in a step-wise manner as follows: i) increase the generation of the PAMAM-CT (G1.5), ii) obtain a PAMAM methyl ester terminated dendrimer, iii) react PAMAM and CMCht (the reaction occurs by a condensation reaction between the methyl ester and amine groups), and iv) convert methyl ester groups, that do not react, into carboxylic groups in the CMCht/PAMAM dendrimer, followed by precipitation. First, the increase of the dendrimers' generation was carried out. For that, an appropriate volume of PAMAM-CT (G1.5) in methanol was transferred to a volumetric flask and the solvent evaporated off under nitrogen gas, and the traces dried under vacuum in order to completely remove the methanol. The starting compound was re-dissolved in ultra-pure water to give a final concentration of 10 mg/mL and the pH was adjusted to 6.5 with dilute hydrochloric acid solution (Riedel de-Haen, Germany). 1-Ethyl-(3-dimethylaminopropyl) carbodiimide hydrochloride (EDC, Fluka) was then added to the solution at a molar ratio sufficient to modify the carboxylate residue of the dendrimers, and the solution was kept under agitation for 30 minutes at room temperature (RT). Ethylenediamine (EDA, Sigma, Germany) was added to the solution at a molar ratio equal to that of EDC and left to react for at least 4 hours. After this period the excess of EDC was removed by dialysis (cellulose tubing, benzoylated for separating compounds with a molecular weight of ≤1200, Sigma, Germany). The compound was used without purification in the next step. After

preparing the PAMAM-amine terminated compound (PAMAM-AT) an exhaustive alkylation of the primary amines (Michael addition) was performed. An appropriate volume of PAMAM-AT was mixed with methanol (Sigma, Germany) and methyl methacrylate). The solution was kept under agitation in a water bath for 24 hours at 50 °C, to obtain the PAMAM-methyl ester. The CMCht in ultrapure water was mixed with the PAMAM-methyl ester dendrimer, which was previously dissolved in a 20/80 water/methanol (v/v) solution. The final solution was diluted by adding methanol and kept under agitation for 72 hours. After this period, CMCht/PAMAM dendrimers with carboxylic-terminated groups were obtained as described elsewhere [27]. CMCht/PAMAM dendrimer nanoparticles were then precipitated after addition of an appropriate volume of a saturated Na_2CO_3 (Aldrich, Germany) solution and cold acetone (Pronalab, Portugal). Precipitates were collected by filtration and dispersed in ultrapure water for dialysis over a period of 48 hours. CMCht/PAMAM dendrimer nanoparticles were obtained by freezing the solution at 80 °C and freeze-drying (Telstar-Cryodos-80, Portugal) up to 7 days to completely remove the solvent. It is worth noting that the CMCht/PAMAM dendrimer nanoparticles are water-soluble at physiological pH.

V-3.2. Labeling of CMCht/PAMAM dendrimer nanoparticles with FITC

The conjugates of CMCht/PAMAM-FITC were obtained by covalently bond the amine group of CMCht and the isothyocianate group of FITC (10 mg/mL FITC (Sigma, Germany) in anhydrous dimethyl sulfoxide (DMSO, Norconcessus) creating a thiourea bond. First, a 10 mg/mL CMCht/PAMAM dendrimer nanoparticle solution was prepared in a carbonate-bicarbonate coupled buffer of pH 9.2. Then, a solution of FITC/DMSO was added under agitation and kept in the dark at 4 °C for 8 hours. At this moment, the FITC-labeled CMCht/PAMAM dendrimer nanoparticle solution was dialyzed against ultra-pure water in order to remove unlinked FITC for 24 hours and filtered (pore size <220 nm) in sterile and dark conditions. The final product was obtained after freeze-drying.

V-3.3. Characterization of CMCht/PAMAM dendrimer nanoparticles

V-3.3.1. Transmission electron microscope (TEM)

The morphology was investigated by transmission electron microscopy, TEM (Philips CM-12, FEI Company, The Netherlands, equipped with a MEGA VIEW-II DOCU camera and Image Software Analyzer SIS NT DOCU). For that, the nanoparticles were stained with 2 % of phosphotungstic acid and placed on copper grids for observation.

V-3.3.2. Atomic force microscopy (AFM)

The morphology of the nanoparticles was also investigated using atomic force microscopy (AFM). First, the freeze-dried CMCht/PAMAM dendrimer nanoparticles were dispersed in ultrapure water to obtain a solution with final concentration of 1 mg/mL and then one drop was placed over a 9.9 mm mica disc (Agar Scientific, England) and blown dried with nitrogen gas for subsequent characterization. Then, the samples were analyzed using the Tapping Mode™ with a MultiMode AFM connected to a NanoScope III controller, both from Veeco, USA, with non-contact silicon nanoprobes (ca 300 kHz) from Nanosensors, Switzerland. All images were plane-fitted using the third degree-flatten procedure included in the NanoScope software version 4.43r8. The morphometric analysis was performed using the same software.

V-3.3.3. Dynamic light scattering (DLS)

Zeta potential and particle size of the CMCht/PAMAM dendrimer nanoparticles were measured in a particle size analyzer (Zetasizer Nano ZS, Malvern Instruments, UK). Particle size analyses were performed by dynamic light scattering (DLS), in an aqueous solution with low concentration of nanoparticles and using disposable sizing cuvettes. Electrophoretic determinations of Zeta potential were investigated using the universal 'dip' cell pH 7.4 in phosphate buffered saline (PBS) solution. Zeta potential was also investigated in water.

V-3.3.4. Nuclear magnetic resonance (NMR) spectroscopy

In this work, for the determination of the structure of the prepared CMCht/PAMAM dendrimer nanoparticles, it was used H^1NMR analyses. For this purpose, nanoparticles were dissolved in deuterated water (D_2O). Then, the NMR spectra were obtained with a Mercury - 400BB operating at a frequency of 399.9 MHz at 50 °C. The one-dimensional 1H spectra were acquired using a 45° pulse, a spectral width of 6.3 kHz and an acquisition time of 2.001 seconds.

V-3.3.5. Differential scanning calorimetry (DSC)

Differential scanning calorimetry (DSC) was performed to study the thermal stability and changes in crystallinity over a range of temperatures. A known mass of powder was placed in an aluminum pan and a lid was crimped onto the pan. The pan was then placed in the sample cell of a DSC module. The temperature of the DSC module was equilibrated at 35 °C and then increased at a rate of 10 °C per minute under a N_2 gas purge until the material began to degrade. The temperatures were obtained for each peak in the resulting curve and provided indications of temperature stability and phase transitions.

V-3.4. *In vitro* studies under static conditions

V-3.4.1. Cell culture

Three cell lines were used: U87MG cells (human glioblastoma cell line), HeLa cells (human cervical cancer cell line) and HCT-116 cells (human colon cancer cell line) were originally obtained from the American Collection of Cell Cultures (ATCC, USA). Cells were continuously grown in Dulbecco's Modified Eagle Medium (DMEM, Gibco, Invitrogen) supplemented with 10 % (v/v) fetal bovine serum and 1 % (v/v) penicillin and streptomycin under standard conditions (37 °C in a humidified atmosphere containing 5 % CO_2). Subcultures of cells were performed when confluence reached values of ~90 %. Then, cells were plated at an initial density of $2x10^4$ cells/well in 24-well plates and exposed to three concentrations of CMCht/PAMAM dendrimer

nanoparticles (0.1, 0.5 and 1 mg/mL) for short-term exposures comprised between 1 and 3 days.

V-3.4.2. Cell viability

For the studied cell types (HeLa, U87MG and HCT-116), cell viability was assessed by the MTS [3-(4,5-dimethylthiazol-2-yl)-5-(3-carboxymethoxyphenyl)-2(4-sulfophenyl)-2H-tetrazolium] test (VWR, Portugal). At each time point, cell culture medium was replaced by culture medium containing MTS in a 5:1 ratio and incubated for 3 hours. Then, 100 μL of solution from each well were transferred to 96-well plates and the optical density was determined at 490 nm. Cultures that were not exposed to the CMCht/PAMAM dendrimer nanoparticles were used as controls.

V-3.4.3. DNA Quantification

To assess the effect of CMCht/PAMAM dendrimer nanoparticles on cancer cells, the total amount of DNA was measured using the fluorimetric double-stranded DNA (dsDNA) quantification kit (Quant-iT™ PicoGreen® dsDNA Assay Kit, Molecular Probes). HeLa, U87MG and HCT-116 cancer cells were washed with sterile PBS and were lysed with 1 mL of ultrapure water in each well. The cellular suspensions were transferred into microtubes and incubated in a water bath at 37 °C for 1 hour, then stored at -80 °C for further analysis. DNA standards were prepared with concentrations varying between 0 and 2 μg/mL. Next, 28.7 μL of sample or standard, 71.3 μL of PicoGreen solution, and 100 μL of Tris–HCl–EDTA buffer were mixed in each well of an opaque 96-well plate (Alfagene, Portugal) and were incubated in the dark for 10 minutes. After, fluorescence was measured using an excitation wavelength of 485 nm and an emission wavelength of 528 nm. A DNA standard curve was prepared with concentrations varying between 0 and 2 μg/mL and sample DNA values were read off from the standard graph.

V-3.5. *In vitro* studies under a microfluidic platform

V-3.5.1. Vena8™ biochips

The Vena8™ biochip from Cellix® (Irland) is constitute by 8 channels with 120 μm of height, 800 μm of width and 2.8 cm of length. Each channel is connected to two microwells (one in each end) where a microfluidic recirculating pump controlled by an iPod Touch (Kima™ pump) is connected. The sample volume of each channel was 10 μL. The chip was fabricated in optically clear acrylic with a substrate thickness of 500 μm, enabling the observation of cells using brightfield, phase contrast imaging and fluorescence microscopy.

V-3.5.2. Cell culture

A semi-automated microfluidic platform, Vena8™ biochip with glass coverslip (Tebu-Bio, Portugal) was used to mimic physiological flow conditions. Each biochip channel was coated with fibronectin (Sigma, Germany) and then placed in a humidified sterile Petri dish, incubated at 37 °C for 1.5 hours. After the incubation period, 15.000 cells (HeLa, U87MG or HCT-116) were gently added into each microchannel and kept in a sterile Petri dish in the incubator for two hours to allow cell adhesion. To prevent drying, after the initial 30 minutes of incubation, complete medium DMEM was added to the channels. Three hours after, cells were exposed to 0.5 mg/mL of CMCht/PAMAM dendrimer nanoparticles for short-term exposures comprised between 1 and 3 days. Medium was added 3 times per day.

V-3.5.3. Cell viability

Cells were seeded at an initial density of 15.000 cells/channel (day 1 time point) and 10.000 (Day 3 time point) and exposed to 0.5 mg/mL of CMCht/PAMAM dendrimer nanoparticles for short-term exposures comprised between 1 and 3 days. The effect of CMCht/PAMAM nanoparticles on cell viability was tested with medium renewal 3 times per day. Cells cultured in complete culture medium were used as controls.

To test cell viability using MTS method, cells from each channel were detached using Tryple Express (Alfagene, Portugal). Cells were aspirated and collected in a 1.5 mL tube. After centrifugation (5 minutes, 1500 rpm) cells were incubated with culture medium containing MTS in a 5:1 ratio and analyzed as aforementioned for 2D standard cell cultures.

V-3.5.4. DNA quantification

To assess the effect of CMCht/PAMAM dendrimer nanoparticles on cancer cells in the microfluidic chip, the total amount of DNA was measured using Quant-iT™ PicoGreen® dsDNA Assay Kit. HeLa, U87MG and HCT-116 cancer cells were plated at a density of 15.000 cells/microchannel and incubated with CMCht/PAMAM dendrimer nanoparticles at a concentration of 0.5 mg/mL up to 1 to 3 days. Cells cultured in complete culture medium were used as controls. After the incubation, cancer cells from each channel were washed with sterile PBS and detached using Tryple Express Enzyme (Alfagene, Portugal). Cells were aspirated and collected in a 1.5 mL tube and lysed with 1 mL of ultrapure water. The cellular suspensions were incubated in a water bath at 37 °C for 1 hour, then stored at -80 °C for further analysis as described previously.

V-3.6. Assessment of internalization efficiency in 2D standard cultures and using a microfluidic platform

V-3.6.1. Fluorescence microscopy

To assess the internalization and possible cell morphological changes at each time point, a cell suspension was prepared and seeded on TCPS coverslips (Sarstedt Inc., USA) in 24-well plates (2 x 10^4 cells/well) and cultured with 0.5 mg/mL FITC-labeled CMCht/PAMAM dendrimer nanoparticles, in standard culture conditions for 1 and 3 days. Then cells were fixed with 4 % (v/v) formalin (Sigma, Germany) and stained for F-actin filaments of the cytoskeleton and nuclei with Texas Red-X phalloidin (Molecular Probes, Invitrogen, USA) and with 4,6-diamidino-2-

phenylindole, dilactate (DAPI blue, Molecular Probes), respectively, following supplier's protocol. For dynamic cultures, cells were cultured as described previously in the microfluidic platform and were fixed with 10 μL/channel of 4 % (v/v) formalin (Sigma, Germany) for 10 minutes. Then, 10 μL/channel of DAPI and Texas Red-X phalloidin were perfused into the microchannels to stain the nuclei and the cytoskeleton F-actin filaments, respectively. Finally, cells were observed under the fluorescence microscope (AxioImager Z1, Zeiss Inc., Germany).

V-3.6.2. Flow cytometry analysis

To quantify the internalization of FITC-labeled CMCht/PAMAM dendrimer nanoparticles, flow cytometry analysis was performed. In static conditions, cancer cells were cultured in the presence of 0.5 mg/mL FITC-labeled CMCht/PAMAM dendrimer nanoparticles in a 6-well plate ($2x10^5$ cells/well). Cells cultured in complete culture medium were used as controls. Cells were released from substratum and a cell strainer was used to avoid cell clusters. Afterwards, 0.5 mL of DMEM complete medium was added to each well and samples transferred to cytometry tubes.

In dynamic conditions, cancer cells were cultured in the presence of 0.5 mg/mL FITC-labeled CMCht/PAMAM dendrimer nanoparticles in the microfluidic chips. Cells cultured in complete culture medium were used as controls. FACS analysis was carried out to perform quantitative analysis on the internalization efficiency as well as cell viability, as follows: each channel was washed with PBS. Then, PBS was aspirated and cells from each channel were detached using 10 μL of Tryple Express and collected in an FACS tube. After centrifugation at 1500 rpm for 5 minutes, cells were re-suspended in 800 μL of a 2 % (v/v) fetal bovine serum in PBS solution. Afterwards, 5 μL of 7-AAD (Taper group, Portugal) was added to each sample for determining the number of dead cells. After this step, cells were loaded in FACSCalibur flow cytometer (BD Biosciences Immunocytometry Systems, USA). Calibrate beads three-color kit (BD CaliBRITE™ beads, USA) was used to adjust the equipment instrument settings before samples are run on the flow cytometer. Finally, data was treated using the FLOWING SOFTWARE 2.

V-4. RESULTS

V-4.1. Characterization of the CMCht/PAMAM dendrimer nanoparticles

In order to gain deeper knowledge on the CMCht/PAMAM dendrimer nanoparticles physicochemical properties, a TEM and AFM study were performed. Their architecture determined in dry conditions is depicted in **Figures IV-1A and I-1B.** From **Figure IV-1A**, it is clearly visible the monodisperse character of these particles, as well as the polymer coating around PAMAM's core and a clear dendron-like morphology, which was further confirmed by AFM analysis as shown in **Figure IV-1B**. In fact, it is possible to observe the 3D AFM image of the CMCht/PAMAM dendrimer nanoparticles, which noticeably shows the consistency of these molecules, *i.e.* nanosphere-like shape. By assessing the particle distribution using DLS, it revealed that the CMCht/PAMAM dendrimer nanoparticles have an average size of 50 nm (**Figure IV-1C**). After the synthesis of the CMCht/PAMAM dendrimer nanoparticles, three types of particles were clearly detected, with sizes approximately 6 ± 1 nm, 54 ± 7 nm and 674 ± 462 nm. The first graph corresponds to the modified dendrimer nanoparticles with carboxymethylchitosan where two peaks are present, corresponding to single and aggregated nanoparticles, respectively. The second graph corresponds to the unmodified PAMAM dendrimer of generation 1.5, also with two visible peaks. These correspond to single and aggregated nanoparticles. Zeta potential data shows that nanoparticles dispersed in water at neutral pH present negative charge of -34.3 ± 3 (mV).

Figure IV-1D shows the H^1NMR spectrum of the synthesized CMCht/PAMAM dendrimer nanoparticles and its comparison with unmodified PAMAM dendrimer and biocompatible polymer carboxymethylchitosan, revealing a singlet at 2.49 ppm, and multiplets from 3.1 to 3.73 ppm and 4.07 ppm associated to the H^2 protons, the ring methine protons (H^3, H^4, H^5 and H^6), and protons of $–CH_2COO-$ groups of the CMCht. Also, peaks at 2.49 and 3.46 ppm appear overlapped as a result of the resonances of the CH_2COO and CH_2 protons of both CMCht and PAMAM. The presence of the peak at ca. 3 ppm and the absence of a peak at 4.3 ppm can indicate that the substitutions occurred mainly on the C2 amino group of CMCht. Finally, DSC

thermogram analysis to assess thermal stability of the modified dendrimer shown in **Figure IV-1E** reveals a Glass transition temperature (Tg) of -13.7 °C and a thermal decomposition at 267 °C.

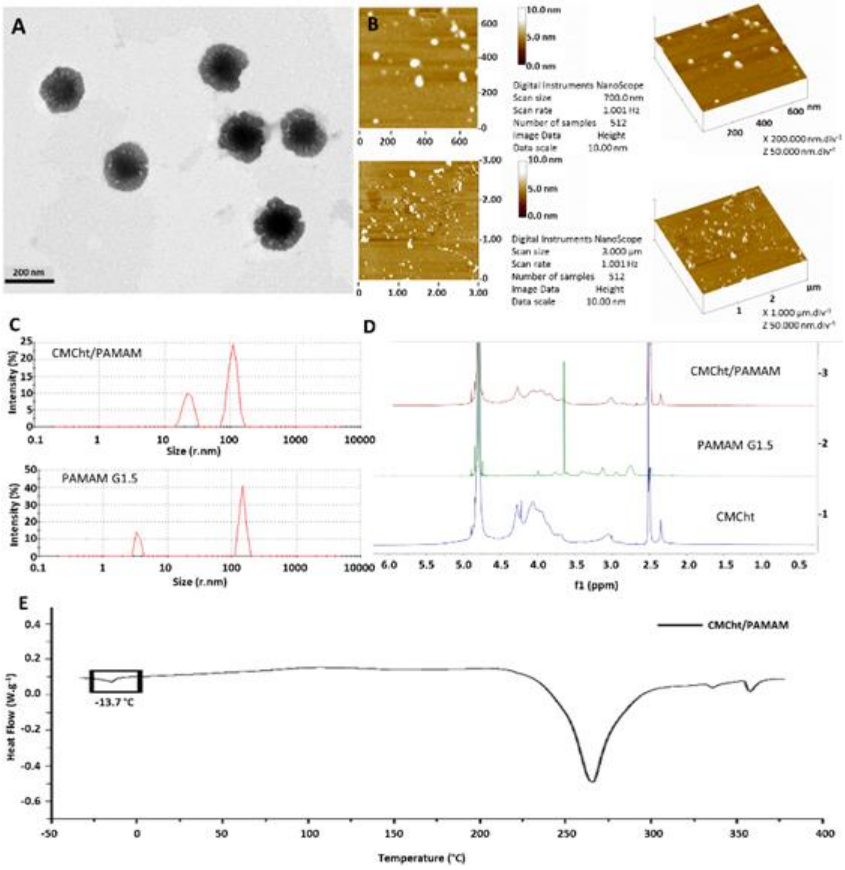

Figure V-1 - Characterization of water soluble nanoparticles. A) Transmission electron microscopy (TEM) image of the CMCht/PAMAM. B) Atomic force microscopy (AFM) images of CMCht/PAMAM on a quartz mica. C) Particle size distribution (nm). D) H1NMR spectra of CMCht/PAMAM, PAMAM G1.5 and CMCht. E) Differential Scanning Calorimetry (DSC) spectrum of CMCht/PAMAM.

V-4.2. Cell viability/proliferation in static conditions

Cell viability and proliferation were determined by means of performing MTS and DNA quantification assays (**Figure IV-2**). The three chosen cancer cell lines were exposed to a range of dendrimer concentrations over a period of 3 days. Our results indicated showed no deleterious effects on cell viability in static culture conditions, when comparing the tested and control samples ($p<0.0001$). Therefore, the tested conditions were not affected significantly by the

presence of CMCht/PAMAM dendrimer nanoparticles. It is clear that all cancer cell lines proliferate in a significant manner from day 1 to day 3 in the absence of nanoparticles (controls). As depicted in **Figure IV-2**, the concentration with less variability, more consistent results (low standard deviations), and more alike to the control group (no statistically significant differences) was 0.5 mg/mL. This preliminary tests allowed us to screen three types of relevant cancer cell lines with a wide range of concentrations and choose the most adequate one to proceed to comparative studies between static and dynamic conditions of culture, in order to validate a model for real time tracking. So, from this point on, all the tests were performed with a dendrimer nanoparticle concentration of 0.5 mg/mL.

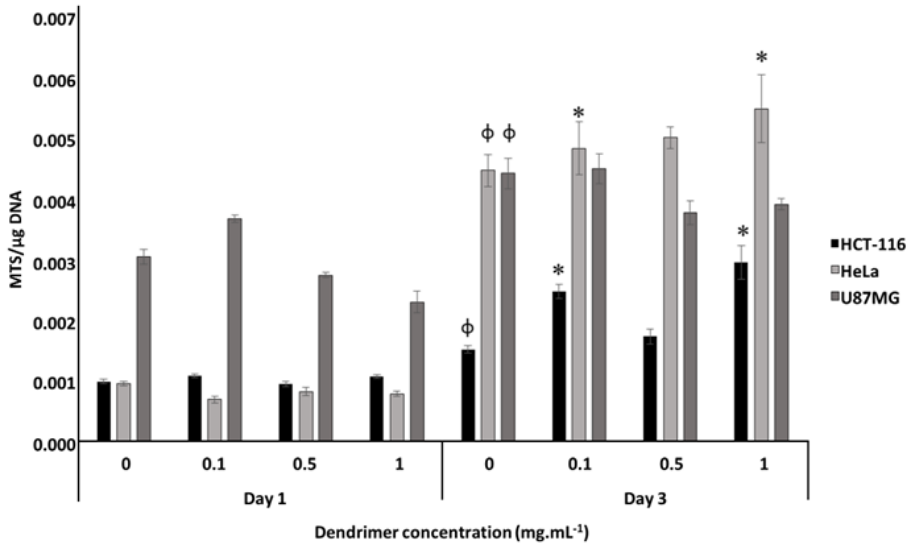

Figure V-2 - Normalization of MTS results by DNA results of HCT-116, HeLa and U87MG human cancer cell lines in static conditions in the presence of CMCht/PAMAM dendrimer nanoparticles. Assays were conducted to assess the cytotoxicity effect of nanoparticles on cell viability at concentrations of 0.1, 0.5 and 1 mg/mL at time points of 1 and 3 days (* indicates significant differences when comparing the different concentrations to control (0 mg/mL) at each time point. Φ indicates significant differences when comparing controls from day 3 to day 1 to determine cell proliferation).

V-4.3. Cell viability/proliferation in dynamic conditions

Figure IV-3 shows the results of the two tested groups (static and dynamic) at day 1 and day 3, in the absence or presence of nanoparticles (0.5 mg/mL), for easy comparison. The results shown represent the normalization between the two tests. Regarding the dynamic condition, HCT-116 cells showed greater sensitivity in the presence of nanoparticles, both in day 1 and day 3,

which is translated into a decrease of viability. U87MG cells, by its turn, showed this significant difference between control and nanoparticles groups only at day 3. However, for HeLa cells, no significant differences were observed in dynamic conditions regarding the effect of nanoparticles.

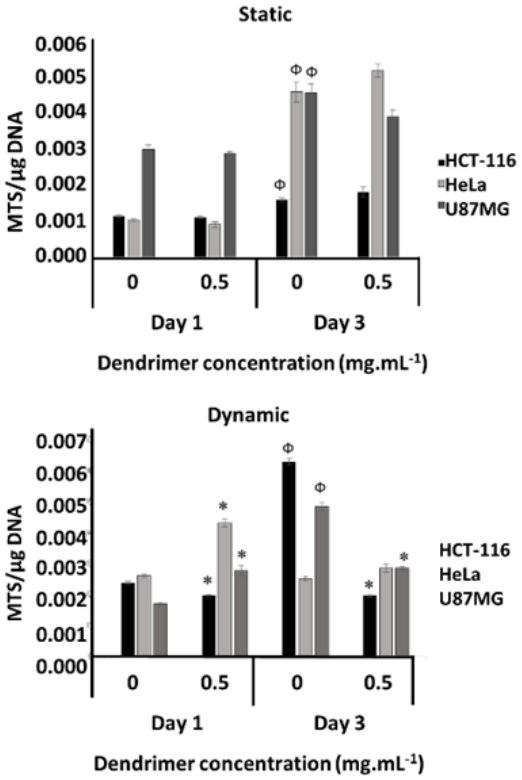

Figure V-3 - Cytotoxicity of CMCht/PAMAM over HCT-116, HeLa and U87MG human cancer cell lines in static and dynamic conditions. Assays were conducted to assess cytotoxicity/viability over the cells at a concentration of 0.5 mg/mL at different time points (days 1 and 3) and it in static and dynamic conditions. (* indicates significant differences when comparing 0.5 mg/mL to control (0 mg/mL) at each time point. Φ indicates significant differences when comparing controls from day 3 to day 1 to determine cell proliferation).

V-4.4. Assessment of nanoparticles cellular uptake in 2D standard cultures

V-4.4.1. Fluorescence microscopy and flow cytometry analysis

Figure IV-4 shows the fluorescence microscopy images obtained after culturing the three cancer cell lines with 0.5 mg/mL of FITC-CMCht/PAMAM for 1 and 3 days in static conditions. As can be observed, all cancer cells were able to internalize the fluorescent labeled

nanoparticles. Nanoparticles are dispersed in the cytoplasm but especially around the nucleus (stained with DAPI). Also, it is clear that the internalization rate tended to increase with time. The microscopic observation of cells showed no relevant cell morphological changes, which corroborate the lack of cytotoxicity.

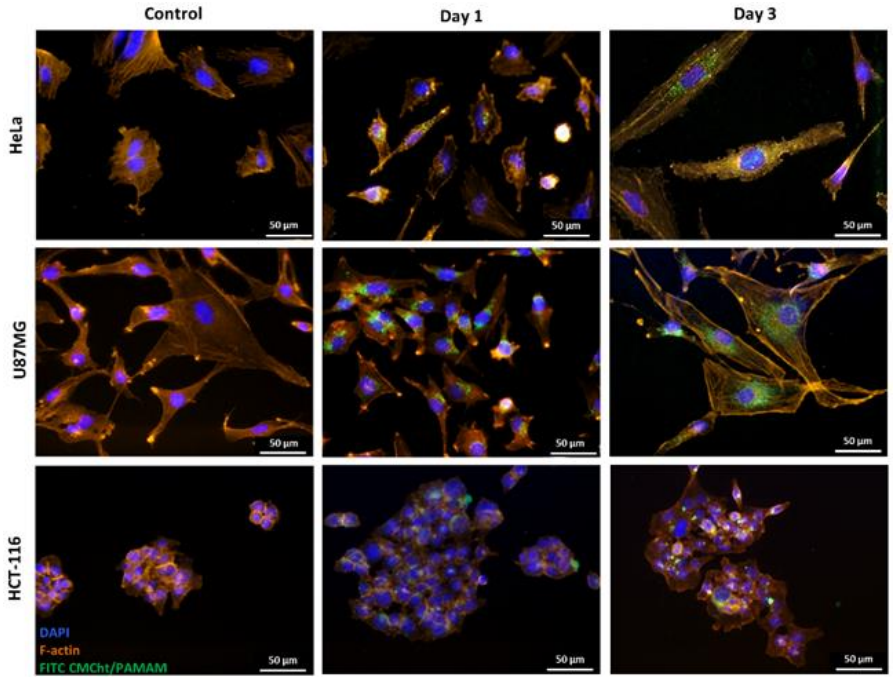

Figure V-4 - Fluorescent microscope images of FITC-labeled CMCht/PAMAM dendrimer nanoparticles (green) internalization in cancer cells labelled with DAPI (nuclei) and Phalloidin (F-actin, cytoskeleton) after 1 and 3 days in direct contact with dendrimer nanoparticles in static conditions.

Quantitative analysis of nanoparticles uptake at the cellular level was performed using flow cytometry analysis. **Table IV-1** shows the percentage of internalization of FITC-labeled CMCht/PAMAM dendrimer nanoparticles by each cell line under static conditions, as well as the percentage of live cells obtained by staining with 7-AAD, determined by flow cytometry. Flow cytometry results of cancer cell lines cultured in the presence of FITC-labeled CMCht/PAMAM dendrimer nanoparticles showed that HeLa cancer cells continued to internalize the nanoparticles along time, starting with an internalization percentage of 87 % by day one, and increasing to 99 % by day 3 (higher fluorescent signals along time). By its turn, U87MG and HCT-116 internalization rates were constant and reached the maximum peak, as almost 100 % of cells showed internalized nanoparticles only after 24 hours. Regarding cell viability in static conditions, it is possible to observe that cells remain viable in the presence of dendrimer

nanoparticles (% of live cells on day 1 is very similar to day 3) and no relevant cytotoxic effects are noted when compared to controls (See **Table IV-1**).

Table V-1 - FACS data of the percentage of internalization of FITC-labeled CMCht/PAMAM dendrimer nanoparticles (NP) and the percentage of live cells (stained with 7AAD), from day 1 to day 3 in static conditions.

Culture conditions	Internalization (%)		Live cells (%)	
Static	Day 1	Day 3	Day 1	Day 3
HeLa (NP)	87	99	96	97
HeLa (Control)	0	0	99	99
U87MG (NP)	98	98	97	95
U87MG (Control)	0	0	99	99
HCT-116 (NP)	100	99	97	97
HCT-116 (control)	0	0	99	100

V-4.5. Assessment of internalization efficiency using a microfluidic platform

V-4.5.1. Fluorescence microscopy and flow cytometry analysis

Figure IV-5 represents a panel of images with results obtained after 1 and 3 days of culture in the presence of FITC-CMCht/PAMAM at a concentration of 0.5 mg/mL, in dynamic culturing conditions. As can be observed, all cancer cells were able to internalize the fluorescent-labeled nanoparticles when cultured in the microfluidic system.

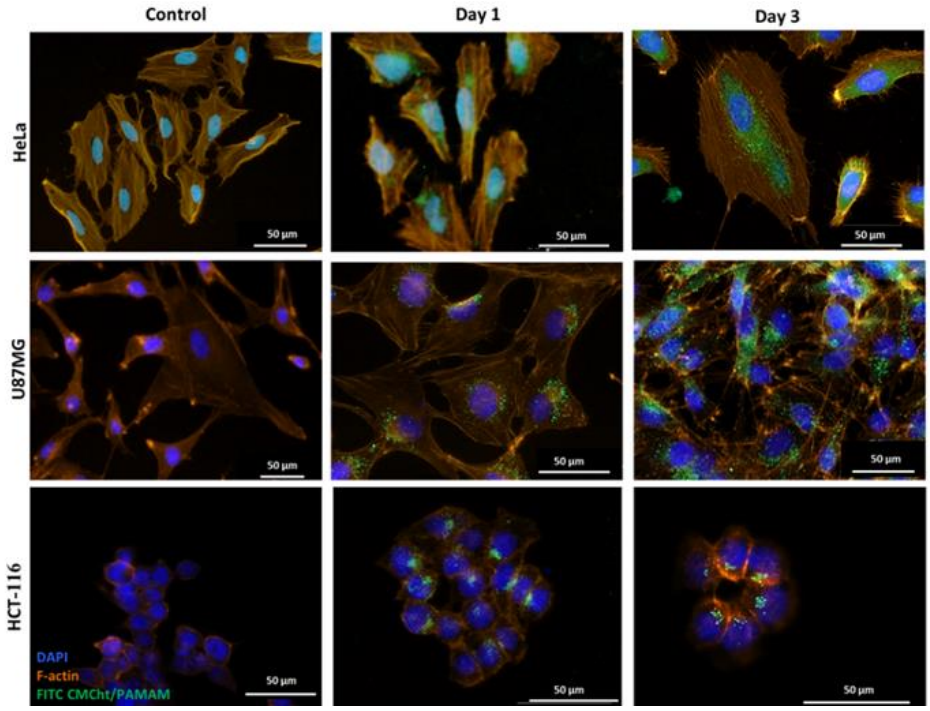

Figure V-5 - Fluorescent microscope images of FITC-labeled CMCht/PAMAM dendrimer nanoparticles (green) internalization in cancer cells labeled with DAPI (nuclei) and Phalloidin (F-actin, cytoskeleton) after 24 hours and 72 hours in direct contact in dynamic conditions.

Flow cytometry studies on cells cultured in dynamic conditions reveal similar results to static conditions when it comes to nanoparticles' internalization performance. Cells are able to internalize nanoparticles almost at the maximum rate by 24 hours after the beginning of the experiment (**Table IV-2).** Concerning cell viability, it is possible to observe differences between the absence and the presence of nanoparticles. In fact, all cancer cells show decreased viability in the presence of nanoparticles. Special emphasis in HCT-116 with a percentage of live cells of 90 % when compared to the respective control (99 %), followed by U87MG with 95% against 99 % of the control, and finally HeLa cells with a percentage of 97 % in the presence of nanoparticles and 100 % in the control. It is worth noticing that the viability in relation to control was kept when analyzing day 3 **(Table IV-2).**

Table V-2 - FACS data of the percentage of internalization of FITC-labeled CMCht/PAMAM dendrimer nanoparticles and the percentage of live cells (stained with 7AAD), from day 1 to day 3 in dynamic conditions.

Culture conditions	Internalization (%)		Live cells (%)	
Dynamic	Day 1	Day 3	Day 1	Day 3
HeLa (NP)	95	100	97	97
HeLa (Control)	0	0	100	100
U87MG (NP)	99	99	95	92
U87MG (Control)	0	0	99	98
HCT-116 (NP)	100	99	90	90
HCT (Control)	0	0	99	99

V-5. DISCUSSION

Although the cancer research field has been evolving along the years, there is still missing a proper tool to track cells and therapy efficiency in real time, allowing the interpretation of their interaction and expediting its translation into the clinics. Cell movement, location and quantification studies require specialized probes that are non-cytotoxic and are available in a range of fluorescent colors to match instrument lasers and filters, and to accommodate co-staining with antibodies or other cell analysis probes.

In light of this, the main goal of this work was aimed at developing a new platform composed of fluorescent-labeled nanoparticles associated with a microfluidic device, which may be useful for the validation of new theranostic approaches. To accomplish this, we investigated the interactions between a new class of labeled nanoparticles, developed previously by our group [28] with several cancer cell lines, both in standard 2D static culture systems and in a dynamic microfluidic chip. The *in vitro* studies demonstrated that cells remain viable in both culturing conditions. However, cell cultures in the dynamic systems displayed higher sensitivity to nanoparticles, disclosing the real importance of a more physiologically relevant model for the development of new cancer therapies, otherwise, no differences in cells response should be found. Additionally, as the developed nanoparticles show internalization rates near to 100 % (all the cells in culture have internalized fluorescent labeled nanoparticles) after 24 hours in culture, they enable real time monitoring of drug delivery systems efficiency accelerating its translation into clinics.

Recently, our group has proposed a strategy to chemically modify PAMAM dendrimer nanoparticles with carboxymethylchitosan in order to achieve water solubility and low cytotoxicity, making them ideal for this purpose [28]. The first steps were to synthetize and modify the nanoparticles and to physico-chemically characterize them, prior to its use in biological studies. The chosen methods are simple and reliable tools to determine chemical composition, morphological features and surface chemistry, such as TEM, AFM, DLS, H^1NMR and DSC methods. In this study, the TEM analysis (**Figure IV-1A**) clearly revealed a dendron-like morphology with a central core and the added carboxymethilchitosan polymer coating. This data was further confirmed by AFM analysis (**Figure IV-1B**) that visibly showed the consistency of these molecules features, *i.e.*, nanosphere-like shape, which is in agreement with previously described results [28, 29].

CMCht/PAMAM dendrimer nanoparticles were also analyzed with DLS. Particle size is one of the most important parameters in drug carriers for intracellular delivery, as well as the surface charge, which was also measured. Three sizes of particles were detected, approximately 6 ± 1 nm, 54 ± 7 and 674 ± 462 (**Figure IV-1C**). In the first graph, where is depicted the analysis of CMCht/PAMAM dendrimer, the first peak corresponds to the modified dendrimer and the second to the aggregates. Concerning the second graph, the first peak matches the size of the isolated unmodified PAMAM G1.5 dendrimer nanoparticles and the second to the size of aggregated nanoparticles. The last group, the aggregated nanoparticles, can be explained by interactions between non-covalent free carboxyl groups of CMCht and/or unmodified PAMAM-Carboxyl terminal dendrimer and amino groups of other CMCht particles, which may promote the formation of nanoparticle aggregates [30]. This is a property involving not only the surface properties of the particles but also their environment, *e.g.* pH, ionic strength, and even the type of ions in the suspension. By its turn, it is expected that CMCht has a good pH and ion sensitivity in aqueous solution due to abundant –COOH and $–NH_2$ groups. These results corroborate the theory that the negatively charged carboxymethyl groups in the CMCht/PAMAM dendrimer nanoparticles are mainly distributed at the surface of the nanoparticles working as a water-soluble coating, as proved by the DLS data.

Regarding the H^1NMR analysis, the singlet at 2.49 ppm and multiplets from 3.1 to 3.73 ppm and 4.07 ppm are associated to the H^2 protons, the ring methine protons (H^3, H^4, H^5 and

H^6), and protons of $–CH_2COO^-$ groups of the CMCht, respectively [30, 31]. Also, the presence of peaks from 1.98 to 3.46 ppm is noteworthy because they point the presence of PAMAM dendrimer. These have been attributed to CH_2COO, CH_2CO and CH_2CN groups. The presence of the peak at ca. 3 ppm and the absence of a peak at 4.3 ppm can indicate that the substitutions occurred mainly on the C2 amino group of CMCht, confirming the modification of the PAMAM dendrimer. SC was used to evaluate the thermal stability of DNA complexed to PAMAM dendrimers SC was used to evaluate the thermal stability of DNA complexed to PAMAM dendrimers. The DSC studies were performed to assess the thermal stability of PAMAM dendrimers modified with carboxymethilchitosan. The thermal degradation was observed at 267 °C indicating that the developed dendrimers are high thermally stable at body temperature. This high value could be due to the presence of hydrogen bonds in the structure of PAMAM, as observed previously [32]. Nevertheless it is lower than the observed in previous studies made with other generations of PAMAM dendrimers [33]. This variation can be explained by the contribution of carboxymethilchitosan polymer. In fact, it was previously shown that the longer the grafted polymers are, the lower the values of thermal degradation obtained, and consequently less stable the dendrimer is [34]. Moreover, a thermal glass transition is clear at -13.7 °C. To the best of our knowledge, this type of characterization has never been done in this specific type of modified dendrimers and therefore could serve as a reference for future works.

Regarding the biological assays, similarly to what has been done by Oliveira *et al.* for neurons, glial cells [29], fibroblasts (L929) and rat bone marrow stromal cells (RBMSCs) [28], the cytotoxic effect of different concentrations of CMCht/PAMAM dendrimer nanoparticles on glioblastoma cancer cells, colon cancer cells and cervical cancer cells, along the time, was the first parameter to be assessed, as a bridge to dynamic experiments. This allowed us to select the higher non-cytotoxic concentration to be used in subsequent assays, which was 0.5 mg/mL. After that, standard 2D culture systems in cell culture TCPS well-plate (static conditions) and cultures inside a microchannel in a microfluidic device (dynamic conditions) were comparatively investigated. The last culture system works as a bridge towards more elaborated 3D models, as it mimics the natural environment that cells and nanoparticles are exposed to, once in systemic circulation *in vivo* [35], regarding confinement, flow and shear stress. **Figure IV-2** represents the results of the screening under static conditions, which indicates highly metabolically active cells.

HCT-116, HeLa and U87MG proliferated well and were viable either in the controls (absence of nanoparticles) or in the presence of nanoparticles at any given concentration. Statistically, it is possible to observe that increasing concentrations of CMCht/PAMAM (0.1, 0.5 and 1 mg/mL) did not affect the viability or proliferation of cancer cell lines. This can be explained by the natural aggressiveness and resistance of cancer cell lines [36] when compared to other cell types as showed in the work of Oliveira *et al* [28, 30]. For so, we decided to use the intermediate concentration: 0.5 mg/mL as it shows no statistical differences when compared to the controls, and because it could potentially increase the number of nanoparticles inside the cells when compared to the lowest concentration (0.1 mg/mL).

When static conditions were compared to dynamic conditions (**Figure IV- 4**), in which cells were exposed to 0.5 mg/mL for the same periods of time, HCT-116 cells showed a clear sensitivity to nanoparticles, especially at day 3, as well as U87MG cells. None of these phenomena were observed in static standard conditions, highlighting the importance of using a system that mimics features of the *in vivo* environment. Therefore, the main differences between the two culture conditions rely on the fact that nanoparticles show no effect on any of the chosen cancer cell lines at any time point in static conditions. Nevertheless, when the same cells were cultured in a confined and dynamic environment they showed to be more sensitive. Moreover, we observed that their growth is much greater in static conditions (statistic differences from day 1 to day 3) which can be due to the fact that they proliferate freely in traditional 2D culture conditions, on contrary to what was observed in dynamic conditions due to the limited space available within the microchannels of the microfluidic device. This is why it is also worth noticing the short time exposures (3 days) used in this work instead of the traditional 14 days' exposure. In fact, microfluidic devices, such as Vena8™ chips, are made to speed up and scale down experiments [37].

Qualitative images obtained with fluorescence microscope revealed that either in static and dynamic conditions, HCT-116, U87MG and HeLa cells were able to broadly internalize fluorescence labeled nanoparticles at a very quick rate after 1 day in culture. The normal morphology of the cells (marked by DAPI and Phalloidin) suggests healthy proliferation and survival under both conditions (**Figure IV-4 and Figure IV- 5**). It is not clear whether the particles are also located inside the nucleus just by observing the microscope images. Further

experiments are required to clarify the fate of these nanoparticles. The same effect has been observed earlier by Oliveira *et al.* [28] in L929 and Saos-2 cell lines.

These findings were latter corroborated by flow cytometry, which was used to quantitatively study the levels of FITC-labeled CMCht/PAMAM dendrimer nanoparticles internalized by cells. Quantitative analysis of nanoparticles uptake at the cellular level is critical for a realistic evaluation of their effects and to compare possible different behaviors among different cell culture times. FACS analysis was performed to circumvent this limitation since each cell line interacts differently with nanoparticles [38].

Results from **Table IV-1** revealed increasing levels of fluorescence for HeLa cells from day 1 (87 %) to day 3 (99 %), in static conditions. By its turn, U87MG and HCT-116 cells' internalization rates were constant and reached the maximum peak, as almost 100 % of cells showed internalized nanoparticles only after 1 day. A similar trend was observed in dynamic conditions (**Table IV-2**). Although HeLa cells showed slower internalization rates, as compared to U87MG and HCT-116 cells, a higher rate of internalization was observed at day 1 when comparing to static conditions (87 % in static vs 95 % in dynamic), which could influence for example the optimization of drug concentration used, showing once again the relevance of using a dynamic system for validation of new therapies. The fact that HeLa cells take more time to internalize nanoparticles in both culture conditions could be related and possibly explain their higher sensitivity. Nevertheless, it is important to point out that almost 100 % of cells were labeled after 1 day, indicating that the developed nanoparticles present great potential as cell tracking system.

Additionally, we used flow cytometry to measure the viability levels of cells in both conditions (static vs dynamic) using 7-AAD. 7-AAD appears to be generally excluded from live cells, creating complexes only with free DNA from dead cells, making it an excellent quantitative indicator of cell viability, as it gives fluorescent signal for dead cells only. By quantifying the percentage of live cells, we observed that there were no significant differences between the controls and the presence of 0.5 mg/mL of nanoparticles in static studies (**Table IV-1**). On the other hand, when seeded and cultured in the microfluidic chips with dynamic flow, cells showed higher sensitivity, displaying higher percentages of dead cells, as depicted in **Table IV-2**. It is worth noticing that the results obtained by flow cytometry analysis corroborate the results of MTS/DNA tests.

In brief, these findings suggest that standard 2D assays underestimated the effect of CMCht/PAMAM dendrimer nanoparticles, while microfluidic chips, which represent a dynamic setting, unraveled the real cytotoxicity and internalization rates of the labeled nanoparticles [39, 40]. This could only be possible due to the combination of dendrimer nanoparticles with fluorescent dye, which allowed real-time monitoring of cells in this new system, envisaging the use for new therapies validation in real time. Despite the interesting data, we envision performing deeper studies to investigate the effect of loading an anti-cancer drug into the NP's on cancer cell lines in the proposed microfluidic chip.

V-6. CONCLUSIONS AND FUTURE PERSPECTIVES

This study provided proof-of-concept on the use of a platform composed of microfluidic chip together with fluorescence labeled dendrimer nanoparticles for the validation of new chemotherapeutic agents. In fact, the results show different responses to the presence of 0.5 mg/mL dendrimer nanoparticles when comparing static to dynamic conditions, with a tendency towards higher sensitivity when subjected to confinement, flow and shear stress (dynamic conditions). Moreover, the observed high internalization rates of the nanoparticles can be beneficial, making them excellent intercellular carrier of anti-cancer drugs.

Recent evidence indicates that 3D and flow models more closely resemble *in vivo* function. For example, plenteous reports have shown improved functionality with 3D cultures and flow cultures for xenobiotic metabolism competence more closely mimicking *in vivo* levels. Therefore, as hypothesized by us, the proposed system has some important features representative of the *in vivo* microenvironment, such as confinement, flow and shear stress. This platform, together with the efficient ability of cell tracking and drug delivery, represents a new step towards dynamic studies in cancer cells in 3D, namely migration and drug testing. Hence, this work further shapes the challenges associated with the use of nanoparticles to help deliver drugs more specifically and effectively to cancer cells as well as to help detect cancer (theranostics). Future nanoparticles and microfluidic models can boost drug validation and the understanding of tumorigenesis processes, essential to move the cancer research field forward in terms of prevention, detection and treatment.

Thus, the microfluidics can enable the development of diagnostics platform and personalized therapies, as it opens the possibility to a valuable system to test and validate new chemotherapeutic agents in a more realistic manner, expediting its translation into clinic.

V-7. ACKNOWLEDGMENTS

F.R. Maia acknowledges ERC-2012-ADG 20120216-321266 (ComplexiTE) for her Postdoc scholarship. J. M. Oliveira thanks Portuguese Foundation for Science and Technology (FCT) for his distinction attributed under the FCT Investigator program (IF/00423/2012). Bruno Costa also thanks Portuguese Foundation for Science and Technology (PTDC/SAU-GMG/113795/2009 and IF/00601/2012 to B.M.C.), Fundação Calouste Gulbenkian (B.M.C.), and Liga Portuguesa Contra o Cancro (B.M.C.). Mariana R. Carvalho also thanks the funding through the LA ICVS/3Bs project (UID/Multi/50026/2013).

V-8. REFERENCES

1. Siegel, R., et al., *Cancer statistics, 2014.* CA Cancer J Clin, 2014. **64**(1): p. 9-29.
2. Ferlay, J., et al., *Cancer incidence and mortality patterns in Europe: estimates for 40 countries in 2012.* Eur J Cancer, 2013. **49**(6): p. 1374-403.
3. Chaffer, C.L. and R.A. Weinberg, *A perspective on cancer cell metastasis.* Science, 2011. **331**(6024): p. 1559-64.
4. Headley, M.B., et al., *Visualization of immediate immune responses to pioneer metastatic cells in the lung.* Nature, 2016. **531**(7595): p. 513-7.
5. Haley, B. and E. Frenkel, *Nanoparticles for drug delivery in cancer treatment.* Urol Oncol, 2008. **26**(1): p. 57-64.
6. Valencia, P.M., et al., *Microfluidic technologies for accelerating the clinical translation of nanoparticles.* Nat Nanotechnol, 2012. **7**(10): p. 623-9.
7. Popovtzer, R., et al., *Targeted gold nanoparticles enable molecular CT imaging of cancer.* Nano Lett, 2008. **8**(12): p. 4593-6.
8. Carvalho, M.R., et al., *Evaluating Biomaterial- and Microfluidic-Based 3D Tumor Models.* Trends in Biotechnology, 2015. **33**(11): p. 667-678.
9. Mestre, T., et al., *Quantification of topological features in cell meshes to explore E-cadherin dysfunction.* Sci Rep, 2016. **6**: p. 25101.
10. Sittampalam, S., et al., *Three-Dimensional Cell Culture Assays: Are They More Predictive of In Vivo Efficacy than 2D Monolayer Cell-Based Assays?* Assay Drug Dev Technol, 2015. **13**(5): p. 254-61.

11. Bhatia, S.N. and D.E. Ingber, *Microfluidic organs-on-chips.* Nat Biotechnol, 2014. **32**(8): p. 760-72.
12. Zhao, L., et al., *Lab-on-a-Chip for anticancer drug screening using quantum dots probe based apoptosis assay.* J Biomed Nanotechnol, 2013. **9**(3): p. 348-56.
13. Zhou, H., L. Zhao, and X. Zhang, *In-channel printing-device opening assay for micropatterning multiple cells and gene analysis.* Anal Chem, 2015. **87**(4): p. 2048-53.
14. Barata, D., C. van Blitterswijk, and P. Habibovic, *High-throughput screening approaches and combinatorial development of biomaterials using microfluidics.* Acta Biomater, 2015.
15. Kuo, C.T., et al., *Modeling of cancer metastasis and drug resistance via biomimetic nano-cilia and microfluidics.* Biomaterials, 2014. **35**(5): p. 1562-71.
16. Bischel, L.L., et al., *Tubeless microfluidic angiogenesis assay with three-dimensional endothelial-lined microvessels.* Biomaterials, 2013. **34**(5): p. 1471-7.
17. Bray, L.J., et al., *Multi-parametric hydrogels support 3D in vitro bioengineered microenvironment models of tumour angiogenesis.* Biomaterials, 2015. **53**(0): p. 609-620.
18. Bersini, S., et al., *A microfluidic 3D in vitro model for specificity of breast cancer metastasis to bone.* Biomaterials, 2014. **35**(8): p. 2454-2461.
19. Dong, Y., et al., *Microfluidics and circulating tumor cells.* J Mol Diagn, 2013. **15**(2): p. 149-57.
20. Chen, L., et al., *Real-time monitoring of a controlled drug delivery system in vivo: construction of a near infrared fluorescence monomer conjugated with pH-responsive polymeric micelles.* Journal of Materials Chemistry B, 2016. **4**(19): p. 3377-3386.
21. Kwak, B., et al., *Simulation of complex transport of nanoparticles around a tumor using tumor-microenvironment-on-chip.* Journal of Controlled Release, 2014. **194**: p. 157-167.
22. Fede, C., et al., *Evaluation of gold nanoparticles toxicity towards human endothelial cells under static and flow conditions.* Microvasc Res, 2015. **97**: p. 147-55.
23. Kesharwani, P., et al., *PAMAM dendrimers as promising nanocarriers for RNAi therapeutics.* Materials Today, 2015. **18**(10): p. 565-572.
24. Wolinsky, J.B. and M.W. Grinstaff, *Therapeutic and diagnostic applications of dendrimers for cancer treatment.* Adv Drug Deliv Rev, 2008. **60**(9): p. 1037-55.
25. Pojo, M., et al., *In vitro evaluation of the cytotoxicity and cellular uptake of CMCht/PAMAM dendrimer nanoparticles by glioblastoma cell models.* Journal of Nanoparticle Research, 2013. **15**(5): p. 1-9.
26. Chen, X.-G. and H.-J. Park, *Chemical characteristics of O-carboxymethyl chitosans related to the preparation conditions.* Carbohydrate Polymers, 2003. **53**(4): p. 355-359.
27. Sashiwa, H., Y. Shigemasa, and R. Roy, *Chemical modification of chitosan. Part 9: Reaction of N-carboxyethylchitosan methyl ester with diamines of acetal ending PAMAM dendrimers.* Carbohydrate Polymers, 2002. **47**(2): p. 201-208.
28. Oliveira, J.M., et al., *Surface Engineered Carboxymethylchitosan/Poly(amidoamine) Dendrimer Nanoparticles for Intracellular Targeting.* Advanced Functional Materials, 2008. **18**(12): p. 1840-1853.
29. Salgado, A.J., et al., *Carboxymethylchitosan/poly(amidoamine) dendrimer nanoparticles in central nervous systems-regenerative medicine: effects on neuron/glial cell viability and internalization efficiency.* Macromol Biosci, 2010. **10**(10): p. 1130-40.

30. Oliveira, J.M., et al., *The osteogenic differentiation of rat bone marrow stromal cells cultured with dexamethasone-loaded carboxymethylchitosan/poly(amidoamine) dendrimer nanoparticles.* Biomaterials, 2009. **30**(5): p. 804-13.
31. Li, Y., et al., *In situ crosslinkable hydrogels formed from modified starch and O-carboxymethyl chitosan.* RSC Advances, 2015. **5**(38): p. 30303-30309.
32. Martin-Rapun, R., et al., *Ionic thermotropic liquid crystal dendrimers.* J Am Chem Soc, 2005. **127**(20): p. 7397-403.
33. Uppuluri, S., et al., *The Properties of Dendritic Polymers I: Generation 5 Poly (amidoamine) Dendrimers*. 1998, DTIC Document.
34. Hui, H., F. Xiao-dong, and C. Zhong-lin, *Thermo- and pH-sensitive dendrimer derivatives with a shell of poly(N,N-dimethylaminoethyl methacrylate) and study of their controlled drug release behavior.* Polymer, 2005. **46**(22): p. 9514-9522.
35. Sato, M., et al., *Microcirculation-on-a-Chip: A Microfluidic Platform for Assaying Blood- and Lymphatic-Vessel Permeability.* PLoS One, 2015. **10**(9): p. e0137301.
36. Kuete, V., et al., *Cytotoxicity of a naturally occurring furoquinoline alkaloid and four acridone alkaloids towards multi-factorial drug-resistant cancer cells.* Phytomedicine, 2015. **22**(10): p. 946-951.
37. Teh, S.Y., et al., *Droplet microfluidics.* Lab Chip, 2008. **8**(2): p. 198-220.
38. Mahmood, M., et al., *Cytotoxicity and biological effects of functional nanomaterials delivered to various cell lines.* J Appl Toxicol, 2010. **30**(1): p. 74-83.
39. Carvalho, M.R., et al., *Evaluating Biomaterial- and Microfluidic-Based 3D Tumor Models.* Trends Biotechnol, 2015. **33**(11): p. 667-78.
40. Horning, J.L., et al., *3-D tumor model for in vitro evaluation of anticancer drugs.* Mol Pharm, 2008. **5**(5): p. 849-62.

Chapter VI

Tuning Enzymatically-crosslinked Silk fibroin Hydrogel Properties for the Development of a Colorectal cancer Extravasation 3D Model on a Chip

Chapter VI

Tuning Enzymatically-crosslinked Silk fibroin Hydrogel Properties for the Development of a Colorectal cancer Extravasation 3D Model on a Chip[1]

ABSTRACT

Microfluidic devices are now the most promising tool to mimic *in vivo* like scenarios such as tumorigenesis and metastasis due to its ability to more closely mimic cell's natural microenvironment (such as three dimensional (3D) environment and continuous perfusion of nutrients). In this study, the ability of 2 % and 3 % enzymatically-crosslinked silk fibroin (SF) hydrogels with different mechanical properties were tested in terms of colorectal cancer cell migration, under different microenvironments in a 3D dynamic model. Matrigel was used as control. Moreover, we present a comprehensive comparison between the traditional Boyden chamber assay and our 3D dynamic microfluidic model in terms of colorectal cancer cell migration. Our results show profound differences between the two used biomaterials and the two migration models, which were explored in terms of mechanical properties of the hydrogels as well as the intrinsic characteristics of the models. Moreover, we validated the developed 3D dynamic model by demonstrating that hVCAM-1 plays a major role in the extravasation process, influencing extravasation rate and traveled distance. Furthermore, the developed model enables precise visualization of cancer cell migration within a 3D matrix in response to microenvironmental cues, shedding light on the importance of biophysical properties in cell behavior.

Keywords: Colorectal cancer; Cell migration; Mechanical properties; Silk.

[1]This chapter is based on the following publication

M. R. Carvalho, F. R. Maia, S. Vieira, R. L. Reis, and J. M. Oliveira. "Tuning Enzymatically-crosslinked Silk fibroin Hydrogel Properties for the Development of a Colorectal cancer Extravasation 3D Model on a Chip". Global Challenges, 2018, 2: 1870164. doi: 10.1002/gch2.201700100.

VI-1. GRAPHICAL ABSTRACT

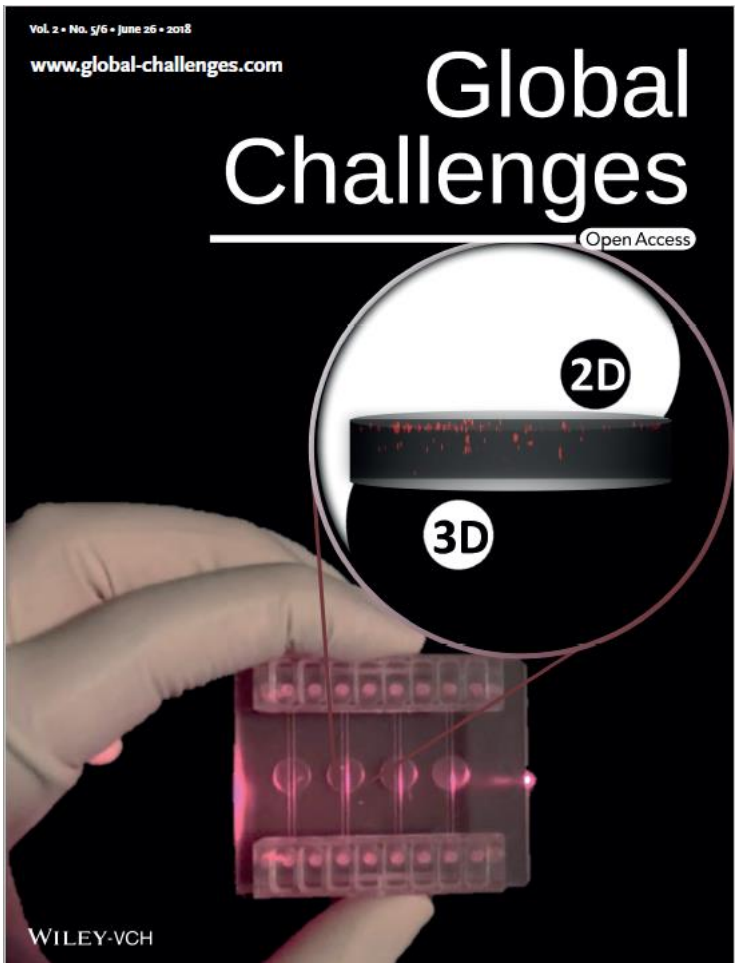

VI-2. INTRODUCTION

Colorectal cancer is a major cause of morbidity and mortality worldwide, and accounts for over 9 % of all cancer incidence. It is the third most common cancer worldwide and affects men and women equally [1].

In order to win the battle against cancer, further advances are in great need to unveil identification of cancer-causing agents in *in vitro* and *in vivo* animal models, as well as for the development of personalized therapies, drug screening, and to provide insightful knowledge on the mechanisms of tumor growth and metastasis [2]. Although *in vivo* animal models comprise the complexity of the metastatic cascade in a living system, visualization of the distinct events is

nearly impossible. In fact, recent studies suggest that the correspondence between animal models and successful clinical trials does not reach 10 % [3]. Furthermore, animal models do not allow control of cell-cell and cell-extracellular matrix (ECM) interactions, making it difficult to really understand the role of each stromal component in the tumorigenesis process. On the other hand, two dimensional (2D) *in vitro* models have reduced physiological relevance, capturing only limited aspects of the tumor microenvironment [4]. Therefore, 3D models, comprising the integration of tissue engineering (TE) strategies with microfluidic technologies have sparked a breakthrough into the design of *in vitro* microfluidic culture models. These better adapt to morphological changes in tissue structure and function over time, providing a level of precision control that could not be achieved before [5]. Microfluidics can provide useful model systems to investigate complex phenomena under combination of multiple controllable biochemical and biophysical microenvironments, coupled with high resolution real time imaging [6, 7].

This type of strategy does provide a powerful tool to develop more *in vivo* - like settings that can be applied to study cancer. Special focus on model dimensionality and microenvironment complexity is given, as a significant amount of experimental evidence has shown that both mechanical and chemical stimuli from the cell microenvironment play a key role in several types of cell behavior, namely in terms of migration [8]. Migration is frequently used as broad term in biology and applies to any directed cell movement, even in a 2D setting [9]. The ability to migrate allows cells to change their position within tissues or between different organs. However, in pathology, invasion is defined as the crossing of (tissue) 3D barriers, into the underlying interstitial tissues by malignant tumor cells [9].

So far, several synthetic and natural hydrogels have been used as ECM - like materials in the *in vitro* cell culture studies, offering characteristics such as biocompatibility and bioactivity, and have undoubtedly been proven to influence cells' behavior and fate [10-12]. However, the full potential of these recent *in vitro* models in research and therapy has remained unrealized, owing to the poorly defined animal-derived matrices in which cells are grown and in particular, mostly limited to use of Matrigel [13]. Trying to address this issue, Gjorevski *et al.* used polyethylene glycol (PEG) hydrogels to define the microenvironmental parameters that govern organoid formation [12]. That study enhanced our understanding of the mechanical regulation of intestinal stem cells by considering the effects of matrix stiffness, which had not been examined before, as

performing controlled mechanical modulations *in vivo* and in Matrigel® is challenging. The authors observed that intestinal stem cell expansion was optimal within matrices of intermediate stiffness (1.3 kPa), but that organoid formation in low stiffness matrices was optimal (150 Pa) [12].

In our study, applying these concepts, we propose the use of a 3D dynamic model using a new biomaterial developed by our group: Horseradish peroxidase crosslinked silk fibroin (SF) hydrogels [14]. The SF hydrogels easily allow the tuning of mechanical properties and identify the most suitable stiffness to study cancer cell migration. Silk is a famous natural fiber produced by the silkworm (*Bombyx mori*) cocoons and is composed of two types of protein (fibroin and sericin), lacking the common motifs such as laminin and collagen. For this reason, silk allows the substrates' mechanical contribution to cell fate to be isolated better than chemically bioactive materials, such as Matrigel. Therefore, we are able to better define and modulate the key ECM parameters that govern colorectal cancer cell migration.

By its turn, Matrigel is used as a control, since it has already been established as 3D substrate for modelling cancer microenvironments [15, 16]. Moreover, cell migration in this new platform is compared to traditional 3D Boyden chamber invasion assay. Regardless of their vast value, they do not provide tight control over the local environment, lack the ability to precisely control the spatial organization of cells in 3D matrices, cell-cell and cell-ECM interactions. Imaging is rather limited, disclosing the 3D microfluidic *in vitro* models' physiological relevance. The evaluation of the effect of hVCAM-1 was also assessed in both invasion models. It is now known that VCAM-1 is involved in mediating tumor cell adhesion to vascular endothelial cells and promoting the metastatic process [17]. Also, serum concentrations of ICAM-1 and VCAM-1 are significantly elevated in the patients with colorectal cancer in comparison with a group of healthy subjects [18]. One of the possible mechanisms is that the rolling cancer cells become activated by locally released chemokines present at the surface of endothelial cells. This triggers the activation of integrins from the cancer cells allowing their firmer adhesion to members of the Ig-CAM family such as ICAM and VCAM-1, initiating the transendothelial migration and therefore the extravasation process [17]. VCAM-1 is therefore thought to play a key role in the process of malignant progression and its presence studied in terms of impact on cell migration [19].

In this work, different concentrations of SF hydrogels were produced as 3D matrices and fine-tuned in terms of mechanical properties by means of varying the concentration of silk solution between 1 and 3 %. The realization of a 3D CRC model was achieved by using a commercially available microfluidic chip (Vena4™, Cellix®) suitable for intravasation and extravasation assays comprising a 3D microwell for the testing of ECM like materials, together with HCT-116 cancer cells. Cell migration studies using this 3D dynamic microfluidic platform in different conditions, as well as the traditional modified Boyden chamber were carried out up to 48 hours days of culturing. Matrigel was used as control. Due to its importance during the metastization of colorectal cancer cells, hydrogels were supplemented with the vascular adhesion molecule hVCAM-1 to validate our model.

VI-3. MATERIALS AND METHODS

VI-3.1. Materials and reagents

Cocoons of *Bombyx mori* were provided by the Portuguese Association of Parents and Friends of Mentally Disabled Citizens (Portugal).

VI-3.2. Preparation of silk fibroin hydrogels

VI-3.2.1. Preparation of silk fibroin solution

The purified silk fibroin (SF) was prepared as described previously by Yan *et al.* [14]. Briefly, SF was dissolved in lithium bromide (9.3 M), followed by dialysis against distilled water for 48 hours before concentrating it using a 20 wt.% poly(ethylene glycol) solution. SF solution of 16 wt.% concentration was used for further hydrogel preparation.

VI-3.2.2. Composition and in situ SF hydrogel formation

Hydrogels were prepared by mixing the concentrated SF solution with PBS at appropriate volumes to make final 1 %, 2 % and 3 % silk solutions. To promote the SF hydrogel formation, 1 mL of SF solution was mixed with Horseradish Peroxidase (HRP) (100 µL) and hydrogen peroxide (H_2O_2) (65 µL) solutions in an eppendorf in a water bath at 37 °C, as optimized previously by our group [14]. HRP solution (0.84 mg/mL) and H_2O_2 (0.36 wt %) were both prepared in PBS. For the outward cell migration (modified Boyden chamber assay), 2 % and 3 % SF hydrogels (10 µL) were placed on top of the fluoroblock membrane (VWR, Portugal) and allowed to crosslink for another 20 minutes. For the 3D dynamic migration assays, 2 % and 3 % SF hydrogel discs were prepared by adding 30 µL of the mixture solutions in a 6 mm diameter silicon mold and placed at 37 °C for crosslinking during 20 minutes. This mold size was used for the crosslinked hydrogel to fit in the Vena4™ microwells. For the SF hydrogels supplemented with hVCAM-1 (10 %) (Prepotech, Portugal), the solution was mixed with hVCAM-1 (20 µg/mL) and then placed in silicon molds for crosslinking for 20 minutes. Afterwards, hydrogels were taken out of the molds, placed in Vena4™ microwell and sealed.

VI-3.3. Preparation of Matrigel coating and hydrogel matrices: composition and *in situ* hydrogel formation

Matrigel coating in outward cell migration (modified Boyden chamber) were reconstituted from Matrigel (BD Biosciences) and diluted (250 µg/mL in 0.01 M Tris) (pH 8.0), NaCl (0.7 %) (Laborspirit, Portugal), according to manufacturer's instructions. Diluted Matrigel was carefully added to the top of the membrane and incubated at 37 °C for 2 hours. Then, the remaining liquid (coating buffer) was carefully removed from the permeable support membrane without disturbing the layer of Matrigel. For the 3D hydrogels, Matrigel were added to the 6 mm diameter silicon molds (30 µL) and placed at 37 °C for 30 minutes. For the hydrogels supplemented with hVCAM-1 (10 %), Matrigel was mixed with hVCAM-1 and then placed in silicon molds for crosslinking for 30 minutes.

VI-3.3.1. Characterization of hydrogels

VI-3.3.2. Mechanical properties determination

The 1 %, 2 % and 3 % SF and Matrigel hydrogels' storage and loss moduli were evaluated by using an oscillatory model in a rheometer (Kinexus Prot, Malvern). For each measurement, SF solution (1mL) was mixed with HRP (100 µL) and H_2O_2 (65 µL), and then the mixture (100 µL) were transferred into 8 mm silicon molds at 37 °C. After crosslinking, hydrogels were placed into the rheometer for evaluation. All samples were assayed using a plate-plate geometry. The measurements were conducted at 37 °C (n =3). Stress sweeps (0.1 Hz) were first performed to determine LVR for all the tested conditions. Frequency sweeps (0.01-1 Hz) were then performed within the LVR. The values of the shear storage modulus (G') presented in **Table V-1** were obtained at a frequency of 0.1 Hz.

VI-3.4. Cell culture

HCT-116 cells (human colon cancer cell line) originally obtained from the American Collection of Cell Cultures (ATCC, USA) were used. Cells were continuously grown in Dulbecco's Modified Eagle Medium (DMEM), (Sigma, Germany) supplemented with 10 % (v/v) fetal bovine serum and 1 % penicillin and streptomycin under standard conditions (37 °C in a humidified atmosphere containing 5 % CO_2). Medium was changed twice a week and subcultures of cells were performed when confluence reached values of ~90 %.

VI-3.5. Outward cell migration (modified Boyden chamber assay)

Cell migration was analyzed using HTS Corning FluoroBlok Cell Culture Inserts (24 well), with an 8 µm pore size (Becton Dickenson, EUA).

First, the SF hydrogels and Matrigel coating were performed as described before. Then, HCT-116 cells were pre-labelled with Cell Tracker Red (Invitrogen, Portugal) for 20 minutes (5 mM), and then seeded on top of the coating/hydrogels (30.000 cells per well). In the upper

chamber, either DMEM medium with 10 % v/v FBS or Serum-free medium were added (300 µL). In the lower chamber, either DMEM medium with 10 % v/v FBS, DMEM supplemented with 10 % v/v hVCAM-1 or with 30 % v/v FBS were added (500 µL). At different time points (0, 2, 5, 24 and 48 hours), fluorescence intensity from the bottom was measured using a microplate spectrofluorimeter (BioTek, Portugal) in area-scan bottom-reading mode, at excitation/emission wavelengths of 553/570 nm. Results are presented as the increase in fluorescence in relation to the time point 0 hours. Fluorescence images of migrating cells were collected using an inverted fluorescence microscope (Leica, Germany). In the last time point (48 hours), cells were fixed with formalin (10 % v/v) (Sigma, Germany) and stained for F-actin filaments of the cytoskeleton and nuclei with Texas Red-X phalloidin (Molecular Probes, Invitrogen, USA) and with 4,6-diamidino-2-phenylindole, dilactate (DAPI blue, Molecular Probes, USA), respectively, following supplier's protocol.

VI-3.6. *In vitro* studies under a 3D microfluidic platform

VI-3.6.1. Vena4™ Microfluidic Chip

The Vena4™ biochip from Cellix® (Irland) is constituted by 4 channels with 100 µm of height, 800 µm of width and 2.8 cm of length. Each channel is connected to two microwells (one in each end) where a microfluidic recirculating pump controlled by an iPod Touch (Kima™ pump) is connected, and a microwell separated by a 8 µm pore size membrane. The sample volume of each channel was 10 µL. The chip was fabricated in optically clear acrylic with a substrate thickness of 500 µm, enabling the observation of cells under a brightfield, fluorescence (Leica, Germany) and confocal microscope (Zeiss, Germany).

VI-3.6.2. Cell migration assay in 3D VenaT4™ biochips

Cell migration under a dynamic 3D microfluidic platform was conducted using VenaT4™ biochips (Cellix®, Irland). Each biochip channel was coated with fibronectin (Sigma, Germany) (100 µg/mL) and placed in a humidified sterile petri dish and incubated at 37 °C for 1.5 hours.

After the incubation period, HCT-116 cells were pre-labeled with red cell tracker CM-DiI Dye (1 µM) (Invitrogen, Portugal) and incubated at 37 °C for 30 minutes. After, labeled cells were seeded on Vena4™ microchannels using a standard yellow pipette (30.000 cells/channel). In order to prevent drying, after the initial 30 minutes of incubation, complete medium DMEM was added to the channels. The hydrogels (3 % and 2 % SF and Matrigel), previously crosslinked in the silicon molds, were placed in the microwell and sealed. At determined time points (0 and 48 hours), the chip was observed under confocal laser scanning microscopy (Leica, Germany) to monitor pre-labeled cells' migration towards the hydrogel with and without hVCAM-1.

VI-3.6.3. ATP quantification

To quantify the viable cells that migrated towards the hydrogel, ATP was measured using CellTiter-Glo Luminescent Cell Viability Assay (Promega, Portugal). For that, hydrogels were removed from Vena4™ Biochips after 48 hours of culture and placed in 96 well plates. Then, the analysis was performed following the manufacturer's instruction. SF and Matrigel hydrogels were used as controls. Briefly, CellTiter-Glo® Reagent agent was added (150 µL) to each well of the 96-well plate and incubated for 10 minutes at room temperature to lysate cells. Then, the cell lysate (100 µL) was transfer to wells of a 96-well white opaque microtiter plate (in triplicate). This plate was loaded into the luminometer (Perkin-Elmer, EUA). The signal intensity of the samples was measured. Light output was given as the integral relative light units (RLUs). ATP measurements were carried out at room temperature. An ATP standard curve was generated using ATP solutions ranging from 5 to 1,000 cells and luminescence readings from experimental samples were fit into this curve to generate moles of ATP.

VI-3.6.4. Live/Dead assay

The viability of cells migrated into the hydrogels was assessed using the Live/Dead assay. Cell-laden matrices were washed three times with PBS (Sigma, Germany), then incubated (10 minutes, 37 °C in the dark) with calcein AM (1 µM, live cells) and propidium iodide (PI, 1.5 µM, dead cells) and washed again. Samples were imaged by confocal laser scanning microscopy.

Two filters were used: for green excitation/emission (495/515 nm) and for red excitation/ emission (510/595 nm).

VI-3.7. Statistical analysis

Statistical analyses were performed using GraphPad Prism 5.0 software version 5.0a. The non-parametric Mann–Whitney test was used to compare two groups, whereas comparison between more than two groups was performed using the Kruskal–Wallis test followed by Dunn's comparison test. A value of $p < 0.05$ was considered statistically significant.

VI-4. RESULTS

VI-4.1. Characterization of hydrogels

VI-4.1.1. Mechanical properties determination: Rheology

The influence of polymer type and concentration of the used hydrogels was studied in terms of their rheological behavior in order to analyze the mechanical properties of the hydrogels. Stress sweeps (0.1 Hz) were first performed to determine the linear viscoelastic region (LVR) for all the tested conditions. Frequency sweeps (0.01–10 Hz) were then performed within the LVR. The values of the shear storage modulus (G') and loss modulus (G'') are presented in **Table V-1** and were obtained at a frequency of 0.1 Hz.

Storage modulus G' is known as the "solid-like" or elastic component of the gel, and G'' (Loss modulus) as the "liquid-like" or viscous component. The system is considered a gel if the value of G' is greater than G", which was confirmed by the results in **Table V-1**, where all the values for the loss modulus are many folds smaller than the storage modulus, which was expected for an hydrogel system that is stable during time. The higher the G', the less it deforms under compression and the more energy it can retain and store.

Table VI-1 – Composition, rheological properties and original mesh size of hydrogels at a frequency of 0.1 Hz.

Type of hydrogel	Cells	Incubation (time)	Storage modulus (G', Pa))	Loss modulus ((G", Pa))
1 % SF	no	30 minutes	65 ± 9	8 ± 5
2 % SF	no	30 minutes	488 ± 72	16 ± 4
3 % SF	no	30 minutes	1136 ± 94	20 ± 3
Matrigel	no	1h	45 ± 15	4 ± 0.5

Indeed, when comparing the G' value between SF hydrogels and Matrigel, the first is much lower, corroborating the fact that even after crosslinking, Matrigel is difficult to handle and is not a consistent material, which is an important feature when considering performing further studies on the hydrogels. When comparing SF hydrogels, the G' of 3 % SF hydrogel is much higher than the 2 %, which is turn is much higher than the 1 % formulation. Consequently, rheology measurements confirm that the stiffness and mechanical properties of the hydrogels increase with increasing polymer concentrations in the case of silk fibroin, and this is due to the increase in the number of polymer chains and crosslinking points within the system, allowing the tuning of mechanical properties and further study of possible applications in cell migration and tumor/spheroid formation.

VI-4.2. Outward cell migration (modified Boyden chamber assay)

This model was chosen to do a comparative study of colorectal cancer cells' behavior regarding cell migration. As performed in our 3D dynamic model, 2 % and 3 % SF and Matrigel were used and the presence/absence of hVCAM-1 in order to have comparable data. Besides, another condition was added in this experiment: a gradient of serum (from 0 % to 30 % (v/v) FBS), generally used as chemoattractant in the modified Boyden chamber assay, to be compared with migration observed with the gradient of hVCAM-1. As this molecule is thought to be involved in colorectal cancer migration and metastasis, it is interesting to compare it with FBS. In the condition described as the control, the upper and lower chamber are filled with normal DMEM medium with no molecules' gradient. Regarding the hydrogels, 10 µL of 2 and 3 % SF hydrogels

were crosslinked at 37 °C on top of the membrane. This is the minimum quantity to cover the surface of the membrane. For Matrigel, manufactures' protocol was followed and a dilution of Matrigel was used to produce a thin coating. Different time points were analyzed to see the progression of migration and corroborate the fact that this kind of phenomena occurs mainly within the first 24 hours, as can be seen in **Figure V-1** [20, 21]. Also, to prevent the quantification of cell proliferation instead of cell migration, the experience was terminated at 48 hours

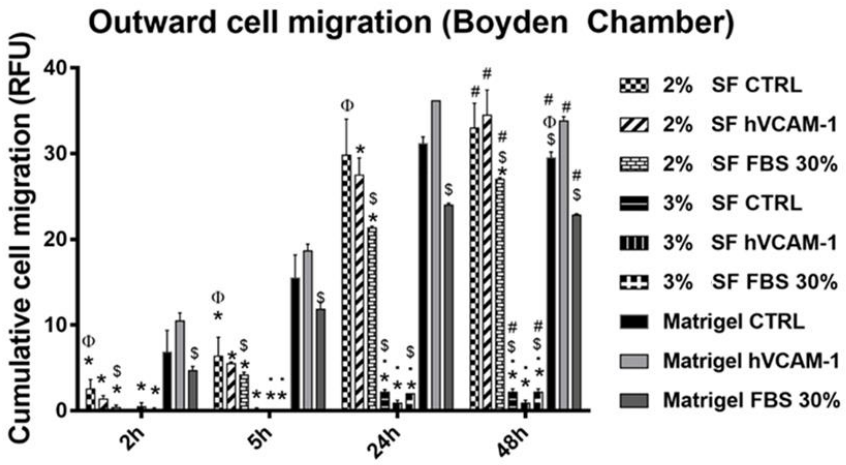

Figure VI-1 - Quantification of outward migration of HCT-116 (labeled with Red Cell Tracker in modified Boyden chamber from 2 and 3 % SF hydrogels and Matrigel coating, in response to the presence of hVCAM-1 and 30 % (v/v) of FBS. (* indicates significant differences when comparing to Matrigel coating at each time point; • indicates significant differences when comparing to 2 % SF at each time point; $ indicates significant differences when comparing to VCAM at each time point; Φ indicates significant differences when comparing to FBS at each time point; # indicates significant differences when comparing to time point 2 hours.

Figure V-1 shows the final results of cumulative cell migration (in terms of fluorescence quantification) from 2 up to 48 hours. Fluorescence at 0 hours was considered our blank. The first noticeable result is that migration phenomena starts almost immediately after the seeding on top of the hydrogels and that the number of cells crossing through the hydrogel and the membrane towards the bottom chamber grows until 48 hours of culturing. At 48 hours, by the end of the experience (the same time point that is going to be analyzed in 3D model Vena4™), and where cell migration is more evident, interesting results can be withdrawn. Both in the case of 2 % SF and Matrigel, there is an intense cell migration in the presence of hVCAM-1,

significantly higher than in the presence of the traditional chemoattractant FBS and the control (absence of any chemoattractant). Interestingly, cell migration to the bottom side of the membrane increases continuously until 48 hours, as all the conditions are significantly different when comparing to time point 2 hours. Maybe one of the most relevant observations in this experiment is that from the beginning, especially at first time points, Matrigel allows more cell migration than 2 and 3 % SF. Alternatively, by the last time-points, there is no substantial differences in the fluorescence intensity between 2 % SF and Matrigel. At last, it becomes clear that 3 % SF allows very little cell migration when comparing to 2 % SF and Matrigel.

The panel represented in **Figure V-2** shows the cells that have migrated thought the hydrogels and across the black membrane of the modified Boyden chamber. Initially, cells were pre labeled with red cell tracker for the quantification analysis, but for better visualization, they were later stained with DAPI (blue- nucleus) and Phalloidin (red – f-actin filaments) and observed under inverted fluorescence microscopy. The first column of the image shows every condition, but without cells. Therefore, the pores of the membrane are clearly visible under red fluorescence and no cells are observable. The second column, described as control, corresponds to the condition in which the upper and lower chambers are filled with normal DMEM medium with no molecules' gradient. Corroborating the results shown in the previous graphic, no cells were observed in the bottom of membranes with 3 % SF hydrogels. In the case of 2 % SF hydrogel and Matrigel coating, it is possible to observe that the cells have migrated and present their normal round shape morphology.

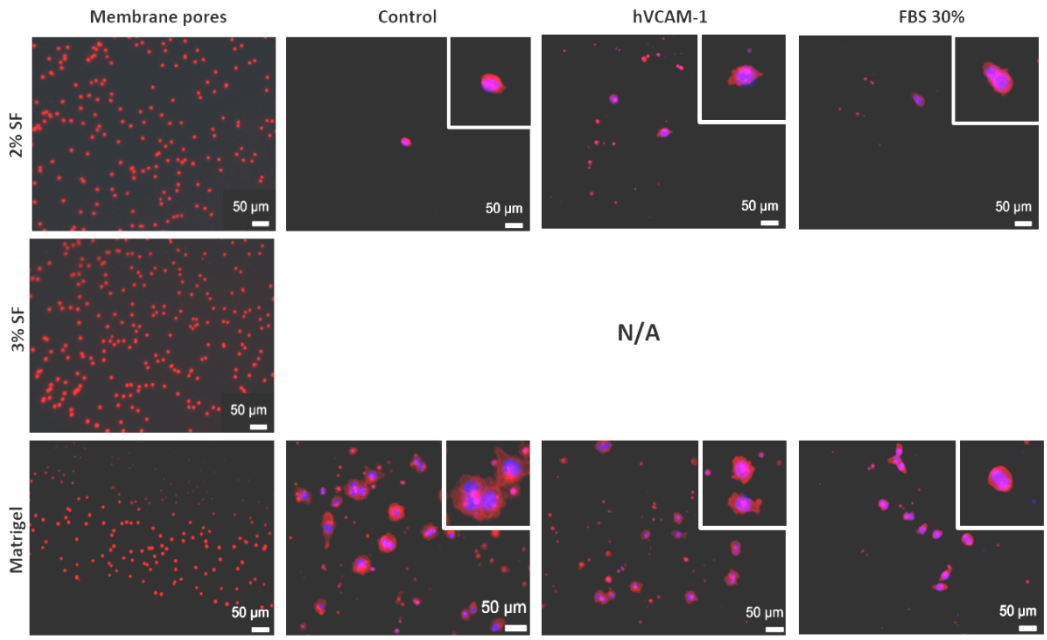

Figure VI-2 - Representative panel of outward migration of HCT-116 cells from 2 % and 3 % SF and Matrigel coating in response to gradients of hVCAM-1 and FBS. Migrating cells attached to the lower side of the insert membrane at 48 hours stained with DAPI (blue) and Phalloidin (Red). The first column represents the pores of the membrane without cells. N/A denotes no cell migration.

VI-4.3. *In vitro* studies under a 3D microfluidic platform

VI-4.3.1. Cell migration assay in 3D VenaT4™ biochips

Although there is still a lot of uncertainty regarding the critical step in the formation of metastatic tumors, the ability of circulating tumor cells to adhere to and transmigrate across the endothelium at a remote site is certainly essential. In the case of this experience, the extravasation is mimicked when adhered red labeled HCT-116 cells seeded on the microchannel and subjected to flow perfusing media, cross the 8 µm pore membrane and migrate towards the underlying hydrogel (from top down) and observed on the confocal microscope, as can be seen in **Figure V-3.**

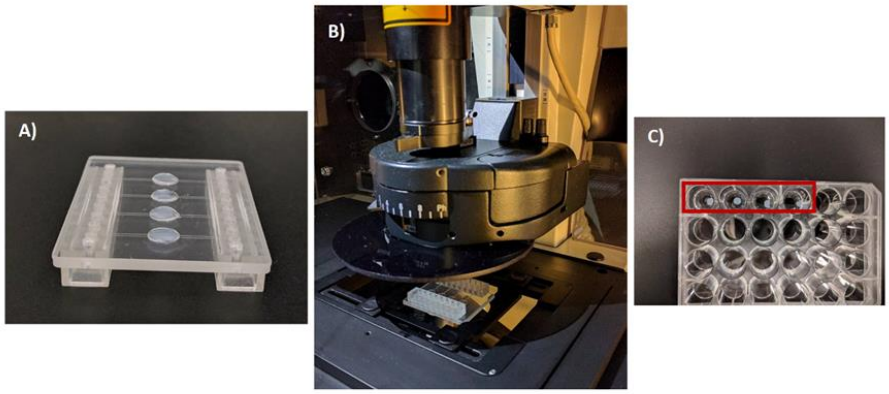

Figure VI-3 - A) Example of Vena4™ chip with SF hydrogels placed on the microwells. B) Vena4™ placed under the confocal microscope for migration studies. C) Retrieval of SF hydrogels out of the microfluidic chip for further analysis

In this case, pre-crosslinked 2 and 3 % SF and Matrigel hydrogels are placed in the microwell under the microchannels. Since literature suggests this type of migration occurs within the first 24 hours of experience, all of our experiments lasted up to 48 hours [21, 22]. Examples of renderings of 3D confocal stacks of all hydrogels are shown in **Figure V-4**. Confocal microscopy images were taken 3 hours after cell seeding, in order to let them adhere to the microchannel in the 3D model (data not shown), and no migration was observed in any of the tested formulations. This means that all of the labeled cells were within the microchannel. After 48 hours of experience, we placed the microchip in the confocal microscope and assessed cell migration. When testing SF hydrogels as ECM mimic alternatives, in the 3 % formulation no cell migration appeared to happen, even in the presence of hVCAM-1. However, when observing migration experiments with 2 % formulation, results show a surprising difference and a large number of cells had crossed the membrane and migrated towards the center of the 2 % SF hydrogel. Moreover, in the case of 2 % SF, in the absence of hVCAM-1, we observed cells migrating about 100 - 150 µm in depth. On the other hand, in the presence of the hVCAM-1, cells could migrate a larger distance, up to 200 µm (see white arrow in **Figure V-4**).

Regarding our control material, Matrigel, as depicted by the representative **Figure V-4**, a few cells crossed the membrane and migrated through the micro porous membrane towards the Matrigel. No apparent exacerbation in terms of cell migration was observed in the presence of hVCAM-1 molecule.

Summarizing the results of cell migration in the 3D microfluidic chip, we observed that when testing SF, the softer hydrogel (2 %) allowed increasing levels of cell migration, and within this condition, the presence of hVCAM-1 was translated in a larger distance traveled by the cells, inside the hydrogel. However, concentrated Matrigel hydrogel, generally used in this types of experiments, do not favor cell migration and no effect of hVCAM-1 is visible.

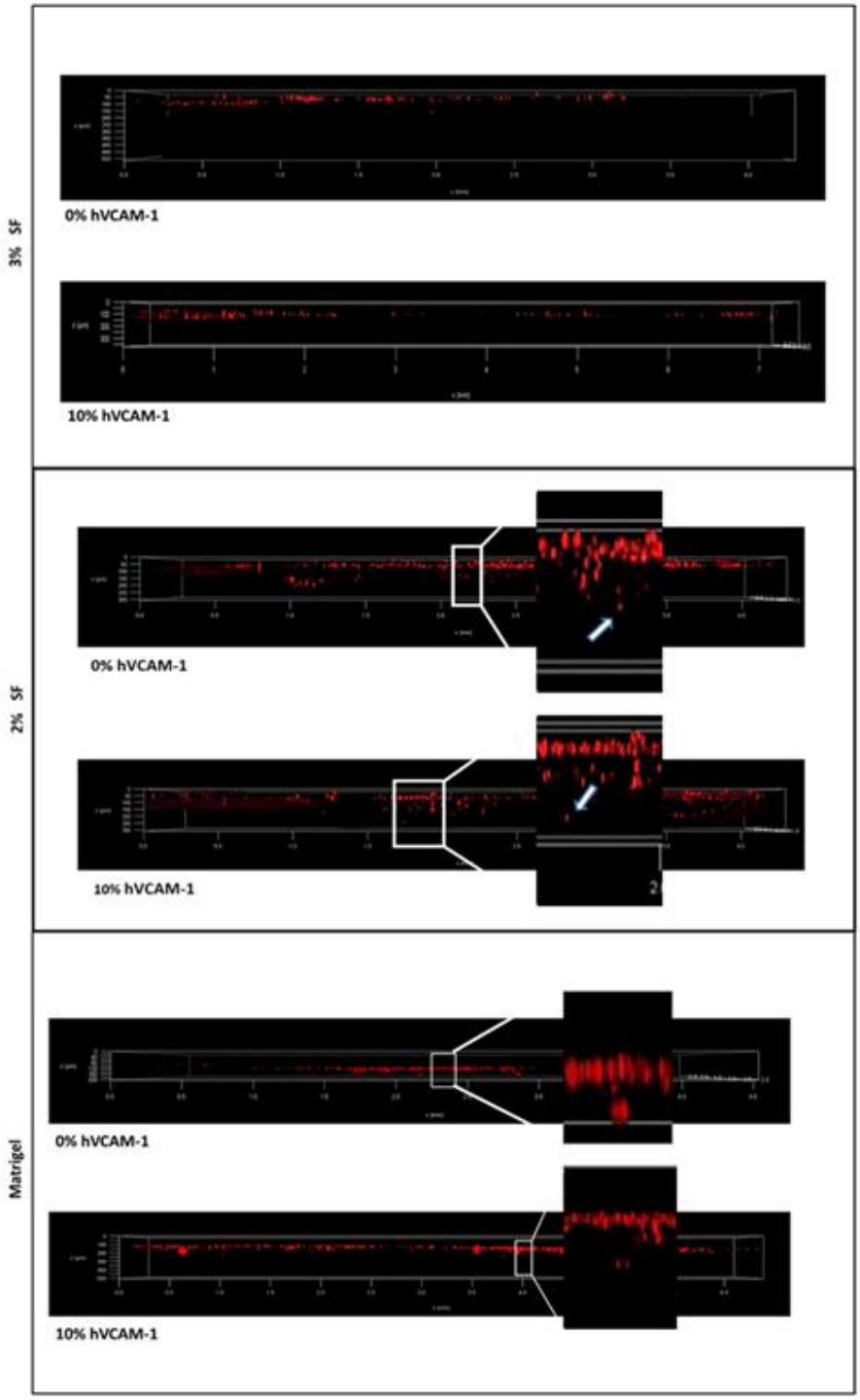

Figure VI-4 - Representative confocal microscopy images of red-labeled HCT-116 cells' migration towards 3 % and 2 % SF hydrogels and Matrigel, (with and without hVCAM-1) in microfluidic chip Vena4™ at 48 hours.

VI-4.3.2. Live/dead assay

After assessing HCT-116 colorectal cancer cells´ migration from the microchannels towards the hydrogels in the Vena4™ chip after 48 hours in culture, we wanted to qualitatively determine cell viability. For that, the same experimental set up was used, but without pre-labeling the cells. After 48 hours, the hydrogels were carefully removed from the Vena4™ microfluidic chip (**Figure V-3C**) and live (green) and dead (red) cells were stained by adding Calcein-AM/Propidium Iodide (PI) and hydrogels observed under confocal microscopy. Calcein-AM fluoresces in green in case of living cells, as it is cleaved by esterases and produces green fluorescence, which is confined in the living cells by an intact cytoplasmic membrane. PI is red as it is able to enter dead cells and nuclei through the damaged membrane and binds to fragmented DNA, emitting a red fluorescence. As observed in the representative panel in **Figure V-5A**, all the cells that have migrated towards the hydrogels in all the conditions were still viable. Although this is not a quantitative assay, it is worth noticing a higher number of (viable) colorectal cancer cells in hydrogels supplemented with hVCAM-1, and even more pronounced in 2 % SF, corroborating the confocal images results seen before on **Figure V-4**. This means that this 3D dynamic model allows for cell viability. The hydrogels are kept hydrated, although they are not submerged in medium, just subjected to media perfusion on top of the microchannels.

VI-4.3.3. ATP quantification

After the extravasation experiments with Vena4™, where the goal was to assess the best formulation to observe cell migration from the microchannel to the underlying hydrogel (confirmed through confocal microscopy), we wanted to quantitatively determine cells viability in the hydrogels. Cells' viability inside the hydrogels is an important parameter to determine their suitability as ECM-like matrices. For that, the extravasation experiment was carried out during 48 hours, after which the hydrogels were retrieved from the microfluidic chip and tested for bioluminescent-based ATP quantification. The reaction was catalyzed by the enzyme luciferase obtained from the firefly (Photinus pyralis). The $MgATP^{2-}$ converts the luciferin into a form which is capable of being catalytically oxidized by the luciferase in a high quantum yield chemiluminescent reaction. Moreover, a calibration curve using as low as 5 cells was used to determine its

correlation with bioluminescent signal in 2D (Supplementary material). Although we cannot directly correlate the number of cells obtained in 2D and 3D, the signal obtained when testing the hydrogels show that the cells remained viable, corroborating the previously showed live/dead assay results, as can be seen in **Figure V-5B**. Also, it was possible to see that, in agreement to what was observed by confocal microscopy, the extravasation experiment performed with 2 % SF shows the strongest signal, being significantly different from the 3 % formulation and Matrigel.

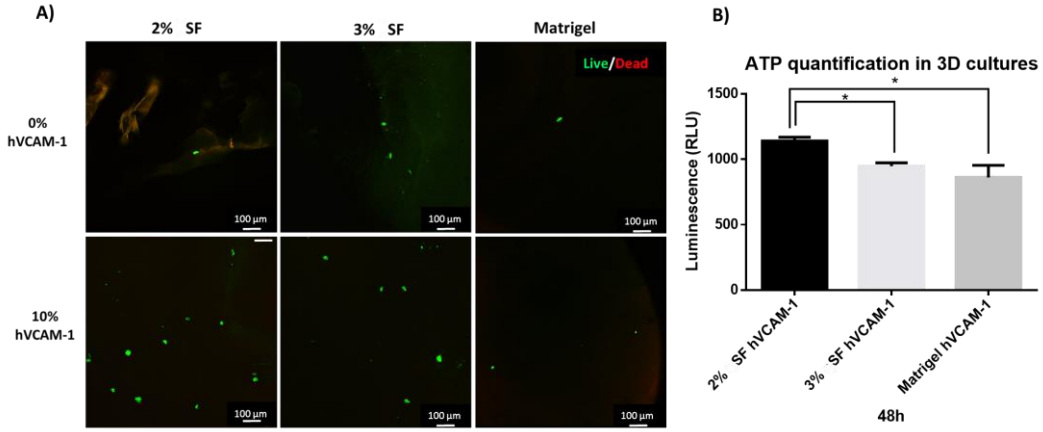

Figure VI-5 - A) Cell viability (live/dead assay) of HCT-116 cells that migrated in the hydrogels after 48 hours of culture in Vena4™ microfluidic chip. B) Cell viability of 3D cultures after 48 hours of culture (2 % and 3 % SF and Matrigel hydrogels with hVCAM-1). Data is presented as mean ± stdev (n=3), (*) denotes statistical differences ($p<0.05$).

VI-5. DISCUSSION

It is now more recognized than ever that the integration of microfluidic techniques together with advanced biomaterials such as ECM mimicking tunable hydrogels can supply a unique platform to develop 3D organized constructs mimicking the *in vivo* tumor microenvironment [23, 24]. Concerning this, it was our goal to take advantage of our group's great expertise in biomaterials and test SF hydrogels in the context of colorectal cancer metastasis. Silk is an excellent candidate for cancer related studies due to its biocompatibility and highly tunable properties [14]. To the best of our knowledge, there has been lacking specific attempts to use tunable silk hydrogels as 3D ECM like materials to push forward the field of colorectal cancer metastasis research, combined with a confocal compatible microfluidic platform.

This innovative work aims at using a dynamic 3D microfluidic platform to test several silk hydrogel formulations for HCT-116 cell migration (extravasation). Also, an extensive comparative study between the traditional modified Boyden chamber assay and our 3D microfluidic chip to assess colorectal cancer cell invasion, using 2 and 3 % SF hydrogels and Matrigel as a control group was performed. Although 1 % SF hydrogels were produced and characterized in terms of rheology, they were not tested for cell migration, as the 2 % silk formulation was the highest formulation to allow HCT-116 cancer cell migration in a dynamic environment, and robust enough to retrieve for further analysis such as ATP quantification and live/dead (**Figure V-3**). Moreover, the influence of hVCAM-1, a molecule widely present in colorectal cancer metastasis processes is also assessed in order to validate our 3D dynamic model [17].

An innovative aspect of our study is that in our proposed 3D model, unlike most models, which focus on seeding cells on hydrogel sheets as well as encapsulating them within the 3D matrices, we seed cells on a microchannel, allow them to adhere, and observe their migration through a microporous 8 µm membrane and towards the hydrogel [25]. Therefore, this extravasation model represents a more realistic scenario of the extravasation process [26]. Literature suggests metastasis assays, being intravasation or extravasation, generally occurs within the first 24 hours of tumor cell contact with the endothelium, therefore we decided to study this phenomena within the first 48 hours [27].

Based on the widely used modified Boyden chamber, we determined cell invasion by quantifying the outward cell migration of fluorescent labeled cells. In this assay, a layer of ECM like matrix is deposited on the porous membrane. Although collagen and laminin are also used, this layer is typically a Matrigel coating [28]. Results of migration show that migration rates are similar between 2 % SF and Matrigel at 48 hours, with a significant increase when in the presence of hVCAM-1 in both cases. This result is relevant because it shows differences between hVCAM-1 and FBS gradients, being the latest, almost always used as chemoattractant [9]. It exposes the real influence of mimicking the *in vivo* microenvironment cues when studying cancer cell migration. Regarding the 3 % SF conditions, it becomes clear that the matrix does not favor cell migration in the Boyden chamber assay. In addition, in the first hours of the assay, results were striking in terms of the difference between cancer cell migration in Matrigel and 2 % SF, showing that Matrigel coating allows significantly more migration than 2 % SF.

When moving to our newly developed 3D microfluidic model, results are outstandingly different. As can be seen in **Figure V-4**, after 48 hours of dynamic culture, when analyzing the tissue engineered 3D model in the confocal microscope, no noticeable cell migration was perceived, and no observable effect was attributed to the presence of hVCAM-1 in the 3 % SF hydrogel. When moving to the 2 % formulation, we observed it allowed for a large number of cells to move from the microfluidic channel, through the microporous membrane and into the hydrogel. In the case of 2 % SF hydrogel crosslinked in the presence of 10 % hVCAM-1, it was translated in a greater distance traveled by the cells. More quantitative assays are needed to corroborate this information, but the representative confocal images leave no doubt about this change of behavior and add evidence on the association of hVCAM-1 with malignant potential in colorectal cancer. On the other hand, when comparing the observations in the two tested scenarios (3D static (modified Boyden chamber assay) and 3D dynamic (our proposed microfluidic model)), a major difference is detected in cell behavior in the case of our control material: Matrigel. Whereas in the Boyden chamber cells migrate in large numbers from the first hours in the Matrigel coating (**Figure V-2**), in the dynamic 3D model, this does not happen (**Figure V-4**). These findings came as a surprise when analyzing the rheology results of the hydrogels. In fact, considering the data from rheology analysis it was expected that 2 % SF, (G' value of 488 ± 72 Pa) allowed less cell migration than Matrigel (G' value of 45 ± 15 Pa), since it is stiffer. Nevertheless, the opposite trend was observed, with more cell migration in the stiffer 2 % silk hydrogel than the softer Matrigel. This phenomena could be explained by the different composition of the hydrogels. In this sense, silk hydrogels has no binding motifs (*e.g.* RGD peptide), but Matrigel has natural mammalian binding motifs. It has already been discussed and reported in the literature a possible biphasic role of Matrigel that can partially explain these phenomena: at low concentration, such as coating, Matrigel facilitates migration, most probably by providing a supportive and growth factor retaining environment. At high concentration, Matrigel slows down migration, possibly due excessive attachment [22]. In the Boyden chamber assay, following suppliers instructions, we used a Matrigel coating by diluting Matrigel to 250 µg/mL, nearly 20 fold less concentrated then the hydrogels used in our 3D dynamic model.

On the other hand, silk hydrogels obtained from *Bombyx mori* are not completely deprived of mammalian binding motifs. Silk proteins are comprised of a main heavy chain, which can be

considered a hydrophobic protein with co-block design [29]. Hydrophilic segments are involved in the self-assembling process, resulting in changes in water content and regulation of the mechanical properties of the final material, which can explain cell migration in these matrices [29]. In addition, two short aminoacid sequences that are RGD-like are present in the N-terminus segment of heavy-chain, VTTDSDGNE and NINDFDED, as well as the recognized fibroblast integrin [29].

In fact, Friedl *et al.* described two different migration movements, mesenchymal and amoeboid migration [30]. In the first, mesenchymal migration, cells exhibit high attachment and cytoskeletal contractility, which allow cells to migrate. But in the second, amoeboid migration, cells present poor attachment and a lack of stress fibers, which results in a round morphology. For so, they develop a strategy that consists in the formation of blebs and the use of propulsive forces to migrate. In this sense, the 2 % SF matrices possess mechanical properties that can allow amoeboid movements [30]. In the case of 3 % matrices, similar results were observed when comparing the Boyden chamber assay to the proposed 3D dynamic model. The resistance to cell migration in the 3 % SF formulation, even in the presence of chemoattractant, can be explained by matrix stiffness. By its turn, a G' value of 1136 ± 94 Pa of the 3 % silk formulation is simply too stiff to allow cell migration through the polymer's fibers, as confirmed by Bott *et al.*, who revealed that in spite of matrix sensitivity to proteases (*e.g.* MMP) and the presence of cell-integrin binding sites, at high stiffness (G′ >1200 Pa) the matrix acts as a barrier for cells cultured in 3D to migrate [31]. As a matter of fact, these results are in alignment with those observed by Gjoresvki *et al.,* showing that in the case of PEG hydrogels, a higher matrix stiffness of 1300 Pa is suitable for cell expansion, but organoid development is optimal in a later stage, in gels with a lower stiffness of around 100 Pa, which can be achieved by the presence of metalloproteinases [12]. In our case, we are interested in studying cell migration, a different phenomenon than cell expansion and organoid formation, where the intermediate stiffness seems to work best. In a further stage, by using longer periods of culture in dynamic conditions, we aim at creating a tumoroid by modulating silk fibroin hydrogels mechanical properties to achieve lower stiffness, such as the 1 % SF formulation (64 ± 9 Pa, **Table V-1**).

It is important to bear in mind that the effects of ECM properties on the normal epithelial morphogenetic program are fundamentally different from those reported for cancer cells in

synthetic gels, most likely reflecting central differences between developmental morphogenesis and tumorigenesis [32]. Matrix stiffness is therefore a crucial biophysical aspect of the tumor microenvironment and, consequently, has been profoundly studied in collagen, polyacrylamide, and Matrigel hydrogels, but not in silk [33]. Therefore, the proposed 3D dynamic model offers an opportunity to better understand the role of mechanical properties of the matrix environment, assessing specific effects of matrix stiffness on colorectal cancer progression [33, 34].

Taken together, these facts can explain the differences we found between the traditional static and dynamic models and disclose the importance of using relevant *in vitro* models.

After our study, we believe we are facing a question of developing a microenvironment mimic material, ultimately choosing between bio-based vs polymer-based ECM like materials. Although there is undoubtedly a growing number of studies based on polymers, Matrigel, a cell secreted protein mixture, has been considered the standard material in terms of cell migration. However, since further development of chip-based 3D cell culture in cancer research will be largely dependent on the improvement of biomaterials that emulate the ECM and the capacity to scale-up these complex technologies, Matrigel may not represent the best choice, for several reasons: Its composition is undefined and cannot be fully controlled, changing from batch to batch, with a complex mixture of components (unknown amounts of growth factors and proteins) that may play a role in cell behavior. In terms of practical use, it's not as user friendly as silk, due to its gelling temperature and stiffness/consistency to perform further tests on the hydrogels [35, 36]. Moreover, it won't allow long term experiments, very much needed to understand the real process of tumor and metastasis formation. Development of integrating TE approaches and microfluidics into easy-to-use, scalable, reproducible and cost-effective systems will be the key to their success and future translation to the market [37].

The Boyden chamber assay, exploiting a chemokine gradient between upper and lower chambers to drive cell invasion and migration, can be readily adapted to model specific extracellular matrix (ECM) chemistries by simple coating procedures and is undoubtedly a precious tool. However, a comprehensive assessment of three-dimensional tumor cell invasion or migratory mechanisms using histological techniques is difficult to achieve in these systems, with metrics restricted to an end-point summation of cell numbers in the lower chamber. Controlling the spatial distribution of cells on extracellular proteins at the 2D interface is challenging and we

anticipate that with scientific research development, biomaterial platforms with controlled *x, y* and *z* internal dimensions will prove a valuable improvement. Additionally, the developed 3D dynamic model presents several advantages such as the microchannels in contact with the 3D microenvironment, flow, the real-time tracking of cells, a fine balance between complexity and experimental control and the ability to isolate the effect of variables. Horseradish crosslinked hydrogels represent a suitable ECM like material, with the advantage of being easily tunable in order to best match the desired application. However, this model still lacks some aspects in order to represent the real complexity of tumor microenvironment. For instance, the use of primary tumor cells (making it a patient specific assay when testing drugs) and a confluent monolayer of endothelial cells along the microchannel will add the very much needed complexity of the cell–cell junctions between endothelial cells and the ECM that they produce, being this our next goal.

VI-6. CONCLUSIONS

3D *In vitro* dynamic models allow scientists to study aspects of the tumor microenvironment using specific extracellular matrices and cell types. Controlling and understanding the effect of the various components of these models pushes the field forward and enables investigation of interactions within the tumor microenvironment, as well as the response to stimuli such as chemoattractants and chemotherapeutics. However, microfluidic models need standardization and reproducible formats suitable for high-throughput applications. If cell migration studies are to be used to test drug efficacy in this context, 3D models have to be reliable with regard to fabrication and incorporation of the most adequate ECM like material to reduce arbitrary cell migration patterns.

We explored for the first time silk hydrogels as ECM like materials to mimic tumor microenvironment and to study colorectal cancer migration, compared to a control group: Matrigel. Moreover, after comparing the proposed 3D dynamic microfluidic model to the traditional Boyden chamber assay, fundamental differences in terms of colorectal cancer cell migration were shown. Ultimately, we developed a tunable Silk hydrogel for the development of a CRC Extravasation 3D Model on a Chip. This model represents a valuable tool to better

understand cell migration and tumorigenesis processes, consisting in a proof of concept, where different materials can be assessed as ECM like materials, as well as the influence of chemoattractants.

VI-7. ACKNOWLEDGMENTS

This article is a result of the project FROnTHERA (NORTE-01-0145-FEDER-000023), supported by Norte Portugal Regional Operational Programme (NORTE 2020), under the PORTUGAL 2020 Partnership Agreement, through the European Regional Development Fund (ERDF). Mariana Carvalho acknowledges her PhD scholarship NORTE-08-5369-FSE-000044, funded by Programa Operacional Regional do Norte, Fundo Social Europeu, Norte2020 TERM&SC. F.R. Maia acknowledges Portuguese Foundation for Science and Technology (FCT) for her Postdoc scholarship (SFRH/BPD/117492/2016). Sílvia Vieira is also greatly acknowledge FCT for her PhD scholarship (SFRH/BD/102710/2014). J. M. Oliveira thanks FCT for his distinction attributed under the FCT Investigator program (IF/00423/2012 and IF/01285/2015).

VI-8. REFERENCES

1. Haggar, F.A. and R.P. Boushey, *Colorectal Cancer Epidemiology: Incidence, Mortality, Survival, and Risk Factors.* Clinics in Colon and Rectal Surgery, 2009. **22**(4): p. 191-197.
2. Carvalho, M.R., et al., *Significance of Tissue-engineered 3D in-vitro models for cancer research and drug screening.* Trends Biotechnol, 2015.
3. Mak, I.W., N. Evaniew, and M. Ghert, *Lost in translation: animal models and clinical trials in cancer treatment.* Am J Transl Res, 2014. **6**(2): p. 114-8.
4. Katt, M.E., et al., *In Vitro Tumor Models: Advantages, Disadvantages, Variables, and Selecting the Right Platform.* Frontiers in Bioengineering and Biotechnology, 2016. **4**: p. 12.
5. Carvalho, M.R., et al., *Evaluating Biomaterial- and Microfluidic-Based 3D Tumor Models.* Trends in Biotechnology. **33**(11): p. 667-678.
6. Wlodkowic, D. and Z. Darzynkiewicz, *Microfluidics: Emerging prospects for anti-cancer drug screening.* World J Clin Oncol, 2010. **1**(1): p. 18-23.
7. Majedi, F.S., et al., *On-Chip Fabrication of Paclitaxel-Loaded Chitosan Nanoparticles for Cancer Therapeutics.* Advanced Functional Materials, 2014. **24**(4): p. 432-441.
8. Maia, F.R., et al., *Matrix-driven formation of mesenchymal stem cell-extracellular matrix microtissues on soft alginate hydrogels.* Acta Biomater, 2014. **10**(7): p. 3197-208.

9. Justus, C.R., et al., *In vitro Cell Migration and Invasion Assays.* Journal of Visualized Experiments : JoVE, 2014(88): p. 51046.
10. Liu, J., et al., *Soft fibrin gels promote selection and growth of tumorigenic cells.* Nat Mater, 2012. **11**(8): p. 734-41.
11. Fang, X., et al., *Novel 3D co-culture model for epithelial-stromal cells interaction in prostate cancer.* PLoS One, 2013. **8**(9): p. e75187.
12. Gjorevski, N., et al., *Designer matrices for intestinal stem cell and organoid culture.* Nature, 2016. **539**(7630): p. 560-564.
13. Fatehullah, A., S.H. Tan, and N. Barker, *Organoids as an in vitro model of human development and disease.* Nat Cell Biol, 2016. **18**(3): p. 246-54.
14. Yan, L.P., et al., *Tumor Growth Suppression Induced by Biomimetic Silk Fibroin Hydrogels.* Sci Rep, 2016. **6**: p. 31037.
15. Benton, G., et al., *Matrigel: From discovery and ECM mimicry to assays and models for cancer research.* Advanced Drug Delivery Reviews, 2014. **79–80**: p. 3-18.
16. Bielecka, Z.F., et al., *Three-dimensional cell culture model utilization in cancer stem cell research.* Biol Rev Camb Philos Soc, 2016.
17. Gout, S. and J. Huot, *Role of Cancer Microenvironment in Metastasis: Focus on Colon Cancer.* Cancer Microenvironment, 2008. **1**(1): p. 69-83.
18. Schlesinger, M. and G. Bendas, *Vascular cell adhesion molecule-1 (VCAM-1)—An increasing insight into its role in tumorigenicity and metastasis.* International Journal of Cancer, 2015. **136**(11): p. 2504-2514.
19. Velikova, G., et al., *Serum concentrations of soluble adhesion molecules in patients with colorectal cancer.* British Journal of Cancer, 1998. **77**(11): p. 1857-1863.
20. Joyce, J.A. and J.W. Pollard, *Microenvironmental regulation of metastasis.* Nat Rev Cancer, 2009. **9**(4): p. 239-52.
21. Bersini, S., et al., *A microfluidic 3D in vitro model for specificity of breast cancer metastasis to bone.* Biomaterials, 2014. **35**(8): p. 2454-61.
22. Anguiano, M., et al., *Characterization of three-dimensional cancer cell migration in mixed collagen-Matrigel scaffolds using microfluidics and image analysis.* PLOS ONE, 2017. **12**(2): p. e0171417.
23. Alemany-Ribes, M. and C.E. Semino, *Bioengineering 3D environments for cancer models.* Adv Drug Deliv Rev, 2014. **79-80**: p. 40-9.
24. Peela, N., et al., *A three dimensional micropatterned tumor model for breast cancer cell migration studies.* Biomaterials, 2016. **81**: p. 72-83.
25. Kraning-Rush, C.M. and C.A. Reinhart-King, *Controlling matrix stiffness and topography for the study of tumor cell migration.* Cell Adh Migr, 2012. **6**(3): p. 274-9.
26. Chen, M.B., et al., *On-chip human microvasculature assay for visualization and quantification of tumor cell extravasation dynamics.* Nat Protoc, 2017. **12**(5): p. 865-880.
27. Jeon, J.S., et al., *In vitro model of tumor cell extravasation.* PLoS One, 2013. **8**(2): p. e56910.
28. Marshall, J., *Transwell® Invasion Assays*, in *Cell Migration: Developmental Methods and Protocols*, C.M. Wells and M. Parsons, Editors. 2011, Humana Press: Totowa, NJ. p. 97-110.
29. Floren, M., C. Migliaresi, and A. Motta, *Processing Techniques and Applications of Silk Hydrogels in Bioengineering.* Journal of Functional Biomaterials, 2016. **7**(3): p. 26.

30. Friedl, P. and K. Wolf, *Plasticity of cell migration: a multiscale tuning model.* The Journal of Cell Biology, 2010. **188**(1): p. 11-19.
31. Bott, K., et al., *The effect of matrix characteristics on fibroblast proliferation in 3D gels.* Biomaterials, 2010. **31**(32): p. 8454-64.
32. Enemchukwu, N.O., et al., *Synthetic matrices reveal contributions of ECM biophysical and biochemical properties to epithelial morphogenesis.* J Cell Biol, 2016. **212**(1): p. 113-24.
33. Tilghman, R.W., et al., *Matrix Rigidity Regulates Cancer Cell Growth by Modulating Cellular Metabolism and Protein Synthesis.* PLoS ONE, 2012. **7**(5): p. e37231.
34. Fischer, R.S., et al., *Stiffness-controlled three-dimensional extracellular matrices for high-resolution imaging of cell behavior.* Nature protocols, 2012. **7**(11): p. 10.1038/nprot.2012.127.
35. Fischbach, C., et al., *Engineering tumors with 3D scaffolds.* Nat Methods, 2007. **4**(10): p. 855-60.
36. Asghar, W., et al., *Engineering cancer microenvironments for in vitro 3-D tumor models.* Materials Today, 2015. **18**(10): p. 539-553.
37. Wong, A.P., et al., *Partitioning microfluidic channels with hydrogel to construct tunable 3-D cellular microenvironments.* Biomaterials, 2008. **29**(12): p. 1853-61.

Chapter VII

Colorectal Tumor-on-a-chip System: A 3D Tool for Precision Onco-nanomedicine

Chapter VII

Colorectal Tumor-on-a-chip System: A 3D Tool for Precision Onco-nanomedicine[1]

ABSTRACT

Awareness that over-simplistic traditional 2-dimensional (2D) *in vitro* and non-representative animal models may not completely emulate the 3D hierarchical complexity of tissues and organs is on the rise. Therefore, posterior translation into successful clinical application is compromised, with a critical negative impact in cancer treatment. To address this dearth, on-chip biomimetic microenvironments powered by microfluidic technologies are being developed to better capture the complexity of *in vivo* pathophysiology. Herein, we describe a "tumor-on-a-chip" model for assessment of precision nanomedicine delivery on which we validate the efficacy of drug-loaded nanoparticles in a gradient fashion. The model validation was performed by viability studies integrated with live imaging to confirm the dose-response effect of cells exposed to the CMCht/PAMAM nanoparticles gradient, with 40 % cell dead after 5 days of Gemcitabine exposure. Besides the advantages of a 3D biomimetic model supported by microfluidic culture, this platform also enables the analysis at the gene expression level. We observed a down-regulation of all the studied genes (MMP-1, Caspase-3 and Ki-67) after 5 days of culture. Overall, this tumor-on chip model clearly represents an important development in the use of precision nanomedicine towards personalized treatment.

Keywods: Microfluidics; 3D tumor model; Colorectal cancer; Nanoparticles.

[1]This chapter is based on the following publication:

M.R.Carvalho, D. Barata, L. M.Teixeira, S. Giselbrecht, R. L. Reis, J. M. Oliveira, R. Truckenmüller, P. Habibovic. "Colorectal tumor-on-a-chip system: a 3D tool for precision onco-nanomedicine". Science Advances, 2019, 5: eaaw1317. doi: 10.1126/sciadv.aaw1317.

VII-1. GRAPHICAL ABSTRACT

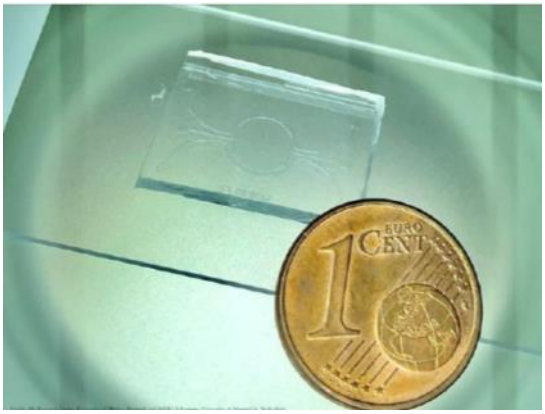

VII-2. INTRODUCTION

Colorectal cancer (CRC) is now the third leading cause of cancer-related death in women and the second leading cause in men, mainly as result of high incidence of cancer metastasis and chemotherapeutic treatments inefficiency [1]. Concerning cancer research, currently available 2D culture systems and animal models used to study the efficacy of chemotherapy do not reproduce the tumor physiology in the human body. As a deleterious consequence, over 80 % of drug candidates of all cancer drugs fail during phase II and phase III clinical trials [2].

The need for a more reliable and predictable screening approach to better assess drug responses in preclinical studies *in vitro* has led to the development of novel methodologies for cell culture, employing *e.g.* microfluidics [2, 3]. Over the past decade, the expansion in the field of microfluidics has helped to establish a new set of standards in the study of basic biological phenomena, especially helpful in the study of pathogenesis and drug development [4]. Microfluidics is by definition the science and technology of systems that process and manipulate small (10^{-9}–10^{-18} L) amounts of fluids by using channels with dimensions from tens to hundreds of micrometers [5]. Here, microfluidic technology offers new opportunities for cell-based sensors and multifunctional platforms for biochemical and biomedical functions under physiologically relevant conditions [6, 7].

In fact, microfluidic technologies enable precise control over small fluid/liquid volumes, compartmentalization and combinatorial factors/materials in a single device, allowing cells to co-

exist in a 3D complex microenvironment [8]. Such kind of platforms have proven useful in unraveling key cellular behavioral aspects of cancer metastases and enabling precise and representative drug screening [6, 9]. In addition, microfluidics have also been successful in the generation of vasculature-like structures, with special emphasis on the vital association between vasculature/angiogenesis and cancer [3, 10-12]. These are useful for revealing the mechanisms in the development of vasculatures, but also as experimental platforms for vascular disease models and drug screening. Another particular feature of microfluidics, which will be employed in this study, is the ability to generate well-controlled gradients of molecules in solution. Gradients of molecules can be generated by advection, being the mass transport by the fluids bulk motion (flow-based gradient generation), or by diffusion, being the spreading of unequally distributed molecules by biased random walk induced by Brownian motion (diffusion-based gradient generation) [13]. The importance of gradient generation relies on the fact that many cell processes work by recognizing the directional information present in gradients, including processes such as chemotaxis, angiogenesis, and diseases such as cancer [14]. In the *in vivo* scenario, chemical microenvironment includes nutrients and oxygen, delivered to cell tissues through a net of vasculature that create important biomolecular gradients within the tissue. The successful development of 3D micro-engineered gradients set the stage for physiologically relevant *in vitro* models, comprising for instance oxygen, chemokines and drug gradients [6, 13, 15]. Another important aspect of our model is the microvasculature. It defines the biological and physical characteristics of the microenvironment within tissues and plays a role in the initiation and progression of many pathologies, including cancer [16]. Microfluidics have also been used in the generation of vasculature-like structures, with special emphasis on the association between vasculature/angiogenesis and cancer [3, 10-12]. In the case of CRC, endothelial cells lining the microvasculature are known to play a critical “gatekeeper” role, which is why we developed our microvasculature model using Human Colonic Microvascular Endothelial cells (HCoMECs) [17].

Regarding CRC treatment, Gemcitabine (2′,2′-difluoro-2′-deoxycytidine) (from now on designated as GEM) is now being tested as treatment for patients with advanced colorectal cancer [18, 19]. However, because of its low molecular weight and high solubility in water, the clinical benefits of GEM are hampered by its short plasma half-life and relative low concentration around tumor sites [20, 21]. Therefore, a search for novel therapeutic strategies is imperative, such as the use of nanoparticles [20].

Our goal was to develop a complex 3D microfluidic chip-based *in vitro* model that emulates the human colorectal tumor microenvironment. This model enables the reconstitution of physiological functions of microvascular tissue, which is instrumental to assess the efficiency of delivery of anti-cancer drug-loaded nanoparticles through a dynamic controllable gradient in a core compartment of the microfluidic chip. Such gradient is generated and maintained by perfused microvasculature-mimicking side channels. Together, these results demonstrate that this 3D platform is suitable for efficacy/toxicity screening in a more physiological environment than previously possible.

VII-3. MATERIALS AND METHODS

VII-3.1. Microfluidic chip design and fabrication

The microfluidic device composed by three main compartments was designed using computer assisted design (CAD) on a photolithography mask, which consisted in: a central chamber for an ECM like hydrogel (5 mm diameter) and a pair of perfusable channels flanking the center chamber (connected to the chamber with a range of pillars that allow the generation of stable gradients by diffusion).

The microfluidic device in poly(dimethylsiloxane) (PDMS, Down Corning) elastomer was fabricated by replica molding from a SU-8 (Microchem)/silicon master, based on a 10:1 ratio to curing agent. The master mold was produced by UV-lithography. After pouring PDMS on mold, the mixture was degassed in a vacuum chamber for air bubble removal, and cured at 80 °C for 1 hour, in the oven. The devices were then cut out by a razor blade, the fluidic connection ports punched, and bonding to a glass slide done after oxygen plasma of both surfaces and conformal contact (Plasma cleaner/sterilizer Harrick®, high RF level, 4 mbar, 120 seconds). Assembly quality control and characterization was done by optical 3D profilometry (Keyence VK-X250, Germany).

VII-3.2. Characterization of the microfluidic device

This microfluidic device functions as a multiphase micro-bioreactor, which was built based on three major compartments: a central chamber seeded with cells embedded in a hydrogel matrix (Matrigel used as model gel), being sided by a pair of channels perfused with culture medium. The central chamber and the lateral channels are separated by small pillars to allow for hydrogel loading of the chamber retained before the channels. Quality check was done by optical microscopy.

VII-3.3. Cell Culture

HCT-116 cells (human colon cancer cell line) were originally obtained from the American Collection of Cell Cultures (ATCC, USA). Cells were cultured in Dulbecco's Modified Eagle Medium (DMEM, Gibco, Invitrogen) supplemented with 10 % (v/v) fetal bovine serum (FBS) and 1 % (v/v) penicillin and streptomycin (pen/strep) solution under standard conditions (37 °C in a humidified atmosphere, 5 % CO_2). HCoMECs (Human Colonic Microvascular Endothelial cells) were obtained from Innoprot and cultured in Endothelial Cell Medium supplemented with 5 % (v/v) FBS, 1 % (v/v) of Endothelial Cell Growth Supplement (ECGS) and 1 % (v/v) of pen/strep solution. Medium was replaced every 3 days. Subculture of cells was performed before 90 % of confluence using 0.25 % (v/v) trypsin/EDTA (GIBCO) for 5 minutes at 37 °C.

VII-3.4. Cell seeding on the chip

HCT-116 cancer cells were re-suspended in Matrigel supplemented with VEFG (100 ng/mL) (R&D Systems) in a density of $10x10^6$ cells/mL, injected in the central chamber of the microfluidic device using a syringe and let incubate for 15 min at 37 °C for crosslinking. After this, the lateral channels were coated using a 10 % Matrigel solution and incubated for 30 minutes at 37 °C. HCoMECs in the same density ($10x10^6$ cells/mL) were seeded on the lateral channels using a pipette and left to adhere for 6 hours. Then, the cells were exposed to a perfusion flow regime at a flow rate of 8 μL/h for the duration of the experiment. At days 1 and 5 days, the cell culture was evaluated using fluorescence microscopy.

VII-3.5. Validation of the co-culture by fluorescence imaging

Prior to seeding in the microfluidic device, HCT-116 and HCoMEC cells were made fluorescent by means of CellTracer™ Far Reed and Yellow (Life Technologies), respectively. These dyes were designed to be easily internalized, passing through cell membrane into cytoplasm. The desired concentration of cells trypsinized, centrifuged and resuspended in dye solution/PBS (at a concentration of 10 μM). The suspension was incubated for 20 minutes at 37 °C (in the dark), and then diluted in five times the original volume of medium, let incubation for 5 minutes and centrifuged. Finally, the pellet was resuspended in fresh medium into a final concentration and cell suspension seeded. Cells in microfluidic culture were observed under fluorescent microscope at day 1 and 5. In addition, afterwards, all microfluidic culture was fixed for the further analysis of the microfluidic co-culture model. Endothelial cells seeded on the lateral channels, cells were stained with DAPI/Phalloidin. Cells were fixed with 4 % paraformaldehyde in PBS for 30 minutes at room temperature (RT), and washed again with PBS. Permeabilization of cells was done with 0.1 % Triton X-100 (Sigma-Aldrich) for 15 minutes at RT, followed by washing with PBS. High-affinity filamentous actin probe Alexa Fluor 594® Phalloidin (Invitrogen™, 1:80) was injected through the channels and let incubate for 30 minutes at RT, washed with PBS, and then incubated with 4',6-diamidino-2-phenylindole (Invitrogen™, DAPI, 1:100) diluted in PBS for 10 minutes at RT.

VII-3.6. Endothelial invasion into microfluidic core and quantification

During cell culture, bright field images were taken with inverted microscope to analyze and quantify in which extent endothelial cells remain on the lateral microchannels or respond to Vascular Endothelial Growth Factor (VEGF) present in the Matrigel in the central chamber. Three images of each time point (day 0, day 2, day 3 and day 5) were analyzed. The length was measured using Image J (Fiji), from the outer limit of the microchannels/hydrogel interface, until the furthest point of the elongated cell(s).

VII-3.7. CMCht/PAMAM dendrimer nanoparticles

VII-3.7.1. Chemical synthesis of CMCht/PAMAM dendrimer nanoparticles

Dendrimer nanoparticles were surface modified as previously described by Oliveira *et al.* [22]. CMCht with a degree of 80 % deacetylation and 47 % substitution of was synthesized by a chemical modification route of chitin (Sigma, Germany) as described by Chen *et al.* [23].

Starburst PAMAM carboxylic acid terminated dendrimers, hereafter designated as PAMAM-CT (G1.5, 20 %wt. methanolic solution) with an ethylenediamine core were purchased (Sigma-Aldrich). CMCht/PAMAM dendrimer nanoparticles were prepared in a step-wise manner as follows: increase the generation of the PAMAM-CT (G1.5), obtaining a PAMAM methyl ester terminated dendrimer, reaction between PAMAM and CMCht (the reaction occurs by a condensation reaction between the methyl ester and amine groups), and conversion of methyl ester groups that do not react into carboxylic groups in the CMCht/PAMAM dendrimer, followed by precipitation.

VII-3.7.2. Labeling of CMCht/PAMAM dendrimer nanoparticles with FITC

The conjugates of CMCht/PAMAM-FITC were obtained by covalently bonding the amine group of CMCht and the isothyocianate group of FITC (10 mg/mL FITC) (Sigma, Germany) in anhydrous dimethyl sulfoxide (DMSO, Norconcessus) creating a thiourea bond. First, a 10 mg/mL CMCht/PAMAM dendrimer nanoparticle solution was prepared in a carbonate-bicarbonate coupled buffer of pH 9.2. Then, a solution of FITC/DMSO was added under agitation and kept in the dark at 4 °C for 8 hours. The FITC-labeled CMCht/PAMAM dendrimer nanoparticle solution was then dialyzed against ultra-pure water. The final product was obtained after freeze-drying.

VII-3.7.3. Gemcitabine incorporation into CMCht/PAMAM dendrimer nanoparticles

GEM was incorporated in the nanoparticles by mixing an aqueous solution of CMCht/PAMAM dendrimer nanoparticles with an aqueous GEM solution with a final

concentration of 0.5 mM. Saturated sodium carbonate solution (Na_2CO_3, Aldrich, Germany) and acetone (Pronalab, Portugal) were then added to the mixture. The resulting precipitates were dialyzed against ultrapure water. GEM-loaded CMCht/ PAMAM dendrimer nanoparticles were obtained by freezing the final solution at -80 °C and freeze-drying (Telstar-Cryodos-80, Spain) the samples for 7 days.

VII-3.7.4. Encapsulation efficiency, drug loading efficiency and release profile studies

For assessing encapsulation efficiency, CMCht/PAMAM (50 mg) was dissolved in 50 mL deionized water. GEM, (7 mg) in 2 mL deionized water was added drop-wise to the dendrimer solution and stirred for 30 minutes. Precipitation of the dendrimers and consequent encapsulation of the drug was induced as described before. Samples were taken before and after precipitation, centrifuged, analyzed by UV-Vis spectrophotometer at 275 nm, in a Hellma Quartz Plate, and compared to a calibration curve.

For evaluating drug-loading efficiency, pre-weighted amount of GEM-loaded CMCht/PAMAM (50 mg) was added to distilled water and sonicated to extract GEM. The extracted GEM concentration was analyzed by UV-Vis spectrophotometer at 270 nm and compared to a calibration curve. The absorbance was used to calculate the percentage of GEM encapsulated. The following **Equations VII-1 and VII-2** were used:

Equation VII-1 – Determination of encapsulation efficiency.

$$\textit{Encapsulation efficiency}\ (\%) = \frac{\textit{Amount of gemcitabine encapsulated}}{\textit{Total gemcitabine added}} X\ 100$$

Equation-VII-2 – Determination of drug loading efficiency.

$$\textit{Drug loading efficiency}\ (\%) = \frac{\textit{Amount of gemcitabine encapsulated}}{\textit{Total weight of nanoparticles}} X\ 100$$

GEM release from nanoparticles was measured by UV spectrophotometry (Shimadzu) at 275 nm, in a Hellma Quartz Plate, after dissolution of 50 mg of GEM-loaded CMCht/PAMAM dendrimer nanoparticles in 5 mL of phosphate buffer saline solution (PBS) with sodium azide

0.01 % (Sigma). The *in vitro* release was performed at 37 °C under stirring at 60 rpm between 0 hours and 5 days timepoints.

VII-3.7.5. Characterization of the CMCht/PAMAM dendrimer nanoparticles by transmission electron microscope (TEM)

The nanoparticles morphology was investigated by transmission electron microscopy (TEM; Philips CM-12, FEI Company, The Netherlands, equipped with a MEGA VIEW-II DOCU camera and Image Software Analyzer SIS NT DOCU) after staining with 2 % of phosphotungstic acid and fixation on copper grids.

VII-3.8. Gradients generation and characterization inside the microfluidic chip

For the generation of a stable gradient through the Matrigel core compartment, a source-sink mechanism was created, with one solution of 0.5 mg/mL FITC-labeled nanoparticles in PBS perfused through one side channel and PBS was perfused through other, using a Nexus 3000 syringe pump (Chemix). Syringes of 3 mL syringes were used to introduce PBS with or without the nanoparticles at a rate of 8 µL/hour. The experiment was performed in a Nikon Eclipse Ti-E fluorescence microscope (Nikon Instruments, Japan) for time lapse imaging of the gradient formation.

Profile and stability of the dynamic gradient was analyzed using NIS-Elements AR (Nikon) software. The chips were analyzed at different time points between 0 and 12 hours with continuous perfusion. Built-in "plot profile" module was used for assessing the gradient intensity and stability over time. The intensity profile corresponds to distance versus intensity. A 3D projection was also reconstructed using software.

VII-3.9. Gemcitabine loaded CMCht/PAMAM dendrimer nanoparticles gradient

After the establishment of the co-culture model, a gradient of GEM release from dendrimer nanoparticles was generated by perfusing GEM-loaded nanoparticles (0.5 mg/mL) in one inlet, and endothelial cell culture medium in the other inlet, using exactly the same experimental

source-sink mechanism used for the establishment and characterization of the nanoparticles gradient. This was achieved by connecting the chip to the tubings into lateral inlets fed by glass syringes (SGE), mounted on a Nexus 3000 syringe pump.

VII-3.10. Live/dead assay

The viability of cells cultured in the microfluidic chips in the presence or absence of GEM loaded dendrimer nanoparticles was assessed using the Live/dead assay. For this, at endpoints, the chip side-channels were washed with PBS (Sigma), and then incubated for 40 minutes with Calcein AM (1 µM, live cells in green) and Ethidium homodimer 1 (6 µM, dead cells in red) and then washed again. Microfluidic chips were then imaged with fluorescence microscope using automated acquisition for Z-stack and multicolor-channel.

VII-3.11. Image processing

Acquired multi-frame multicolour images were combined either using Nikon AR or FIJI software (open-source software ImageJ focused on biological image analysis) for operations of processing such as rotation, crop, color balance and related assemblies, considering initial scales and aspect ratios. High-resolution Z-stack images were processed for 3D reconstruction through deconvolution and 3D projections made by NIS-Elements AR (Nikon) software.

VII-3.12. RT-PCR analysis

After each culture time, Matrigel from the central chamber was retrieved by punching with a 5 mm sterile biopsy punch (WPI) and placed in 24 well plates. Samples were washed with PBS solution and Matrigel was depolymerized by incubation with 1 mL of MatriSperse Cell Recovery Solution (BD Biosciences) for 30 minutes at 4 °C. After complete release from the Matrigel, cells were transferred to an Eppendorf tube and centrifuged to a pellet by centrifugation at 300 G for 5 minutes. Cells were washed with cold PBS and centrifuged again. Total RNA was extracted from cells recovered from the 3D cultures using Phasemaker Tubes (Invitrogen), following the manufacturer's instructions. The pellet was then immersed in 500 mL of TRIZOL Reagent and

stored at -80 °C until further use. RNA quantification and purity were assessed using a NanoDrop ND-1000 spectrophotometer (NanoDrop Technologies). cDNA was synthetized according to the protocol from iScript cDNA Synthesis Kit (Bio-Rad). The obtained cDNA was used as template for the amplification of the target genes using the iQSYBR Green Supermix (Bio-Rad), according to manufacturer's instructions. The primers sequence, specific for each gene, namely Ribossomal Protein S27a (RPS27A), Caspase-3 (Casp3), Ki-67 and Matrix metalloproteinase-1 (MMP-1) are described in **Table VII-1**. The transcripts expression data were normalized to the endogenous housekeeping gene RPS27A and the relative quantification was calculated normalizing the obtained results for each target gene at each timepoint in basal culture conditions (controls), according to the Livak ($2^{\Delta\Delta CT}$) method [24]. Three samples of each group were tested at each time-point, in three independent experiments.

Table VIVII-1 – Primers list for the studied genes.

Oligo Name	Sequence 5' to 3'
Casp-3 (human) F	GAAATTGTGGAATTGATGCGTGA
Casp-3 (human) R	CTACAACGATCCCCTCTGAAAAA
MMP-1 (human) F	GGGGCTTTGATGTACCCTAGC
MMP-1 (human) R	TGTCACACGCTTTTGGGGTTT
Ki67 (human) F	GCTGGCTCCTGTTCACGTA
Ki67 (human) R	CTGGGCTACACTGAGCACC
RPS27A (human) F	GCTTGCCAGCAAAGATCAGT
RPS27A (human) R	GAGGTTGAACCCTCGGATAC

VII-3.13. Immunohistochemistry

Microfluidic chip was processed for immunohistochemistry by perfusion of reagents, through both side inlets. After cell culture, chip was washed with PBS, the cells were fixed with 4 % paraformaldehyde in PBS for 30 min at room temperature (RT), and washed again with PBS. Permeabilization of cells was done with 0.1 % (v/v) Triton X-100 (Sigma-Aldrich) for 15 minutes at RT, followed by washing and incubation with blocking solution CAS-Block (Thermo Fisher Scientific) for 30 minutes at 37 °C. Primary antibody for Ki-67 diluted in CAS-Block (rabbit, ab833 R&D Systems, 1:100) was subsequently incubated overnight at 4 °C. Samples were washed with PBS and incubated with the secondary antibody Alexa Fluor ® 488 conjugated (1:500, anti-rabbit, R&D Systems) together with high-affinity filamentous actin probe phalloidin

conjugated with Alexa Fluor ® 594 (Invitrogen™, 1:80) in CAS-block for 3 hour at RT. The samples were then washed with PBS, incubated with 4',6-diamidino-2-phenylindole (Invitrogen™, DAPI, 1:100 in PBS) for 10 minutes at RT, and finally washed twice with PBS. The samples were kept in PBS in the dark at 4 °C until image analysis. High magnification images were acquired with Nikon Eclipse Ti-E, using automated acquisition for Z-stack and multicolor-channel.

VII-3.14. Statistical analysis

Statistical analysis was performed using GraphPad Prism 5.0a software. The non-parametric Mann–Whitney test was used to compare two groups. A value of $p < 0.05$ was considered statistically significant. For multiple comparisons, the parametric tests One-Way ANOVA was used, with $p < 0.05$ considered statistically significant.

VII-4. RESULTS

VII-4.1. Microfluidic chip fabrication and characterization

The aim of this work was to develop an in-house customized 3D microfluidic model that emulates the human colorectal tumor microenvironment and enables the reconstitution of physiological functions of microvascular tissue. The criteria for designing the model had to comprise features that permitted the generation of soluble compounds' gradient for the assessment of the delivery efficiency of anti-cancer drug loaded nanoparticles. Moreover, easy-to-use, possibility of real time imaging, performance of immunocytochemistry and cell retrieval after the experiments for Real Time – Polymerase Chain Reaction (RT-PCR) analysis were requirements of this platform. In addition to having to meet certain conditions in terms of operation and design, the choice of material for fabrication, the geometry, dimensions of the culture chamber and fluid flow control are some important considerations when designing the device. The developed microfluidic chip is made using poly(dimethylsiloxane) (PDMS). The 3D map of the final design is created by laser-reading the wafer's surface at 50 x magnification, as can be observed in **Figure VII-1A**. In this sense, our microfluidic device has three compartments: a circular central chamber for the ECM like hydrogel (Matrigel) with 5 mm diameter and 126 μm

in depth, with a separate inlet and outlet. The central chamber is laterally sided by a pair of perfused channels, 100 µm wide and 126 µm in depth, that are not interconnected between them **(Figure VII–1B)**.

To evaluate the maintenance of the co-culture over the course of 5 days, Matrigel supported CRC cells were labeled with CellTrace™ Red (red) and HCoMECs with CellTrace™ Yellow (yellow), as shown in **Figure VII-1C)**. The endothelial cells were cultured in a 3D vessel-like fashion, attaching to the walls of the lateral channels of the microfluidic chip. As expected, these cells respond to a signal of VEGF that has been loaded in the Matrigel, by migrating from the lateral channels towards the hydrogel through the interspacings between the pillars that separate the two compartments. The "microvasculature" component was characterized by obtaining a 3D representation (through actin/nuclei fluorescent stain of HCoMECs), to observe the morphology of the colonic endothelial cells lining the lateral channel structure after 5 days under perfusion of media **(Figure VII–1D).**

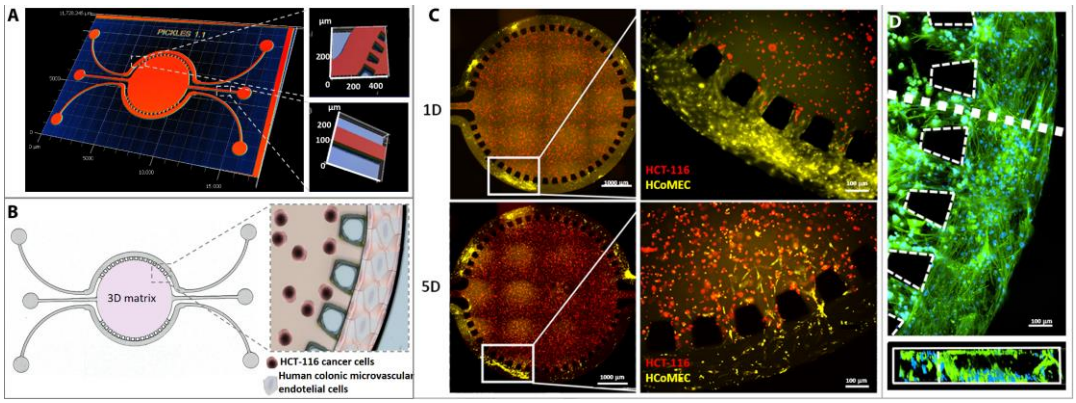

Figure VII-1 - Design and characterization of the microfluidic chip. A) Profilometer characterization: 3D map of the microfluidic chip. Representative image of quality control and characterization of the microfluidic chip features. The central chamber is 5 mm in diameter and 126 µm in depth, with a separate inlet and outlet for hydrogel injection. The two lateral channels, each 100 µm wide and 126 µm deep, are not interconnected, opening up the possibility of perfusing two distinct solutions. B) Schematic of chip design and zoom in of the concept of colorectal tumor-on-a-chip model: round microfluidic central chamber in which HCT-116 cancer cells are embedded in Matrigel; HCoMECs are seeded in the side channels to form a 3D vessel-like assembly. C) Establishment of a microvascular 3D microenvironment of colorectal tumor-on-a-chip: HTC-116 CRC cells embedded in Matrigel (in central chamber, stained in red) and HCoMECs (in lateral microchannels, stained in yellow) at day 1 and 5 of culture. Endothelial cells start to invade the central chamber filled with Matrigel in response to VEGF presence. D) Fluorescence microscopy image of microfluidic lateral channel mimicking pre-vascularization with HCoMECs cells after 5 days of culture (DAPI blue – Nuclei; Phalloidin green – F-actin filaments); Representative fluorescence microscopy close-up image of microchannel cross

section showing endothelial cells aligning and creating an endothelialized lumen within the microchannel.

VII-4.2. Endothelial Invasion

The three-dimensional formation of endothelial sprouts in a microfluidic device and the changes in cellular organization during early stages of invasion were examined. This invasion is oriented directly towards the source of VEGF in the Matrigel, despite the fact that cell migration from the endothelium is not physically constrained in any direction by the system design (**Figure VII–2A**). Sprouting quantification shows that HCoMECs could progress up to 500 µm after 5 days. The leading tip cells is replete with filopodia-like protrusions, morphologically recapitulating *in vivo* endothelial-cell sprouting. As the sprouts continued to invade and extend throughout the 3D matrix, they become longer, contain progressively more cells, and begin to form interconnected branches, as it occurs in early stages of tumor development [25] (**Figure VII-2B**, zoom in at day 3). Although we are not mimicking the angiogenesis phenomena *per se* on this model, we observe that endothelial cells invade the hydrogel core but do not form anastomosis.

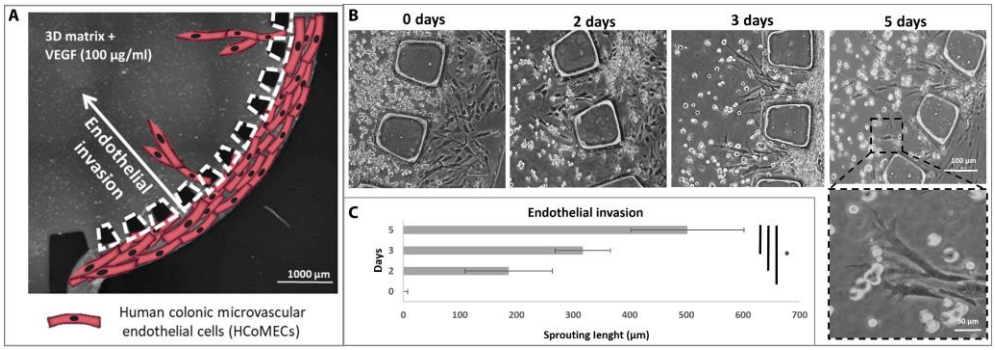

Figure VII-2 - Endothelial cell invasion. A) Schematic representation of HCoMECS cells in the lateral channels invading the central chamber in response to the presence of VEGF mixed in the Matrigel; B) Formation of endothelial sprouts in the microfluidic device: representative bright field images of the chip taken at determined time points were analyzed in Image J. C) Quantification of endothelial invasion. Data is presented as mean ± stdev (n=9), (*) denotes statistical differences ($p < 0.01$).

VII-4.3. Validation of the integrated microfluidic gradient chip device

Ultimately, in this work, we aim to establish a 3D cancer microfluidic cell culture for onco-nanomedicine efficacy. Through its architecture, the platform offers the possibility to observe the

effect of several concentrations of GEM-loaded CMCht/PAMAM dendrimer nanoparticles, as they penetrate the HCT-116 laden-hydrogel in a gradient fashion. As a result, from one experiment, a real-time response of the cancer cells in a gradient-like fashion is obtained, as occurs in a physiological concentric tumor microenvironment. For this purpose, the formation of the gradient was validated using fluorescent labeled CMCht/PAMAM dendrimer nanoparticles prior to the GEM release. It is noteworthy that these nanoparticles present remarkable physicochemical and biological properties such as solubility in water, biocompatibility and ability to be easily surface modified. Therefore they have great potential to be used in fundamental cell biology studies as well as for intracellular drug delivery [26].

The CMCht/PAMAM dendrimer nanoparticles were synthetized and characterized previously, showing an average size of 50 nm [22, 27] (**Figure VII–3A**). As depicted in **Figure VII–3B**), after 60 minutes, a gradient of fluorescence was established in the cell culture chamber, and maintained for at least 12 hours of continuous lateral perfusion, exhibiting a quasi-linear fluorescent profile (from 100 % at the source to 0 % at the sink) (**Figure VII-3C**). A 3D projection of FITC-labeled nanoparticles' gradient according to surface fluorescence intensity (**Figure VII–3D**) also confirms these findings.

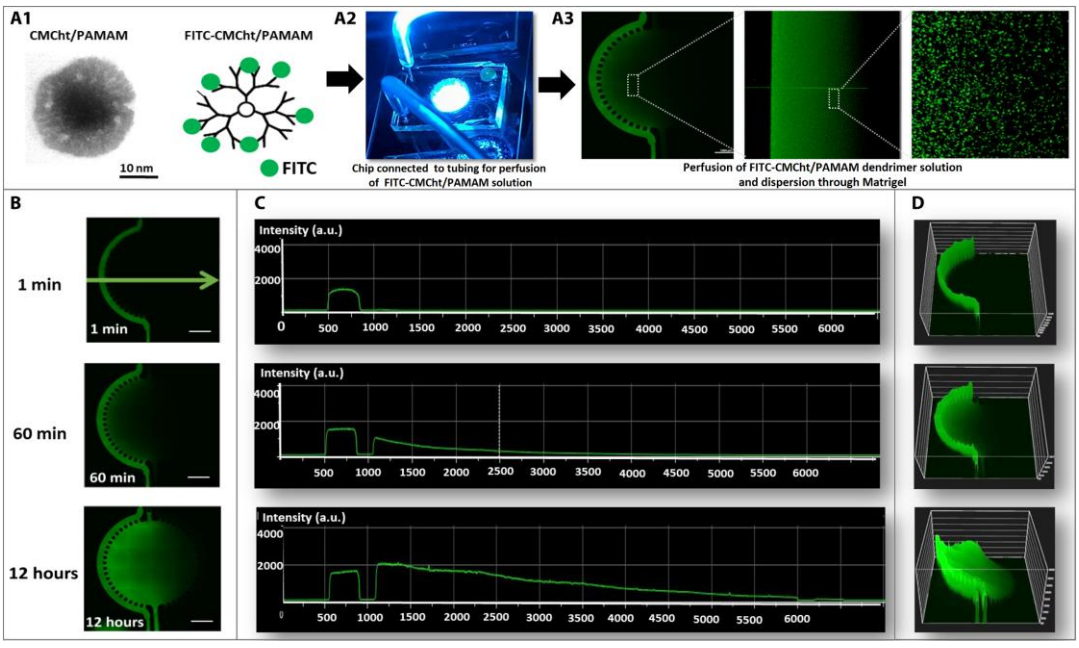

Figure VII-3 - Schematic representation of fluorescent nanoparticle gradient formation. A) Transmission electron microscopy image of individual CMCht/PAMAM dendrimer nanoparticle, representative image of chip connected to tubing perfusing the nanoparticle solution, and zoom in confocal microscopy image confirming FITC-labeled CMCht/PAMAM dendrimer nanoparticles' dispersion in Matrigel. B) Panel of

fluorescent microscope images of FITC-labeled nanoparticles' gradient up to 12 hours. C) Quantification of fluorescence: intensity (arbitrary units) *vs* distance (µm) across the chip up to 12 hours (measurements according to the direction of the green arrow indicated in B). D) 3D projection of FITC-labeled nanoparticles' gradient according to fluorescence intensity.

VII-4.4. Drug Screening Validation

We aimed to establish an image-based method to investigate the concentration-dependent response of cells inside the microfluidic device by creating a gradient of concentrations of GEM. To investigate the concentration-dependent toxicity on cancer cells inside the microfluidic chip, the survival response of cells of the CRC cell line HCT-116 embedded within Matrigel was examined. The cells were allowed to adhere and develop for 12 hours prior to drug exposure. The exposure of the cells to the delivery-induced gradient of GEM was generated from a maximum concentration of 0.5 mg/mL of dendrimer nanoparticles sourced from one microvasculature lumen perfused with them and diffused through the hydrogel core towards the opposite side (**Figure VII-3**).

GEM-loaded nanoparticles were studied in terms of encapsulation efficiency and drug-loading efficiency. The encapsulation efficiency of GEM-CMCht/PAMAM was 52.99 % ± 3.5 %, and the drug-loading efficiency was 9.42 % ± 3.5 %. The *in vitro* release profiles of GEM-loaded CMCht/PAMAM were recorded in a cumulative release curve during 5 days. As shown in **Figure VII-4**, after 6 hours, around 40 % of the drug was released, which shows that GEM-loaded CMCht/PAMAM can retain their stability in solution. Thereafter, the nanoparticles showed an accelerated release, where more than half of the GEM was released by 24 hours (**Figure VII-4A**).

In addition, an important event to notice is the immediate internalization of the nanoparticles after contact with cells, as shown in our previous study [27], decreasing the chance of drug degradation. Such intracellular release mechanism represents a key factor of the significance of GEM loaded nanoparticles as an anti-tumoral agent [28].

Live experiments were similarly performed using the same type and concentration profiles for the sake of reproducibility and final measurement co-relation. In order to quantify cells' response to GEM, we segmented the circular area of the chip (core) into 6 concentric areas, as represented in **Figure VII-4B**. Thereby, the following nomenclature was used: M1, M2, M3 was

assigned to the areas of the chip subjected to culture medium (**Figure VII-4B**, left side), and D1, D2 and D3 to the areas of the chip subjected to drug (**Figure VII-4B**, right side).

After 1 and 5 days of exposure to GEM, the viability of CRC cells was evaluated in the 3D matrix, under perfusion at side-channels. The controls, at both time points (**Figure VII-4C/D**) indicate insignificant levels of cell death, demonstrating the microfluidics' model ability to support a stable and viable co-culture of HCoMECs and HCT-116 CRC cells in contiguous compartments under perfusion. Cell viability in controls show that oxygen can freely permeate to the cells either through PDMS or the hydrogel matrix, while being fed for nutrients dynamically by perfusion of side channels (**Figure VII - 4B**). On the other hand, in the presence of GEM-loaded CMCht/PAMAM dendrimer nanoparticles, cell death occurs in a gradient manner, with a step-wise decay in toxicity, *i.e.* less linear than the concentration release profile of GEM previously quantified. This indicates that GEM could be efficiently released from the nanoparticles and taken up by the cancer cells while remaining an active anti-cancer drug, in its soluble form (**Figure VII-4C**). The cell death induced by the anti-cancer drug was more efficient within the first 150 μm of the cell culture, which might be due to an eventual threshold of drug efficacy on cells. This concentration effect has been consistent over time, with the cell death values increasing from day 1 to day 5 (**Figure VII-4C).**

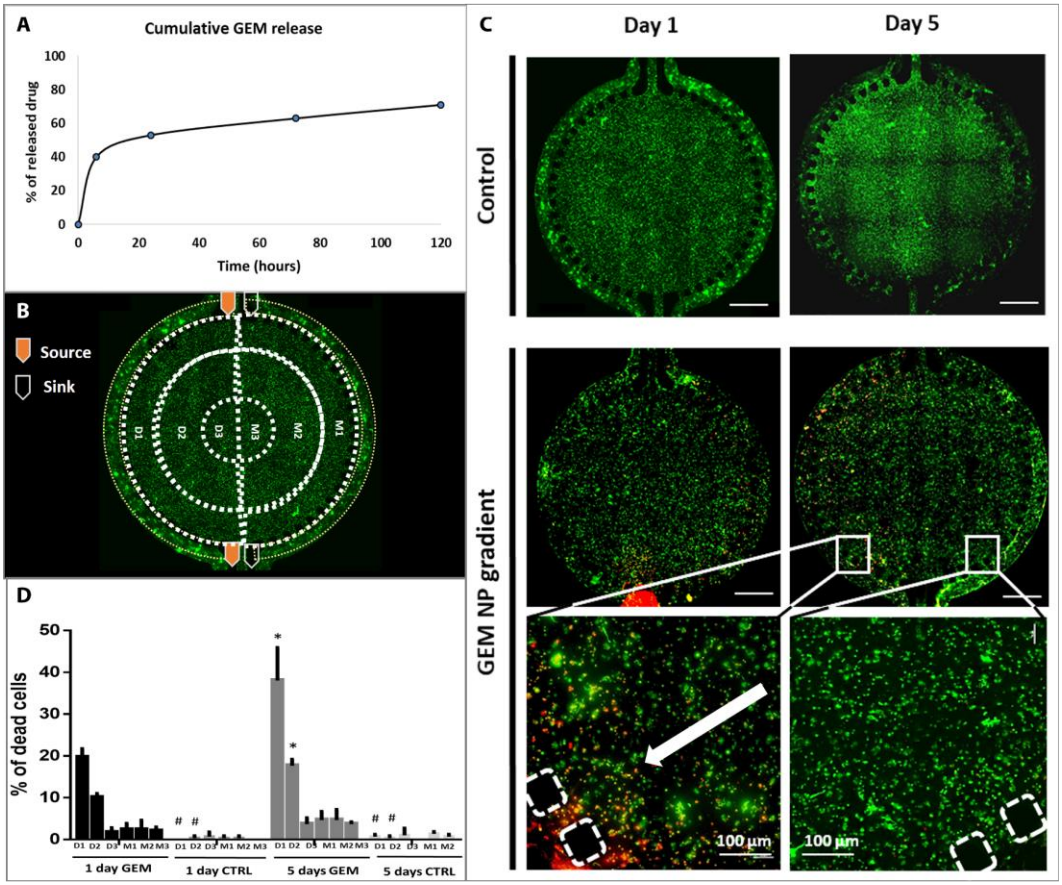

Figure VII-4 - GEM drug effect on colorectal-tumor-model. A) Release profile of GEM: cumulative release (hours) of GEM at pH 7.4 in PBS, at 37 °C and stirred at 60 rpm, determined by UV spectrophotometer set at 275 nm. The results are expressed as mean ± stdev, n=6. B) Schematic representation of experimental set-up (perfusion of culture medium through one in- and one outlet and of culture medium supplemented with 0.5 mg/mL GEM-loaded dendrimer nanoparticles through the other in- and outlet); the areas defined for cell death quantification are delimited by dashed lines and each ring assigned D1-D3 and M1-M3. C) Representative panels of fluorescence microscopic images of live/dead assay performed on microfluidic chip at days 1 and 5. D) Quantification of cell death, represented as percentage, based on the microscopy data. Data is presented as mean ± stdev (n=3), (*) denotes statistical differences ($p < 0.05$). Scale bar 1000 µm.

VII-4.5. Gene Expression Analysis and Immunocytochemistry on a Chip

To the best of our knowledge, very few organ-on-chip models allow for gene expression analysis of the cells cultured therein due to the small mRNA content accessible from the chip's culture chambers. On a sub-set of corresponding experiments, exposure to GEM-loaded CMCht/PAMAM dendrimer nanoparticles was tested as single-concentration exposure per device (GEM-loaded CMCht/PAMAM perfused through both inlets), not as a gradient, to demonstrate the

potential of the platform for evaluating gene expression as function of dose-response. To this end, two representative conditions of previous experiments, *i.e.* 0 and 0.5 mg/mL (on continuously perfused media) were tested as proof-of-concept for the suitability of the model for RT-PCR and gene studying. 0 mg/mL represents our control group. At each time point (1 and 5 days), cells were extracted from the device, and RNA was extracted from cells – after hydrogel removal (**Figure VII-5A**) for analysis of mRNA expression of Caspase-3, Ki-67 and MMP-1 by real time PCR. These markers where chosen to allow the evaluation of the effect of cytotoxic compounds: MMP-1 because of its relationship with the metastatic phenotype [29], Caspase-3 because it is involved in apoptosis, and Ki-67 as a universal marker for proliferation.

In general, a down-regulation is observed for all genes when comparing day 1 to day 5, as shown in **Figure VII-5**. Compared to the controls, MMP-1 expression is down-regulated, 0.5- and 0.2-fold for day 1 and 5, respectively. Similarly, for Caspase-3, at day 1, no statistical differences between the control and GEM-treated cells is observed. For Ki-67 expression, no significant effect of the exposure to GEM was observed at day 1, which can be due to the limited time for the compound to act on the cells and affect their proliferation. However, at day 5 a statistical significant effect of GEM is observed, with a 0.4 fold decrease in the expression of Ki-67 compared to the control. These results demonstrate the suitability of our platform for assessing gene expression.

Concerning Ki-67 immunofluorescence on the microfluidic chip shown in **Figure VII-5C**), the marker is expressed only when the nanoparticles are absent, which confirms the PCR data. These qualitative results translate the presence of Ki-67-positive cells, corresponding to proliferating tumor cells in the area of the chip more subjected to drug-free media, in contrast to Ki-67-negative cells present in the matrix regions close to the perfusion source of GEM loaded CMCht/PAMAM dendrimer nanoparticle media.

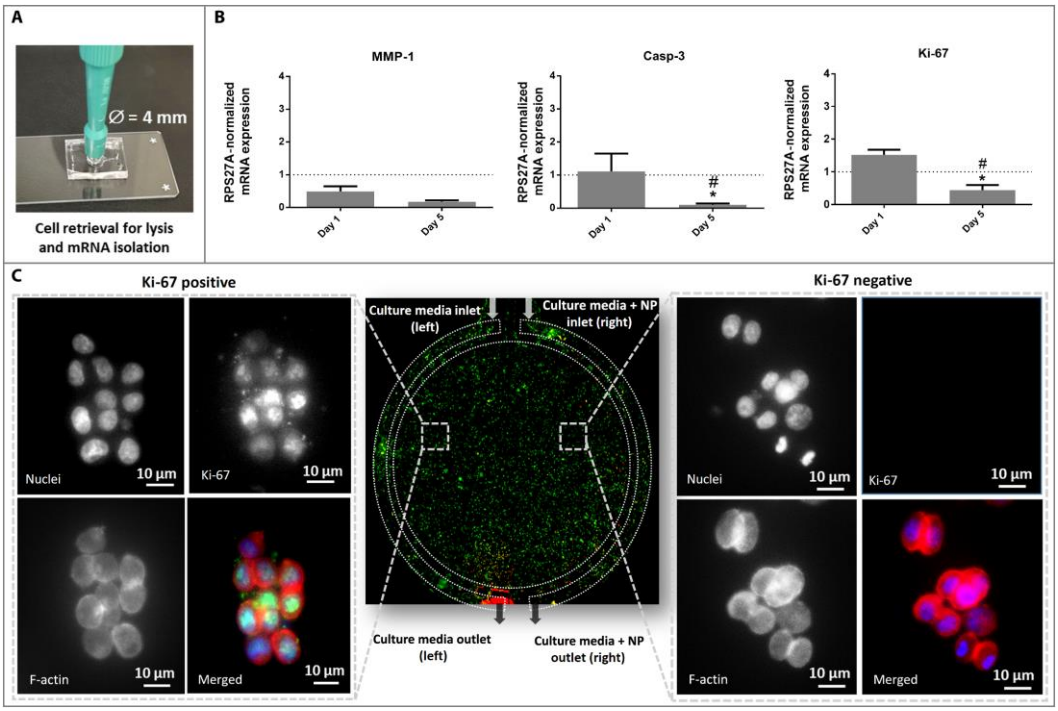

Figure VII-5 - Gene expression analysis and immunocytochemistry on a chip. A) Representation of hydrogel retrieval containing HCT-116 cells from the chip for gene expression analysis. B) Gene expression of Ki-67, Caspase-3 and MMP-1, in the absence (control) and presence of gemcitabine, at day 1 and day 5. The values for controls are represented by the dashed line. * Significant differences when comparing the same condition at two different time points; # significant differences when comparing to controls at the same time point. Data represent mean values of 3 independent experiments ± stdev. C) Immunohistochemistry: in the center, a representative image of the entire chip is depicted. The lateral images represent the zoom in at the cell level showing the immunocytochemistry Ki-67 staining after 5 days in culture (panels showing DAPI nuclei staining blue, Ki-67 staining green, F-actin staining red and merged image in colors).

VII-5. Discussion

The design of our new microfluidic chip resembles the traditional ECM-containing devices, where endothelial monolayers are cultured onto the sidewall of an extracellular matrix material, that separates two microfluidic channels [30]. In our model, the "tumor" core defined by the hydrogel is supported by an adjacent "microvascular" network fed by external syringe pumps, supporting physiological events specific of each cells type. The lumen-like channels deliver nutrients to surrounding tissues sufficient to support robust growth. This opens up the possibility of perfusing two distinct solutions in each side of the central chamber containing Matrigel and the

cancer cells encapsulated therein, and therefore the ability to produce and maintain stable gradients. Around the inner part of the chamber we designed micro pillars to help retain Matrigel when injected into the chamber, creating enough superficial tension and avoiding leakage towards the lateral channels (**Figure VII-1C**). Furthermore, the liquid continuity between the side channels and the culture chamber was ensured by these small pillars, which act as resistors, preventing the shear stress to be transmitted to the cell culture chamber [31]. The chip is made using PDMS due to its several unique properties, which make it a suitable choice for microfluidic application: PDMS is inexpensive, easy to handle, gas permeable (assuring the supply of oxygen to the cells), and transparent, properties needed for the imaging [32]. Corroborating this, our results show the CRC cells in red and endothelial cells in yellow clearly proliferating, elongating in the direction of the flow and covering the whole lateral channels, consequently forming a vessel-like structure at day 5. Interestingly, we observed an endothelial 3D macro structure invading the central chamber through the pillars, in response to the VEFG, defining an early stage of sprouting (**Figures VII-1C and D**).

When characterizing the microfluidic co-culture, the sprouting phenomena caught our attention. Angiogenesis is a complex morphogenetic process where endothelial cells from pre-existing vessels invade the matrix as multicellular sprouts to form new vessels [33]. For capillary sprouting and blood vessel formation, both proliferation and migration are important, but how these two events are coordinated during the extension process is not fully clear [34]. Pro-angiogenic signals, such as VEGF, promote processes such as proliferation, endothelial motility and filopodia extension [35]. Evidence from preclinical and clinical studies indicates VEGF is the predominant angiogenic factor in human colon cancer and is associated with formation of metastases and poor prognosis [36]. So far, innumerous models tried to recreate this phenomena [34, 37, 38]. For instance, the tube formation assay involves the reorganization of endothelial cells seeded at Matrigel's surface to form cords similar to vascular networks. Still they lack important features observed in native angiogenesis including directional invasion of cells into a 3D extracellular matrix (ECM), proper polarization of the luminal, lumen formation, and support of fluid flow [39]. Although it has been stated before that we are not trying to recreate an anastomosis in the central chamber, the fact that we cannot observe it can be explained by several factors, for example, by the fact that the central chamber of the device is too large to observe such events. Nevertheless, from a technical perspective, this feature allows higher

volumetric hosting of HCT-116 cells, which enables quantitative analysis of gene expression on this tissue (*i.e.*, enough cells for PCR analysis). Another factor is probably the lack of support cells, such as perycites. This cell type would help to stabilize vessel formation and therefore permit the bridging of sprouts over longer distances of cell culture regions [40]. As our goal was uniquely to use the side channels to create a perfusable lateral channel with a lumen, we seeded the endothelial cells in the lateral channel, and not in the central chamber. However, it is interesting to see the natural behavior of the endothelial cells invading the Matrigel filled chamber with the cancer cells and further characterize our model. As conclusion, this biomimetic model is able to reconstitute the beginning of the angiogenic sprouting process.

To generate a stable gradient, one of the main goals of this project, the CMCht/PAMAM dendrimer nanoparticles were chosen. Their proven ability to act as drug release vehicles inside the cells, as well as cell trackers (when surface modified with a fluorescence molecule such as FITC [22, 27]) made them excellent candidates. One of the initial concerns was the ability of these nanoparticles to perfuse through Matrigel's fiber network. As observed in **Figure VII–3A**, the nanoparticles disperse widely when perfused in the lateral channels, in a gradient fashion. The real time observation and establishment of a fluorescent gradient generated by the perfusion of the FITC-labeled nanoparticles was essential to move on to drug screening assays, using the same flow and the same nanoparticles, this time releasing the drug overtime.

Regarding the GEM release from the dendrimer nanoparticles in the microfluidic model, a concentration of 0.5 mg/mL was chosen with the rationale to a) avoid the cytotoxic effect of the nanoparticles and b) enable continuous and sustained intracellular drug delivery by the nanoparticles and therewith a high efficacy, as was demonstrated by the viability results (**Figure VII-4**) and qPCR data (**Figure VII- 5**). Also, nanoparticles are highly advantageous when comparing to the golden standard clinical delivery of one bulk delivery (every two weeks), more prone to result in secondary undesirable effects.

Given that the gradient we observed was more or less concentrically generated from the periphery towards the center of the chamber, the areas defined for quantification followed this geometry. Apparently, lower amounts of nanoparticles leading to drug release in the areas further away from the source are not sufficient to induce cell death. Higher drug efficacy at D1-D2 regions seems to define a cut-off area on the action range of the nanomedicines in the matrix

delineated by the Matrigel cell-culture. Another important aspect to consider when analyzing the data is that although we were not quantifying cell death among endothelial cells, it is visible that both the cancer cells and the vasculature are sensitive to standard-of-care chemotherapeutic Gemcitabine. Targeting of the nanoparticles towards CRC cells and minimizing deleterious effects on endothelial cells would be of extreme usefulness and constitutes the next step of this work. No significant differences are observed between the controls at both days or between the controls and the areas subjected to culture medium M1, M2 and M3. It is interesting to note that even after 5 days of exposure to the maximum concentration of drug possible in this model (area D1), only about 40 % of cell death was observed. This low cell death level is in agreement with previous studies, corroborating the fact that 3D cultures usually show a reduced sensitivity to anticancer drugs [41]. This can be due to various factors, including matrix stiffness, which was reported to be closely related to tumor chemoresistance decreased penetration of anti-cancer drugs, increased pro-survival signaling, and/or up-regulation of genes conferring drug resistance.

Moreover, cells could be in the process of dying at the analysis time, but not yet dead and therefore not quantified in this screening, since the ethidium homodimer only stains dead cells. This microfluidic chip also allows the use of other stainings.

To the best of our knowledge, very few organ-on-chip models allow for gene expression analysis of the cells cultured therein due to the small mRNA content accessible from the chip's culture chambers. Moreover, the need to use hydrogels such as Matrigel to replicate the intricate 3D microenvironment in which cells live makes it harder to retrieve them for genetic analysis in good conditions. This analysis works as a proof-of-concept to demonstrate the versatility of this platform to work both as a drug screening platform and allowing genetic analysis. One of the main challenges of this task was to effectively retrieve HTC-116 cells from the Matrigel inside the 5 mm central chamber of the microfluidic device. The strategy we developed involves punching out the central chamber with a sterile surgical 5 mm punch and dissolving the Matrigel with encapsulated cancer cells in Recovery Solution. Results show a down regulation of all genes tested. MMP-1 is a collagenase that degrades ECM, specifically targeting type I, II and III collagens, the major components of the interstitial stroma [42]. It has been suggested to be associated with an advanced stage of colon cancer with poor prognosis and has emerged as a new oncogenesis and metastasis target for treatment of diverse cancers [43]. However,

molecular factors that contribute directly to tumor cell vascular penetration and the extent of MMP-1 activity in the presence of chemotherapeutic drugs has not been fully identified [44, 45]. For example, Khanna *et al*. [46] used small interfering RNA (siRNA) against proto-oncoprotein Ets-1 in gemcitabine-resistant cells, and demonstrated a reversal in gemcitabine chemosensitivity, translated in a marked reduction in the expression of MMP-1[46]. Given this evidence, it makes sense that exposing HCT-116 cells to an anti-cancer drug would lead to the down regulation of the expression of MMP-1, as observed, however, with no statistical differences. Regarding caspase-3 results**,** the down regulation obtained over the two timepoints corroborates the previous live/dead assay results, where at day 1 the extent of cell death due to GEM exposure is less pronounced than day 5 (although with no statistical differences when compared to the respective control). Nevertheless, at the later time point, the expression of Caspase-3 is downregulated, even though we see a clear increase in cell death in the live/dead experiments performed before. Recently, caspase activity identified in the absence of cell death has sparked strong interest in caspase functions in non-apoptotic cellular responses, suggesting that caspases can be activated without inducing or even before apoptosis occurs [47]. Several pathways can be related to GEM-induced apoptosis. On one hand, literature evidence exists for caspase-dependent apoptosis [48], while other studies describe GEM-induced apoptosis via reactive oxygen species generation, without increase in Caspase-3 [49]. In addition, GEM-induced apoptosis is also related to signal-regulated kinase (ERK), Akt, Bcl-2 and p38 mitogen-activated protein kinase (MAPK) pathways, and not only Caspase-3 [50].

When looking at Ki-67 expression, a significant difference in cells exposed to the drug from day 1 to day 5 reveals that the drug decreased cell proliferation. Its increased expression in human cancer specimens generally denotes an aggressive phenotype, although new studies suggest that this process is more complex than initially thought [51]. However, the fact that many aggressive cancers have high expression of Ki-67 relative to normal and quiescent cells suggests that Ki-67 might be an attractive target for cancer therapy if its role as a driver of carcinogenesis were validated.

The developed tumor-on-chip platform comprising a human CRC-like core and surrounding vascularized microtissue is a promising tool to be used in onco-medicine, either for high-content image-based screenings or gene expression analysis to study drug-dose responses. Based on a

robust dynamic microfluidic system with a viable co-culture of HTC-116 CRC cells and HCoMECS, this platform was validated as tumor-on-chip *in vitro* platform suitable for assessing an anti-cancer nanoparticle-based deliverable.

Although very useful as a high-throughput system for drug testing, our model does not comprise an oxygen gradient, common to the *in vivo* cancer microenvironment. Generating such a gradient would require inclusion of another complex feature in this already complex model, and will be considered as a part of the future work. In this study, the in-house-synthetized dendrimer nanoparticles were used as a model for nanomaterial based anti-cancer therapeutics. The fluorescently-modified nanoparticles successfully acted as a tracking tool that allowed the real-time imaging of the nanoparticle location, whereas drug-loaded particles functioned as an effective delivery vehicle of GEM in a gradient fashion. The resulting data sets enabled the definition of precise ranges of action of these anti-cancer nanoparticles, taking into account the complexity of the tumor microenvironment, including the critical microvasculature component. Highlights the importance of the high range of concentrations in a single experiment at this model, which has an impact on its robustness as a validation tool This tumor-on-chip device enabled both the performance of RT-PCR and immunocytochemistry stainings as the drug was being delivered to the tumor core. Technically, we proved that cells can easily be extracted from the chip and studied in terms of gene expression, providing valuable information on the mechanisms underlying the drug effect. Through this 3D microfluidic cell culture, the study of phenomena such as vascularization and oncogenesis in dynamic conditions may provide a powerful insight on the cancer stage prognosis and eventually on depicting a treatment option. Such capabilities are of high value, especially if using patient cells, and, thus, for precision therapy screenings on personalized medicine.

Most of all, the greatest advantages of our platform compared to others of the same type (central chamber for 3D matrix laterally sided by perfusable channels) are: 1) facile molecular cell analysis; 2) physiologically inspired design of radial drug penetration into solid tumors; 3) hybrid co-culture system to show efficiency of drug penetration through a micro-vascular network into a cancer-mimicking tissue, comprised of a supporting relevant matrix with colorectal cancer cells; 4) real-time imaging of drug delivery and its effect on cell viability; 5) design compatible with assessing physiologically-relevant cell migration, thus metastatic events (not the scope of the

current manuscript); and 6) system easily combined with organoid seeding of the central chamber.

VII-6. Conclusions

This platform has the potential to further study the EPR effect by controlling the permeability of the vascular network, *e.g.* by readjusting the distance between pillars. Moreover, tumor cell stress can be studied by *e.g.* varying the flow rates and, thus, exposing the cells to shear stresses. Also, while tumor cell signaling was not studied here, this could be done by analyzing the medium collected in the outlet for e.g. soluble factors profiling. The potential for further application is vast, from testing various types and sizes of particles and patient-derived cells, to bringing this tool closer to a clinical and pharmaceutical translatable setting in further research.

Taken together, this platform can potentially lead to breakthrough discoveries not only in basic research but also related to clinical applications, namely in CRC field.

VII-7. Acknowledgments

The project FROnTHERA (NORTE-01-0145-FEDER-000023), supported by Norte Portugal Regional Operational Programme (NORTE 2020), under the PORTUGAL 2020 Partnership Agreement, through the European Regional Development Fund (ERDF). Mariana Carvalho acknowledges her PhD scholarship NORTE-08-5369-FSE- 000044, funded by Programa Operacional Regional do Norte, Fundo Social Europeu, Norte2020 TERM&SC and EMBO Short-Term Fellowship 7232. J. M. Oliveira thanks FCT for his distinction attributed under the FCT Investigator program (IF/00423/2012 and IF/01285/2015. This work was partially supported by the IET Harvey Engineering Research Award 2018 (ENG ThE CANCER) and with the support of the Dutch Province of Limburg.

VII-8. REFERENCES

1. Vatandoust, S., T.J. Price, and C.S. Karapetis, *Colorectal cancer: Metastases to a single organ.* World Journal of Gastroenterology, 2015. **21**(41): p. 11767-11776.
2. Carvalho, M.R., et al., *Anti-Cancer Drug Validation: the Contribution of Tissue Engineered Models.* Stem Cell Rev, 2017.
3. Phan, D.T.T., et al., *A vascularized and perfused organ-on-a-chip platform for large-scale drug screening applications.* Lab Chip, 2017. **17**(3): p. 511-520.
4. Barata, D., C. van Blitterswijk, and P. Habibovic, *High-throughput screening approaches and combinatorial development of biomaterials using microfluidics.* Acta Biomaterialia, 2016. **34**(Supplement C): p. 1-20.
5. Foudeh, A.M., et al., *Microfluidic designs and techniques using lab-on-a-chip devices for pathogen detection for point-of-care diagnostics.* Lab Chip, 2012. **12**(18): p. 3249-66.
6. Orcheston-Findlay, L., et al., *A microfluidic gradient generator to simulate the oxygen microenvironment in cancer cell culture.* Microelectronic Engineering, 2018. **195**: p. 107-113.
7. Bott, K., et al., *The effect of matrix characteristics on fibroblast proliferation in 3D gels.* Biomaterials, 2010. **31**(32): p. 8454-64.
8. Barata, D., C. van Blitterswijk, and P. Habibovic, *High-throughput screening approaches and combinatorial development of biomaterials using microfluidics.* Acta Biomaterialia, 2016. **34**: p. 1-20.
9. Ma, Y.-H.V., et al., *A review of microfluidic approaches for investigating cancer extravasation during metastasis.* Microsystems &Amp; Nanoengineering, 2018. **4**: p. 17104.
10. Wan, L., et al., *Mimicking Embedded Vasculature Structure for 3D Cancer on a Chip Approaches through Micromilling.* Scientific Reports, 2017. **7**(1): p. 16724.
11. Chen, M.B., et al., *On-chip human microvasculature assay for visualization and quantification of tumor cell extravasation dynamics.* Nat Protoc, 2017. **12**(5): p. 865-880.
12. Zervantonakis, I.K., et al., *Three-dimensional microfluidic model for tumor cell intravasation and endothelial barrier function.* Proc Natl Acad Sci U S A, 2012. **109**(34): p. 13515-20.
13. Berthier, E. and D.J. Beebe, *Gradient generation platforms: new directions for an established microfluidic technology.* Lab Chip, 2014. **14**(17): p. 3241-7.
14. Keenan, T.M. and A. Folch, *Biomolecular gradients in cell culture systems.* Lab on a chip, 2008. **8**(1): p. 10.1039/b711887b.
15. Schwarz, J., et al., *A microfluidic device for measuring cell migration towards substrate-bound and soluble chemokine gradients.* Scientific Reports, 2016. **6**: p. 36440.
16. Fouad, Y.A. and C. Aanei, *Revisiting the hallmarks of cancer.* Am J Cancer Res, 2017. **7**(5): p. 1016-1036.
17. Shangguan, W., et al., *Endothelium originated from colorectal cancer stem cells constitute cancer blood vessels.* Cancer Science, 2017. **108**(7): p. 1357-1367.
18. Jiménez-Fonseca, P., et al., *Gemcitabine plus capecitabine (Gem–Cape) biweekly in chemorefractory metastatic colorectal cancer.* Clinical & Translational Oncology, 2015. **17**(5): p. 384-392.
19. ClinicalTrials.gov. *Gemcitabine in Treating Patients With Advanced Colorectal Cancer*. 2017 23th May 2018]; Available from: https://clinicaltrials.gov/ct2/show/NCT00007943.

20. Yu, X., et al., *An in vitro and in vivo study of gemcitabine-loaded albumin nanoparticles in a pancreatic cancer cell line.* International Journal of Nanomedicine, 2015. **10**: p. 6825-6834.
21. Saif, M.W., et al., *The efficacy of gemcitabine as salvage treatment in patients with refractory advanced colorectal cancer (CRC): a single institution experience.* Anticancer Res, 2011. **31**(9): p. 2971-4.
22. Oliveira, J.M., et al., *Surface Engineered Carboxymethylchitosan/Poly(amidoamine) Dendrimer Nanoparticles for Intracellular Targeting.* Advanced Functional Materials, 2008. **18**(12): p. 1840-1853.
23. Chen, X.-G. and H.-J. Park, *Chemical characteristics of O-carboxymethyl chitosans related to the preparation conditions.* Carbohydrate Polymers, 2003. **53**(4): p. 355-359.
24. Livak, K.J. and T.D. Schmittgen, *Analysis of Relative Gene Expression Data Using Real-Time Quantitative PCR and the 2−Δ Δ CT Method.* Methods, 2001. **25**(4): p. 402-408.
25. Jacquemet, G., H. Hamidi, and J. Ivaska, *Filopodia in cell adhesion, 3D migration and cancer cell invasion.* Current Opinion in Cell Biology, 2015. **36**: p. 23-31.
26. Oliveira, J.M., et al., *The osteogenic differentiation of rat bone marrow stromal cells cultured with dexamethasone-loaded carboxymethylchitosan/poly(amidoamine) dendrimer nanoparticles.* Biomaterials, 2009. **30**(5): p. 804-13.
27. Carvalho, M.R., et al., *A semiautomated microfluidic platform for real-time investigation of nanoparticles' cellular uptake and cancer cells' tracking.* Nanomedicine (Lond), 2017. **12**(6): p. 581-596.
28. Han, H., et al., *Enzyme-sensitive gemcitabine conjugated albumin nanoparticles as a versatile theranostic nanoplatform for pancreatic cancer treatment.* Journal of Colloid and Interface Science, 2017. **507**: p. 217-224.
29. Bendardaf, R., et al., *MMP-1 (collagenase-1) expression in primary colorectal cancer and its metastases.* Scand J Gastroenterol, 2007. **42**(12): p. 1473-8.
30. Bogorad, M.I., et al., *Review: in vitro microvessel models.* Lab on a Chip, 2015. **15**(22): p. 4242-4255.
31. Barata, D., et al., *Development of a shear stress-free microfluidic gradient generator capable of quantitatively analyzing single-cell morphology.* Biomed Microdevices, 2017. **19**(4): p. 81.
32. Markov, D.A., et al., *Variation in diffusion of gases through PDMS due to plasma surface treatment and storage conditions.* Biomed Microdevices, 2014. **16**(1): p. 91-6.
33. Nishida, N., et al., *Angiogenesis in Cancer.* Vascular Health and Risk Management, 2006. **2**(3): p. 213-219.
34. Yeon, J.H., et al., *In vitro formation and characterization of a perfusable three-dimensional tubular capillary network in microfluidic devices.* Lab Chip, 2012. **12**(16): p. 2815-22.
35. Weis, S., et al., *Endothelial barrier disruption by VEGF-mediated Src activity potentiates tumor cell extravasation and metastasis.* J Cell Biol, 2004. **167**(2): p. 223-9.
36. Bendardaf, R., et al., *The effect of vascular endothelial growth factor-1 expression on survival of advanced colorectal cancer patients.* The Libyan Journal of Medicine, 2017. **12**(1): p. 1290741.
37. Tahergorabi, Z. and M. Khazaei, *A Review on Angiogenesis and Its Assays.* Iranian Journal of Basic Medical Sciences, 2012. **15**(6): p. 1110-1126.
38. Song, W., et al., *Tumor-derived extracellular vesicles in angiogenesis.* Biomedicine & Pharmacotherapy, 2018. **102**: p. 1203-1208.

39. Nguyen, D.H., et al., *Biomimetic model to reconstitute angiogenic sprouting morphogenesis in vitro.* Proc Natl Acad Sci U S A, 2013. **110**(17): p. 6712-7.
40. Nguyen, D.-H.T., et al., *Biomimetic model to reconstitute angiogenic sprouting morphogenesis in vitro.* Proceedings of the National Academy of Sciences, 2013. **110**(17): p. 6712-6717.
41. Wen, Z., et al., *A spheroid-based 3-D culture model for pancreatic cancer drug testing, using the acid phosphatase assay.* Braz J Med Biol Res, 2013. **46**(7): p. 634-42.
42. Shen, C.J., et al., *MMP1 expression is activated by Slug and enhances multi-drug resistance (MDR) in breast cancer.* PLoS One, 2017. **12**(3): p. e0174487.
43. Foley, C.J., et al., *Matrix metalloprotease-1a promotes tumorigenesis and metastasis.* J Biol Chem, 2012. **287**(29): p. 24330-8.
44. Benbow, U., et al., *Selective modulation of collagenase 1 gene expression by the chemotherapeutic agent doxorubicin.* Clin Cancer Res, 1999. **5**(1): p. 203-8.
45. Said, A.H., J.-P. Raufman, and G. Xie, *The Role of Matrix Metalloproteinases in Colorectal Cancer.* Cancers, 2014. **6**(1): p. 366-375.
46. Khanna, A., et al., *Ets-1 expression and gemcitabine chemoresistance in pancreatic cancer cells.* Cell Mol Biol Lett, 2011. **16**(1): p. 101-13.
47. Kuranaga, E., *Beyond apoptosis: caspase regulatory mechanisms and functions in vivo.* Genes Cells, 2012. **17**(2): p. 83-97.
48. Chandler, N.M., J.J. Canete, and M.P. Callery, *Caspase-3 drives apoptosis in pancreatic cancer cells after treatment with gemcitabine.* J Gastrointest Surg, 2004. **8**(8): p. 1072-8.
49. Guo, Y., et al., *Overexpression of heat shock protein 27 (HSP27) increases gemcitabine sensitivity in pancreatic cancer cells through S-phase arrest and apoptosis.* J Cell Mol Med, 2015. **19**(2): p. 340-50.
50. Kao, Y.-T., et al., *Involvement of p38 mitogen-activated protein kinase in acquired gemcitabine-resistant human urothelial carcinoma sublines.* The Kaohsiung Journal of Medical Sciences, 2014. **30**(7): p. 323-330.
51. Melling, N., et al., *High Ki67 expression is an independent good prognostic marker in colorectal cancer.* J Clin Pathol, 2016. **69**(3): p. 209-14.

Chapter VIII

Peptide-modified Dendrimer Nanoparticles for Targeted Therapy of Colorectal Cancer

Chapter VIII

Peptide-modified Dendrimer Nanoparticles for Targeted Therapy of Colorectal Cancer[1]

ABSTRACT

Peptides have recently emerged as a promising class of targeting ligands for specific drug delivery in cancer treatment, which avoid undesirable side effects of the systemic administration of chemotherapeutics. Their conjugation with nanoparticles have demonstrated to improve the functionality of peptides resulting in a versatile platform for biomedical applications. In this work, we describe the development of carboxymethylchitosan/poly(amidoamine) (CMCht/PAMAM) dendrimer nanoparticles functionalized with YIGSR laminin receptor binding peptide for the active targeting and specific delivery of therapeutic agents into colorectal cancer cells. The successful functionalization was confirmed by several physico-chemical characterization techniques. The selectivity of the YIGSR-CMCht/PAMAM dendrimer nanoparticles was first validated *in vitro* using a micropatterned array of 67kDa laminin receptor. Next, the specificity of YIGSR-CMCht/PAMAM dendrimers nanoparticles towards laminin receptor was further confirmed both in 2D and 3D settings using HCT-116 colorectal cancer cells and L929 fibroblasts in co-culture. Finally, gemcitabine-loaded YIGSR-CMCht/PAMAM dendrimer nanoparticles induced a targeted mortality on HCT-116 cancer cells in a co-culture scenario. Overall, our study shows solid evidences that YIGSR laminin receptor binding peptide coupled to CMCht/PAMAM dendrimer nanoparticles may be employed as an anti-cancerous target for the specific and intracellular delivery of chemotherapeutic agents.

Keywords: Targeting; Dendrimer nanoparticles; Colorectal cancer; Micropatterning.

[1]This chapter is based on the following publication:

M. R. Carvalho, C. R. Carvalho, F.R. Maia, D. Caballero, S. C. Kundu, R. L. Reis, J. M. Oliveira. "Peptide-modified dendrimer nanoparticles for targeted therapy of colorectal cancer" Advanced Therapeutics, 2019, 1900231. doi: 10.1002/adtp.201900132.

VIII-1. Graphical Abstract

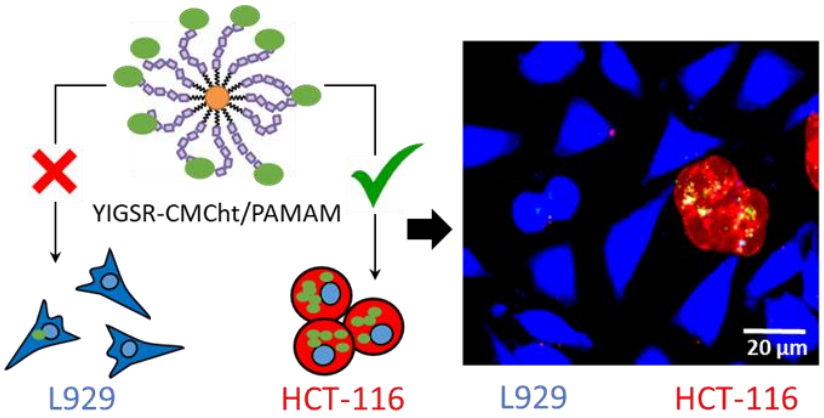

VIII-2. Introduction

Cancer is a leading cause of death worldwide, with more than 10 million new cases each year, and an estimation of ~13.1 million cancer-related deaths by 2030 [1]. Typically, cytotoxic chemotherapies have a narrow therapeutic window, with high peaks of plasma concentration. This leads to high-dose requirements with adverse side effects, reduced therapeutic indices, non-specific targeting, and development of multiple drug resistance [2].

Nanotechnology has evolved as an exciting platform in the field of cancer research with promises to improve the pharmacology of current cancer therapeutics [3]. Drug-loaded nanoparticles (NPs) offer several advantages over free drugs. This includes their capabilities to encapsulate large amounts of chemotherapeutic agents, a prolonged half-life, and an increased targeting efficiency leading to reduced toxicity [4]. Nanoparticle size, core properties, and surface modifications are considered as key factors affecting the clearance rate and organ distribution [5]. A significant number of nanomaterials, including inorganic nanoparticles, liposomes, micelles, and polymers have been developed for targeted drug delivery in cancer [6, 7]. Dendrimers are considered a promising alternative because of their advanced capabilities, which make them ideal tools for targeted drug delivery. As an example, they can increase the solubility and bioavailability of hydrophobic drugs [8]. Further, their architecture and availability of active functional groups allow the easy addition of moieties and the encapsulation of drugs [8].

Different types of active tumor-targeted ligands, such as RGD peptide, folic acid, and transferrin, have been employed in conjunction with NPs to specifically direct and enhance drug accumulation in

the tumor [9]. In particular, doxorubicin-loaded HPMA-copolymer conjugated with GE11 oligopeptide have been employed to specifically target colorectal cancer (CRC) cells with EGFR overexpression. A high cellular uptake of the doxorubicin-loaded NP was observed, achieving a selective release of the drug [10]. Similarly, a multifunctional nanosystem based on methotrexate-loaded guar gum NPs functionalized with folic acid (MTXFA-GGNP) has been employed to release methotrexate at colonic pH values (6.8) in CRC. Interestingly, the engineered NPs displayed preferential *in vivo* uptake in colon tissue [11]. However, most of these approaches were mainly studied in 2D environments. In addition, these studies also lacked a visual representation and analysis of NPs internalization in a co-culture scenario, and importantly, their validation using native-like 3D settings.

Despite all the efforts invested in the development of targeted drug delivery systems for improved cancer therapeutics, their performance is still limited for medical applications. New approaches are needed to target efficiently and precisely the cancer cells. In this regard, the YIGSR laminin receptor binding peptide has demonstrated to be a promising class of targeting ligand for specific drug delivery in cancer treatment. Cancer cells from various sources express high levels of the 67 kDa laminin receptor (67LR) [12], including bile duct carcinoma, colorectal carcinoma, cervical cancer, and breast carcinoma [13], which are shown to be correlated with tumor invasiveness [14]. Earlier work has demonstrated that the laminin binding capacity of plasma membranes isolated from human invasive breast carcinomas is 50-fold greater than that of membranes from benign lesions or normal tissue[15].

In this study, we hypothesize that the peptide sequence YIGSR grafted onto carboxymethylchitosan/poly(amidoamine) (CMCht/PAMAM) dendrimer NPs promotes specific and targeted internalization into CRC cells [16]. To this end, we first characterize the morphology and successful functionalization of CMCht/PAMAM and YIGSR-modified CMCht/PAMAM dendrimer NPs by AFM, TEM, DLS and H^1NMR. The selectivity of the YIGSR-CMCht/PAMAM dendrimer nanoparticles was first validated *in vitro* using a micropatterned array of 67kDa laminin receptor. Next, we investigate the effect of both types of dendrimer NPs on the viability of HCT-116 CRC cells or L929 fibroblasts. Next, the targeted internalization of the NPs is assessed in a co-culture of HCT-116 CRC cells and L929 fibroblasts both in traditional well plates (2D) or encapsulated within a 3D Matrigel® matrix.

VIII-3. MATERIALS AND METHODS

VIII-3.1. Synthesis of the CMCht/PAMAM dendrimer nanoparticles

Dendrimer NPs where fabricated as described elsewhere [16]. Briefly, by using a chemical modification route of chitin (Sigma, Germany), we synthesized CMCht with a degree of deacetylation of 80 % and degree of substitution of 47 %. CMCht/PAMAM dendrimer NPs were prepared in a step-wise manner as follows: first, the increase of the dendrimers' generation was carried out. An appropriate volume of PAMAM-CT (G1.5) in methanol was transferred to a volumetric flask. The starting compound was re-dissolved in ultrapure water to give a final concentration of 10 mg/mL and the pH was adjusted to 6.5 with dilute hydrochloric acid solution (Riedel de-Haen, Germany). 1-ethyl-(3-dimethylaminopropyl) carbodiimide hydrochloride (EDC, Fluka, Portugal) was then added to the solution at a molar ratio sufficient to modify the carboxylate residue of the dendrimers. The solution was kept under agitation for 30 minutes at room temperature (RT). Ethylenediamine (EDA, Sigma, Germany) was added to the solution at a molar ratio equal to that of EDC and left to react for 4 hours. After this period the excess of EDC was removed by dialysis (cellulose tubing, benzoylated for separating compounds with a MW ≤ 1200, Sigma, Germany). After preparing the PAMAM-amine terminated compound, an exhaustive alkylation of the primary amines (Michael addition) was performed. An appropriate volume of PAMAM-amine terminated was mixed with methanol (Sigma, Germany) and methyl methacrylate. CMCht/PAMAM dendrimer NPs were then precipitated after addition of an appropriate volume of a saturated Na_2CO_3 (Sigma, Germany) solution and cold acetone (Pronalab, Portugal). Precipitates were collected by filtration and dispersed in ultrapure water for dialysis over a period of 48 hours. Finally, CMCht/PAMAM dendrimer NPs were obtained by freezing the solution at -80 °C and freeze-dried (Telstar-Cryodos-80) for 7 days.

VIII-3.2. Peptide attachment onto CMCht/PAMAM dendrimer nanoparticles

The attachment of YIGSR peptide (Genscript Corp, Piscataway, NJ, USA) to the NPs was performed via carbodiimide chemistry to form an amide bond between the carboxyl groups on the NPs and the amine groups at the YIGSR N-terminal end group. CMCht/PAMAM 1 % wt. was prepared in buffer 2-(N-morpholino)ethanesulfonic acid (MES), Sigma Aldrich, Germany), and mixed with the appropriate

amount of NHS-Sulfo, EDC and a 10 mg/mL YIGSR peptide solution (dissolved in MES buffer). The solution was stirred for 24 hours and the NPs were recovered by dialysis against ultrapure water for 48 hours followed by freeze-drying process for 7 days.

VIII-3.3. Labelling of CMCht/PAMAM dendrimer nanoparticles with FITC

The conjugates of CMCht/PAMAM-FITC were obtained by covalently bonding the CMCht amine group and the isothyocianate group of FITC (10 mg/mL) (Sigma, Germany) in anhydrous dimethyl sulfoxide (DMSO, Norconcessus, Portugal) creating a thiourea bond. First, a 10 mg/mL CMCht/PAMAM dendrimer NPs solution was prepared in a carbonate-bicarbonate coupled buffer at pH 9.2. Then, a solution of FITC/DMSO was added under agitation and kept in the dark at 4 °C for 8 hours. Next, the FITC-labeled CMCht/PAMAM dendrimer NPs solution was dialyzed against ultrapure water for 24 hours to remove unlinked FITC and filtered (pore size < 220 nm) in sterile and dark conditions. The final product was obtained after freeze-drying.

VIII-3.4. Gemcitabine incorporation into CMCht/PAMAM dendrimer nanoparticles

Gemcitabine (GEM) was incorporated in the NPs by mixing an aqueous solution of YIGSR-CMCht/PAMAM dendrimer NPs with an aqueous GEM solution with a final concentration of $5x10^{4}$ M. Saturated sodium carbonate solution (Na_2CO_3) and acetone were then added to the mixture. The resulting precipitates were dialyzed against ultrapure water. GEM-loaded YIGSR-CMCht/PAMAM dendrimer NPs were obtained by freezing the final solution at -80 °C and freeze-drying the samples.

VIII-3.5. Characterization of the CMCht/PAMAM dendrimer nanoparticles

VIII-3.5.1. Protein quantification

The concentration of YIGSR peptide grafted onto the dendrimer NPs was estimated by UV spectroscopy (between 200 nm and 275 nm) and the Micro-BCA (562 nm) protein quantification assay using a microplate reader (BIO-TEK, EUA). Samples of CMCht/PAMAM and modified YIGSR-

CMCht/PAMAM dendrimer NPs were dissolved in ultrapure water at a final concentration of 1 % and compared to standards for protein quantification in triplicates.

VIII-3.5.2. Dynamic light scattering (DLS)

Zeta potential and the size of the CMCht/PAMAM and YIGSR-CMCht/PAMAM dendrimer NPs were measured in a particle size analyzer (Zetasizer Nano ZS, Malvern Instruments, UK). Particle size analyses were performed by dynamic light scattering (DLS) in phosphate buffered saline (PBS) at pH 7.4 with low concentration of NPs and using disposable sizing cuvettes. Electrophoretic determinations of Zeta potential were investigated using the universal 'dip' cell at pH 7.4 in PBS solution. Zeta potential was also investigated in water.

VIII-3.5.3. Nuclear magnetic resonance spectroscopy (NMR)

The structure of CMCht/PAMAM and YIGSR-CMCht/PAMAM dendrimer NPs was determined by H^1NMR. Both types of NPs were dissolved in deuterated water (D_2O). Then, the NMR spectra were obtained with a Mercury -400BB operating at a frequency of 399.9 MHz at 50 °C. The one-dimensional 1H spectra were acquired using a 45° pulse, a spectral width of 6.3 kHz and an acquisition time of 2.001

VIII-3.5.4. Scanning Transmission Electron Microscopy (STEM)

Dendrimer NPs morphology was investigated by STEM (Philips CM-12, FEI, The Netherlands), equipped with a MEGA VIEW-II DOCU camera and Image Software Analyzer SIS NT DOCU. For that, the NPs were stained with 2 % of phosphotungstic acid and placed on the copper grids for observation,

VIII-3.5.5. Fourier Transform Infrared (FTIR)

The dried dendrimer NPs, prior to, and after YIGSR attachment, were mixed with potassium bromide (KBr) and placed between two disks. Pressure was applied (4.5 metric tons, Carver Inc) on the disk to form a pellet. The spectrum of the formed pellet was measured by FTIR spectroscopy (Exuinox 55, Bruker Optics Inc., USA) in the range of 400 and 3500 cm^{-1}.

VIII-3.5.6. Microcontact printing

Poly(dimethylsiloxane) (PDMS) 1:10 (v/v), Sylgard 184; Dow Corning) stamps were replicated from an SU-8 mold (MicroChem) fabricated by UV-photolithography (MIDAS MDA-400MA). The PDMS stamp was rendered hydrophilic by plasma treatment to maximize 67 LR patterning. Glass coverslips were plasma treated for 1 minute and incubated for 1 hour under anoxic conditions in anhydrous methanol solution of 5 % (v/v) 3-aminopropyl) triethoxysilane (APTES). Next, the samples were washed with methanol followed by ultrapure water. Then, APTES-functionalized coverslips were incubated for 30 minutes in a solution of 1 % (v/v) gluteraldehyde in ultrapure water. The micropatterned PDMS stamp was incubated with 10 μg/mL LR protein (Abcam, Portugal) solution for 2 hours and excess was removed by nitrogen drying. Immediately, the PDMS stamp containing the laminin receptor was placed in contact with the functionalized glass coverslip for 5 minutes. After releasing the stamp, FITC-labeled YIGSR-CMCht/PAMAM dendrimer NPs were incubated overnight.

VIII-3.6. *In vitro* cell culture in 2D and 3D platforms

VIII-3.6.1. Cell culture

Human HCT-116 colorectal cancer cells and L929 fibroblast were obtained from the American Collection of Cell Cultures (ATCC, USA). Cells were grown in Dulbecco's Modified Eagle Medium (Sigma Aldrich, Germany) supplemented with 10 % (v/v) fetal bovine serum and 1 % (v/v) penicillin/streptomycin (Gibco, USA) at 37 °C and 5 % CO_2. Subcultures of cells were performed when confluence reached values of ~90 %. Then, cells were plated at an initial density of $1x10^4$ cells per well in a 24-well plate for metabolic activity and DNA quantification. Co-cultures were used for internalization studies ($1x10^4$ of each cell type in 24 well plates).

VIII-3.6.2. Immunocytochemistry

L929 were pre-stained in red with CellTracker™CM DiI (1 μM) and seeded at an initial density of $1x10^4$ cells per well in a 24-well plate. At days 1 and 3, HCT-116 cancer cells and L929 fibroblasts in co-culture were fixed with 4 % formalin (Sigma Aldrich, Germany) for 10 minutes and washed with PBS. Cells were permeabilized with 0.1 % (v/v) Triton X-100 (Sigma Aldrich, Germany) in PBS for 5 minutes

and blocked with 3 % BSA (Sigma Aldrich, Germany) in PBS for 30 minutes. Immunolabeling was performed using a rabbit anti-human monoclonal antibody against 67 kDa LR (Abcam, 1:200) as primary antibody, prepared in PBS 1 % BSA and incubated overnight at 4 °C. The samples were incubated for 1 hour at RT with the respective secondary fluorochrome-conjugated antibodies, anti-rabbit/mouse IgG (Invitrogen, dilution 1:1000). Immunofluorescence was observed under transmitted fluorescence microscopy (Zeiss, Germany) (LR in green: ex/em 488/517; Cell Tracker™CM DiI in red: ex/em 594/618).

VIII-3.6.3. Metabolic activity

Alamar blue (AB) assay was performed according to supplier's instructions to assess the metabolic activity of cells. The effect of CMCht/PAMAM, YIGSR-CMCht/PAMAM and GEM-YIGSR-CMCht/PAMAM dendrimer NPs was assessed in terms of metabolic activity in each cell type separately. After 24 hours and 72 hours in culture, specific cell culture medium containing 20 % (v/v) AB was added to the different culture wells. The system was incubated for 4 hours after which fluorescence was monitored at 590 nm emission wavelength (excitation wavelength 530 nm), using a microplate reader (FL 600, Bio-Tek Instruments). After each AB determination, cells were rinsed with PBS and fresh culture medium was added to continue the culture. Medium with 20 % (v/v) AB was used as a blank.

VIII-3.6.4. DNA quantification

To assess the effect of CMCht/PAMAM, YIGSR-CMCht/PAMAM and GEM-YIGSR-CMCht/PAMAM dendrimer NPs on the cancer cells and fibroblasts separately, the total amount of DNA was measured using the fluorimetric double-stranded DNA (dsDNA) quantification kit (Quant-iT™ PicoGreen® dsDNA Assay Kit, Molecular Probes). The cells were washed with sterile PBS and lysed with 1 mL of ultrapure water in each well. The cellular suspensions were transferred into microtubes, incubated in a water bath at 37 °C for 1 hour, and stored at -80 °C for further analysis. DNA standards were prepared with concentrations varying between 0 and 2 μg/mL. Next, 28.7 μL of sample (or DNA standard), 71.3 μL of PicoGreen and 100 μL of TE buffer were mixed in each well of an opaque 96-well plate (Alfagene, Portugal), according to the manufacturer's protocol. Next, after 10 minutes incubation at RT,

fluorescence was measured using an excitation and emission wavelengths of 485 nm and 528 nm, respectively. Sample DNA values were read off from DNA standard curve.

VIII-3.6.5. Live/dead assay

The cell viability was assessed by calcein-AM and propidium iodide (PI; Life Technologies, Carlsbad, CA, USA) staining. L929 cells were first stained with CellTracker Blue CMAC (Alfagene, Portugal), whereas HCT-116 cells were left unstained. After 72 hours, three samples were incubated in 1 µg/mL calcein-AM and 5 µg/mL PI prepared in DMEM low glucose supplemented with sodium bicarbonate and 1 % (v/v) antibiotic/antimycotic solution for 30 minutes in the dark at 37 °C in the 5 % CO_2. After washing in PBS, samples were immediately analyzed in a confocal microscopy (Calcein-AM in green: ex/em 495/515 nm; PI in red: ex/em 495/635 nm; CellTracker Blue CMAC in blue: ex/em 353/466 nm) (Leica, SP8, Germany).

VIII-3.6.6. Cellular uptake

HCT-116 colorectal cancer cells and L929 fibroblasts were pre-stained in Far Red and in Blue CMAC CellTracker (Alfagene, Portugal), respectively. After 30 minutes incubation at 37 °C, cells were seeded in co-culture at a density of $1x10^4$ cells (each type)/well in 24 well plates, and allowed to adhere overnight. Then, the culture medium was replaced by fresh one supplemented with FITC-CMCht/PAMAM and FITC-YIGSR-CMCht/PAMAM dendrimer NPs at a final concentration of 0.5 mg/mL. At 24 hours and 72 hours, cells were washed with PBS, fixed with 4 % (v/v) formalin for 20 minutes at RT, washed again 3 times with PBS, and permeabilized with 0.2 % (v/v) Triton X-100 in PBS for 10 minutes. Next, cells were washed with PBS. The cell nuclei were stained with DAPI and F-actin with Phalloidin, as described above. The cells were imaged by confocal microscopy to assess the internalization of NPs (FITC – 488 nm). For 3D studies, the same procedure was used. In this case, the cells were encapsulated into a 50 µL of Matrigel matrix (Enzifarma, Portugal).

VIII-3.6.7. Flow cytometry analysis

For internalization analysis, the cells were co-cultured in medium supplemented with 0.5 mg/mL of FITC-labeled YIGSR-CMCht/PAMAM dendrimer NPs in 24-well plates ($1x10^4$ cells; each type/well).

Cells cultured in complete culture medium were used as controls. After 24 hours and 72 hours, the cells were trypsinized (TrypleX, Life technologies, USA) and a cell strainer was used to avoid cell clusters. Next, 0.5 mL of DMEM complete medium was added to each well and the samples were transferred to flow cytometry tubes. To distinguish cells in co-culture, 10 µL of PE-CD44 antibody (Abcam, Portugal) was incubated with HCT-116 cells for 20 minutes at RT. After washing with 2 mL of 2 % (v/v) FBS in PBS, the tubes were centrifuged at 300 rpm for 5 minutes and re-suspended in 1 % (v/v) formalin in PBS. The cell suspensions were analyzed in FACSCalibur flow cytometer (BD Biosciences, USA). A similar approach was followed for cell viability studies. In this case, the tubes were centrifuged at 300 rpm for 5 minutes and HCT-116 were stained with FITC-CD44 (Abcam, Portugal) for 30 minutes and re-suspended in 2 % (v/v) FBS in PBS. Then, 1 µL of PI were added to suspensions and incubated for 10 minutes at RT, after which they were analyzed by FACSCalibur flow cytometer. For internalization and cell viability assays in 3D, cells encapsulated in Matrigel were retrieved using 500 µL of Corning Cell Recovery Solution (Corning, USA) for 30 minutes at 4 °C and the subsequent protocol was performed as previously described.

For all assays, calibrate beads three-color kit (BD CaliBRITE™ beads, USA) was used to adjust the instrument settings before samples are run on the flow cytometer. Finally, data were analyzed using the Flowing Software 2.

VIII-3.6.8. Statistical analysis

Statistical analysis was performed using GraphPad Prism 5.0 software version 5.0a. The non-parametric Mann–Whitney test was used to compare two groups, whereas comparison between more than two groups was performed using the Kruskal–Wallis test followed by Dunn's comparison test. A value of $p < 0.05$ was considered statistically significant.

VIII-4. Results and Discussion

VIII-4.1. Physico-chemical characterization of dendrimer nanoparticles

We first investigated the attachment of the YIGSR peptide on the dendrimer NPs surface via carbodiimide chemistry **(Figure VIII-1A)**, and the morphology and size of both type of NPs. STEM images

revealed a monodisperse round-shaped morphology **(Figure VIII-1B)**, which was confirmed by AFM measurements (see **Supplementary Information VIII-S1A**). These results suggested the successful grafting of the peptide sequence, which conferred the YIGSR-CMCht/PAMAM dendrimer NPs a larger size. DLS was used to quantify the size of the NPs. **Figure VIII-1C** shows the peaks associated with both the CMCht/PAMAM and YIGSR-CMCht/PAMAM dendrimer NPs. In the former, two main peaks were obtained, which corresponded to individual and aggregated NPs. The first peak provided the average size of the individual NPs was 54 ± 7 nm, whereas the second one corresponded to NP aggregates with a much bigger size. In contrast, YIGSR-CMCht/PAMAM dendrimer NPs displayed three peaks. The first peak located around 6 nm corresponded to unreacted PAMAM G1.5. The reason is that the first step in the synthesis of the dendrimer NPs is increasing the generation of the PAMAM-CT (G 1.5), which has a theoretical size equal to the one provided by the peak, and therefore, this peak was assumed to correspond to unreacted G1.5. The second peak located around 130 ± 20 nm corresponds to the YIGSR-modified dendrimer NPs. Finally, the last peak is associated with aggregated NPs. Altogether, these results show that attachment of the peptide significantly increased the size of the NPs by ~2.5-fold without affecting the NPs polydispersity index (PDI) with values of 0.29 and 0.37 for CMCht/PAMAM and YIGSR-CMCht/PAMAM PDI, respectively.

Figure VIII-1D shows the FTIR spectrum of the CMCht/PAMAM and the newly modified YIGSR-CMCht/PAMAM dendrimer NPs. The spectrum of the modified NPs shows an increase in peak intensity at 1700 cm^{-1} attributed to the amide II and C-N stretching vibrations [17]. This is an evidence of the presence of amine groups as well as of the chemical bonding between the CMCht/PAMAM and the peptide. Similarly, the 520 cm^{-1} free amino acid peak and the 1120 cm^{-1} NH_3 vibration appear after NP modification [12, 18]. Moreover, both NPs showed characteristic peaks, such as the strong and broad peak of absorption at ~3400 cm^{-1}, which are assigned to the stretching vibration of the structural N-H overlapping the O-H stretching. Similarly, the attachment of the YIGSR peptide was further confirmed by the analysis of the chemical signature obtained by H^1NMR (Figure VIII-1E) [19]. Bearing in mind the analysis of H^1NMR spectra (see **Supplementary Information VIII-S2**), we can state that the signature protons of CH_2 and CH_3 of the YIGSR peptide are present in the YIGSR-CMCht/PAMAM around 2 and 3 ppm, indicating the successful grafting of the peptide. Moreover, the broad singlet at 3.02 ppm of the CMCht/PAMAM is also present in the modified nanoparticles. Taken together, the results obtained indicate that the peptide was successfully conjugated to the NPs.

We next measured the Zeta potential values of both unmodified CMCht/PAMAM and YIGSR-modified CMCht/PAMAM dendrimer NPs. Figure 1 F shows that the formers have a value of -14.7 ± 3.0 mV in PBS and -34.3 ± 3.0 mV in ddH_20. In contrast, YIGSR-modified CMCht/PAMAM dendrimer NPs have a value of -9.3 ± 0.8 mV in PBS and -19.3 ± 0.8 mV in ddH_20. The difference between YIGSR-modified dendrimer NPs (less negative) and unmodified NPs (more negative), indicates a reduction in the number of carboxylic acid groups on the NPs surface following peptide binding. Moreover, the addition of the positively-charged Arginine present in the peptide sequence suggests a successful grafting. It is expected that CMCht has a good pH and ion sensitivity in aqueous solution due to abundant –COOH and $–NH_2$ groups. On the other hand, since the Zeta potential of NPs is determined by their surface properties, this data shows the negatively charged carboxymethyl groups in the CMCht/PAMAM dendrimer NPs. The different Zeta potential values obtained in ddH_20 and PBS can be explained by the fact that the CMCht behaves as a weak polyanionic polyelectrolyte at physiological pH, *i.e.*, the amino groups are not protonated and most of carboxyl groups are not dissociated.

Further characterization was achieved by quantifying the amount of coupled peptide using the BCA protein quantification assay and compared to a standard curve using BSA **(Figure VIII-1G)**. Results show a significant difference between the levels of protein on non-modified and YIGSR-grafted CMCht/PAMAM dendrimer NPs. The former shows an amount of 3.60 ± 1.62 µg/mL, whereas the later has a concentration of 71.00 ± 3.75 µg/mL. This indicates that the peptide sequence YIGSR is successfully attached to the dendrimer NPs. Finally, the presence of the peptide on the CMCht/PAMAM dendrimer NPs was investigated by UV spectroscopy (**Supplementary Information VIII-S1B**). The peptide sequence YIGSR incorporates the amino acid tyrosine, which exhibits two characteristic absorbance peaks in the UV spectral region at approximately 230 nm and 280 nm [20]. The UV spectra were obtained using CMCht/PAMAM and modified YIGSR-CMCht/PAMAM dendrimer NPs for comparison. Two peaks located around 275 nm were observed. This indicated that the peptide is effectively grafted to the polymer backbone.

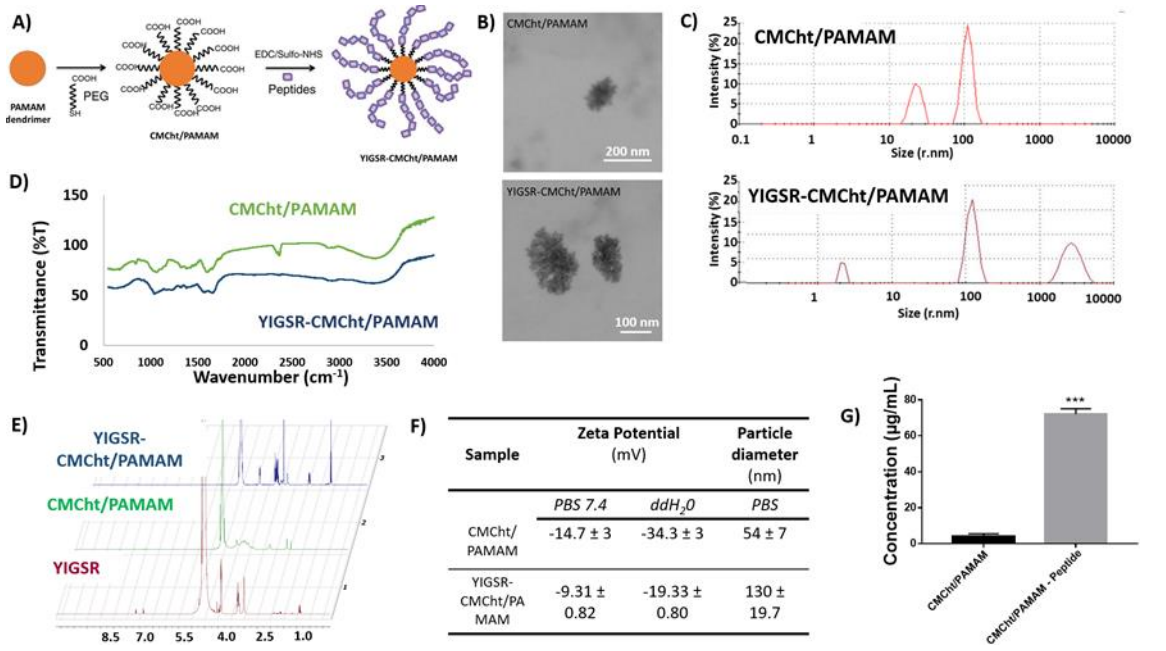

Figure VIII-1 - Physico-chemical characterization of dendrimer nanoparticles. (A) Schematic representation of the dendrimer NPs modification with YIGSR peptide from laminin via carbodiimide chemistry. (B) STEM image of CMCht/PAMAM and YIGSR-CMCht/PAMAM dendrimer NPs. (C) Representative graphic of the particle size distribution of CMCht/PAMAM and YIGSR-CMCht/PAMAM NPs, showing that the peptide sequence conferred the NPs a larger size. (D) FTIR analysis of CMCht/PAMAM and YIGSR-CMCht/PAMAM dendrimer NPs, showing an increase in intensity of the bands at 1700 cm^{-1} for YIGSR-CMCht/PAMAM dendrimers. (E) H^1NMR spectra of YIGSR-CMCht/PAMAM, CMCht/PAMAM, and YIGSR. The YIGSR-CMCht/PAMAM shows a peak at 3 ppm and no peak at 4.3 ppm suggesting that the substitutions occurred mainly on the C2 amino group of CMCht. (F) Table of the mean NP diameter and Zeta potential in PBS and ddH_2O, showing an increase in diameter and a decrease in Zeta potential upon the addition of YIGSR. (G) Determination of peptide concentration by protein quantification (BCA protein quantification) in CMCht/PAMAM and YIGSR-CMCht/PAMAM.

VIII-4.2. Targeted detection of FITC-YIGSR-CMCht/PAMAM on a micropatterned laminin receptor array

The 67 kDa high affinity LR is a non-integrin cell surface receptor of the extracellular matrix. The expression of this receptor is thought to be increased in neoplastic cells, which directly correlates with an enhanced invasiveness and metastatic potential [21]. To confirm this higher expression, we first performed an immunocytochemistry analysis to assess qualitatively the differences in LR expression in HCT-116 and L929 cells at 24 h and 72 h. HCT-116 cells displayed round morphologies and proliferated forming dense aggregates **(Figure VIII-2A)**. In contrary, L929 fibroblasts showed highly spread phenotypes. Importantly, HCT-116 displayed a large LR signal both at 24 hours and 72 hours. This is in contrast to L929 fibroblasts, which showed a low LR expression. Taken together, these results

suggest that the 67 kDa LR may be employed as a cancer-specific target to specifically deliver drug-loaded YIGSR-CMCht/PAMAM dendrimer NPs in a precise and efficient manner.

Next, we evaluated *in vitro* the specificity of the YIGSR-CMCht/PAMAM dendrimer NPs toward the LR. For this, an array of 67 kDa LR was micropatterned on a functionalized glass coverslip by micro-contact printing to recreate *in vitro* the physiological target **(Figure VIII-2B)**. Next, FITC-labeled YIGSR-CMCht/PAMAM dendrimer NPs were incubated on top of the LR array. We observed that the FITC-labelled NPs attached mainly on top of the triangular micropatterned regions, which contained the 67 kDa LR protein. Overall, these results show a strong affinity of between the NPs grafted with a portion of YIGSR peptide and the LR protein. However, more complex experiments involving protein receptors other than LR may need to be also tested to univocally prove a really specific affinity for this receptor.

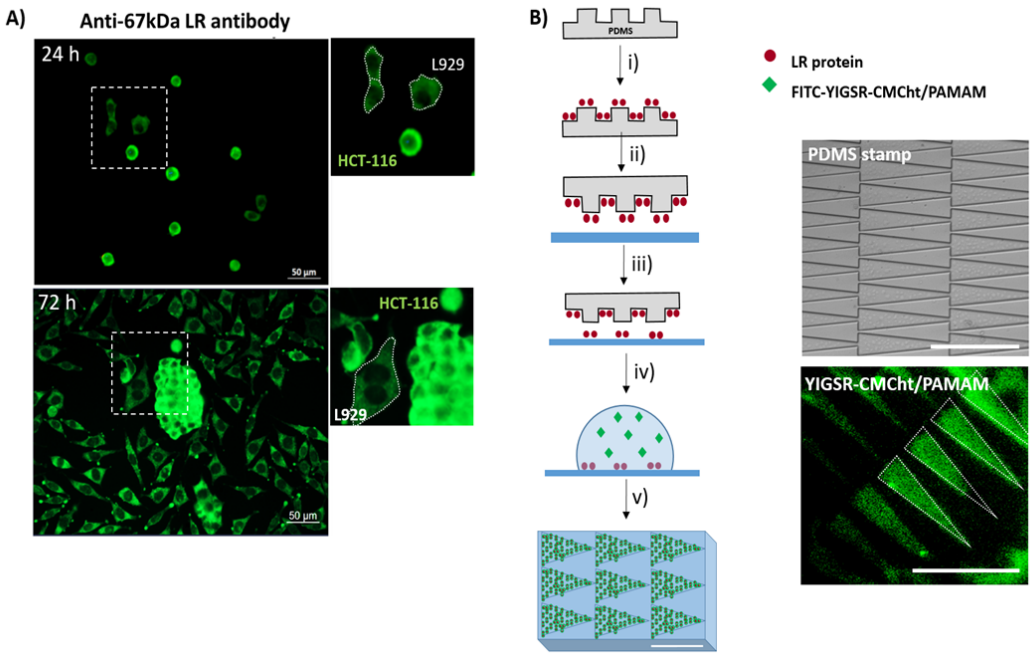

Figure VIII-2 - Specificity of FITC-YIGSR-CMCht/PAMAM dendrimer NPs on a micropatterned LR array. (A) Immunocytochemistry of anti-67kDa LR (green) performed on a co-culture of HCT-116 CRC cells and L929 fibroblasts (stained in red; See supplementary Information S3) cells at 24 h and 72 h. An overexpression of LR on HCT-116 is visible at both time points. (B) ***(Left)*** **Schematic representation of the steps involved in the microcontact printing of the LR: (i) incubation of the PDMS stamp with the LR solution; (ii) microcontact printing of the LR on top of a functionalized (APTES 5 % and glutaraldehyde) glass coverslip; (iii) PDMS stamp removal and rinsing with ddH_2O; (iv) incubation with FITC-YIGSR-CMCht/PAMAM; and (v) rinse with ddH_2O to remove the excess of FITC-YIGSR-CMCht/PAMAM.** ***(Right)*** **Representative brightfield and fluorescence microscopy images of the PDMS stamp and FITC-YIGSR-CMCht/PAMAM NPs array displaying the triangular micro-sized LR features. Scale bar: 100 µm.**

VIII-4.3. Cytotoxicity tests: metabolic activity and cell proliferation

The cytotoxicity of the dendrimer NPs was assessed by measuring cell metabolic activities and proliferations by means of Alamar blue and DNA quantification assays. HCT-116 cancer cells and L929 fibroblasts were exposed to CMCht/PAMAM, YIGSR-CMCht/PAMAM, and GEM-YIGSR-CMCht/PAMAM at a final concentration of 0.5 mg/mL over a period of 72 hours. This value was selected taking into consideration the maximum concentration of pure dendrimer NPs (*i.e.* non-modified) that may be employed without observing any cytotoxic effect [16]. It is important to notice that both the metabolic activity and cell viability were assessed in monoculture to discard the possibility of inherent toxicities of non-modified and modified dendrimer NPs. Both HCT-116 cancer cells and L929 fibroblasts significantly proliferated from day 1 to day 3 in the absence (control) and presence of CMCht/PAMAM and YIGSR-CMCht/PAMAM NPs **(Figure VIII-3)**. The obtained results showed no deleterious effects of the non-modified CMCht/PAMAM and the YIGSR-CMCht/PAMAM dendrimer NPs on cell viability and proliferation in both cell types. This indicates that the grafting of the YIGSR sequence did not significantly affect cellular behavior.

Conversely, GEM-loaded YIGSR-CMCht/PAMAM NPs had a clear cytotoxicity in both cell types due to the release of the drug, as demonstrated by the decrease in the metabolic activity and DNA amount **(Figure VIII-3A** and **Figure VIII-3B).** Interestingly, this effect was mostly observed at early time points in HCT-116 cancer cells in contrast to L929 fibroblasts, where the cytotoxicity was only observed at 72 hours. This suggests that the drug was internalized faster in HCT-116 cancer cells due to LR overexpression. For L929 fibroblasts, viability was most likely affected by the release of GEM from the NPs. Regarding the release of GEM from the NPs, and its potential *in vivo* side effects, it is plausible that the NPs release some amount of drug in the medium before it is internalized by the cells. However,

its effect should not be significant because the same conditions and time-points were tested in co-culture (similar to *in vivo* scenario) with an increased cell death for HCT-116 cancer cells. Overall, we do not anticipate any significant adverse effect of the released drug, within the range of the used concentrations, on non-cancerous cells when eventually used *in vivo*. Moreover, it is worth noticing that these effects were observed when HCT-116 and L929 were cultured in separate, and not in co-culture. Only after assessing the non-cytotoxic effects of the peptide modification in mono-culture, its effect in co-culture was investigated. Overall, these results indicate that GEM-loaded YIGSR-CMCht/PAMAM NPs affected the viability and proliferation of HCT-116 cancer cells and L929 fibroblasts in contrast to non-modified and peptide-grafted dendrimer NPs, but in different time scales.

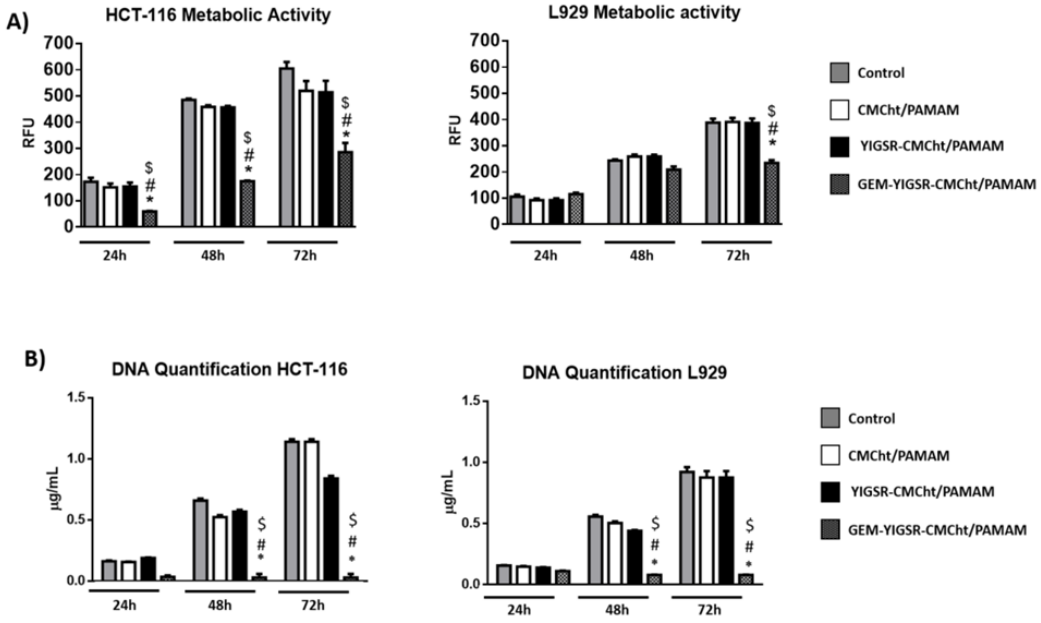

Figure VIII-3 - Cytotoxicity studies. (A) Metabolic activity determined by Alamar blue, and (B) DNA quantification results of HCT-116 and L929 cells in the presence of 0.5 mg/mL of CMCht/PAMAM, YIGSR-CMCht/PAMAM, and GEM-loaded YIGSR-CMCht/PAMAM, at 24 hours, 48 hours and 72 hours. *Significant differences when comparing the different conditions with control (0 mg/mL) at each time point. # significant differences were observed when comparing to CMCht/PAMAM at each time point. $ Significant differences were observed when comparing to YIGSR-CMCht/PAMAM at each time point. $P < 0.05$.

VIII-4.4. Targeted internalization of dendrimer nanoparticles in 2D and 3D

We next investigated whether the attachment of YIGSR on the surface of the dendrimer NPs influenced their preferential uptake by HCT-116 cancer cells, which overexpress 67 kDa LR at their surface, in a co-culture with L929 fibroblasts (see **Figure VIII-4A**). Nanoparticle internalization was first

investigated in 2D. As expected, FITC-CMCht/PAMAM NPs widely internalized in both cell types at 24 hours and 72 hours, and localized in the cytoplasm and around the nucleus **(Figure VIII-4B)** [16, 19]. In contrast, the peptide-modified YIGSR-CMCht/PAMAM dendrimer NPs internalized preferentially into HCT-116 cancer cells (red) at 24 hours when seeded in a co-culture with L929 fibroblasts (blue). Importantly, a qualitative increase in the number of internalized NPs could be observed from 24 hours to 72 hours. This suggested that peptide-grafted NPs were specifically targeted towards HCT-116 cells overexpressing 67 kDa LR.

We next used an *in vivo*-like 3D scenario to determine the efficiency of the cellular uptake mediated by the targeted interaction of the YIGSR peptide with the LR. For this, we encapsulated HCT-116 cancer cells and L929 fibroblasts into a 3D matrix of Matrigel®. **Figure VIII-4B** (bottom) shows the cells cultured in the absence (control) and presence of CMCht/PAMAM and YIGSR-CMCht/PAMAM dendrimer NPs. We first investigated whether the NPs were capable to diffuse across the meshes of the hydrogel and target the HCT-116 cells. After 24 hours no significant internalization of both CMCht/PAMAM and YIGSR-CMCht/PAMAM NPs was observed (data not shown). Instead, the NPs aggregated in the outer membrane of the cells (see **Supplementary Information VIII-S1E**). This phenomenon may be a consequence of NPs diffusing through the dense mesh of the crosslinked hydrogel, and therefore, taking longer than in 2D to interact with cells and internalize. In contrast, after 72 hours, FITC-labeled NPs spread all across the 3D hydrogel accumulating both inside and around the HCT-116 cells. Notably, it was found that YIGSR-CMCht/PAMAM NPs internalized preferentially into the HCT-116 cancer cells **(Figure VIII-4B1)**, white arrowheads). In contrast, L929 fibroblasts did not show any significant evidence of NPs internalization (see **Figure VIII-4B2)**). These results highlight the differences between 2D and 3D scenarios in drug delivery applications, even in terms of simple biological processes such as the internalization of NPs.

We next quantified the amount of NPs that were internalized in both conditions (2D vs 3D). To this end, flow cytometry analysis was performed using the same experimental conditions. HCT-116 cancer cells were stained with an anti-CD44 antibody-PE (see **Supplementary Information VIII-S1C**). In this case, only the HCT-116 cells were stained, serving as a differential marker. The obtained results were in agreement with the fluorescence microscopy results. In 2D, a maximum internalization of NPs (96.27 %) for the HCT-116 cells was observed at 24 hours, compared to the low internalization (2.97 %) in L929 fibroblasts (**Figure VIII-4C**, left). At 72 hours, the internalization of NPs increased slightly (98.45 % for HCT-116 cancer cells and 6.56 % for L929 fibroblasts). This clearly showed the lower levels of

internalization in L929 fibroblasts when compared to those of HCT-116 cancer cells. In contrast, in 3D scenario, we found that the overall levels of internalization were not as high as in 2D (**Figure VIII-4C**, right). After 24 hours, the level of internalization of targeted NPs in HCT-116 cancer cells and L929 fibroblasts was 65.52 % and 3.54 %, respectively. At 72 hours, these values increased up to 85.44 % and 9.95 %, respectively. As mentioned previously, these differences between 2D and 3D may be related to the fact that in 3D dendrimer NPs need to diffuse through the dense hydrogel mesh to target the encapsulated cells.

Together, these results indicate a targeted internalization of YIGSR-CMCht/PAMAM dendrimer NPs towards HCT-116 cells overexpressing 67 kDa LR both in 2D and 3D. However, different levels of internalization levels were obtained when comparing both conditions, reinforcing that traditional 2D models may poorly correlate with human disease states.

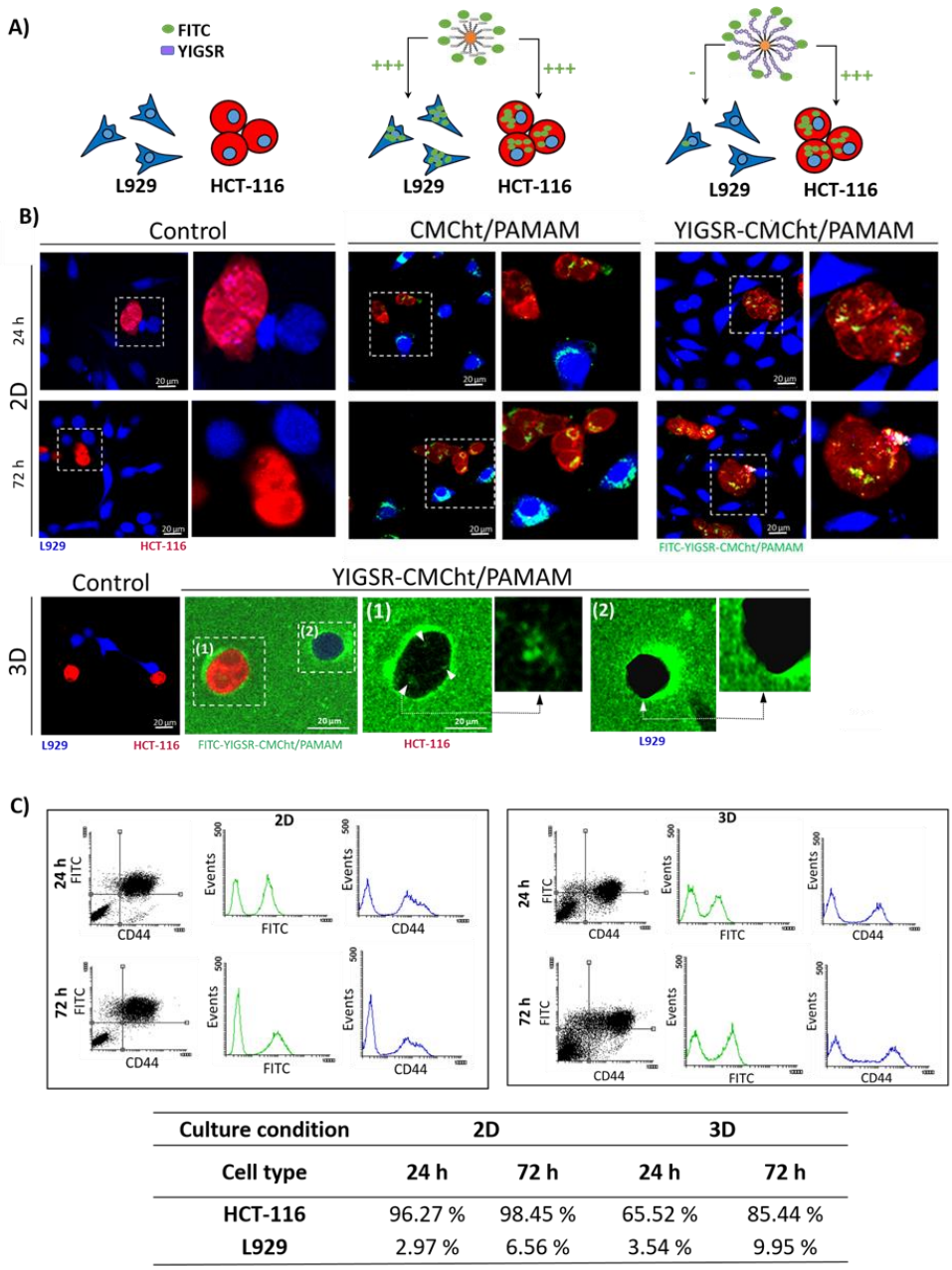

Culture condition	2D		3D	
Cell type	24 h	72 h	24 h	72 h
HCT-116	96.27 %	98.45 %	65.52 %	85.44 %
L929	2.97 %	6.56 %	3.54 %	9.95 %

Figure VIII-4 - Internalization of dendrimer nanoparticles. A) Schematics of the different conditions studied. B) Confocal microscopy images of HCT-116 cancer cells (red) and L929 fibroblasts (blue) co-culture in the presence of YIGSR-CMCht/PAMAM and CMCht/PAMAM dendrimer NPs in (top) 2D for 24 hours and 72 hours, and (bottom) in 3D for 72 hours. In the latter, (1) and (2) show a higher magnification of HCT-116 and L929 cells, respectively, showing the internalization of YIGSR-CMCht/PAMAM dendrimer NPs exclusively for HCT-116 (observed only with the 488 nm filter). Inset images show a more detailed view of the NPs (indicated by white arrowheads). (C) Flow cytometry results of NPs internalization in co-culture in both 2D and 3D for 24 hours and 72 hours. Scale bars: 20 µm.

VIII-4.5. Targeted gemcitabine delivery using dendrimer nanoparticles in 2D and 3D

After verifying the targeted and preferential internalization of YIGSR-CMCht/PAMAM NPs towards HCT-116 cancer cells, we next investigated the gemcitabine (GEM) release from YIGSR-CMCht/PAMAM in a co-culture of HCT-116 cancer cells and L929 fibroblasts in 2D and 3D [22]. In a previous work, we demonstrated an encapsulation efficiency of GEM into CMCht/PAMAM NPs of 52.99 % ± 3.50 %, with a drug-loading efficiency of 9.42 % ± 3.50 % [23]. First, the viability of cells was analyzed by Live/Dead assay in a 2D co-culture at 24 hours and 72 hours in the presence of GEM-YIGSR-CMCht/PAMAM (**Figure VIII-5A).** The results show that L929 fibroblasts (in blue) were not substantially affected by the GEM-YIGSR-CMCht/PAMAM NPs; they were co-stained in blue and in green (live cells). In contrast, HCT-116 cancer cells (unstained) displayed a larger mortality at 24 hours (red - dead cells) (**Figure VIII-5A**) indicating a specific GEM release inside these cells. It is worth noticing that most of the cancer cells were alive at 24 hours. However, they displayed an elongated – perturbed – phenotype with the appearance of blebs, which suggested the beginning of the apoptotic process [24]. In contrast, this was not observed in L929 cells. This was more stringent at 72 hours, where mainly HCT-116 cancer cells were dead. In contrast, L929 were mostly alive, displaying a morphology consistent with its normal phenotype and not significantly perturbed. We confirmed these qualitative observations by quantifying the amount of live/dead cells by flow cytometry. For this, CD44-FITC was used to label HCT-116 cancer cells, while L929 fibroblasts were CD44 negative and PI labelled the dead cells. Figure 5 B shows a 4.70 % of cell death (PI staining) in the CD44 positive population (HCT-116) in 2D at 24 hours, and 3.44 % for the CD44 negative population (L929). Although not very substantial at such early time point, there is a difference between both cell death values, being higher for cancer HCT-116 cells. The same trend was observed in 3D, where cell death for the CD44 positive (HCT-116) and negative (L929) populations was 30.16 % and 26.07 %, respectively. Note that the percentage of overall cell death is higher in 3D than in 2D. This phenomenon could be related to the process of retrieving cells from the hydrogel. This process consists of leaving the hydrogels in the recovery solution at 4 °C for at least 30 minutes. This may damage the cells, and therefore, may explain the increase in percentage of cell death.

At 72 hours, we observed a high level of internalization in HCT-116 cancer cells in 2D compared to L929 fibroblasts. This resulted in a significantly higher level of cell death (68.72 %) observed in the CD44 positive population (HCT-116) compared to L929 fibroblasts (3.20 %); this was in agreement with the previously studied internalization phenomena. In 3D, after exposing the co-culture to GEM-YIGSR-CMCht/PAMAM for 72 hours, cell death percentage of the CD44 positive population (HCT-116) was

31.15 %, while for the CD44 negative population (L929) was 19.52 %. These results show that the intracellular release of GEM was successfully achieved mainly toward cancer cells. However, when comparing the same condition at 24 hours, we observed that the level of cell death did not increase significantly. This could be explained by several possible factors: (i) the GEM is released within the first 24 hours, being almost 40 % released in the first 6 hours of culture [23]. Since a static culture is employed and fresh medium is not added, the drug levels are stable, therefore, cell death is also stable both at 24 hours and 72 hours; (ii) internalization rates do not drastically increase from 24 hours to 72 hours in 3D. This also corroborates the fact that there is no significant difference in the amount of drug available inside the cells to induce apoptosis from 24 hours to 72 hours; and (iii). At 72 hours cells seem to be in the beginning of the process of apoptosis (**Figure VIII-5A**), as suggested by the presence of both green and red signals. This also suggests that HCT-116 cancer cells may take longer time to complete the cell death process and to be detected by flow cytometry.

Taken together, these results suggest the successful targeting and release of the GEM-YIGSR-CMCht/PAMAM dendrimers NPs into the HCT-116 cells taking advantage of the 67 kDa LR overexpression on the cell surface.

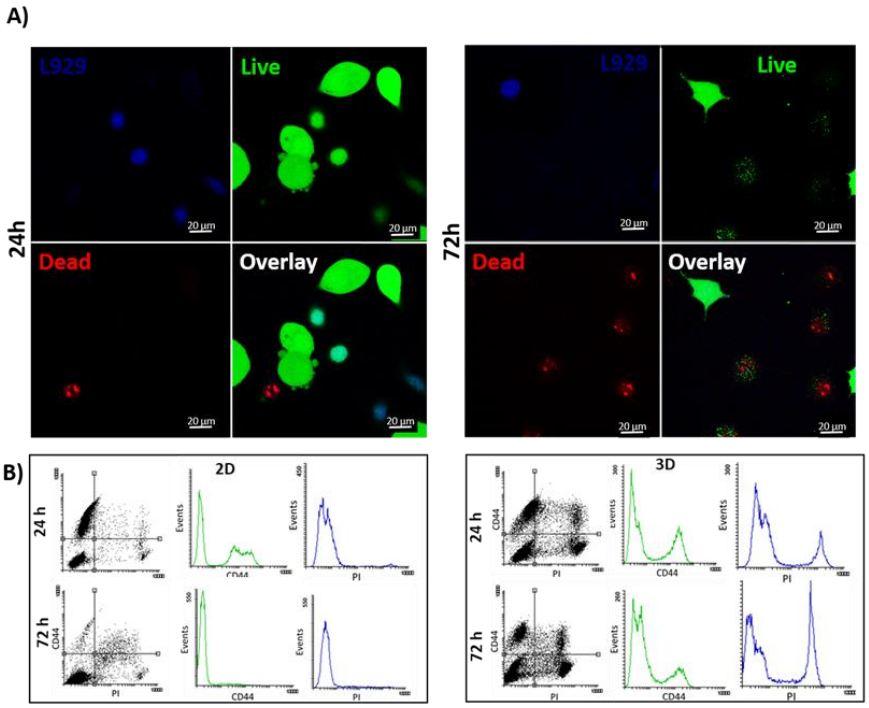

Culture condition	2D		3D	
Cell type	24 h	72 h	24 h	72 h
HCT-116	4.70 %	68.72%	30.16 %	31.15 %
L929	3.44 %	3.20%	26.07 %	19.52 %

Figure VIII-5 - The cell viabilities of HCT-116 and L929 cells in the presence of GEM-YIGSR-CMCht/PAMAM dendrimers. (A) Live/Dead assay performed on a co-culture of HCT-116 (unstained) and L929 (in blue) cells at 24 hours and 72 hours in 2D. (B) Flow cytometry analysis of cell viabilities in the presence of GEM-YIGSR-CMCht/PAMAM in a co-culture of HCT-116 (CD44 positive) and L929 cells (CD44 negative cells).

Finally, the rationale of using YIGSR (a peptide derived from laminin) as a tumor targeting is based on the solid evidences that the levels of expression of the 67 kDa LR directly correlate with the invasiveness and metastatic potential in numerous tumors.[14, 15, 25]. It is our goal to further test these newly developed NPs using primary colorectal cancer cells and non-cancerous colorectal cells in a dynamic microfluidic system, in order to better mimic the native scenario.

Overall, the future perspective of targeted NPs for cancer research is promising. Several formulations currently under pre-clinical and clinical studies for CRC may soon reach the market. A future challenge common to recent technologies, with no exception for targeted NPs, is the need for implementation of systems or protocols to determine the molecular expression profile of tumors from patients with CRC. Its classification according to the genetic profile, stage of tumor development, and putative targeting molecules are imperative [26]. By achieving this, the rational administration of

precise-targeted nanomedicines containing the most effective drug combination may revolutionize the way cancer is treated.

VIII-5. Conclusions

The conjugation of ligands as peptides, aptamers and other small molecules, such as antibodies, on the surface of nanoparticles with the purpose of cell targeting has resulted in a new generation of nanoparticles for cancer therapy with enhanced *in vitro* and *in vivo* specificity. The present work first demonstrates by a simple micro-pattern assay that YIGSR laminin peptide on the surface of CMCht/PAMAM NPs links selectively to 67 kDa receptor protein. It is also demonstrated in this work that the attachment of YIGSR peptide on the surface of CMCht/PAMAM dendrimer NPs leads to their targeting and preferential uptake by HCT-116 cells, and consequently, releasing of the anti-cancer drug intracellularly, when in co-culture with fibroblasts. The novel nanoparticles demonstrate that they may be considered as a promising tool for targeted drug delivery in colorectal cancer cells and other types of cancer, whose cells expresses high levels of the 67LR. In the future, such technology will need to be evaluated in other CRC cell lines and primary cells to fully disclose the potential of YIGSR-targeted NPs in cancer therapeutics. Finally, the potential of YIGSR-CMCht/PAMAM NPs for further applications is immense. This tool may bring closer to a clinical and pharmaceutical translatable setting for continuing research.

VIII-6. Acknowledgments

This work was financially supported through the project FROnTHERA (NORTE-01-0145-FEDER-000023), Norte Portugal Regional Operational Programme (NORTE 2020), under the Portugal 2020 Partnership Agreement, through the European Regional Development Fund (ERDF); M. C. for her PhD scholarship NORTE-08-5369-FSE- 000044, funded by Programa Operacional Regional do Norte, Fundo Social Europeu, Norte 2020 TERM&SC and EMBO Short-Term Fellowship 7232. .R. M. acknowledges FCT for her work contract under the Transitional Rule DL 57/2016 (CTTI-57/18-I3BS(5)). J. M. O. for his distinction attributed under the FCT Investigator program (IF/00423/2012 and IF/01285/2015); D.C. and S.C.K. for the Portuguese Foundation for Science and Technology (FCT) under the scope of the project 2MATCH (PTDC/BTMORG/28070/2017) funded by the Programa Operacional Regional do

Norte supported by European Regional Development Funds (ERDF); partially supported by the IET Harvey Engineering Research Award 2018 (ENG ThE CANCER) and the European Union Framework Program for Research and Innovation Horizon 2020 on FoReCaST project under grant agreement no. 668983.

VIII-7. REFERENCES

1. Siegel, R.L., K.D. Miller, and A. Jemal, *Cancer statistics, 2018.* 2018. **68**(1): p. 7-30.
2. Wu, H., et al., *Hydroxyethyl starch stabilized polydopamine nanoparticles for cancer chemotherapy.* Chemical Engineering Journal, 2018. **349**: p. 129-145.
3. Senapati, S., et al., *Controlled drug delivery vehicles for cancer treatment and their performance.* Signal Transduction and Targeted Therapy, 2018. **3**(1): p. 7.
4. Sztandera, K., M. Gorzkiewicz, and B. Klajnert-Maculewicz, *Gold Nanoparticles in Cancer Treatment.* Mol Pharm, 2018.
5. Alexis, F., et al., *Factors affecting the clearance and biodistribution of polymeric nanoparticles.* Mol Pharm, 2008. **5**(4): p. 505-15.
6. Bae, K.H., H.J. Chung, and T.G. Park, *Nanomaterials for cancer therapy and imaging.* Molecules and cells, 2011. **31**(4): p. 295-302.
7. Kedar, U., et al., *Advances in polymeric micelles for drug delivery and tumor targeting.* Nanomedicine, 2010. **6**(6): p. 714-29.
8. Palmerston Mendes, L., J. Pan, and V.P. Torchilin, *Dendrimers as Nanocarriers for Nucleic Acid and Drug Delivery in Cancer Therapy.* Molecules (Basel, Switzerland), 2017. **22**(9): p. 1401.
9. Yu, B., et al., *Receptor-targeted nanocarriers for therapeutic delivery to cancer.* Molecular membrane biology, 2010. **27**(7): p. 286-298.
10. Kopansky, E., Y. Shamay, and A. David, *Peptide-directed HPMA copolymer-doxorubicin conjugates as targeted therapeutics for colorectal cancer.* J Drug Target, 2011. **19**(10): p. 933-43.
11. Sharma, M., et al., *Folic acid conjugated guar gum nanoparticles for targeting methotrexate to colon cancer.* J Biomed Nanotechnol, 2013. **9**(1): p. 96-106.
12. Sarfati, G., et al., *Targeting of polymeric nanoparticles to lung metastases by surface-attachment of YIGSR peptide from laminin.* Biomaterials, 2011. **32**(1): p. 152-161.
13. Kumazoe, M., et al., *67-kDa laminin receptor increases cGMP to induce cancer-selective apoptosis.* J Clin Invest, 2013. **123**(2): p. 787-99.
14. Vacca, A., et al., *Melanocyte tumor progression is associated with changes in angiogenesis and expression of the 67-kilodalton laminin receptor.* Cancer, 1993. **72**(2): p. 455-61.
15. Shi, Y.E., et al., *Expression of 67 kDa laminin receptor in human breast cancer cells: regulation by progestins.* Clin Exp Metastasis, 1993. **11**(3): p. 251-61.
16. Carvalho, M.R., et al., *A semiautomated microfluidic platform for real-time investigation of nanoparticles' cellular uptake and cancer cells' tracking.* Nanomedicine (Lond), 2017. **12**(6): p. 581-596.
17. Cerqueira, S.R., et al., *Multifunctionalized CMCht/PAMAM dendrimer nanoparticles modulate the cellular uptake by astrocytes and oligodendrocytes in primary cultures of glial cells.* Macromol Biosci, 2012. **12**(5): p. 591-7.

18. Valodkar, M., et al., *Biocompatible synthesis of peptide capped copper nanoparticles and their biological effect on tumor cells.* Materials Chemistry and Physics, 2011. **128**(1): p. 83-89.
19. Oliveira, J.M., et al., *Surface Engineered Carboxymethylchitosan/Poly(amidoamine) Dendrimer Nanoparticles for Intracellular Targeting.* Advanced Functional Materials, 2008. **18**(12): p. 1840-1853.
20. Maia, F.R., et al., *Effect of Cell Density on Mesenchymal Stem Cells Aggregation in RGD-Alginate 3D Matrices under Osteoinductive Conditions.* Macromolecular Bioscience, 2014. **14**(6): p. 759-771.
21. Rea, V.E., et al., *67 kDa laminin receptor: structure, function and role in cancer and infection.* Infez Med, 2012. **20 Suppl 2**: p. 8-12.
22. Jiménez-Fonseca, P., et al., *Gemcitabine plus capecitabine (Gem–Cape) biweekly in chemorefractory metastatic colorectal cancer.* Clinical & Translational Oncology, 2015. **17**(5): p. 384-392.
23. Carvalho, M.R., et al., *Colorectal tumor-on-a-chip system: A 3D tool for precision onco-nanomedicine.* Sci Adv, 2019. **5**(5): p. eaaw1317.
24. Rudolf, E. and M. Cervinka, *Membrane blebbing in cancer cells treated with various apoptotic inducers.* Acta Medica (Hradec Kralove), 2005. **48**(1): p. 29-34.
25. Ardini, E., et al., *Identification of a novel function for 67-kDa laminin receptor: increase in laminin degradation rate and release of motility fragments.* Cancer Res, 2002. **62**(5): p. 1321-5.
26. Cisterna, B.A., et al., *Targeted nanoparticles for colorectal cancer.* Nanomedicine (Lond), 2016. **11**(18): p. 2443-56.

VIII-8. SUPPLEMENTARY FIGURE

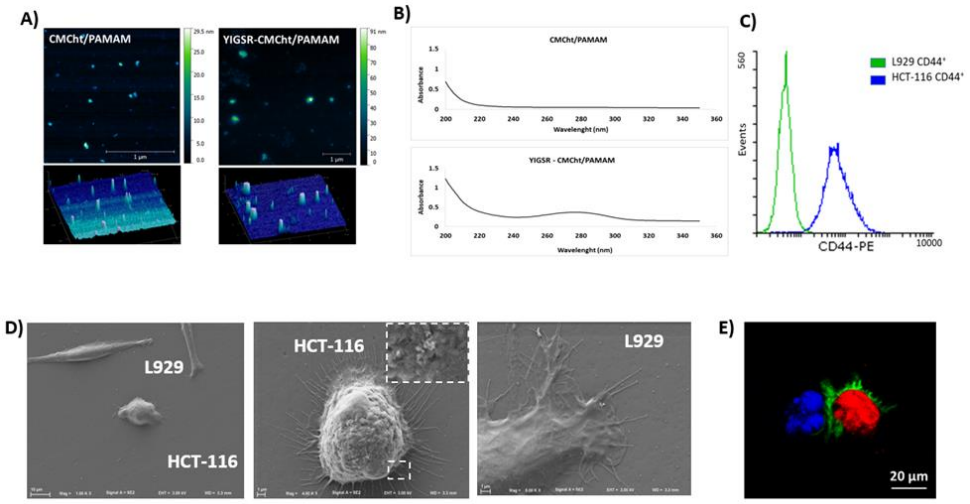

Supplementary Figure VIII-1 - Nanoparticles characterization. (A) AFM images of the CMCht/PAMAM and YIGSR-CMCht/PAMAM NPs with respective 3D projection; (B) Peptide determination by UV spectroscopy; (C) Flow Cytometry graphic showing selective binding of CD44 antibody to HCT-116 in a co-culture suspension with L929 cells; (D) SEM images of a co-culture of HCT-116 cells and L929 cells: close ups showing the nanoparticles do not agglomerate on the cell's surface, but are widely internalized instead; and (E) Confocal

image of HCT-116 (red) and L929 cells (blue) in 3D, in the presence of FITC-YIGSR-CMCht/PAMAM NPs at 24 hours.

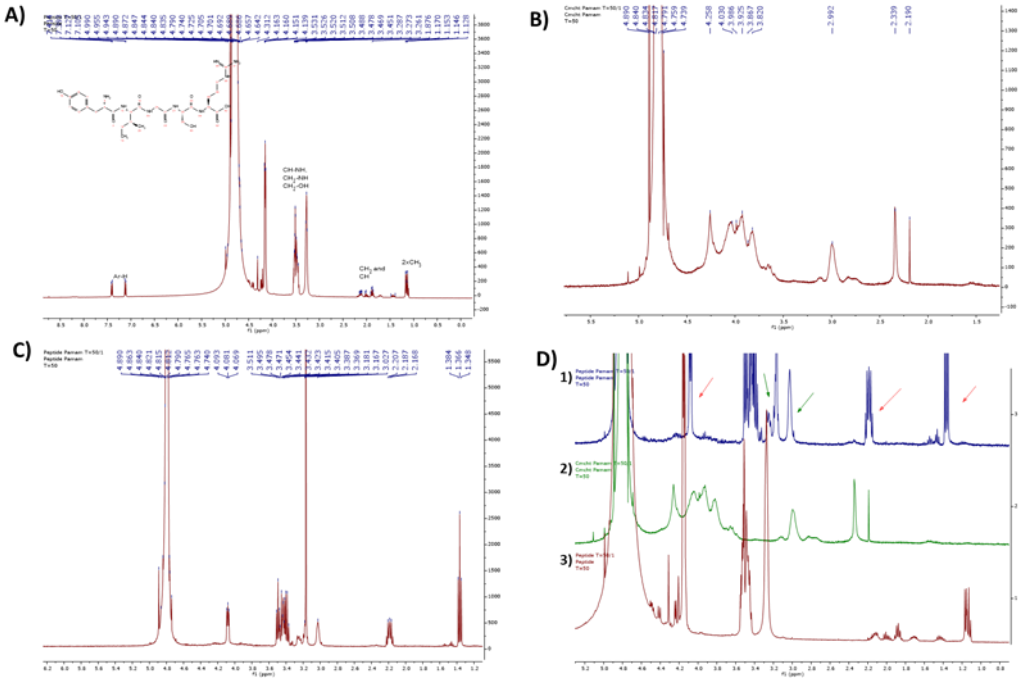

Supplementary Figure VIII-2 - H¹NMR analysis of YIGSR peptide, CMCht/PAMAM, and YIGSR-CMCht/PAMAM. A) H¹NMR (D_2O, 400 MHz) spectra of the peptide YIGSR with its chemical structure and main peaks. B) H¹NMR (D_2O, 400 MHz) spectra of CMCht/PAMAM with peak assignments. C) H¹NMR (D_2O, 400 MHz) spectra of the modified YIGSR-CMCht/PAMAM and respective peak assignment. D) H¹NMR (D_2O, 400 MHz) spectra of: the modified YIGSR-CMCht/PAMAM (D1); CMCht/PAMAM dendrimer (D2), and theYIGSR (D3), with arrows indicating the main peaks with the peaks marked the color according to the respective provenance.

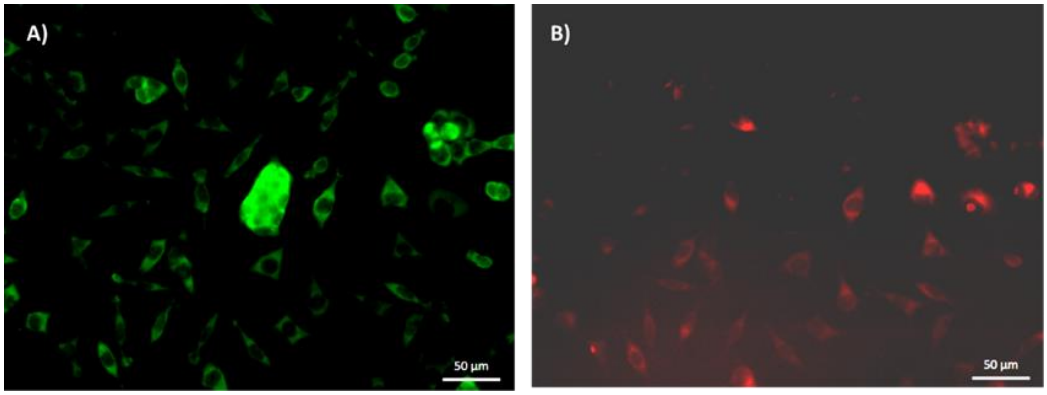

Supplementary Figure VIII-3 - Immunocytochemistry of anti-67kDa LR (green). Pannel A shows 488 filter (green) for the 67 kDa receptor, and panel B shows 594 filter (red) performed on a co-culture of HCT-116 CRC cells and L929

fibroblasts (previsouly stained in red) cells at 72 hours, proving that the cluster of HCT-116 overexpressing 67 kDa receptor consists in fact of cancer cells, and not L929.

Chapter IX

Patent – Enzymatically Crosslinked Silk Fibroin hydrogel microfluidic platform, methods of production and uses thereof

Chapter IX

Patent - Enzymatically Crosslinked Silk Fibroin Hydrogel Microfluidic platform, Methods of Production and Uses Thereof

ABSTRACT

The present disclosure relates to a transparent enzymatically crosslinked silk fibroin hydrogel-based microfluidic device that may be used *ex vivo* and *in vivo*, in tissue engineering applications, organ or tissue disease models, tissue-, organ- and body-on-a-chip, drug discovery, drug screening, tissue implant, tissue regeneration, and implantable microdevices.

[1]This chapter is based on the following publication:

M. R. Carvalho. D. Caballero, C. R. Carvalho, J. B. Costa, V. Ribeiro, Oliveira J. M., Kundu S. C., Reis R. L. Enzymatically Crosslinked Silk Fibroin hydrogel microfluidic platform, methods of production and uses thereof. (Filed, 2019).

IX-1. TECHNICAL FIELD

The present disclosure relates to an implantable enzymatically crosslinked silk fibroin amorphous hydrogel-based microfluidic device and methods of producing said device.

The disclosed transparent enzymatically crosslinked silk fibroin hydrogel-based microfluidic device may be used, *ex vivo* and *in vivo*, in tissue engineering applications, organ or tissue disease models, tissue-, organ- and body-on-a-chip, drug discovery, drug screening, tissue implant, tissue regeneration, and implantable microdevices.

IX-2. BACKGROUND

Biomedical research has increasingly moved towards the design, fabrication and implementation of microfluidic-based systems to efficiently improve point-of-care technologies such as drug discovery or drug screening, diagnostics, tissue engineering and regenerative medicine. The advent of microfluidic field has enabled precise fluidic manipulation and control of extremely small volumes. Due to its unique properties, poly(dimethylsiloxane) (PDMS) have typically been employed in the development of microfluidic systems. PDMS revolutionized traditional microfluidics which was previously based on silicon and glass. However, more biologically relevant, synthetic and natural hydrogel materials have recently been utilized in microfluidics fabrication to address the limitations of PDMS. PDMS has limited mechanical and biochemical properties. Typical hydrogels include collagen, gelatin, gelatin methacrylate (GelMA), agarose, alginate and other extracellular matrix proteins [1-4]. These hydrogel materials are cell-compatible, enabling better interfaces, namely with three-dimensional cell cultures.

Nevertheless, the mechanical properties of the existing hydrogel-based microfluidic materials such as their stiffness, only covers a limited range of native tissues, which limits their utility in mimicking the physiological conditions of the native tissue. Additionally, the degradability of the reported microfluidic hydrogel materials is far from desired. This is mainly because they are either not degradable or are only stable over a limited range of time frames thus challenging their use in tissue regeneration.

Microfluidic fabrication typically involves non-degradable materials including silicon and polydimethylsiloxane (PDMS) [5]. However, these devices are generally not implantable mainly because they are non-degradable, and can induce inflammation and trigger foreign body reaction. Strategies for

developing more natural implantable systems comprise the use of agarose, gelatin, collagen and alginate [6-10]. However, they do not present the best tunable stiffness properties. They are not flexible enough to mimic the desired tissue. More recently, new biomaterials such as silk fibroin have been employed for tissue engineering applications. Recently, silk fibroin has been used for the development of primitive microfluidic systems. The combination of microfluidics and silk fibroin hydrogel offers a lot of advantages. Silk fibroin is FDA approved and has gained a lot of attention in the tissue engineering and regenerative medicine due to its excellent mechanical, biochemical, and cellular properties coupled with its biocompatibility, flexibility, degradation properties, water-based processing, and the presence of easily accessible chemical groups for functional modifications. This makes silk fibroin an ideal biomaterial for the development of implantable microfluidic systems [11, 12].

A novel class of enzymatically crosslinked silk fibroin hydrogels have recently been reported but their exploitation has mostly been limited to engineering *in vitro* 3D extracellular matrix (ECM) mimics for cancer research studies (*e.g.* cancer invasion, migration, proliferation, and others), bioinks, and as conduits for peripheral nerve regeneration applications [12, 13]. The horseradish peroxidase (HRP)/hydrogen peroxide (H_2O_2) cross-linking approach is used in polymers containing, or functionalized, with phenol group-containing molecules, including tyrosine, tyramine or aminophenol [14].

Very few works describing the use of silk fibroin as an implantable material have been reported in literature. Bettinger *et al.* [14] reported the fabrication of primitive microfluidic devices made by laminating water-stable micro-moulded silk fibroin membranes in β-sheet which were modified with macroscopic fluidic connections [15].

Document WO 2008/108838 A3 describes silk-based systems and devices such as microfluidic devices and methods for fabricating the same. However, in this document, silk solution is simply allowed to solidify on the molds. No enzymatic crosslinking is employed to form a hydrogel. The resulting device is therefore in a film or layer of silk, resulting in β-Sheet conformation after initial processing.

Document US008975073B2 describes a microfluidic device comprising silk films coupled together to form a microchannel. However, it is described that the devices are fabricated by laminating micro-molded and flat silk fibroin layers. Microfluidic layers are stacked, aligned, and bonded together at 70

°C, for 18 hours, under mechanical pressure, Additional 8 % aqueous silk fibroin solution is used at the interface of the microfluidic layers. After the assembly was completed, the device was incubated in a 37 °C oven for 5 to 10 minutes to completely melt the gelatin, which was subsequently removed by flushing the channel with deionized water. The method described in this document is substantially different from the method disclosed in the present disclosure as the method disclosed in this document does not involve the use of silk fibroin solution at different concentrations and different ratios.

Document WO 2010/123945 A2 document describes silk fibroin hydrogels and uses thereof. This document discloses purified silk fibroin and method of purifying silk fibroins. This document also discloses hydrogels comprising silk fibroin with or without an amphiphilic peptide and methods for making hydrogels comprising silk fibroin.

Document WO18025186 describes enzymatic cross-linking of silk fibroin using horse radish and hydroxide peroxidase to obtain a hydrogel. However, the hydrogel obtained is only an intermediate step in the process of fabricating the final crystalline and tubular silk conduits disclosed. The silk fibroin hydrogel described in this document is therefore an intermediate product of nerve guidance conduits.

These facts are disclosed in order to illustrate the technical problem addressed by the present disclosure.

IX-3. GENERAL DESCRIPTION

The present disclosure relates to an implantable enzymatically crosslinked silk fibroin hydrogel-based microfluidic device and methods of producing said device.

The disclosed enzymatically crosslinked silk fibroin hydrogel-based microfluidic device may be used in tissue engineering applications, organ or tissue disease models, drug discovery, drug screening, tissue implant, tissue regeneration or as implantable microdevices.

The present disclosure relates to a new methodology that comprises the use of an enzymatically cross-linked silk fibroin hydrogel for the microfabrication of a flexible, elastic and biodegradable 3D microfluidic chip with implantable characteristics. This methodology overcomes the problems of previously developed PDMS microfluidic platforms.

Specifically, this methodology overcomes the issues previously described by enzymatically cross-linking silk fibroin hydrogel, using horseradish peroxidase as enzyme and H_2O_2 as enzyme substrate to modify the silk fibroin solution into a hydrogel.

Silk is a naturally derived protein biomaterial with excellent biocompatibility and controllable degradation rates, thus suitable for tissue engineering and regenerative medicine applications. The new formulation is based on rapidly responsive silk fibroin hydrogels formed by a horseradish peroxidase (HRP) crosslinking reaction at physiological conditions, with potential use as an artificial biomimetic three-dimensional (3D) matrix. An advantage of using the method disclosed in the present disclosure is the ability to directly produce silk fibroin hydrogel microfluidic device in an amorphous state this presents an opportunity to induce β-sheet conformation later, in many different ways, if necessary.

This is the first time that silk fibroin hydrogel is employed in microfluidic technology for the production of enzymatically cross-linked silk fibroin hydrogel-based microfluidic device.

This horseradish peroxidase – H_2O_2 cross-linking approach allows the development of a substantially silk fibroin-based microfluidic device made of a flexible, implantable, biocompatible and biodegradable biomaterial. This hydrogel retains the amorphous protein structure for at least 7 days, allowing for cell encapsulation. Silk fibroin hydrogel resolution allows for the fabrication of micro-and nano-sized features, such as microchannels.

In an embodiment, the method of producing silk fibroin hydrogel-based microfluidic device comprises:

(i) the use of UV-photolithography for the fabrication of microfluidic channels;

(ii) replica molding of the fabricated structures using a polymeric material (PDMS, and others such as polycarbonate (PC), polystyrene (PS), polyvinyl chloride (PVC), polyimide (PI);

(iii) TCS-silanization and second replica molding of the microfluidic structures using a polymeric material (PDMS, and others);

(iv) replication of the microfluidic structures using silk fibroin hydrogel;

(v) characterization of this process with respect to microstructural fidelity and cell viability.

In an embodiment, an initially produced aqueous silk solution is transformed into an amorphous and transparent hydrogel through a peroxidase-mediated cross-link reaction.

In an embodiment, silk fibroin was combined with horseradish peroxidase solution (HRP type VI, 0.84 mg/mL) and hydrogen peroxide solution (H_2O_2, 0.36 wt.%).

IX-4. BRIEF DESCRIPTION OF THE DRAWINGS

The following figures provide preferred embodiments for illustrating the disclosure and should not be seen as limiting the scope of invention.

Figure IX-1 illustrates the process of producing the PDMS mold used to produce the enzymatically crosslinked silk fibroin hydrogel-based microfluidic device.

Figure IX-2 shows ATR-FTIR spectra for the enzymatically crosslinked silk fibroin hydrogel (with 12 % concentration of silk fibroin) retaining the amorphous protein structure for at least 7 days.

Figure IX-3 demonstrates the flexibility and elasticity of the transparent enzymatically crosslinked silk fibroin hydrogel at day 1 and at day 3.

Figure IX-4 schematically illustrates an exemplification of the structure of the enzymatically crosslinked silk fibroin microfluidic device. In this case, including a meandering serpentine channel, inlets and outlets. **Figure IX-4A** is without dimensions while **Figure IX-4B** is dimensions in μm.

Figure IX-5 shows SEM images of the 3D enzymatically crosslinked silk fibroin hydrogel structures after drying using point drying. Scale bars: 500 μm (a and b), and 100 μm (c).

Figure IX-6 schematically illustrates an example of what the enzymatically crosslinked silk fibroin hydrogel can be used for.

Figure IX-7 shows confocal microscopy images as described in the schematics of **Figure IX-6**: endothelial cells seeded on the microchannel while colorectal cells are encapsulated throughout the enzymatically crosslinked silk fibroin microfluidic device.

Figure IX-8 shows the viability of cells encapsulated in the enzymatically crosslinked silk fibroin hydrogel-based microfluidic device. Live/dead assay was performed and observed under confocal microscope.

Figure IX-9 shows the perfusion of blue ink through the inlet (A); formation of soluble food colouring ink gradient (B); and diffusion of ink visible in the microchannels, allowing for the formation of diffusion gradients of drugs/nanoparticles (C).

Figure IX-10 shows liquid perfusion thought the enzymatically crosslinked silk fibroin hydrogel-based microfluidic device's microchannel. A) Shows perfusion of blue ink through the inlet. B1) and B2) show magnified images of liquid perfusion inside the serpentine microchannel

IX-5. DETAILED DESCRIPTION

The present disclosure relates to an implantable enzymatically crosslinked silk fibroin microfluidic device and methods of producing said device.

The disclosed enzymatically crosslinked silk fibroin microfluidic device may be used in tissue engineering applications, organ or tissue disease models, drug discovery, drug screening, tissue implant, tissue regeneration or as implantable microdevices.

In an embodiment, the method for producing a flexible, elastic, biodegradable and implantable microfluidic device made substantially of enzymatically crosslinked silk fibroin hydrogel comprises the following:

Produce a SU-8 master mold with desired microchannels.

Add polymethylsiloxane (PDMS) solution at a ratio of 10:1 pre-polymer:crosslinker ($v_{pre\text{-}polymer}/v_{crosslinker}$, and/or $w_{pre\text{-}polymer}/w_{crosslinker}$) to the SU-8 master mold and allow the PDMS to cure in order to obtain a PDMS mold which is a negative master replica of the SU-8 master mold.

Silanization of the PDMS negative master mold. This process is intended to passivate the PDMS surface to allow the fabrication of a second (positive) PDMS replica.

Pour PDMS solution at a ratio of 10:1 pre-polymer:crosslinker ($v_{pre\text{-}polymer}/v_{crosslinker}$, and/or $w_{pre\text{-}polymer}/w_{crosslinker}$) on top of the TCS-silanized negative PDMS master, degas, and cure until it is completely cured.

Peel off the negative PDMS mold to obtain a positive PDMS master mold.

Prepare an aqueous silk fibroin solution with a concentration of at least 3 % (wt%), preferably from 5-25 % (wt%), more preferably 15-16 %.

Add horseradish peroxidase and hydrogen peroxide to the aqueous silk fibroin solution to form an enzymatically cross-linked silk fibroin hydrogel;

Add silk fibroin solution at the desired concentration into the positive PDMS mold and incubate to form a hydrogel membrane.

In an embodiment, the SU-8 master mold is produced using UV-photolithography.

In an embodiment, the SU-8 master mold is preferably produced on a silicon wafer.

In an embodiment, the PDMS is added to the SU-8 master mold and cured for at least 3 hours, preferably for a duration from 3 hours to 12 hours, at about 37 °C.

In an embodiment, the salinization of the PDMS mold is by vapour phase method or aqueous method, preferably by trichloro(1H,1H,2H,2H-perfluorooctyl)silane (TCS) method. The purpose of the TCS layer is to aid the subsequent removal of the negative PDMS mold by preventing it from adhering to the first SU-8 master mold. In particular: place the PDMS mold in vacuum (*e.g.*, desiccator) in the presence of a drop (drop volume from 5 µL to 100 µL) of pure TCS silanizing agent at room temperature. Afterwards, release from vacuum and store at about 70 °C for at least 1 hour.

In an embodiment, the PDMS solution is allowed to cure on the TCS-silanized negative PDMS master for at least 3 hours, preferably for a duration from 3 hours to 12 hours, at about 37 °C, until the solution is completely cured.

In an embodiment, the silk fibroin solution is added to the positive PDMS mold and incubated for at least 1 hour, preferably for a duration from 1 hour to 5 hours, at about 37 °C.

Figure IX-1 illustrates the process of producing the PDMS mold used to produce the silk fibroin hydrogel-based microfluidic device.

In an embodiment for better results, the thickness of the enzymatically crosslinked silk fibroin hydrogel layer can be controlled by controlling the volume of silk solution poured into the PDMS molds.

In an embodiment, for better results, the mechanical properties of the silk fibroin hydrogel can be tuned by changing the concentration of silk fibroin proteins. In an embodiment, for better results, the silk fibroin hydrogel is enzymatically cross-linked with horseradish peroxidase and hydrogen peroxide,

but other peroxidases and oxidizers may be used. In an embodiment, for better results, the silk hydrogel is functionalized with drugs or chemo-attractants.

In an embodiment, for better results, the hydrogel comprises from 3 % up to 25 % (wt %) of silk fibroin, preferably from 8% to 20 % (wt %) of silk fibroin, more preferably from 10% to 12 % (wt %) of silk fibroin.

In an embodiment, an initially produced aqueous silk solution is transformed into an amorphous and transparent hydrogel, through a peroxidase-mediated cross-linking reaction.

In an embodiment, the enzymatically crosslinked silk fibroin hydrogel retains the amorphous protein structure for at least 7 days, allowing for cell encapsulation.

Figure IX-2 shows ATR-FTIR spectra for the 3D enzymatically crosslinked silk fibroin hydrogel (with 12 % concentration of silk fibroin) retaining the amorphous protein structure for at least 7 days.

In an embodiment, for better results, the enzymatically crosslinked silk fibroin microfluidic device further comprises a biological active agent, a therapeutic agent, an additive, a pharmaceutically acceptable excipient, a pharmaceutically acceptable carrier, and mixtures thereof.

In an embodiment, the enzymatically crosslinked silk fibroin hydrogel-based microfluidic device functions to mimic the extracellular matrices (ECM) of the body. For example, the silk fibroin hydrogel-based microfluidic device may serve as a physical support and/or an adhesive substrate for isolated cells during *in vitro* culture and subsequent implantation. As the transplanted cell populations grow and the cells function normally, the cells will begin to secrete their own ECM support and the silk-based microdevice may then biodegrade. The biodegradation of the silk fibroin hydrogel-based microfluidic device may be controlled by various manufacturing techniques known in the art.

In an embodiment, the enzymatically crosslinked silk fibroin hydrogel-based microfluidic devices are mechanically robust, transparent, flexible, elastic and possess microchannels with different geometries and sizes for seeding cells and flowing fluids (including body fluids) through the device.

Figure IX-3 demonstrates the flexibility and elasticity of the transparent silk fibroin hydrogel at day 1 and at day 3.

Figure IX-4 schematically illustrates an exemplification of the structure of the enzymatically crosslinked silk fibroin microfluidic device. In this case, including a serpentine channel, inlets and outlets, without (A) and with (B) dimensions in μm.

Figure IX-5 Scanning Electron Microscope (SEM) images of the 3D silk hydrogel structures after drying using critical point drying. Scale bars: 500 μm (a and b), and 100 μm (c).

In an embodiment, the enzymatically crosslinked silk fibroin hydrogel-based microfluidic devices are fabricated to support the growth of cells, including but not limited to eukaryotic cells (cancer cells, stromal cells, immune system, or endothelial cells). Other cell types could also be added as required.

In an embodiment, a portion of a surface of the microchannels in the silk fibroin hydrogel-based microfluidic device supports cell growth, in their native morphology.

In an embodiment, a portion of the enzymatically crosslinked silk fibroin hydrogel-based microfluidic device supports cell growth by encapsulating cells.

Figure IX-6 schematically illustrates an example of what can be done using the hydrogel. For example, colorectal cancer microenvironment can be mimicked by seeding human colonic microvascular endothelial cells inside the microchannels, invading the matrix in response to VEGF gradients, while HCT-116 colorectal cells are encapsulated in the silk.

In an embodiment, the enzymatically crosslinked silk fibroin hydrogel-based microfluidic devices are fabricated to support the growth of cells, including but not limited to eukaryotic cells (cancer cells, stromal cells, immune system, or endothelial cells). Other cell types could also be added as required.

Figure IX-7 shows the confocal microscopy images as described in the schematics of **Figure IX-6:** endothelial cells seeded on the microchannel, while colorectal cells are encapsulated throughout the enzymatically crosslinked silk hydrogel microfluidic device.

Figure IX-8 shows the viability of cells encapsulated in the enzymatically crosslinked silk fibroin hydrogel-based microfluidic device. Live/dead assay was performed and observed under confocal microscope. Live/dead assay was performed and observed under confocal microscope. Live cells are stained in green, while dead cells are stained in red.

Figure IX-9 shows the perfusion of blue ink through the inlet (A); formation of soluble ink gradient (B); and diffusion of food colouring ink visible in the microchannels, allowing for the formation of diffusion gradients of drugs/nanoparticles (C).

In an embodiment, oscillatory rheological measurements were performed to determine the rheological properties of the enzymatically cross-linked silk fibrin hydrogels at different concentration (6 %, 12 %, and 14 % of silk solution). The results were compared to PDMS.

Figure IX-10 shows liquid perfusion through the enzymatically crosslinked silk fibroin hydrogel-based microfluidic device's microchannel. (A) Shows perfusion of blue ink through the inlet. (B1) and (B2) show magnified images of liquid perfusion inside the serpentine microchannel.

Table IX-1 - Composition, rheological properties of hydrogels at a frequency of 0.1 Hz.

Name	Cells	Incubation Time (minutes)	Storage modulus (G', Pa)	Loss modulus (G", Pa)
6 %	no	30	1963±151	30±16
12 %	no	30	6585 ± 253	152 ± 48
14 %	no	30	7173 ± 605	387 ± 64

The term "comprising" whenever used in this document is intended to indicate the presence of stated features, integers, steps, components, but not to preclude the presence or addition of one or more other features, integers, steps, components or groups thereof.

The disclosure should not be seen in any way restricted to the embodiments described and a person with ordinary skill in the art will foresee many possibilities to modifications thereof.

The above described embodiments are combinable.

IX-6. CLAIMS

1. An enzymatically cross-linked silk fibroin hydrogel microfluidic device; wherein said device is flexible and elastic; and wherein said microfluidic device comprises a microchannel configured to allow liquid media to flow.

2. The enzymatically cross-linked silk fibroin microfluidic device according to the previous claim wherein the hydrogel is transparent, preferably for at least 7 days.

3. The enzymatically cross-linked silk fibroin microfluidic device according to any of the previous claims wherein the hydrogel is biodegradable.

4. The enzymatically cross-linked silk fibroin microfluidic device according to any of the previous claims wherein the device is implantable.

5. The enzymatically cross-linked silk fibroin microfluidic device according to any of the previous claims wherein the silk fibroin hydrogel retains its amorphous protein structure for at least 7 days.

6. The enzymatically cross-linked silk fibroin microfluidic device according to any of the previous claims wherein the enzymatic cross-linking of the silk fibroin hydrogel is by an enzyme horseradish peroxidase and an oxidizer hydrogen peroxide.

7. The enzymatically cross-linked silk fibroin microfluidic device according to any of the previous claims wherein the concentration of silk fibroin is from 3 % to 25 % (wt.%) of silk fibroin, preferably from 8 % to 20 % (wt %) of silk fibroin, more preferably from 10 % to 12 % (wt %) of silk fibroin.

8. The enzymatically cross-linked silk fibroin microfluidic device according to any of the previous claims wherein the device further comprises extracellular matrix, growth factor, drug, cell, and combinations thereof.

9. The enzymatically cross-linked silk fibroin microfluidic device according to any of the previous claim wherein the cell is selected from the list: cancer cell, stromal cell, immune system, endothelial cell, or combinations thereof.

10. The enzymatically cross-linked silk fibroin microfluidic device according to any of the previous claims further comprising:

an inlet for liquid media to enter the microfluidic device;

an intermediate meandering section for liquid media to flow;

a first microchannel connecting the inlet and the intermediate meandering microchannel;

an outlet for liquid media to exit the microfluidic device;

a second microchannel connecting the outlet and the intermediate meandering part.

11. The enzymatically cross-linked silk fibroin microfluidic device according to the previous claim wherein the length of the device is from 150 mm to 5 mm, preferably 75 mm to 10 mm, more preferably 42 mm.

12. The enzymatically cross-linked silk fibroin microfluidic device according to the previous claim wherein the width of the inlet and the outlet are each from 10 mm to 200 μm, preferably 5 mm to 500 μm, more preferably 1 mm.

13. The enzymatically cross-linked silk fibroin microfluidic device according to the previous claim wherein the thickness of the intermediate meandering section from 20 mm to 1 mm, preferably 10 mm to 2 mm, more preferably 6.5 mm.

14. The enzymatically cross-linked silk fibroin microfluidic device according to the previous claim wherein the width of the microchannel is from 10 μm to 2 mm, preferably 100 μm to 1 mm, more preferably 200 μm.

15. An enzymatically cross-linked silk fibroin hydrogel for use in medicine or veterinary, wherein the enzymatically cross-linked silk fibroin hydrogel is administrated in the form of an implantable microfluidic device.

16. The enzymatically cross-linked silk fibroin hydrogel according to the previous claim for use in tissue engineering, organ disease models, tissue disease models, drug discovery, drug screening, tissue implant or tissue regeneration.

17. A Kit comprising an implantable microfluidic device or a hydrogel according to any of the previous claims.

18. The kit or the hydrogel according to the previous claim wherein the kit further comprises at least one of the following components: Cells, growth factor, therapeutic agent, and mixtures thereof.

19. A method of producing the implantable microfluidic device according to any of the previous claims comprising the following steps:

obtaining a polymethylsiloxane silanized master mold with predetermined microchannels;

preparing an enzymatically cross-linked silk fibroin hydrogel with horseradish peroxidase and hydrogen peroxide;

adding the silk fibroin hydrogel into the positive PDMS mold and incubate to form a hydrogel membrane.

20. The method of producing the implantable microfluidic device according to the previous claim comprising the following steps:

obtaining a master mold with predetermined microchannels, preferably a SU-8 master mold;

adding a polymethylsiloxane (PDMS) solution, preferably at a ratio of 10:1 pre-polymer:crosslinker, ($v_{pre\text{-}polymer}/v_{crosslinker,}$ and/or $w_{pre\text{-}polymer}/w_{crosslinker}$), to the master mold and allow the PDMS to cure in order to obtain a PDMS negative master mold which is a negative master mold replica; silanizing of the PDMS negative master mold to obtain a TCS-silanized negative PDMS master; pouring a second PDMS solution, preferably at a ratio of 10:1 pre-polymer:crosslinker ($v_{pre\text{-}polymer}/v_{crosslinker}$, and/or $w_{pre\text{-}polymer}/w_{crosslinker}$) on top of the TCS-silanized negative PDMS master, degas, and cure;

peeling off the negative PDMS mold to obtain a positive PDMS master mold;

preparing an enzymatically cross-linked silk fibroin hydrogel with horseradish peroxidase and hydrogen peroxide;

adding the silk fibroin hydrogel into the positive PDMS mold and incubate to form a hydrogel membrane.

21. The method of producing the implantable microfluidic device according to any of the previous claims 21-22 wherein the aqueous silk fibroin solution has a silk fibroin concentration of at least 3 % (wt.%), preferably from 3-25 % (wt.%), more preferably from 8 to 20 % (wt.%), more preferably from 10 to 12 % (wt.%).

22. The method of producing the implantable enzymatically cross-linked silk fibroin microfluidic device according to any of the previous claims 21-23 wherein the SU-8 master mold is produced using UV-photolithography.

23. The method of producing the enzymatically cross-linked silk fibroin implantable microfluidic device according to any of the previous claims 21-24 wherein the PDMS is added to the SU-8 master mold and cured for at least 3 hours, preferably for a duration from 3 hours to 12 hours, at about 37 °C.

24. The method of producing the implantable enzymatically cross-linked silk fibroin microfluidic device according to any of the previous claims 21-25 wherein the PDMS solution is allowed to cure on the TCS-silanized negative PDMS master for at least 3 hours, preferably for a duration from 3 hours to 12 hours, at about 37 °C, until the solution is completely cured.

25. The method of producing the implantable enzymatically cross-linked silk fibroin microfluidic device according to any of the previous claims 21-26 wherein the silk fibroin solution is added to the positive PDMS mold and incubated for at least 1 hour, preferably for a duration from 1 hour to 5 hours, at about 37 °C.

IX-7. LIST OF FIGURES

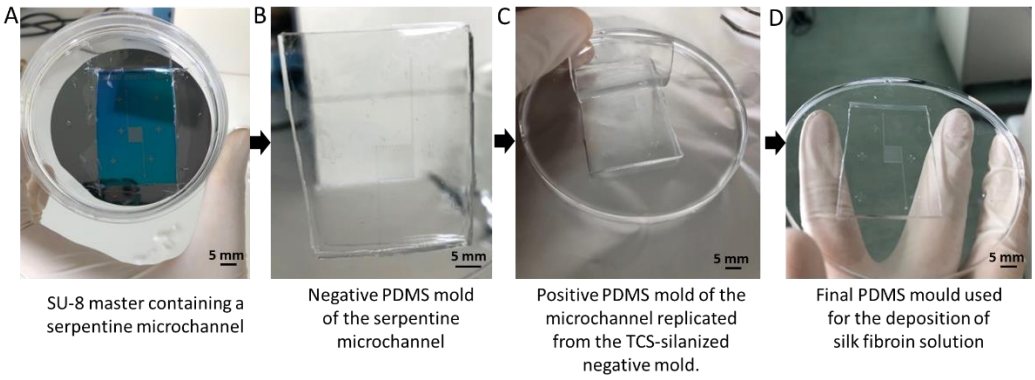

Figure IX-1 - Illustration the process of producing the PDMS mold used to produce the enzymatically crosslinked silk fibroin hydrogel-based microfluidic device.

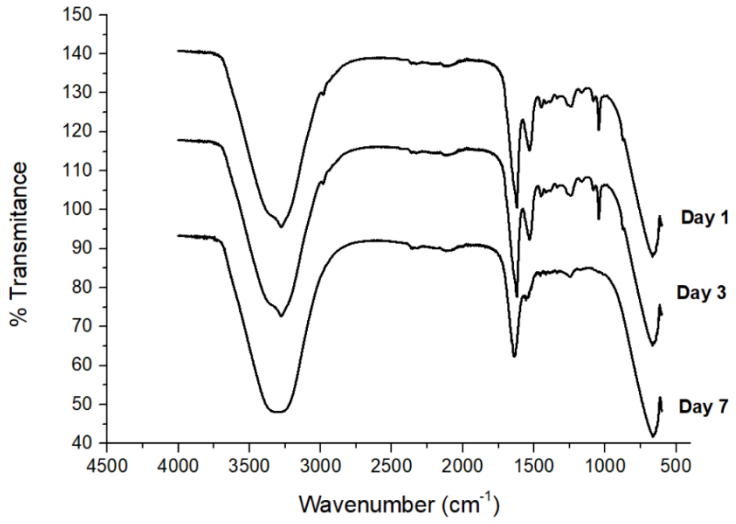

Figure IX-2 – ATR-FTIR spectra for the enzymatically crosslinked silk fibroin hydrogel (with 12 % concentration of silk fibroin) retaining the amorphous protein structure for at least 7 days.

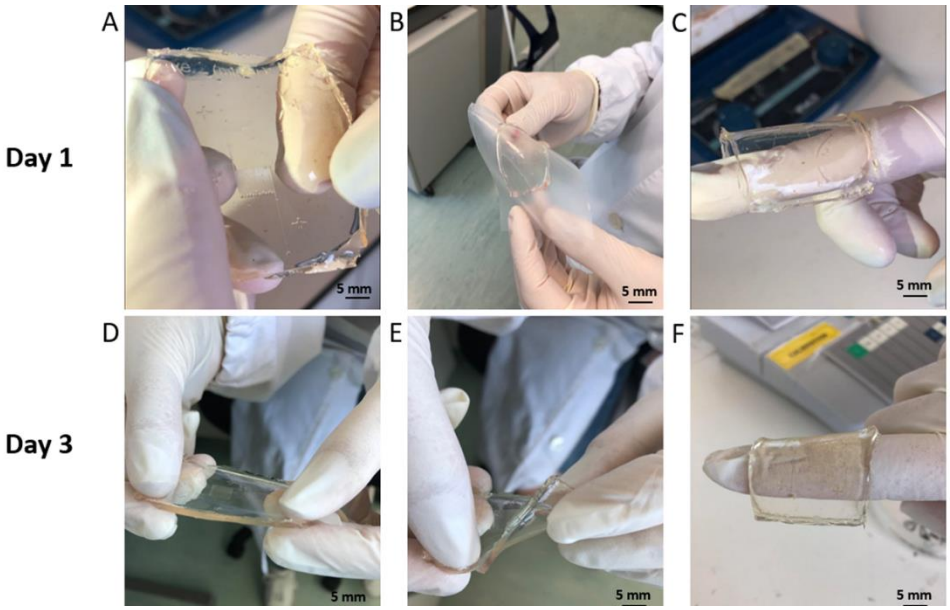

Figure IX-3 – Demonstration of the flexibility and elasticity of the transparent enzymatically crosslinked silk fibroin hydrogel at day 1 and at day 3.

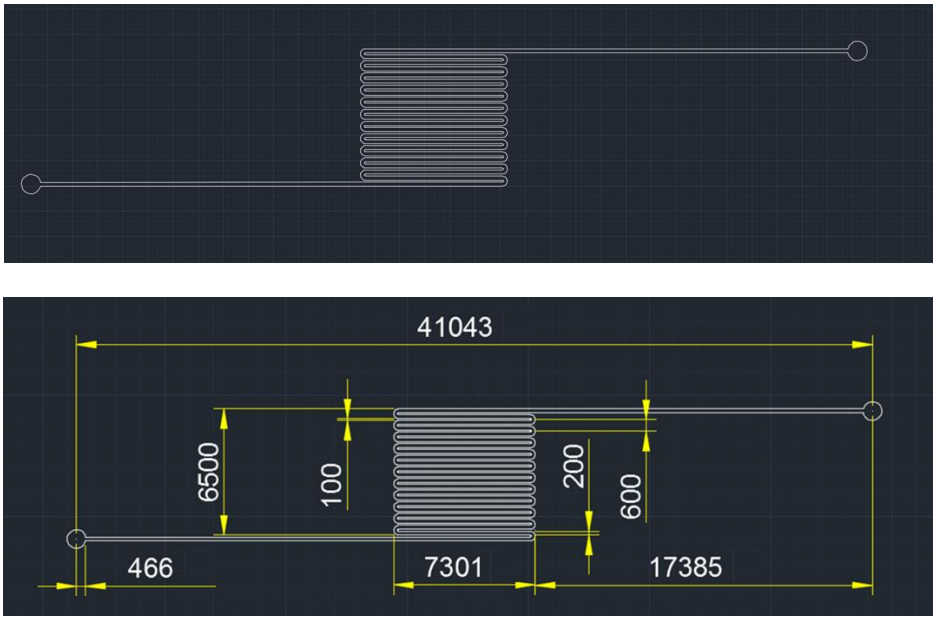

Figure IX-4 - Schematically illustrates an exemplification of the structure of the enzymatically crosslinked silk fibroin microfluidic device. In this case, including a meandering serpentine channel, inlets and outlets. Figure 4A is without dimensions while Figure 4B is dimensions in µm.

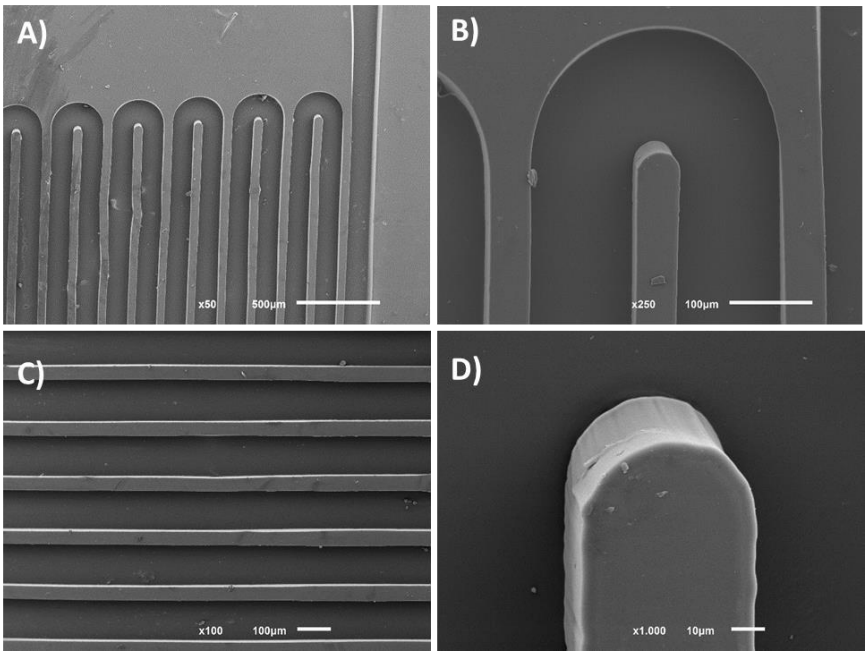

Figure IX-5 - SEM images of the 3D enzymatically crosslinked silk fibroin hydrogel structures after drying using point drying. Scale bars: 500 µm (a and b), and 100 µm (c).

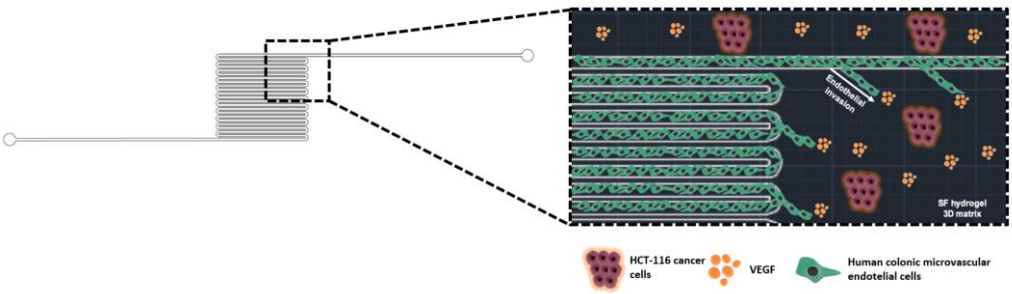

Figure IX-6 - Schematically illustration of an example of what the enzymatically crosslinked silk fibroin hydrogel can be used for.

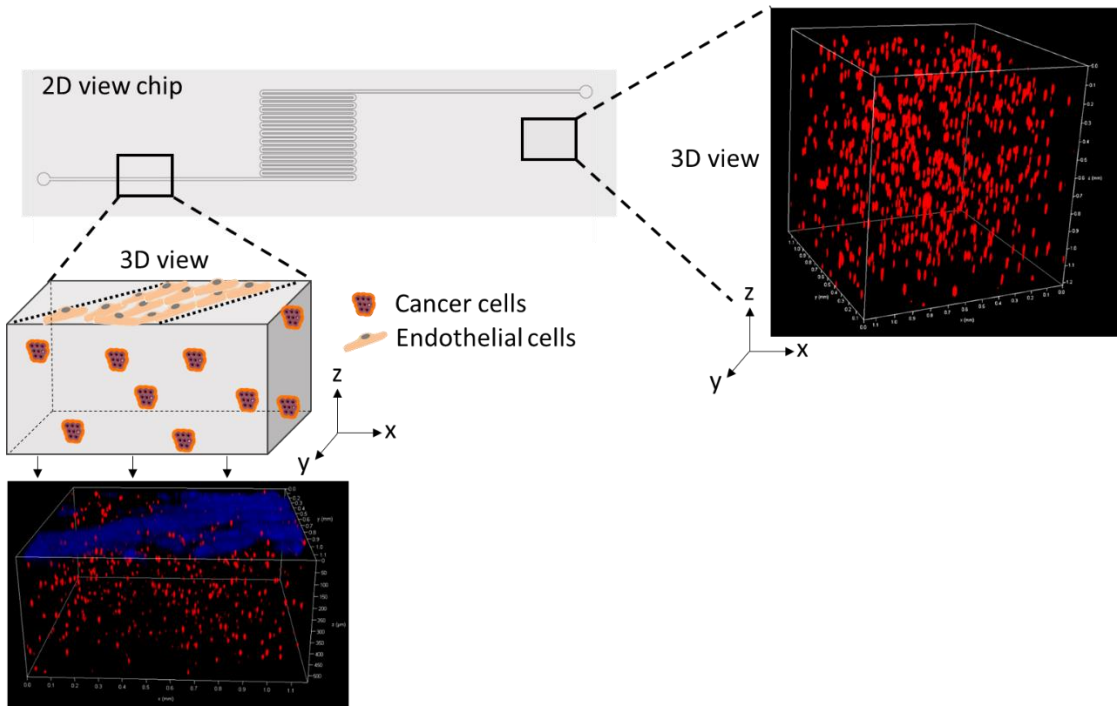

Figure IX-7 - Confocal microscopy images as described in the schematics of figure 6: endothelial cells seeded on the microchannel while colorectal cells are encapsulated throughout the enzymatically crosslinked silk fibroin microfluidic device.

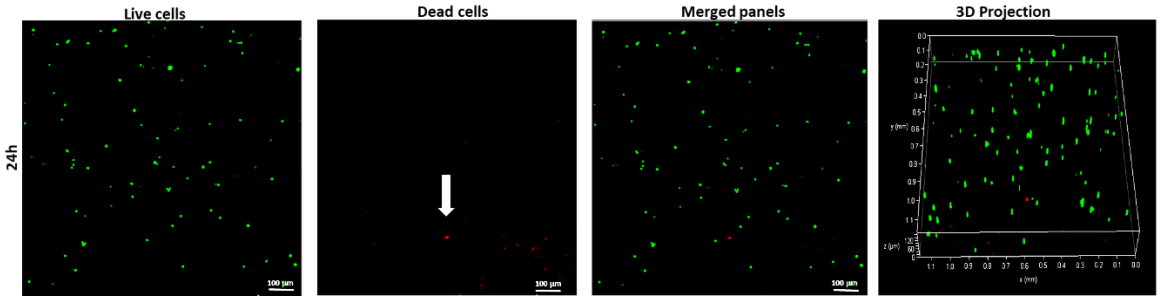

Figure IX-8 - Viability of cells encapsulated in the enzymatically crosslinked silk fibroin hydrogel-based microfluidic device. Live/dead assay was performed and observed under confocal microscope.

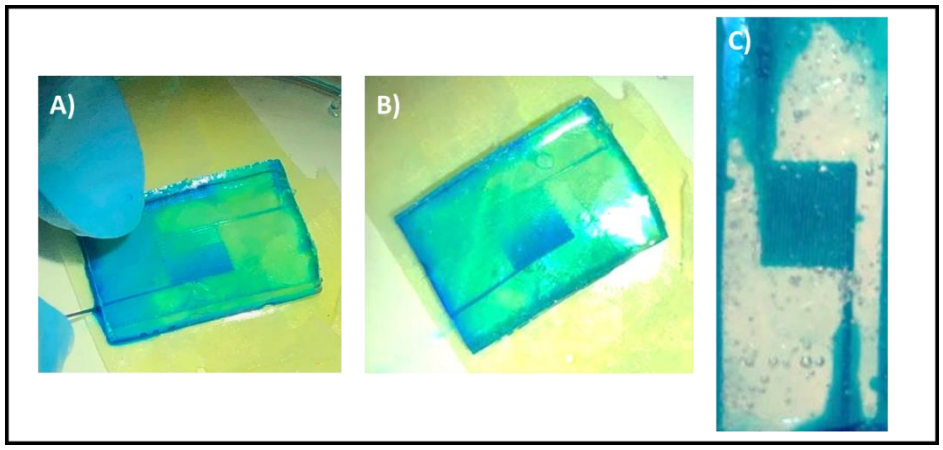

Figure IX-9 - Perfusion of blue ink through the inlet (A); formation of soluble food colouring ink gradient (B); and diffusion of ink visible in the microchannels, allowing for the formation of diffusion gradients of drugs/nanoparticles.

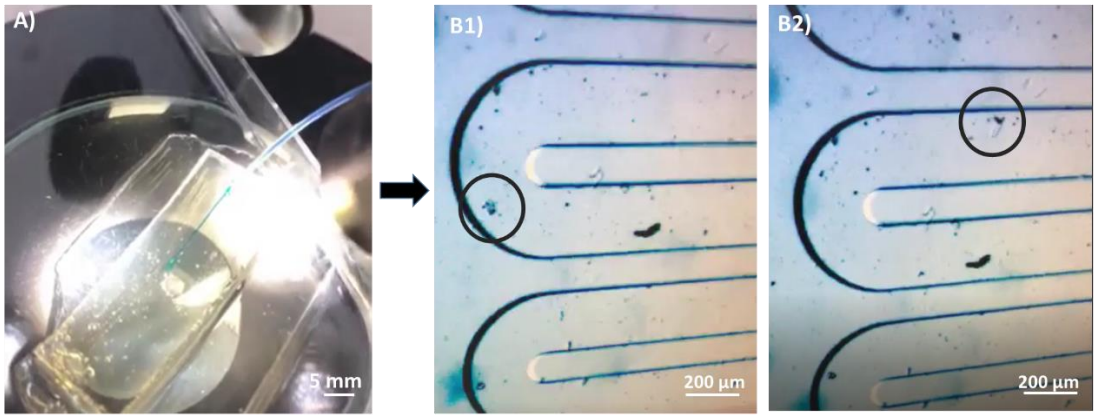

Figure IX-10 - Liquid perfusion through the enzymatically crosslinked silk fibroin hydrogel-based microfluidic device's microchannel. (A) Shows perfusion of blue ink through the inlet. (B1) and (B2) show magnified images of liquid perfusion inside the serpentine microchannel (or meandering section).

IX-8. REFERENCES

1. Buchanan, C.F., et al., *Three-dimensional microfluidic collagen hydrogels for investigating flow-mediated tumor-endothelial signaling and vascular organization.* Tissue engineering. Part C, Methods, 2014. **20**(1): p. 64-75.
2. Liu, J., et al., *Hydrogels for Engineering of Perfusable Vascular Networks.* International journal of molecular sciences, 2015. **16**(7): p. 15997-16016.
3. Johann, R. and P. Renaud, *Microfluidic patterning of alginate hydrogels*. Vol. 2. 2007. 73-9.
4. Lee, Y., et al., *Photo-crosslinkable hydrogel-based 3D microfluidic culture device: Microfluidics and Miniaturization*. Vol. 36. 2015.
5. Chen, C., et al., *3D-printed Microfluidic Devices: Fabrication, Advantages and Limitations-a Mini Review.* Anal Methods, 2016. **8**(31): p. 6005-6012.
6. Chung, B.G., et al., *Microfluidic fabrication of microengineered hydrogels and their application in tissue engineering.* Lab Chip, 2012. **12**(1): p. 45-59.

7. Ling, Y., et al., *A cell-laden microfluidic hydrogel.* Lab on a Chip, 2007. **7**(6): p. 756-762.
8. Bertassoni, L.E., et al., *Hydrogel bioprinted microchannel networks for vascularization of tissue engineering constructs.* Lab on a Chip, 2014. **14**(13): p. 2202-2211.
9. Gillette, B.M., et al., *In situ collagen assembly for integrating microfabricated three-dimensional cell-seeded matrices.* Nat Mater, 2008. **7**(8): p. 636-40.
10. Choi, N.W., et al., *Microfluidic scaffolds for tissue engineering.* Nat Mater, 2007. **6**(11): p. 908-15.
11. Carvalho, M.R., et al., *Microfluidics: Tuning Enzymatically Crosslinked Silk Fibroin Hydrogel Properties for the Development of a Colorectal Cancer Extravasation 3D Model on a Chip (Global Challenges 5-6/2018).* Global Challenges, 2018. **2**(5-6): p. 1870164.
12. Carvalho, C.R., et al., *Tunable Enzymatically Cross-Linked Silk Fibroin Tubular Conduits for Guided Tissue Regeneration.* 2018. **7**(17): p. e1800186.
13. Costa, J.B., et al., *INKS FOR 3D PRINTING, METHODS OF PRODUCTION AND USES THEREOF*. Patent WO/2018/225049.
14. Teixeira, L.S., et al., *Enzyme-catalyzed crosslinkable hydrogels: emerging strategies for tissue engineering.* Biomaterials, 2012. **33**(5): p. 1281-90.
15. Bettinger, C.J., et al., *Silk Fibroin Microfluidic Devices.* Adv Mater, 2007. **19**(5): p. 2847-2850.

SECTION 4

Conclusions and Future Perspectives

Chapter X

Conclusions and Future Perspectives

Chapter X

Conclusions and Future perspectives

X-1. GENERAL CONCLUSIONS

Colorectal cancer represents the most prevalent cause of cancer-related deaths, mainly resulting from its metastatic nature. Conventional adjuvant therapies for colorectal cancer including chemo, radiotherapies and biological agents have improved cancer therapy, but they carry serious side effects such as the development of drug resistance and toxicity to healthy cells. All of the above are strong indicators suggesting that we need better strategies to fight colorectal cancer. More importantly, science needs to move forward with the development and screening of new chemotherapeutic drugs, since in the particular case of cancer drugs, studies report that the average rate of successful translation from animal models to clinical cancer trials is less than 8 %.

The major goal of the work developed under the scope of the present thesis was to develop new strategies to improve the state of the art in what regards 3D microfluidic *in vitro* models for colorectal cancer research, with a strong approach on dendrimer nanoparticles and natural-origin polymers, such as carboxymethilchitosan and silk fibroin.

To improve the state of the art, the development of dendrimer nanoparticles (targeted and not targeted); the understanding of the fundamental differences between cancer research experiments in 2D vs. 3D; the differences between static conditions vs. dynamic conditions, and the exploration of new extracellular matrix-like materials to be used as alternative to Matrigel®, seems like a promising option leading to a successful outcome. These were the goals of the first experimental chapters of this thesis. All the technologies studied and proposed procured to match the main drawbacks identified in the literature and attempted to overcome them, recurring to innovative and more precise technologies.

In **Chapter V**, the goal of this work was to develop a platform composed of labeled dendrimer nanoparticles and a microfluidic device for real-time monitoring of cancer cells' fate. Also, it was important to study the influence of a dynamic environment (*e.g.* perfusion of FITC-labeled carboxymethylchitosan/poly(amidoamine) dendrimer nanoparticles in the internalization levels and potential cytotoxicity in three different cancer cell lines (glioblastoma, colorectal and cervical cancer).

When compared to the traditional 2D culture flasks, cells cultured under perfusion showed higher sensitivity to the nanoparticles. Reports in the literature had shown the opposite result, being gold nanoparticles less toxic e dynamic conditions. This is evidence that efforts have to be done in order to improve our experimental designs in an attempt to get closer to more relevant (*in vivo* like) conditions. After the extensive characterization performed on the dendrimer nanoparticles, including differential scanning calorimetry (that had never been performed in carboxymethylchitosan/poly(amidoamine)), further biological work led to the conclusion that a carboxymethylchitosan/poly(amidoamine) dendrimer concentration of 0.5 mg/mL was ideal for further studies, since it was demonstrated not to be cytotoxic in dynamic conditions. By the end of this first chapter, the proposed microfluidic-based was validated for real-time monitoring of nanoparticles fate, which upon more studies, namely the assessment of an anticancer drug release effect, could be used for cancer theranostics.

In **Chapter VI**, the thesis focuses on colorectal cancer, and there is an increase in the complexity of the microfluidic platform used. Moreover, it was aimed at moving forward the general knowledge in terms of understanding the specific contribution of the mechanical properties of materials/hydrogels used as extracellular matrix like materials in 3D cancer models. Silk was chosen due to its unique properties, both biologic and mechanical, as well as the ability to isolate the effect of the mechanical properties due to the lack of mammalian motifs. Moreover, we were able to compared cancer cell migration in the commercial Vena4™ microfluidic platform with the traditionally used Boyden chamber assay, to assess any particular differences. 2 and 3 % enzymatically crosslinked silk fibroin hydrogels were chosen based on a previous screening, and compared to Matrigel® (gold standard extracellular matrix material). The conclusions of this work were striking: when comparing colorectal cancer cell migration in 3D. Although Matrigel® is much softer (seen in rheological analysis) and often chosen as the main extracellular matrix like material, 2 % silk hydrogel allowed more intense cellular migration (despite the higher stiffness). Moreover, in the Boyden chamber assay the results were not similar, being the migration levels comparable between 2 % silk fibroin and Matrigel®. Again, evidence was shown that the models chosen to perform cancer studies play an important role in the results that are obtained, as well as the materials. Controlling and understanding the effect of the various components of these models pushes the field forward and enables investigation of interactions within the tumor microenvironment, as well as the response to stimuli, such as chemoattractants and chemotherapeutics.

For the purpose of **Chapter VII,** a very fruitful collaboration was established between 3Bs Research Group and MERLN Institute (Maastricht University, Netherlands). The main goal was to develop a 3D microfluidic platform with the following requirements: ease of use; mimic the colorectal tumor complexity (vascular and tumor parts), possibility to create gradients; possibility of real-time imaging; performance of immunocytochemistry and cell retrieval after the experiments for polymerase chain reaction (PCR) analysis. This task was achieved using the design explored in **Chapter VII**, and by means of successfully establishing a dynamic co-culture of colonic endothelial microvascular cells and HCT-116 colorectal cancer cells embedded in Matrigel® in central chamber. Most of all, the advantages of our platform as compared to others of the same type found in the literature (central chamber for 3D matrix laterally sided by perfusable channels) are: 1) facile molecular cell analysis; 2) physiologically inspired design of radial drug penetration into solid tumors; 3) hybrid co-culture system to show efficiency of drug penetration through a micro-vascular network into a cancer-mimicking tissue, comprised of a supporting relevant matrix with colorectal cancer cells; 4) real-time imaging of drug delivery and its effect on cell viability; 5) design compatible with assessing physiologically-relevant cell migration, thus metastatic events (not the scope of the current manuscript); and, 6) system easily combinable with organoid seeding of the central chamber, which allows for the integration of other models. In general, we were able to generate stable gradients of nanoparticles releasing gemcitabine, resulting in a gradient of colorectal cancer cell death. Moreover, we observed a down-regulation for all genes teste (MMP-1, Caspase-3 and Ki-67). This model was validated as a platform for precision drug screening that can later be applied in personalized medicine.

Following the observations on **Chapter VII** regarding the deleterious side-effects of gemcitabine release over the endothelial cells, it was of crucial importance the development of a strategy for targeting the nanoparticles internalization (and its consequent drug release) in colorectal cancer cells, for a more effective treatment and reduced toxicity. To achieve this goal, **Chapter VIII** aimed at carboxymethylchitosan/poly(amidoamine) targeting towards colorectal cancer cells via interaction with the laminin receptor, whose expression is known to be upregulated in some types of cancer (*e.g.* breast and ovarian cancer). Overall, this study provided a proof-of-concept for the ability of surface attached YIGSR, a laminin-derived peptide, to carboxymethylchitosan/poly(amidoamine) to target over-expressing laminin receptor HCT-116 colorectal cancer cells, when in co-culture with L929 cells. This was observed when co-cultures were seeded in traditional 2D well-plates or in a Matrigel® drop (3D). Not only the preferential internalization was demonstrated, but also the effect of gemcitabine drug release

from these modified nanoparticles was assessed in these systems. Results show clear preferential internalization of nanoparticles in cancer cells, as well as higher levels of cancer cell death when in the presence of other non-cancerous cell types.

Chapter IX is focused on an international patent which discloses a new methodology to obtain the transparent enzymatically crosslinked silk fibroin hydrogel-based microfluidic device, as well as their possible applications in Tissue Engineering and biomedical field in general. The innovation of the method relied on the transformation of an initially produced aqueous silk fibroin solution into an amorphous and optically transparent hydrogel, through a horseradish peroxidase-mediated crosslink reaction. Combining this technology with the use of microfabrication (namely UV-photolithography and replica moulding) for the fabrication of microfluidic channels, it is possible to obtain a fully transparent and flexible microfluidic silk platform. This methodology allowed overcoming the problems of previously developed PDMS microfluidic platforms, making it implantable due to silk fibroin biocompatibility and biodegradability. After the initial laboratorial work performed in the scope of the patent, the method for fabricating an enzymatically cross-linked silk fibroin hydrogel microfluidic device; flexible and elastic; comprising microchannels configured to allow liquid media to flow, was developed. This platform can find use in medicine or veterinary, wherein the enzymatically cross-linked silk fibroin hydrogel is administrated in the form of an implantable microfluidic device. Chemoattractants, therapeutic drugs or other molecules of interest can be easily incorporated in the silk fibroin solution, even in the form of gradients Therefore, it can be used in tissue engineering, organ disease models, tissue disease models, drug discovery, drug screening, tissue implant or tissue regeneration. The developed enzymatically crosslinked silk fibroin microfluidic platform is transparent, flexible and reproducible, allowing as well as the possibility of modulating the mechanical properties according to the tissue that is being studied.

X-2. FUTURE RESEARCH DIRECTIONS

This thesis aimed at combining several fields of research for the purpose of moving forward and increasing the current knowledge on cancer research, specifically colorectal cancer research. For this, nanotechnology principles were combined with microfluidics and tissue engineering concepts. To date, despite the remarkable advances and progresses in colorectal cancer studies, there is no ideal microfluidic model that could guarantee future success in clinical trials, or ideal drug-loaded nanoparticle that would undoubtedly treat colorectal cancer. One of the problems that has slowed down

the development and approval of new anticancer therapies is the lack of pre-clinical models that can be used to identify key molecular, cellular and biophysical features of human cancer progression. This is because most *in vitro* cancer models fail to faithfully recapitulate the native tissue and organ microenvironment in which tumors form, which substantially contributes to the complex pathophysiology of the disease. More complex *in vitro* cancer models have been developed, including transwell cell cultures, spheroids and organoids grown within flexible extracellular matrix gels, which better mimic normal and cancerous tissue development than cells maintained on conventional 2D substrates. But these models still lack the tissue–tissue interfaces, organ-level structures, fluid flows and mechanical cues that cells experience within living organs, and furthermore, it is difficult to collect samples from the different tissue micro-compartments. Microfluidic devices are among the most promising tools to overcome these hurdles and best mimic *in vivo* like conditions, either in normal or disease scenarios, such as tumorigenesis or pathogenesis. Together with the potential of biomaterials as artificial extracellular matrix, its combination with microfluidics represents the ability to more closely mimic cells' natural microenvironment, concerning its three-dimensional nature, continuous perfusion with nutrients and cells' crosstalk. Due to miniaturization and increased experimental throughput, microfluidics have generated significant interest in the drug discovery and development domain. In its turn, biomaterials are gradually being developed as *in vitro* microenvironments mimicking *in vivo* cell niches. It was one of our main goals to explore the newly developed enzymatically crosslinked silk fibroin hydrogels as a new biomaterial, isolating the effects of mechanical properties. It is believed that chip-based 3D cell culture in cancer research will be largely dependent on the improvement of biomaterials that can best emulate the extracellular matrix and the capacity to scale-up these complex technologies. Moreover, microfluidic models need standardization and reproducible formats suitable for high-throughput applications. If cell migration studies are to be used to test drug efficacy in this context, these models have to be reliable in what regards its fabrication and incorporation of the most adequate biomaterials to reduce arbitrary cell migration patterns.

Regarding the use of dendrimer nanoparticles, its future application to nanomedicine depends on batch-to-batch reproducibility of the final materials' properties. Therefore, to advance with dendrimer-based materials into clinical trials it is crucial to develop well-defined multifunctional dendrimers with a controlled number and location of drugs, targeting groups, imaging agents, solubilizing agents and/or other relevant motifs. Recent developments on synthetic tools are defying the outdated perception that dendrimers' synthesis is complex, slow, tedious and cost-prohibitive. Indeed, the very low amount of

dendrimers to be used in therapeutic applications will most likely dilute their cost, making their cost/benefit relationship promising for further product development. The next steps in the dendrimer field will be very challenging and exciting, because it is time to meet the high expectations that were placed on dendrimers.

From a practical point of view, there is a never ending myriad of possibilities when it comes to complementing and deepening the developed work. The first one would be the use of primary cells from colon, either normal or cancerous. No work is fully complete without testing the developed technologies in primary cells. For this, the already established collaborations with local hospitals for the acquisition of colorectal biopsies would be of crucial importance, making the performed tests adjustable to the proof-of-concept approach for personalized medicine. An *in silico* model of the distribution of the nanoparticles thought the central chamber would be a plus to complement **Chapter VII**. The real possibility of developing a computer mathematical model correlating the exact fluorescence intensity with drug release concentration present at each point would be of added value and could consist of a continuation of this work. Regarding **Chapter VIII,** an *in vivo* study in mice to determine the effect of drug loaded targeted nanoparticles in colorectal cancer induced mice would be of added value.

One particularly promising strategy to be pursued in this line of work would be the circulating tumor cells approach. Using an implantable microfluidic device such as the one developed in this thesis in **Chapter IX**, could be able to recruit and capture circulating tumor cells in the patient, being later subjected to drugs screening. Owing to the less-invasive nature of this procedure, chemotherapy could be tested, and routine monitoring of cancer progression could be achieved. Although promising, implantability tests have to be performed in mouse models first, which will be the next immediate step.

As a conclusion of this thesis, although significant steps have been taken separately in what regards the study of biomaterials in the tumorigenesis processes and cancer cell migration, development of drug screening technologies, and nanoparticle targeting, studies involving all of the aforementioned technologies still have to be performed to test all these technologies together.

Before the fight against cancer is finally won, the advances in in the mentioned fields will continue to help researchers achieve a better understanding of cancer biology as well as develop novel therapeutic strategies aiming personalized treatments.